



TECHNISCHE
UNIVERSITÄT
WIEN
Vienna University of Technology

DISSERTATION

INHOMOGENEOUS MAGNETIZATION PROCESSES IN ADVANCED RECORDING MEDIA

Ausgeführt zum Zwecke der Erlangung des akademischen Grades
eines Doktors der Technischen Wissenschaften

Unter der Leitung von
Univ. Prof. Dipl. –Ing. Dr. Techn. Josef Fidler
Institute für Festkörperphysik / E138

eingereicht an der Technischen Universität Wien
Fakultät für Physik

durch

Jehyun LEE
Matr.Nr. 0827169
Fendigasse 27/4
1050 Wien

Wien, am 18. Mai 2011

Deine Zauber binden wieder
그대의 마법으로 다시 뭉쳐
Was die Mode streng geteilt;
비록 문화는 다를지라도
Alle Menschen werden Brüder
모든 인류는 형제가 된다.
Wo dein sanfter Flügel weilt.
그대의 다정한 날개가 깃들이는 곳.

Die Ode „An die Freude“, Gedichte Friedrich Schillers (1785)
Die 9. Sinfonie in d-Moll op. 125, Ludwig van Beethoven (1824)

실러 作詩, 베토벤 作曲. “환희의 송가”中.

2011년 5월 13일 밤, Wiener Festwochen Eröffnung 이 열린 시청사 광장에서
아내와 함께 들으며 오스트리아 사람들과 함께 부른다.

ABSTRACT

Magnetization reversal processes of magnetic recording media are determined by the intrinsic properties such as crystalline anisotropy K_1 and saturation magnetization J_S , extrinsic properties such as shape, size and distribution of phases, and the external field gradient applied on the media. Taking advantage of finite element micromagnetic simulations, the detailed reversal processes and the influence of the intrinsic and extrinsic properties on the reversal behavior have been studied. The main objective of the thesis was to study advanced recording media, with a bit size smaller than 25 nm, corresponding to an areal density of at least 1 Tb/in². For this dimension the media has a relatively small crystalline anisotropy $K_1 < 1 \text{ MJ/m}^3$ which is sufficient for the “Stoner-Wohlfarth” coherent rotation process. The magnetization reversal process becomes inhomogeneous as the K_1 increases larger than 1 MJ/m³ and the domain wall width gets comparable with the bit dimension. The reversal by nucleation of reversal domains and the domain wall motion are more dominant, if the media exhibit a narrow domain wall followed by large K_1 values. The concept of exchange spring media which consist of hard and soft magnetic layers, is one of the most promising structure for the switching of hard magnetic nano sized grains and avoiding the superparamagnetic effect of thermal switching. In the exchange spring media, a reversal domain is nucleated in the soft magnetic layer followed by the expansion into the the hard layer.

Various stacks of exchange spring media, FePtCu L1₀(hard) / [Co/Pt]_N(soft) and FePt L1₀(hard)/ FePt A1(soft) were investigated. The microstructure of exchange spring media was directly studied using nanoanalytical and high resolution transmission electron microscopy (TEM). In the FePtCu/ [Co/Pt]_N multilayer exchange spring media, the interface recrystallization and element interdiffusion between the hard/soft interface by heat treatment were found. For the case of the sputtered FePt L1₀/ FePt A1 structure a rough interphase boundary between the L1₀ and the A1 phase was found. The TEM results were implemented to the finite element models for micromagnetic simulations. The switching field of the FePtCu hard layer was effectively reduced up to 40 % as the interlayer exchange coupling to the [Co/Pt]_N soft layer increases. The prediction of the switching field reduction has been proved by the experiment. Strong interlayer coupling supported domain wall propagation to the hard layer. In the FePt L1₀/ FePt A1 structure,

the spike of the hard layer at the rough interphase boundary helped domain wall propagation into the hard layer, therefore the switching field was reduced by 84 % compared with the single hard phase media only. The inhomogeneity of magnetization switching is also triggered by inhomogeneous external fields such as write head fields applied on recording media during the bit write process. The inhomogeneous write head field was obtained by analytic equations and the finite element method. Under the inhomogeneous magnetic head field, jitter transition between individual grains was reduced by 40 % in the exchange spring media with a top soft layer exposed to the stronger field. . On the other hand in the particulate media composed of hexagonal barium ferrite (h-BaFe), the individual particles were switched by coherent rotation only if the external field was larger than the switching field of the individual particle. The h-BaFe particulate media recording simulations were performed for linear densities larger than 400 kfc/in media varying head type, head field strength and head to media distance. Comparing various particulate media with sputtered CoCrPt-SiO₂ granular media it have been shown that the Lindholm ring head and single pole tip (SPT) head exhibit a similar signal to noise ratio in the written state. The best performance was found for the case of the SPT head with a soft underlayer, if the particles are perpendicularly oriented to the recording plane.

Another outcome of the thesis is to find out the contributions of the intrinsic and extrinsic properties on the switching field distribution (SFD) for 1 Tb/in² hard disk media for based on the bit patterned media concept. The SFD increases proportional to the deviation of the crystalline anisotropy and the bit diameter, whereas a drastic increase is induced by a small amount of the easy axis misorientation.

This study demonstrates the relationship between the inhomogeneity of the properties and the inhomogeneous reversal processes. The inhomogeneities of the intrinsic and extrinsic parameters with a phase distribution effectively resulted in the inhomogeneous reversals, as well as inhomogeneous external field gradient does.

ACKNOWLEDGEMENTS

It was one day in February, 2005. I came to 8th floor of Freihaus, Vienna University of Technology, and introduced myself as “please call me Mr. Lee ☺”. After one year I come to know a little bit about Austrian wine, beer, music, ski and micromagnetic simulations. Then I could not imagine that I can return to Vienna again and become real a part of the Advanced Magnetism Group, of Josef Fidler and Dieter Suess, with a strong relationship with Thomas Schrefl in Sankt Pölten University of Applied Physics.

I do not know the proper word to express my great thanks to Josef, Dieter and Thomas. In my times in Vienna, they are great supervisors not only on research, but also on life itself. They always give me a fresh stimulation and show me a new horizon I’ve never aware of. The attitude of yours on research and life will guide me in my lifetime.

Josef, thank you for believing me for many years. Even though (I feel that) I did not satisfied you in every time, but your endless trust made me much stronger. Therefore I could encourage myself to do better in the next time. You taught me how to stand up on my own feet. Also thanks to all of your kindness and taking care of me. When I become your age, I’d like to have your gentle Charisma. I wish you to keep your health and smile for next many tens of years!

I have to say how *wirklich* fortunate it was for me to meet Dieter. Full of energy, always activated and caring others. I have a dream that one day in Kitzbühel, with the vigorous skiers, with a piece of living octopus having in our teeth chewing, shouting out the words of hurray and cheering, one day right down on a slope of Jochberg Austrians and Koreans will be able to go through the deep powder snow together like Herman Maier and Toby Dawson! ;)

Thomas, it was a pity for me to have less chance to be with you in last three years. I think I was too tensed in some sence and too obsessed in fulfilling my duty, therefore I could not make enough time to spend time with you and many other friends. In spite of the few times we met in last years, a problem of mine was solved whenever you came to Vienna! Sometimes with your timely advise, and sometimes with a hint uprose during the discussions. I wish to be like you, inspiring the people around.

Speical thanks should be given to the USTEM members: Prof. Peter Schattschneider, Prof. Johanness Bernardi, Dr. Michael Stöger-Pollach, Prof. Peter Pongratz, Dr. Lawrence & Karin

Whitmore, Dr. Sabine Schwarz, Tomasz Wojcik and Jakob Gruber. I have disturbed them too much with a lot of questions. Without their kindness, it would not be possible for me to learn and operate TEM.

Of course, I appreciate my colleagues, Markus Fuger, Barbara Dymerska, Bernhard Bergmair, Stefan Suess, Thomas Huber, Florian Bruckner and Christian Vogler. They gave me smile and beer in the hard working times. They also solved many private difficulties caused by the language barrier and different cultures.

It was a very nice experience for me to collaborate with foreign groups.

Two weeks spent in Chemnitz with Prof. Manfred Albrecht, Dr. Denys Makarov and Dr. Christoph Brombacher was very beneficial for me. Working with very motivated people boosted me as well. The experience of producing a paper in two weeks gave me a great self-confidence, and most of all, it was a great fun to totally devoting myself on work!

Greek group, Dr. Dimitris Niarchos and Dr. Vasilis Alexandrakis gave me a rare chance to concentrate on a material which is very well known, but also very unique idea is included. At first time it was not easy, but with a strong assist of Barbara (thanks again!), I could enjoy exciting times *inside* TEM, like surfing the universe. I wish them to achieve a brilliant success.

I deeply thanks to Michael Sharrock and Barry Schechtman of INSIC consortium. They showed me a way of working with intensive feedback. Their motivated features stimulated me to go deeper, do better and think more. I believe they have sown a seed of self-motivation in my mind.

아들과 딸을 먼 이국에 보내놓은 채 믿고 기다리며 외로움을 많이 삭였을 인천과 목포의 부모님들, 진심으로 감사드립니다. 어느새 엄마가 된, 그러나 내 눈에는 항상 어린 동생과 착한 매제, 아랫입술을 죽 내밀고 꽃향기를 맡는 모습이 귀여운 조카 훈호. 아내에게 엄마 같은 처형과 속 깊은 형님, '이모 남편'에게 책가방을 붙여서 그려주는 꼬마 화가 지우. 남자답게 잘 생겨서 부러운 처남. 모두들 언제나 건강하시길 빌어요.

그리고 항상 일에 파묻혀있는 내 옆에서 많이 힘들었을텐데 힘든 내색을 하지 않은 채, 내가 넘어지려 할 때는 받쳐주고, 흔들리려 할 때는 중심을 잡아준 현명한 아내, 최지애에게 그 누구보다 큰 감사와 사랑을 드립니다.

TABLE OF CONTENTS

	Page
ABSTRACT	i
ACKNOWLEDGEMENTS	iii
LIST OF TABLES	ix
LIST OF FIGURES	x
1. Introduction	1
1.1. Ferromagnetism	4
(1) Quantum Mechanics on Magnetism	4
(2) Thermodynamics in Magnetism.....	7
1.2. Magnetic Reversal Modes	10
(1) Coherent Rotation	10
(2) Incoherent Rotations: Curling and Buckling	13
(3) Domain wall motion: Domain Nucleation and Propagation.....	17
(4) Precessional Motion	22
1.3. Numerical Micromagnetics	25
(1) Introduction of numerical micromagnetics	25
(2) Finite Difference Method Micromagnetics.....	29
(3) Finite Element Method Micromagnetics.....	30
(4) Energy barrier estimation : Nudged Elastic Band Method	35
2. Inhomogeneous Writing Magnetic Fields for Magnetic Recording	40
2.1. Longitudinal Head Field	40
(1) Karlqvist Head	40

(2) Lindholm Head	44
(3) Szczech Head	47
(4) Comparison of ring type heads	51
2.2. Perpendicular Head Field	53
(1) Single Pole Tip (SPT) Head.....	53
(2) SPT Head With Soft Underlayer (SUL)	55
2.3. Writing Head Fields Summary.....	56
3. Advanced Recording Media.....	58
3.1. Introduction: Recording Materials and Exchange Spring Scheme	58
(1) Trilemma.....	58
(2) Writing Process	59
- Using fully integrated micromagnetics	61
- Using precomputed field box	62
(3) Read Back Process	63
3.2. Bit Patterned Media (BPM).....	66
(1) BPM Designed for High Density Recording	66
(2) Contributions on Switching Field Distribution (SFD).....	68
(3) BPM Material Design: Exchange Spring BPM	76
(4) Writing on Exchange Spring BPM with a Moving Writing Head.....	77
- Influence of the head excitation position and write head field strength.....	78
- Effective Head Field Gradients in Exchange Spring Media.....	82
(5) FePtCu L1 ₀ / [Co/Pt] _N Exchange Spring Media	91
- Experiments (by TU Chemnitz, Germany)	91
- Microstructure Investigation	97
- Micromagnetic Simulations.....	103
- Conclusion.....	108

(6) FePt L1 ₀ / FePt A1 Graded Media	109
- Experiments with XRD analysis (by NCSR “D”, Greece).....	111
- Microstructure Investigation using TEM	118
- Micromagnetic Simulations.....	134
3.3. Particulate Media.....	146
(1) Introduction	146
(2) Hexagonal BaFe (h-BaFe) Particulate Media	147
- Writing Performance as a Function of Head to Media Distance.....	147
- Writing Performance under Various Writing Heads	161
3.4. Sputtered Film	166
(1) CoCrPt-SiO ₂ Granular Media	168
- Modeling from TEM Image	168
- Recording Performance	170
(2) [Co/Pt] _N Percolated Media.....	172
- Experiments (by TU Chemnitz, Germany, CNRS, France and SuperSTEM Laboratory Daresbury, UK).....	175
- Micromagnetic Simulations on Pinning/ Depinning Behavior	186
- Conclusion.....	196
4. Conclusion	197
REFERENCE.....	199
APPENDIX.....	219
- Preprocessing	219
: krnmaker	219
: cubearraymaker	221
: phasemaker	222

: replace-data.....	223
: replace-line	223
: anafield	224
: hexGen.....	226
- Postprocessing	227
: SFTPautodownmaker	227
: inp2dat	228
: inp2mag	230
: inisort	230
: SNR calculation using SignalAdd	231
LEBENSLAUF (Curriculum Vitae).....	234

LIST OF TABLES

Table	Page
Table 1. List of the various micromagnetic programs and their source.....	26
Table 2. Material parameters for trilayer exchange spring media.	77
Table 3. Comparison of K_{\max}, first derivative of Δp, and Energy barrier at 300 K and $K_{\text{hard}}/K_{\text{max}} = 1$.	85
Table 4. Geometric and magnetic properties of particulate media models. $\langle\theta\rangle$ and $\langle\varphi\rangle$ are the mean values of azimuth angle θ and polar angle φ, respectively.....	149

LIST OF FIGURES

Figure	Page
Fig. 1. The figure for the first magnetic recorder suggested by Valdemar Poulsen [1].....	1
Fig. 2. Commercial hard disk capacity over time [7].....	2
Fig. 3. Normalized anisotropy surfaces for (a) isotropic materials, (b) uniaxial anisotropic materials, (c) cubic anisotropic materials with $K_1 > 0$ and (d) cubic anisotropic materials with $K_1 < 0$. The three green lines are the x, y, z axes.....	6
Fig. 4. Phase diagrams of easy directions in (a) uniaxial and (b) cubic crystals [9].	6
Fig. 5. Normalized anisotropy surfaces for (a) conical anisotropy and (b) $\langle 110 \rangle$ easy axes.....	7
Fig. 6. Schematic diagram of a spheroid with an easy axis along the z-axis and magnetization M_s, under external field H_{ext}. The angle between the easy axis and external field is θ, whereas the one between the easy axis and the magnetization direction is φ.	10
Fig. 7. Hysteresis curves of a spherical single domain particle for different angles between anisotropy axis and external field.....	12
Fig. 8. Switching field by Stoner-Wohlfarth coherent rotation, (left) as a function of field applied angle and (right) reduced easy axis field and hard axis field, in	

other words, Stoner-Wohlfarth astroid. The axes z and x corresponds to the easy axis and the hard axis shown in Fig. 6. 12

Fig. 9. Three different nucleation modes. (a) homogeneous magnetization (b) curling, and (c) buckling..... 13

Fig. 10. Review of three different nucleation modes. (a) homogeneous rotations, (b) buckling, and (c) curling. The center of the curling mode is pointing out of (or into) the plane [21]. 14

Fig. 11. Hysteresis loops measured from nanomagnets of diameter (d) and thickness (t): (a) $d = 300$ nm, $t = 10$ nm; (b) $d = 100$ nm, $t = 10$ nm. The schematic annotation shows the magnetization within a circular nanomagnet, assuming a field oriented up the page [20]. 14

Fig. 12. The spin instabilities modes obtained with micromagnetic calculations for the circular dots with the $R = 0.1$ (a), 0.2 (b), and $0.25 \mu\text{m}$ (c) and fixed $L = 30$ nm. 15

Fig. 13. Hysteresis loops measured as a function of diameter (d) and thickness (t) from circular nanomagnets. For each loop the horizontal axis is applied field and the vertical axis is magnetization [20]. 16

Fig. 14. Characteristic laminar domain pattern of platelets for different Q -parameters. (a) Landau structure in $\langle 100 \rangle$ - α -Fe platelets. (b) Partial Landau–Kittel structure for intermediate Q values (Co). (c) Open Kittel structure for hard magnetic uniaxial crystals with $Q \geq 1$ (FeNdB) [9] 17

Fig. 15. Model of soft magnetic planar nucleus of width $2r_0$. Left side: Hex is perpendicular to the stripe, right one is parallel [9]. 18

Fig. 16. Schematic diagrams of Néel wall and Bloch wall 19

Fig. 17. The nucleation field (dashed) and coercive force (full curve) in terms of the coercive force of perfect material, as functions of the defect size, d . [23]..... 20

Fig. 18. Nucleation field of prolate spheroids (aspect ratio: 8) as a function of the field angle for (a) vanishing magnetocrystalline anisotropy (curling mode) and (b) for moderate uniaxial magnetocrystalline anisotropy.. The curve labeled SW gives the switching field due to the Stoner-Wohlfarth theory and the dashed line gives the corresponding coercivity [25]. 20

Fig. 19. Schematic representation of the coercive field as a function of the particle diameter D (solid line) perfect particle, and (dashed) imperfect particle [9]. 21

Fig. 20. Magnetic torque and damping applied on a spin J 22

Fig. 21. Exact magnetization trajectory of a non lossy macrospin film of initial magnetization along x when subjected to a transverse field $h = 0.01$ applied along y , with $N_z = 1$. The uniaxial anisotropy is along x . The anisotropy field is varied from $h_k = 0.01, 0.016, 0.02, 0.03$ and 0.1 . The two later h_k values correspond to anisotropy-dominated trajectories. (a) Trajectory in the zy plane. (B) Trajectory in the (xz) plane. (c) Vector m (in the text, u) trajectory when initial magnetization is along x . Inset: Definition of the axes. The ellipse stands for the anisotropic macrospin [26]..... 24

Fig. 22. Comparison of simulation packages for the bar example. Initial magnetization is $(M_x, M_y, M_z) = (0.707, 0, 0.707) \times 0.86$ MA/m. M increases over time, as the system tries to avoid strong magnetic effective surface charges on the long sides of the bar [55]. 27

Fig. 23. Comparison of sphere models generated for FDM and FEM [59]...... 27

Fig. 24. Frequency vs. current density for Finite Difference simulations (black squares), Finite Element simulations (red triangles), and macrospin simulations (black line) [60]...... 28

Fig. 25. Schematic discretization of a given region in the (x,y)/(x,t) plane, subdivided into FD elements, in which the micromagnetic equations are satisfied [61]...... 29

Fig. 26. Nodal linear basis functions and common support of two basis function. 31

Fig. 27. A schematic diagram of the boundary of a magnetic model. V and ∂V stand for the volume domain and its boundary 32

Fig. 28. Schematic of the simulation cycle of a typical finite element micromagnetic package such as MAGPAR [64]...... 34

Fig. 29. (a) A schematic diagram of an exchange coupled relatively soft magnet on top and relatively hard one at bottom. They are exchange coupled with an exchange coefficient A . $K_1 = 2 \times K_2$. The energy landscape of their rotation process are shown for the contribution of exchange coupling is (b) strong and (c) weak. The amount of A in (b) is 100 times larger than in (c). Stray field interaction was neglected in all cases. 36

Fig. 30. (a) Energy along the initial path and final path. (b) Magnetization configurations of the magnetization along the initial (a-b-c-d-e) and the final (a-b'-c'-d'-e) path. 38

Fig. 31. (a) Sketch of the recording head. (b) The air gaps are exaggerated. [69]. 40

Fig. 32. Magnetization of a demagnetized medium prior to recording a transition [70].	41
Fig. 33. Total head field H_t and its components H_x and H_y as functions of position below a recorcing head for $y = 0.15 \mu\text{m}$ [70].	41
Fig. 34. Two-dimensional representation of the gap [71].	42
Fig. 35. Alternate representations of field configuration below gap [71].	43
Fig. 36. Various boundary conditions to calculate the stray field partly. (a) $+x$-limited semi-infinite, (b) $-x$-limited semi-infinite, (c) infinite in both directions and (d) Superposition of wedges to obtain finite gap, finite width head [72].	44
Fig. 37. Magnetic fields at $y = g/2$ for (a) zero width head, (b) finite width head, $w = 2g$, and (c) semi-infinite width head. Components are: longitudinal (H_x), vertical (H_y), and transverse (H_z) [72].	46
Fig. 38. Geometry for the head design with a finite pole lengths [74].	47
Fig. 39. (a) Comparison of exp. plot of H_x vs. x and plot from Eq. (66) with $g = p = q = 1$, $y = 0.063$, $D = F = 0.09$, and $E = G = 0.9$. (b) Comparison of exp. plot of H_y vs. x and plot from eq. (71) [73].	50
Fig. 40. Comparison among the ring type head field, Karlqvist, Lindholm and Szczech. The undershoot factor of the Szczech head is varied between 0 and 1. In above figures, the strength of the down track field component is marked as blue, and the one of the perpendicular one is red.	51
Fig. 41. Representation of prismatic magnet, by magnetic surface poles and equivalent surface currents of uniform magnetization along the z-axis	53

Fig. 42. Overview of the perpendicular recording geometry with a SUL. The figure on the right shows a blow-up of the dashed rectangle where the final recording occurs. The effect of the SUL can be thought of as an additional image pole that is located in the SUL, thus forming a ring head turned sideways. For all pictures, it is assumed that the medium moves and the head is at rest [3]. 55

Fig. 43. (a) Schematic diagrams of Lindholm, single pole tip (SPT) and SPT with soft underlayer (SUL). The small cross presents the position where the deep gap field (in Lindholm head) and base field (in SPT and SPT with SUL) are defined. (b) Writing head field strength on xy plane (above) and head field strength along down track distance. H_x and H_z stands for the down track direction and perpendicular direction, respectively. H_{tot} is total field strength resulted from H_x and H_y 56

Fig. 44. The trilemma of magnetic recording: achieving high medium SNR requires the utilization of small gains. Small grains have energy barriers (KV) that are too small to ensure thermal stability of the recorded information. An increase in the anisotropy energy density K increases the required write field beyond the capability of available head materials..... 58

Fig. 45. Finite element models for fully integrated perpendicular magnetic recording. (a) The writing module is consisted of coil, head (with shield, optionally), SUL and media. The writing head pole tip with media is enlarged in (b). The media is placed very below writing head. 60

Fig. 46. Fully integrated micromagnetic writing simulation processes..... 60

Fig. 47. Writing process using precomputed field box. 61

Fig. 48. Three methods of the read back process. (a) Direct read back calculation using fully integrated micromagnetic simulation. (b) Field box calculation of the written bits on media, “imprint”. (c) Using reciprocity theorem. 64

Fig. 49. The procedure to build double Szczech head field for analytic read head model. 65

Fig. 50. Comparison between conventional multigrain media media and bit patterned media [96]..... 66

Fig. 51. Patterned media: fabrication overview [97] 67

Fig. 52. (a) AFM and (b) corresponding MFM image of the patterned area (dot size = 30 nm, pitch = 60 nm). The sample is in the demagnetized state and one row of nanostructures is highlighted for comparison. (c) Kerr magnetometry of the continuous planar film (solid) and the patterned media (open). 70

Fig. 53. Electron microscopy image of the FePtCu bits. (a) Top view SEM image with a size distribution. (b) Cross sectional TEM image. (c) High resolution TEM image of a single bit. The inset image is the FFT of the lattice fringes. (d) FEM model of a bit with a diameter D and misorientation of the easy axis θ 71

Fig. 54. Switching fields as a function of the (a) crystalline anisotropy K_1 compared with anisotropy constant $H_k = 2K_1/M_s$ the (b) misorientation θ . The inset in (a) shows the Gaussian distribution of K_1 , and the attached numbers on the lines denotes the misorientation θ , and (c) the bit diameter D for the cases of $\theta = 0$. In (a) and (b) the bit diameter D is fixed as 30 nm. 73

Fig. 55. Contributions of the misorientation θ , bit diameter D , and the K_1 deviation σ_{K_1}/K_1 on the switching field distribution. The absolute (SFD, in kOe)

and the relative ($SFD/H_{sw,avg}$, dimensionless) are written on each bar which represents the cumulative switching probability. 74

Fig. 56. (a) Magnetization curves with various field applying angle. (b) Nucleation field (square), switching field (circle) and coercive field (triangle) as a function of the field applied angle. The Stoner-Wohlfarth coherent rotation curve and the Kondorsky curves are presented for comparison. 78

Fig. 57. Magnetization processes from dynamic micromagnetic simulations with TUCH-03, in the cases of grain position varied from 20 to 55 nm. (a) Initial positions of the recording head and grains for each cases, (b) scale factor application as a function of time, (c) Magnetization behaviors of the grain, in a given position and scale factor. 80

Fig. 58. Phase diagrams of successful switching events (blue), as a function of the grain position and head field scale factor. 81

Fig. 59. (a) Finite element model and schematic of the recording head with coil. (b) The decoupled grains are shown with the recording head model. The saturation magnetic polarization is $J_s = 0.7$ T, exchange constant $A = 10$ pJ/m, and the Gilbert damping constant $\alpha = 0.05$. The initial trailing edge position is $x = 0$ nm at $t=0$ ns. 84

Fig. 60. (a) Head field profile on xy plane at $z = -1$ nm (left) and $z = -21$ nm (right). The attached numbers on the contour denote the z-component of the head field. (b) Transient state of the recording simulation ($t = 0.4$ ns) of a single phase medium with $K_{hard} = 0.2$ MJ/m³. The position of the head (8 nm), the head field gradient, and the magnetization status of the media of the same are shown after 0.4 ns. 87

Fig. 61. (a) Schematic of the investigated media models (K_{hard} colored dark blue, K_{soft} light blue) (b) The displacement of the bit transition Δp as a function of the normalized anisotropy constant, $K_{\text{hard}}/K_{\text{max}}$, is shown for all media. The data were fitted using a negative exponential curve. (c) The first derivative of (b) as a function of the normalized crystalline anisotropy $K_{\text{hard}}/K_{\text{max}}$. (d) The energy barrier of the models as a function of $K_{\text{hard}}/K_{\text{max}}$ 89

Fig. 62. Schematic sketch of (upper) FePtCu layer formation and (lower) FePtCu/[Co/Pt]_N exchange spring media structure. 92

Fig. 63. (a) SQUID hysteresis loops of a hard magnetic FePtCu alloy film measured in the out-of-plane and in-plane geometry. (b-d) Series of out-of-plane hysteresis loops taken on FePtCu/[Co/Pt]_N samples with different bilayer number N (solid symbols) and after a RTA process (open symbols). The insets in (b-d) represent the first derivative of the hysteresis loops revealing the evolution of the switching field distribution as well as switching field of the hard and soft layers. 94

Fig. 64. Switching field dependence of the hard and soft layers as function of the soft layer thickness (solid symbol), and after applying a RTA process (open symbols). 95

Fig. 65. Bright field images of the (a) as-prepared and (b) RTA treated FePtCu/[Co/Pt]₁₆ exchange coupled composite, with selective area diffraction patterns of (c) as-prepared and (d) RTA treated specimen. 99

Fig. 66. Cross sectional images of as-prepared (a, c, e) and RTA treated (b, d, f) specimens with their SADPs (g, h), respectively. (c) and (d) shows the dark field images of [Co/Pt] (111), and (e) and (f) shows the dark field images of FePtCu (001)..... 99

Fig. 67. High resolution cross sectional images of the (a) as-prepared and (b) RTA treated specimen. The reduced FFT images are corresponding to the squares marked on the high resolution images. 101

Fig. 68. Chemical analysis results using (a~d) EDS line scan on STEM and (e) EFTEM element map. (a) and (c) are the STEM HAADF image of as-prepared specimen, where (b) and (d) are those of RTA treated one..... 103

Fig. 69. (a) Finite element model for micromagnetic simulation. (b) M-H curves with varied interlayer exchange constants, A_{int} , keeping $K_{soft} = 0.3 \text{ MJ/m}^3$ and $t_{soft} = 5 \text{ nm}$ fixed. (c) Switching field of the soft and hard layer as a function of the interlayer exchange constant. 106

Fig. 70. Calculated M-H curves of exchange spring media using different soft layer thicknesses, t_{soft} , for (a) $K_{soft} = 0.3 \text{ MJ/m}^3$ and (b) $K_{soft} = 0.35 \text{ MJ/m}^3$. (c) Contour map of the hard layer switching field $\mu_0 H_{0hard}$ as a function of the interlayer exchange constant and the soft layer thickness keeping $K_{soft} = 0.4 \text{ MJ/m}^3$ fixed. The phase boundary between the two-step loop to a single-step reversal of the EEC media is marked with a dashed line. Phase boundaries for $K_{soft} = 0.3 \text{ MJ/m}^3$ (dotted line) and 0.5 MJ/m^3 (solid line) are also shown..... 107

Fig. 71. Phase diagram of FePt. $L1_0$ ordered phase is to be formed if the portion of Fe and Pt are comparable [150]..... 110

Fig. 72. calculated ESO curve using Fe edge of EXAFS showing the variation of ESO versus substrate temperature. The results of ordering parameter examined by XRD are superimposed [147]..... 110

Fig. 73. (a) Magnifications of the double diffraction peaks (200) and (002) and (b) the (400) and (004) diffraction peaks of the hard(11.5 nm)FePt($L1_0$)/graded(30

nm)FePt(L1₀ to A1) composite; dotted lines indicate the positions of the peaks. X-ray spectrum of (c) hard(11.5 nm)/graded(30 nm) composite and 5 nm single layers deposited at different temperatures (d) 600, (e) 450, (f) 300 °C, and (g) RT.

..... 113

Fig. 74. (002) Rocking curves of hard(11.5 nm)FePt(L1₀)/graded(30 nm)FePt(L1₀ to A1) composite (solid squares) and (200) rocking curves of 5nm single layers deposited at layers deposited at different temperatures 600 °C (open squares), 450 °C (open triangles), 300 °C (solid triangles), and RT (solid circles). The scale of intensity axis is logarithmic. 115

Fig. 75. AFM image of 11.5 nm single hard FePt (L1₀) layer deposited at 700 °C. 115

Fig. 76. (a) Hysteresis loops with field parallel (solid symbols) and perpendicular (open symbols) to the film plane of hard(11.5 nm)/graded(12 nm) composite deposited at varying temperature from 700 to 420 °C and (b) a single hard layer 11.5 nm deposited at 700 °C..... 117

Fig. 77. Dependence of the coercive field H_c of hard(11.5 nm)/graded(t_g nm) system on the thickness of the graded layer t_g 117

Fig. 78. Cross sectional (a) bright field (BF) image and (b) dark field (DF) image of FePt L1₀ (001) plane. Selective area diffraction image (a) taken experimentally and (d) simulation results for the case of FePt A1 phase and FePt L1₀ phase coexist. 119

Fig. 79. (a) High resolution TEM (HRTEM) image of FePt film grown at 200°C. (b) Reduced FFT images of each parts in (a). The numbers assigned on each figures correspond to the site marked in (a)..... 120

Fig. 80. HRTEM image at the interface between MgO substrate and FePt film. 121

Fig. 81. (a) Relatively low magnification TEM BF image and (b) selective area diffraction pattern..... 122

Fig. 82. (a) HRTEM image of the FePt film grown at 500°C, and (b) reduced FFT results of the site 1 and 2. 122

Fig. 83. (a) Diffraction patterns of crystal A and B. (b) Overlapping of the diffraction pattern of A and B for the case of both crystals are diffracted by the common incident beam. (c) Overlapping of the diffraction pattern of A and B for the case of the diffraction of crystal A was occurred by a diffracted beam of crystal B. (d) Schematic diagram of double diffractions..... 123

Fig. 84. (a) SEM plan view image of the FePt L10/graded (700°C → 600°C). TEM plan view bright field images (a) relatively lower magnification and (b) relatively high magnification. (d) electron diffraction pattern with a double diffraction.... 125

Fig. 85. Cross sectional (a) bright field image and (b) selective area diffraction patterns, comparison between simulation (left) and experiment (right). (c) and (d) represents the dark field images corresponding A1+L1₀ (2,0,2) and L1₀ (2,0,1), respectively. 126

Fig. 86. (a) Cross section image of a single bit and (b) HRTEM image of the marked site in (a). (c) and (d) are the reduced FFT results of site 1 and 2, respectively. The distances marked with an arrow in each figure are (c) 0.190 nm and (d) 0.386 nm, corresponding to (002) and (001) distance of A1 phase and L1₀ phase, respectively..... 127

Fig. 87. L1₀ phase and A1 phase with the phase boundary between them judged by HRTEM images. The average thickness of the L1₀ phase and A1 phase are found to be 13.1 nm and 11.3 nm, respectively. 127

Fig. 88. (a) SEM plan view image of the FePt L1₀/graded (700°C → 450°C). TEM plan view bright field images (a) relatively lower magnification and (b) relatively high magnification. (d) Electron diffraction pattern with a double diffraction... 129

Fig. 89. Cross sectional (a) bright field image and (b) selective area diffraction patterns. (c) and (d) represents the dark field images corresponding A1+L1₀ (0,0,2) and L1₀ (0,0,1), respectively..... 130

Fig. 90. L1₀ phase and A1 phase with the phase boundary between them judged by HRTEM images. Regions of which structure was hard to judge were found near L1₀/A1 interphase boundary..... 130

Fig. 91. (a) SEM plan view image of the FePt L1₀/graded (700°C → 262°C). TEM plan view bright field images (a) relatively lower magnification and (b) relatively high magnification. (d) Electron diffraction pattern with a double diffraction... 132

Fig. 92. Cross sectional (a) bright field image and (b) selective area diffraction patterns. (c), (d) and (e) represents the dark field images corresponding A1+L1₀ (0,0,2), L1₀ (0,0,1) and MgO (0,0,2), respectively. (f) The dark field images are overlapped to figure out the interfaces between the phases..... 132

Fig. 93. L1₀ phase and A1 phase with the phase boundary between them judged by HRTEM images..... 133

Fig. 94. Probable structures of FePt graded media. For the cases of (1) lattice parameters are gradually decreasing, as well as material parameters, (2) fcc phase

is formed by nucleation and growth mechanism and (3) FePt phase is formed more probably in lower temperatures. 134

Fig. 95. Schematic structures of the stacked graded media and phase graded media. Bilayer structure is included in the category of stacked graded media. Phase graded media is varied for 4 cases with various shapes of interface..... 136

Fig. 96. Hysteresis curves of the bilayer, graded, G-01 and G-03 media. The crystalline anisotropy of the soft layer is varied from 0 to 0.8 MJ/m³. The hysteresis curves are compared with that of fct FePt single layer. 136

Fig. 97. Summary of coercivities of the Stacked Graded Media and Phase Graded Media..... 137

Fig. 98. (a) The phase graded media model for the case of the linear phase transformations with 15 nm thick graded layer. (b) Phase profile comparison between the linearly, logistically graded media and bilayer. The bilayer consists of only hard and soft layers. 139

Fig. 99. (a) Schematic structure of the phase graded media and averaged stacked graded media. (b) Comparison of the switching field between the graded media and the bilayer. (c) Minimum Comparison of the energy barrier as a function of the graded layer thickness. (For the bilayer, the x axis in (b) and (c) describes the thickness of the soft layer.)..... 142

Fig. 100. (a) Magnetization reversal of two-dimensional simplified models. (b) Magnetization configuration of the domain wall motion at the marked points on the demagnetization curve. The material boundaries of the advanced stacked graded media are marked only right half, for better visibility..... 144

Fig. 101. (a) Coordinate system of our simulations. X axis is corresponding to the down track direction of magnetic tape recording media, where y and z axes are the cross track direction and the perpendicular direction, respectively. (b) Top view 100 nm x 100 nm sized images of the longitudinally (#L), randomly (#R), and perpendicularly (#P) oriented media. (c) Hysteresis loops of the models, under homogeneous longitudinal field. (d) Hysteresis loops of the models, under homogeneous perpendicular field..... 148

Fig. 102. Maximum x- and z-directional Karlqvist head field components and Stoner-Wohlfarth switching field $H_{SW} = \left(H_x^{\frac{2}{3}} + H_z^{\frac{2}{3}} \right)^{\frac{3}{2}}$ 150

Fig. 103. (a) Schematic diagram of the writing process. The d_{write} denotes the distance between the Karlqvist writing head and media. (b) x- and z-directional magnetization components of the media, when $d_{write} = 40$ nm..... 152

Fig. 104. Read-back process using reciprocity theorem. The field box generated by the read head is passing through the media with a given read distance d_{read} . The interaction between the field box and the written bits induces the changes of the magnetic interaction energy, which is regarded as the read back signal. 152

Fig. 105. (a) Read-back signals of the bits written on a part of #L, #R and #P media. The x-and z-directional magnetization components of the bits written on the (b) #L media, (c) #R media and (d) #P media, with the read-back signal of the same area. 153

Fig. 106. Read-back signal properties of the bits written in fixed read head to media distances. The average amplitude of the (a) signal and the (b) SNR as a function of the write head to media distance..... 157

Fig. 107. Read-back signal properties of the bits written in fixed write head to media distances. The average amplitude of the (a) signal and the (b) SNR as a function of the read head to media distance..... 158

Fig. 108. The SNR as a function of the signal frequency, of the #L media at $d_{write} = 100$ nm and $d_{read} = 80$ nm (left) and of the #P media at $d_{write} = 20$ nm and $d_{read} = 40$ nm (right). The signal frequency of 0.0083 nm^{-1} corresponding 423 kfcf is marked with arrows 160

Fig. 109. Head field profiles of the Lindholm head, SPT head without SUL and SPT head with SUL. The dashed line indicates the position of h-BaFe media is supposed to be placed. The numbers attached on the isolines show the strength of the Stoner-Wohlfarth field in Tesla..... 162

Fig. 110. Snapshots of the writing processes using (a) Lindholm head, (b) SPT head without SUL and (c) SPT head with SUL..... 163

Fig. 111. Bit transition parameter a and signal scale b for (a) #P media and (b) #R media. The volume distribution $\sigma_V/V = 50\%$ 164

Fig. 112. Signal to noise ratio (SNR) of #P and #R h-BaFe particulate media written with Lindholm, SPT, and SPT head with SUL, in various linear densities. 165

Fig. 113. Schematic diagram of the sputtering mechanism in the constraint chamber [182]..... 166

Fig. 114. Schematic diagram of the Facing Target Sputtering (FTS). 167

Fig. 115. Voronoi tessellation of a set of point particles. Voronoi cells are convex and their edges join at trivalent vertices [187]. 168

Fig. 116. Procedures for image process for grain detection to build finite element models..... 169

Fig. 117. Schematic diagram of CoCrPt-SiO₂ sputtered media prepared by face target sputtering [194]. 170

Fig. 118. (a) Plan view of the written bit states of perpendicularly aligned (#P) h-BaFe media, and the CoCrPt-SiO₂ sputtered media. The bits are written using SPT head with SUL, with a head to media distance $d = 40$ nm. (b) Perpendicular magnetization component of the two media as a function of down track distance. The black line indicate the written bit states of h-BaFe media, and the red one is for the sputtered one. 171

Fig. 119. SEM image of the as-prepared ZrO₂ nanoporated membrane..... 176

Fig. 120. TEM micrographs of the sample after Co/Pt multilayer deposition. The components of this film can be distinguished in the images as indicated. The multilayer structure is visible. The different types of edges in the zirconia layer and magnetic layer stack are (a) step edge, (b) inclined edge, and (c) combination of a small step and an inclination (right side of the perforation). 178

Fig. 121. Polar MOKE hysteresis loop taken at $\theta = 0^\circ$ 179

Fig. 122. (a) Remanence curves taken at different θ . (b) Angular dependence of the switching field. The Kondorsky-like [Kondorsky 1940] [24] behavior (dashed curve) and the fit according to Ghidini [212] (dotted curve) with a quality factor of $Q=2.4$ have been plotted for comparison. 181

Fig. 123. ((a)–(d)) In-field MFM images of Co/Pt multilayers grown on a ZrO₂ nanoporated membrane. The applied field is indicated in the respective panel. The measurement is started from an ac-demagnetized state. The scale bar in panel (a) applies to all panels. (e) Initial magnetization curve of Co/Pt constructed from the analysis of the MFM images. The dotted line is a guide to the eye. 183

Fig. 124. High-resolution in-field MFM images taken on the sample in various applied fields: (a) 0.50 kOe, (b) 1.00 kOe, (c) 1.50 kOe, (d) 1.75 kOe. At fields below 1.50 kOe, only slight changes in the domain configuration are observed ((a), (b)). At higher fields, domains vanish rapidly ((c), (d)) by forming elongated features, which are not favorable in a film with a low number of pinning sites. The scale bar in panel (d) applies to all panels. The displacement of the domain wall indicated in panel (a) and (b) of about 30 nm is in good agreement with the period of the underlying nanoporated ZrO₂ template (34 nm)..... 185

Fig. 125. (a) Applied field profile for domain wall motion as a function of time. (b) Magnetization of the PPM model as a function of applied field, for the case of $A_{int} = 0$. (c) Sum of exchange energy and anisotropy energy ($e_{exch} + e_{ani}$) compared with the detailed magnetization shown in (b). 188

Fig. 126. (a) Initial magnetization states for two types of PPM (b) Domain wall displacement in increasing applied field H..... 189

Fig. 127. (a) Depinning fields H_d of the percolated media as a function of the intergranular exchange coupling constant A_{int} between magnetic nanoparticles and film. The attached numbers are the pinning fields of the media without magnetic particles. (b) The range $0 < A_{int} < 0.1$ pJ/m is enlarged with a linear scale of A_{int} . Please note that the key applies for both panels of the figure. 191

Fig. 128. Nucleation fields and saturation fields of the percolated film, as a function of A_{int} , under the presence of demagnetization field. 192

Fig. 129. Written bit states on the perpendicular percolated media. 193

Fig. 130. A modified PPM model for considering realistic geometry, with an inclination angle θ 194

Fig. 131. PPM models with inclined rims (a) without and (b) with magnetic dots inside nanoporations. In (b) the intergranular exchange coupling coefficient $A_{int} = 0.5$ pJ/m. (c-d) Angular dependency of the switching field with various inclination angle θ . (c) is for the model (a) without magnetic dots, where (d) is for (b)..... 195

Fig. 132. A rectangular model with 450 (30 x1x15) cubes, of which x, y, z edge lengths are 1 nm. The intergranular phase thickness is fixed as 0.1 nm. 221

Fig. 133. Phase 1 and 2 assigned on the volumes of the model shown in Fig. 132, with the same portions of them. Red and blue grains stand for the phase 1 and 2, respectively. 222

Fig. 134. Longitudinal and perpendicular head field profile of the Lindholm head, with gap length = 100nm and head width = 100 nm. The field profiles are calculated in a field box of which down track and cross track dimensions are 400 nm and 600 nm, respectively..... 225

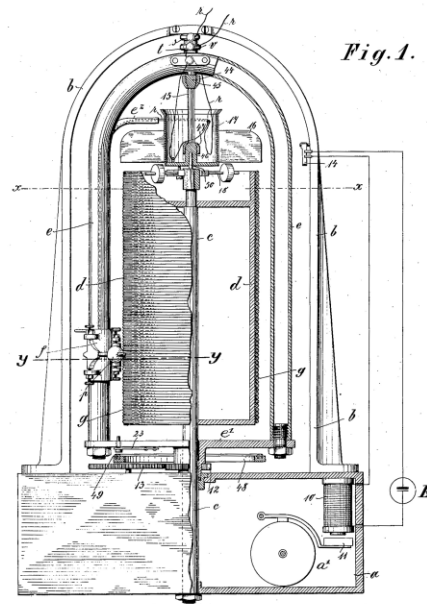
Fig. 135. Scale factor generated by the parameters described above, scftr = 1.186, rtime = 0.1, headv = 20.0, mleng = 1200, mthod = 1 and bleng = 60.0. 226

Fig. 136. Visualization of the same model and data using (a) paraview and (b) Tecplot.....	228
Fig. 137. Data structure comparison between UCD format and Tecplot format.	229
Fig. 138. Bit transition estimations on h-BaFe particulate media.	229
Fig. 139. Data structure of .dat file generated by inp2mag.....	230
Fig. 140. (a) Written bits of the CoCrPt-SiO₂ sputtered media using SPT head with SUL. (b) Comparison of magnetization analysis from .dat file produced by inp2mag, and .txt file by inisort.	231
Fig. 141. An example of SNR calculation procedure used in this thesis, for h-BaFe particulate media.	232

1. Introduction

Magnetic recording industry have been growing since it was invented by Valdemar Poulsen in 1898 [1], accompanied with the development of magnetic recording materials and techniques to write and read the information on them. At the beginning magnetic recording technology was invented for sound recording and reproducing. When the first magnetic tape was invented in 1933 by AEG and presented at the Berlin exhibition in August, 1935, people were amazed to be able to hear their voices an instant after being recorded [2]. Later, with invention of the computer and its development, the tape recording techniques has evolved into the tape drive system in 1951. Since then magnetic recording technique started to be applied for general information.

No. 661,619. V. POULSEN. Patented Nov. 13, 1900.
METHOD OF RECORDING AND REPRODUCING SOUNDS OR SIGNALS.
(Application filed July 8, 1899.) 3 Sheets—Sheet 1.
(No Model.)



Witnesses:
Frank J. Ober
Walter M. Chapin

Inventor:
Valdemar Poulsen.
by W. G. Schaeffer
Att. 3.

Fig. 1. The figure for the first magnetic recorder suggested by Valdemar Poulsen [1].

The usage of magnetic materials as a storage device is once more boosted up by invention of hard disk drive in 1956. Hard disk drive is designed for a special feature: random access. The name of the first hard disk developed by IBM, RAMAC stands for Random Access Method of Accounting and Control [3]. The capacity of the first hard disk was only 5 MB, however, it started to be expanding exponentially as shown in Fig. 2. Recently a prototype 4 TB hard disk drive is released, Samsung Spinpoint EcoGreen F6 4TB [4]. 1 TB data is stored in a platter using perpendicular magnetic recording technology, corresponding to 800 Gb/in², which is very close to the world record in laboratory, 960 Gb/in² [5]. The highest recording density achieved by tape recording media is 29.5 Gb/in² [6]. In spite of the difference between the recording densities and media type of hard disk and tape recording, the recording procedure is basically same.

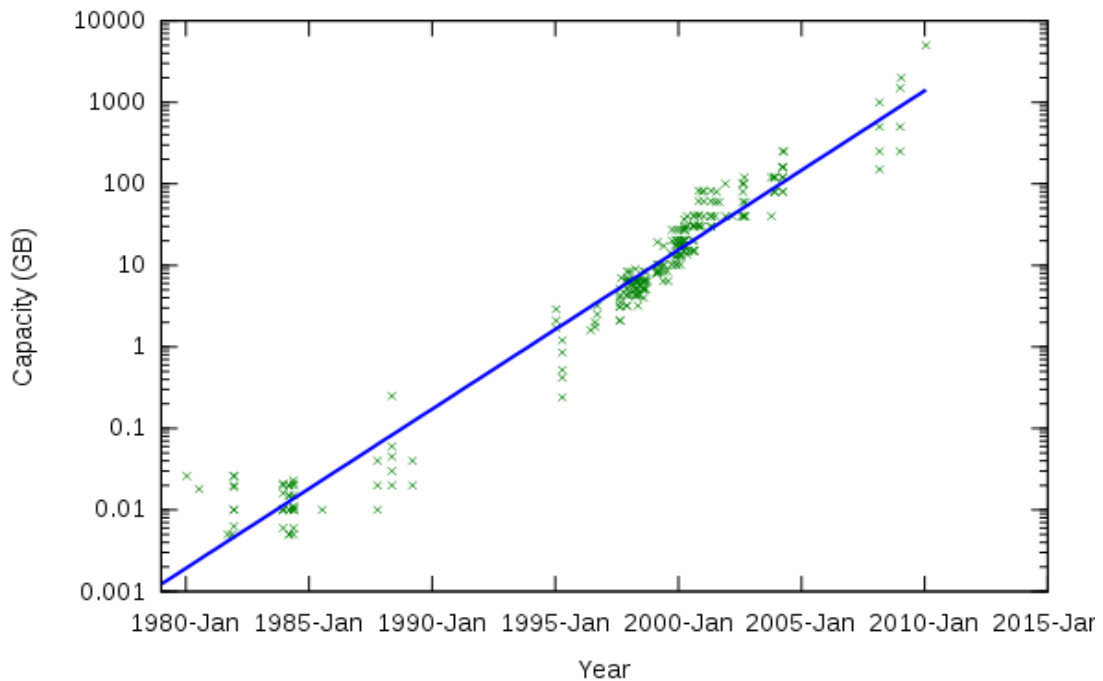


Fig. 2. Commercial hard disk capacity over time [7].

In both types of magnetic recording media, magnetic materials are deposited on top of the substrate. The write head flies above the recording media applying strong stray field on it to magnetize a small part of the media, in other words, to write a bit on it. The switching process of the individual bit is a complex function among the magnetic properties and geometric dimensions of the media, 3-dimensional head field profiles including its gradient and interaction between writing head and media. In principle it is known that a tiny magnetic particle is reversed by coherent rotation, however, the irregularities applied on the particle induce inhomogeneity in reversal process. If the media is composed of more than two magnetic layers which interacts one another, or its shape is not simple such as a film with a lot of irregular antidots, magnetization switching process is triggered at a site where the magnetic energy is the most unstable. For instance, even in a small sized single crystal magnetic particle, an irregular shape leads inhomogeneous stray field distribution, consequently the particle is likely to be reversed starting from the part. If the media is composed of more than two magnetic materials with different properties, and moreover, the applied field is not homogeneous, the incoherency would be much stronger.

The inhomogeneous magnetization switching is inevitable in reality; actually it is getting more serious in advanced magnetic recording media. In this thesis the influence of the inhomogeneous recording and the way to take advantage of it is going to be shown, with development of advanced magnetic recording media to utilize the inhomogeneous magnetization switching behavior.

1.1. Ferromagnetism

(1) Quantum Mechanics on Magnetism

If somebody asks you “what is the most outstanding feature of ferromagnetic materials?” then you can say “exchange interactions between spins”. The atomic spins in ferromagnetic materials interact with each other, each of them trying to align the others in its own direction. The force between the spins is called exchange interaction. The exchange energy E_{exch} between spin \mathbf{S}_i and \mathbf{S}_j is proportional to $\mathbf{S}_i \cdot \mathbf{S}_j$, therefore

$$E_{\text{exch}} = -2 \sum_{i \neq j} J_{ij}(\mathbf{r}_{ij}) \mathbf{S}_i(\mathbf{r}_i) \cdot \mathbf{S}_j(\mathbf{r}_j) \quad (1)$$

J_{ij} denotes the exchange integral between the spins \mathbf{S}_i and \mathbf{S}_j at positions \mathbf{r}_i and \mathbf{r}_j , with $\mathbf{r}_{ij} = \mathbf{r}_j - \mathbf{r}_i$. The factor 2 comes from the fact that the double sum in Eq. (1) actually contains the particular spin twice: once under its name \mathbf{S}_i , and once as \mathbf{S}_j . In short-range exchange interactions, \mathbf{r}_{ij} denotes the nearest neighbor distances and J_{ij} is replaced with the one with only nearest neighbor interactions, J_0 . Under the assumption that the spins \mathbf{S}_i and \mathbf{S}_j has the same scale S , the exchange energy is described as

$$E_{\text{exch}} = A \int_V \sum_j (\nabla u_j)^2 dV, \quad (2)$$

where u_j is the unit vector of a Cartesian coordinate system along the direction j , and the coefficient A is defined as

$$A = \frac{2J_0 S^2}{a} c. \quad (3)$$

In Eq.(3) $c = 1$ for the cubic primitive lattice, $c = 2$ for the bcc lattice and $c = 4$ for the fcc lattice [8-9].

The spins also interact with lattices themselves are located in. The spin-orbit interaction causes the magnetocrystalline anisotropy. The electron orbits are linked to the crystallographic structure, and by their interaction with the spins they make the latter prefer to align along well-defined crystallographic axis. There are therefore directions in space in which it is easier to magnetize a given crystal than in other directions, so-called easy axis [8]. The direction of magnetization follows the easy axis determined by the crystalline anisotropy energy. The crystalline anisotropy energy is expressed as

$$E_{ani} = \int_V \left(K_0 + K_1 \sin^2 \theta + K_2 \sin^4 \theta + \dots \right) dV \quad \text{and} \quad (4)$$

$$E_{ani} = \int_V \left(K_0 + K_1 \sum_{i \neq j} \gamma_i^2 \gamma_j^2 + K_2 \gamma_1^2 \gamma_2^2 \gamma_3^2 \right) dV \quad (5)$$

for uniaxial and cubic anisotropy, respectively. In Eq.(4) θ stands for the angle between magnetization vector and easy axis. In Eq.(5), γ_i refers to cubic axes. K_1 and K_2 are energy densities derived from experiment, and can exist with either a positive or negative sign. When $K_1 > 0$ the axis is easy, when $K_1 < 0$ the axis becomes hard [10]. Fig. 3(a) shows the normalized anisotropy surfaces for isotropic materials (i.e. $\text{Ni}_{80}\text{Fe}_{20}$). In these materials the amount of anisotropy constant is actually zero, but the Fig. 3(a) is drawn as a sphere to show that it does not have any specific easy axis. The anisotropy surfaces for anisotropy materials are shown in Fig. 3(b) to Fig. 3(d). The material with uniaxial crystalline anisotropy, such as Co single crystal has the anisotropy surface such as Fig. 3(b) for the case of (0001) direction is parallel to z axis. Usually hexagonal crystals have the uniaxial crystalline anisotropy.

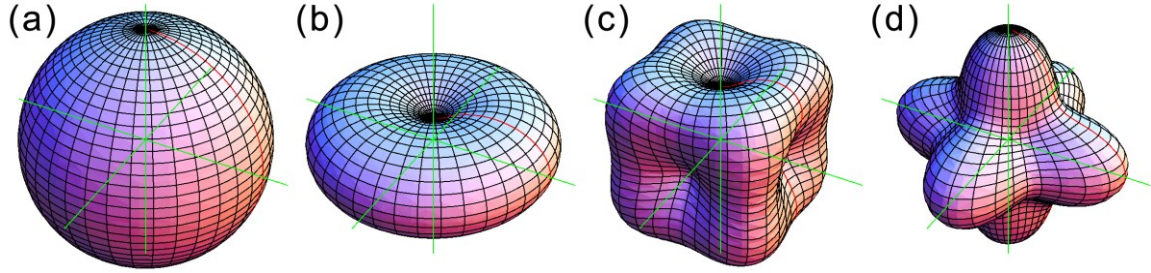


Fig. 3. Normalized anisotropy surfaces for (a) isotropic materials, (b) uniaxial anisotropic materials, (c) cubic anisotropic materials with $K_1 > 0$ and (d) cubic anisotropic materials with $K_1 < 0$. The three green lines are the x, y, z axes.

Cubic anisotropy has two cases of easy axis: $K_1 > 0$ and $K_1 < 0$. If $K_1 > 0$ (for example, α -Fe) the anisotropy energy has the minimum along the x, y and z directions. However, if the $K_1 > 0$ like Ni single crystal, $\langle 111 \rangle$ directions becomes the easy axes because the orthogonal axes are hard to be magnetized than other direction. Precisely speaking, the easy axes are determined by the extra conditions that minimize the energies described in Eq. (4) and (5). Taking into account the anisotropy constants K_1 and K_2 only the easy axes for cubic crystals are visualized in Fig. 4(a) and (b) for uniaxial and cubic anisotropy, respectively.

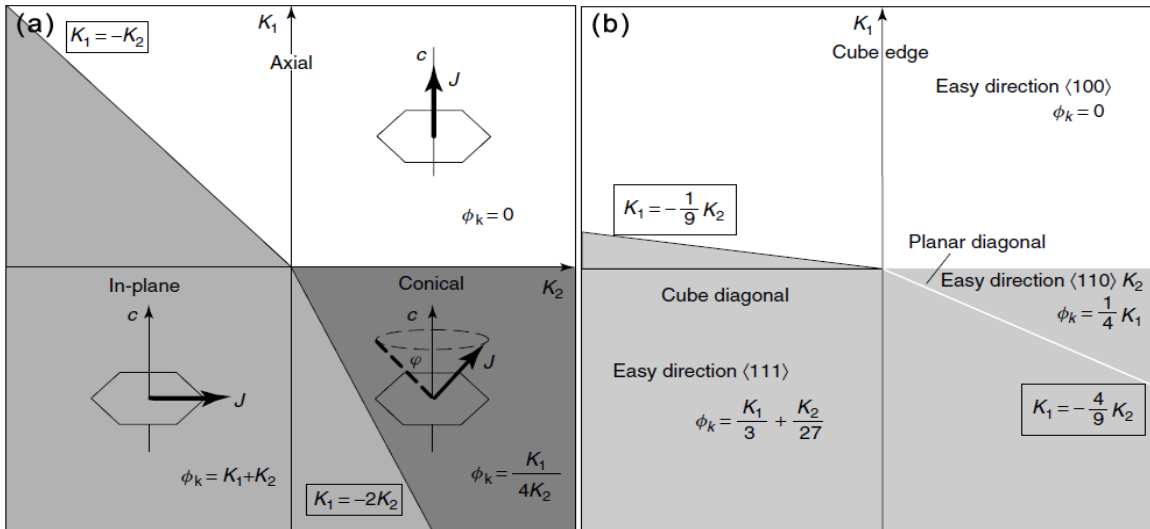


Fig. 4. Phase diagrams of easy directions in (a) uniaxial and (b) cubic crystals [9].

For the case of the hexagonal crystal has the conical easy axes distributions,

$$\sin \varphi = \sqrt{-\frac{K_1}{2K_2}}. \quad (6)$$

The special cases of the conical anisotropy and $\langle 110 \rangle$ easy axes are presented in Fig. 5(a) and (b), respectively. These cases are owing to the competition between the crystalline anisotropy constants along the orthogonal axes. In uniaxial crystalline anisotropy, the anisotropy constant is often referred as K_U due to the uniqueness of the easy axis.

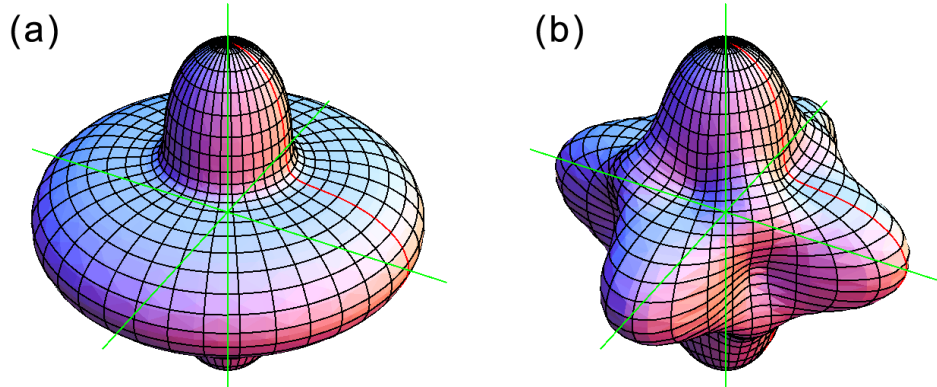


Fig. 5. Normalized anisotropy surfaces for (a) conical anisotropy and (b) $\langle 110 \rangle$ easy axes.

(2) Thermodynamics in Magnetism

In this session the magnetic energies in relatively larger scales will be treated: the magnetostatic energy. Magnetostatic energy is regarded as two independent parts: One is the case of external field is applied known as the Zeeman energy, and the other one comes from the magnetic dipole, often denoted as stray field energy.

The presence of the spins, especially aligned spins in a direction in ferromagnetic materials induce the spontaneous magnetization \mathbf{M}_S , or spontaneous polarization \mathbf{J}_S defined as

$$\mathbf{J}_S(\mathbf{r}) = \mu_0 \mathbf{M}_S(\mathbf{r}) = |\mathbf{J}_S(\mathbf{r})|(\gamma_1(\mathbf{r})\mathbf{u}_1 + \gamma_2(\mathbf{r})\mathbf{u}_2 + \gamma_3(\mathbf{r})\mathbf{u}_3). \quad (7)$$

The local spontaneous magnetization of the magnetic ion at position \mathbf{r} , the atomic volume per magnetic ion is Ω becomes

$$\mathbf{M}_S(\mathbf{r}) = g\mu_B \mathbf{S}_i(\mathbf{r})/\Omega(\mathbf{r}). \quad (8)$$

with $g \approx 2$ the spin g -factor and μ_B is the Bohr magneton. The local magnetic moment is

$$\mu_i(\mathbf{r}) = g\mu_B \mathbf{S}_i(\mathbf{r}). \quad (9)$$

Therefore if an external field $\mathbf{B}_{ext}(\mathbf{r}_i)$ is applied on a set of spins, the Zeeman energy becomes

$$\begin{aligned} E_{Zeeman} &= -g\mu_B \sum_i \mathbf{S}_i(\mathbf{r}_i) \cdot \mathbf{B}_{ext}(\mathbf{r}_i) \\ &= -g\mu_0 \mu_B \sum_i \mathbf{S}_i(\mathbf{r}_i) \cdot \mathbf{H}_{ext}(\mathbf{r}_i) \\ &= -\int_V \mu_0 \mathbf{H}_{ext}(\mathbf{r}) \cdot \mathbf{M}_S(\mathbf{r}) dV \\ &= -\int_V \mathbf{H}_{ext}(\mathbf{r}) \cdot \mathbf{J}_S(\mathbf{r}) dV. \end{aligned} \quad (10)$$

The stray field energy is to be obtained by summation over all dipole fields of the individual magnetic moments ‘homogeneous in the given volume’ in Eq. (9)

$$\mathbf{H}_S(\mathbf{r}) = \frac{1}{4\pi} \sum_i \left(\frac{\mu_i(\mathbf{r})}{|\mathbf{r} - \mathbf{r}_i|^3} - \frac{3(\mu_i(\mathbf{r}) \cdot (\mathbf{r} - \mathbf{r}_i)) \cdot (\mathbf{r} - \mathbf{r}_i)}{|\mathbf{r} - \mathbf{r}_i|^5} \right). \quad (11)$$

There have been many previous researches on the solution of Eq. (11) [11-13]. In this thesis the details of the mathematical derivation is not expressed. Likewise the Zeeman energy calculation the stray field energy is the integral of the product of the saturation polarization and the stray field on that point.

$$E_{stray} = -\int_V \mathbf{H}_S(\mathbf{r}) \cdot \mathbf{J}_S(\mathbf{r}) dV. \quad (12)$$

Classically, the conclusion of the calculation of the stray field is summarized as the summation of the contribution of the surface charges $\sigma(\mathbf{r})$ and the volume charges $\rho(\mathbf{r})$

$$E_{stray} = -\frac{1}{2} \mu_0 \int_S \sigma(\mathbf{r}) U(\mathbf{r}) dS - \frac{1}{2} \mu_0 \int_S \rho(\mathbf{r}) U(\mathbf{r}) dV, \quad (13)$$

where U is the scalar potential according to $\mathbf{H}_S(\mathbf{r}) = -\nabla U(\mathbf{r})$.

The stray field energy has been calculated by assuming a spheroid [14], in these days, a numerical method using boundary element method (BEM) are becoming more popular especially coupled with finite element method (FEM) [15-17].

Total Gibbs free energy of a magnet is given by the summation of the energy components described above: Exchange energy, crystalline anisotropy energy, Zeeman energy and stray field energy as following.

$$\begin{aligned} E_{tot} &= \int_V (e_{exch} + e_{ani} + e_{Zeeman} + e_{stray}) dV \\ &= \int_V \left(A \left((\nabla u_x)^2 + (\nabla u_y)^2 + (\nabla u_z)^2 \right) + \right. \\ &\quad \left. (K_0 + K_1 \sin^2 \theta + \dots) - \mathbf{H}_{ext}(\mathbf{r}) \cdot \mathbf{J}_S(\mathbf{r}) - \mathbf{H}_S(\mathbf{r}) \cdot \mathbf{J}_S(\mathbf{r}) \right) dV \end{aligned} \quad (14)$$

1.2. Magnetic Reversal Modes

(1) Coherent Rotation

External field strength to reverse a magnetization of a part of magnet is able to be estimated from Eq. (14), finding the \mathbf{H}_{ext} which makes the total Gibbs free energy less than 0 [18]. Several assumptions are needed to solve the equation analytically. For example, by assuming the magnetization vectors in all entire magnetic body are homogeneous ($\mathbf{J}_S(\mathbf{r}) = \mathbf{J}_S$, $E_{\text{exch}} = 0$), the Gibbs free energy of the uniaxial crystalline anisotropic magnet shown in Eq. (14) becomes simpler:

$$E_{\text{tot}} = \int_V \left((K_0 + K_1 \sin^2 \theta + \dots) - \mathbf{H}_{\text{ext}}(\mathbf{r}) \cdot \mathbf{J}_S(\mathbf{r}) - \mathbf{H}_S(\mathbf{r}) \cdot \mathbf{J}_S(\mathbf{r}) \right) dV \quad (15)$$

If the rotation of the spontaneous magnetization is assumed to take place in the xz plane and is described by the rotation angle φ , the stray field components are

$$H_{S,x} = -N_{\perp} M_S \sin \varphi, \quad \text{and} \quad H_{S,z} = -N_{\parallel} M_S \cos \varphi \quad (16)$$

with the demagnetization factors N_{\parallel} and N_{\perp} for parallel and perpendicular to the c-axis.

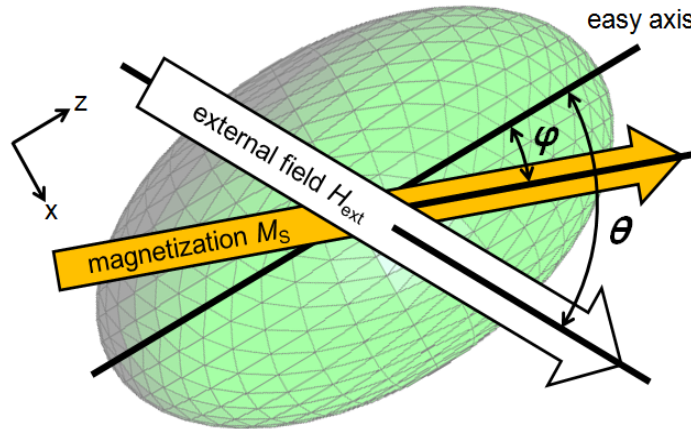


Fig. 6. Schematic diagram of a spheroid with an easy axis along the z-axis and magnetization M_S , under external field H_{ext} . The angle between the easy axis and external field is θ , whereas the one between the easy axis and the magnetization direction is φ .

Then the simplified equation Eq.(15) becomes

$$E_{tot} = \int_V \left(K_1 \sin^2 \varphi + K_2 \sin^4 \varphi + \frac{1}{2} \mu_0 N_{\perp} M_S^2 \sin^2 \varphi + \frac{1}{2} \mu_0 N_{\parallel} M_S^2 \cos^2 \varphi - \mu_0 H_{ext} M_S \cos(\theta - \varphi) \right) dV. \quad (17)$$

Assuming the external field H_{ext} is applied at angle with θ , the equilibrium is obtained when the first derivation of the above equation becomes zero,

$$K_1 \sin 2\varphi + 2K_2 \sin^2 \varphi \sin 2\varphi + \frac{1}{2} \mu_0 M_S^2 (N_{\perp} - N_{\parallel}) \sin 2\varphi - \mu_0 H_{ext} M_S \cos(\theta - \varphi) = 0. \quad (18)$$

Eq. (18) can be expressed in simpler way,

$$(K_1 + K_d) \sin 2\varphi + 2K_2 \sin^2 \varphi \sin 2\varphi - \mu_0 H_{ext} M_S \cos(\theta - \varphi) = 0 \quad (19)$$

by defining

$$K_d = \frac{1}{2} \mu_0 M_S^2 (N_{\perp} - N_{\parallel}) \quad (20)$$

as an effective shape anisotropy constant.

The solution of Eq. (19) yields a general switching field as a function of the material parameters and the applied field angle θ ,

$$H_{SW} = \frac{2(K_1 + K_d)}{\mu_0 M_S} \frac{1}{\left((\cos \theta)^{2/3} + (\sin \theta)^{2/3} \right)^{3/2}} = H_{SW}^0 \frac{1}{\left((\cos \theta)^{2/3} + (\sin \theta)^{2/3} \right)^{3/2}}, \text{ where } H_{SW}^0 = \frac{2(K_1 + K_d)}{\mu_0 M_S} \quad (21)$$

so called Stoner-Wohlfarth equation, derived by Stoner and Wohlfarth in 1948 [19].

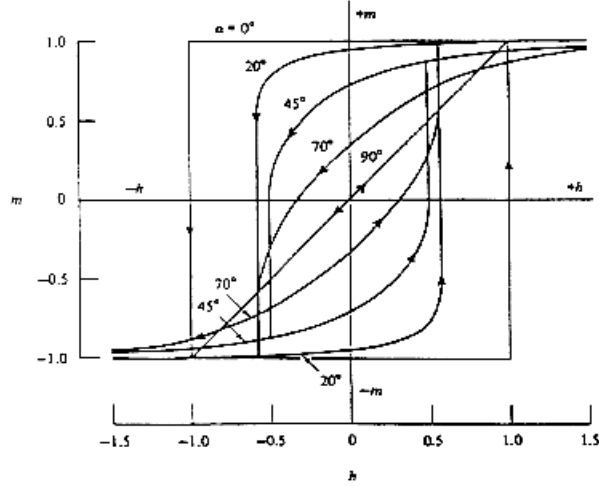


Fig. 7. Hysteresis curves of a spherical single domain particle for different angles between anisotropy axis and external field

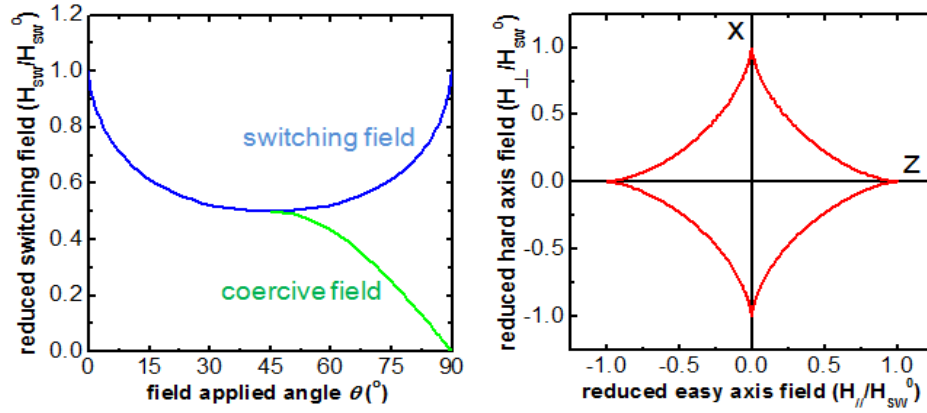


Fig. 8. Switching field by Stoner-Wohlfarth coherent rotation, (left) as a function of field applied angle and (right) reduced easy axis field and hard axis field, in other words, Stoner-Wohlfarth astroid. The axes z and x corresponds to the easy axis and the hard axis shown in Fig. 6.

The angular dependency of the switching field obtained by Stoner-Wohlfarth coherent rotation is shown in Fig. 8. The switching field is maximized at the field angle of 0° and 90° as $H_{SW}^0 = 2(K_1 + K_d)/\mu_0 M_S$, and minimized at 45° as half of it. The field angle is considered as the H_{ext} was applied in two directions, easy axis and hard axis. Due to the shape of the curve, it is called as ‘‘Stoner-Wohlfarth astroid’’.

(2) Incoherent Rotations: Curling and Buckling

The coherent rotation has a very well aligned spins in a direction. In this case strong stray field is generated that the total energy of the system increases, and the amount of the increment is getting larger in bigger model. The magnet which has a certain dimension that the stray field energy makes the magnetic body unstable, the spins are bent each other to reduce total energy, especially during the magnetization reversal process. This mode, where the spins are heading each others' tail is called as *curling mode*, as shown in Fig. 10(c). The ideal curling mode is characterized by a vanishing stray field totally, i.e., $\nabla \cdot \mathbf{M}_S = 0$ and $\mathbf{n} \cdot \mathbf{M}_S = 0$ [8-9]. In the book of Aharoni [8] and Kronmüller [9], the curling mode is explained based on a cylindrical model in Fig. 9(b). But in these days, the curling mode is more invited as a form of vortex mode [20]. Likewise, the Buckling mode has been regarded as a state of alternating surface charges as shown in Fig. 9(c) [8-9].

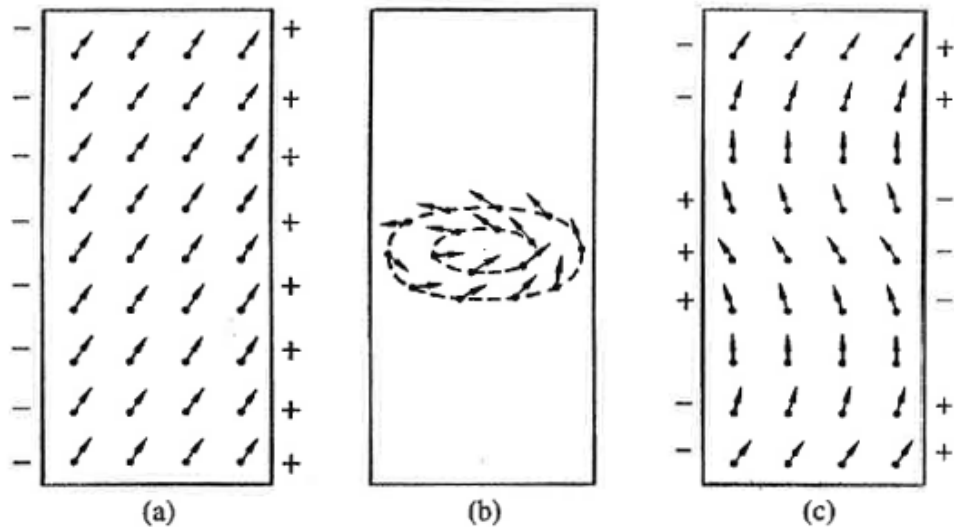


Fig. 9. Three different nucleation modes. (a) homogeneous magnetization (b) curling, and (c) buckling.

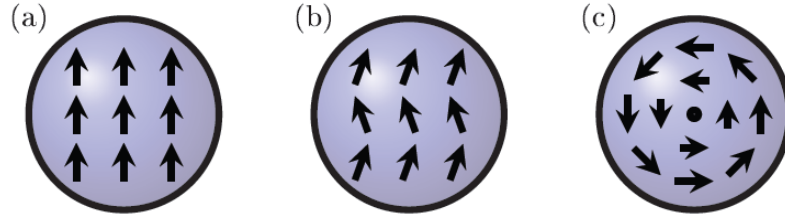


Fig. 10. Review of three different nucleation modes. (a) homogeneous rotations, (b) buckling, and (c) curling. The center of the curling mode is pointing out of (or into) the plane [21].

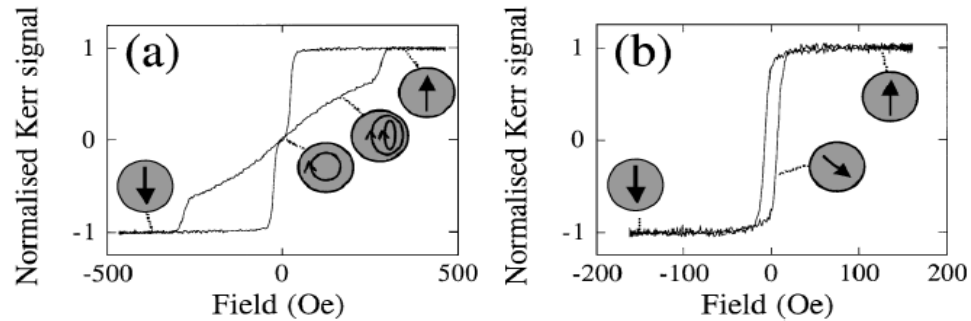


Fig. 11. Hysteresis loops measured from nanomagnets of diameter (d) and thickness (t): (a) $d = 300$ nm, $t = 10$ nm; (b) $d = 100$ nm, $t = 10$ nm. The schematic annotation shows the magnetization within a circular nanomagnet, assuming a field oriented up the page [20].

Fig. 11 shows the magnetization curves measured from permalloy disks, in different diameter. For the case of the diameter $d = 100$ nm Fig. 11(b), the ferromagnetic dot is reversed by coherent rotation showing magnetization curve of which shape is predicted and explained in the previous session (Fig. 7). But if the diameter becomes much larger, $d = 300$ nm in Fig. 11(a), an inhomogeneous reversal process based on curling appears. The spins of the specimen are circulated to reduce stray field energy. At the center of the circulating spins, a vortex exists. The vortex structure is initiated by spin instability shown in Fig. 12, corresponds to the Buckling mode: the increase of exchange energy is compensated by the reduced stray field energy due to the alternating surface charges.

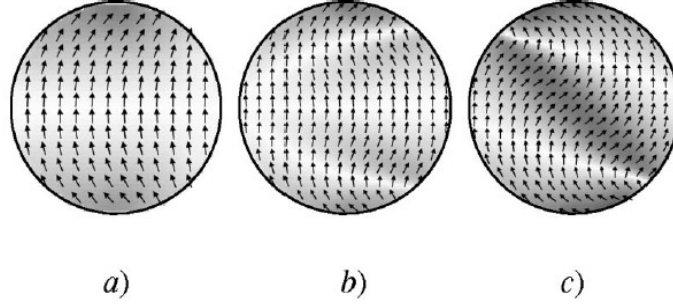


Fig. 12. The spin instabilities modes obtained with micromagnetic calculations for the circular dots with the $R = 0.1$ (a), 0.2 (b), and $0.25 \mu\text{m}$ (c) and fixed $L = 30 \text{ nm}$.

The nucleation field for the magnetization reversal of cylindrical structure is obtained by considering the curling and buckling mode as following [22].

$$H_N = \frac{2K_1}{\mu_0 M_S} + \frac{2A}{\mu_0 M_S} \left[\frac{1.84}{R} \right]^2 - \frac{1}{2} M_S (1 - \varepsilon) \quad (22)$$

where the parameter ε describes the effect of the alternating and reduced surface charges at the cylinder surface and at the ends. For diameter $R > 10 \text{ nm}$ ε decreases according to a $R^{-2/3}$ law. More practically, Guslienko has suggested an analytic equation for the vortex nucleation field for curling mode reversal.

$$H_N(\beta, R) = 4\pi M_S \left(F_1(\beta) - F_2(\beta) - \frac{1}{\pi} \left(\frac{\xi_0}{R} \right)^2 \right) \quad (23)$$

In Eq. (23) each terms are defined as

$$F_\mu(\beta) = \int_0^\infty \frac{dt}{t} \left(1 - \frac{1 - \exp(-\beta t)}{\beta t} \right) J_\mu^2(t) \quad (24)$$

where

$\beta = \text{thickness} / \text{radius}$

ξ_0 : exchange length

$J_\mu(t)$: Bessel's function

μ : an integer

R : radius

The magnetization reversal curves of permalloy magnetic dots as a function of diameter (d) and thickness (t) are shown below, Fig. 13 [20]. The coherent reversal and vortex motion mode is recognized by the shape of the loops, comparing with Fig. 11.

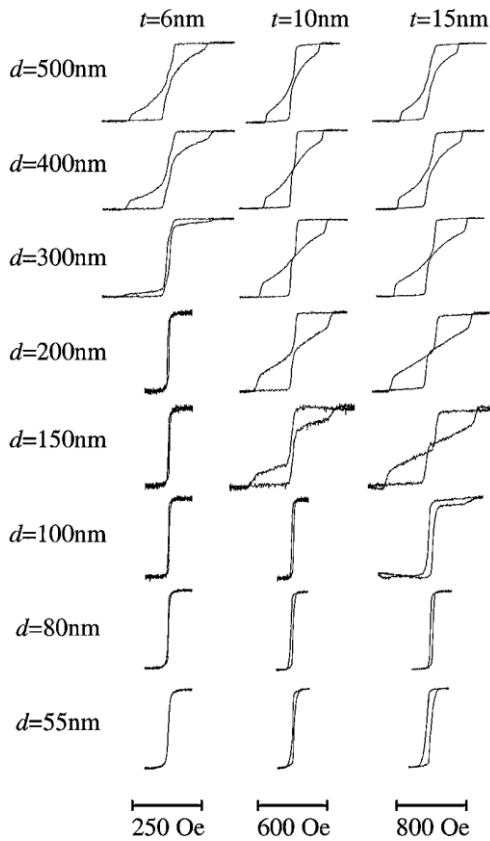


Fig. 13. Hysteresis loops measured as a function of diameter (d) and thickness (t) from circular nanomagnets. For each loop the horizontal axis is applied field and the vertical axis is magnetization [20].

(3) Domain wall motion: Domain Nucleation and Propagation

As addressed in the previous session, the spins of a magnet tend to compensate stray fields to lower the magnetic energy. But also the spins are likely to be align themselves parallel to each other to reduce exchange energy. Moreover, if the material has a strong crystalline anisotropy, the spins also tend to be aligned along the easy axes. Consequently ferromagnetic materials in the global demagnetized state are subdivided into domains within which the spontaneous magnetization lies parallel to an easy direction as revealed in Fig. 14. The tendency to reduce stray field is also observed in magnetization reversal process.

In 1960 Aharoni has suggested a reversal process through nucleation and propagation, triggered by a certain imperfections [23]. In his manuscript, he is saying as following: “Crystal imperfections such as dislocations, impurities, cavities, etc., seem the most probable explanation for the success of the theory in the cases of small particles and its failure in the case of large particles, since one would expect the probability of finding an imperfection to increase with particle size.”.

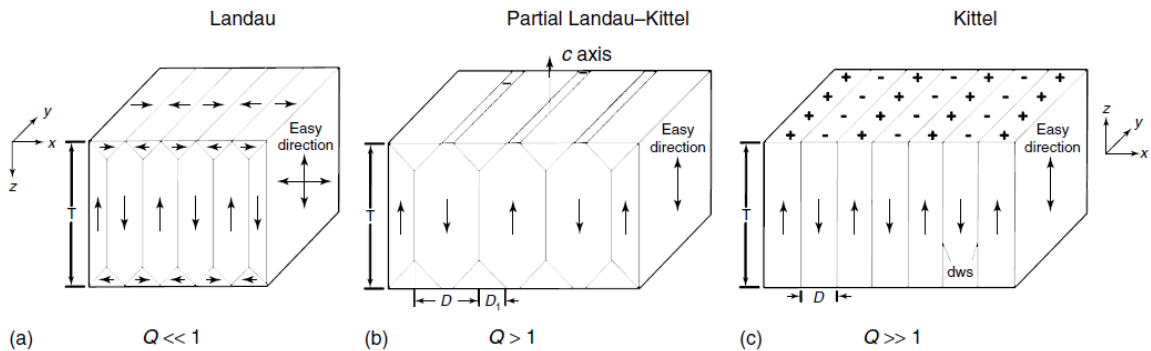


Fig. 14. Characteristic laminar domain pattern of platelets for different Q -parameters. (a) Landau structure in $\langle 100 \rangle$ - α -Fe platelets. (b) Partial Landau-Kittel structure for intermediate Q values (Co). (c) Open Kittel structure for hard magnetic uniaxial crystals with $Q \geq 1$ (FeNdB) [9]

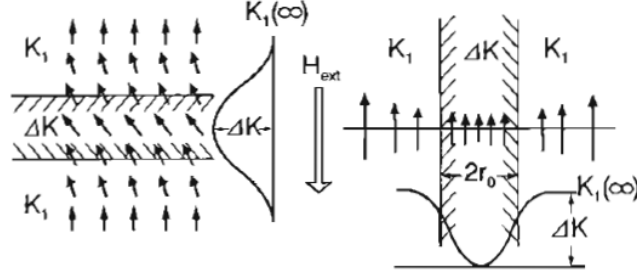


Fig. 15. Model of soft magnetic planar nucleus of width $2r_0$. Left side: H_{ext} is perpendicular to the stripe, right one is parallel [9].

In order to treat this behavior in analytic way, a planar region of thickness $2r_0$ with crystal anisotropy K_p in a hard matrix with K_1 is assumed. Fig. 15 presents the geometry of this nucleation region, where under the action of a magnetic field a rotation process takes place leading to an inversely magnetized region. Taking account of the magnetization rotation and its magnetostatic and exchange influence in the magnetic energy equation (14), the nucleation field of the first case – magnetization is perpendicular to the plane is given by

$$\begin{aligned}
 H_{nucl.} &= \frac{2K_p}{\mu_0 M_S} - \frac{1}{2} M_S + \frac{A\pi^2}{2r_0^2 \mu_0 M_S} \\
 &= \frac{2K_p}{J_S} - \frac{1}{2\mu_0} J_S + \frac{A\pi^2}{2r_0^2 J_S}
 \end{aligned} \tag{25}$$

For the case of the magnetization is parallel to the interface plane, the nucleation field is as following [9].

$$H_{nucl.} = \frac{2K_1}{\mu_0 M_S} \left(1 - \frac{\pi^2 (A/K_1)}{4\pi^2 r_0^2} \left[1 - \sqrt{1 + \frac{4(K_1 - K_p)r_0^2}{A}} \right]^2 \right) - \left(\frac{1}{2} + N_d \right) M_S \tag{26}$$

The nucleated reversal domain and the previous domain have a domain wall between them, in domain wall the spin configuration is gradually changing from one domain's to the other's. The domain wall has very large exchange energy owing to the drastically varying spin alignment. Based on the main feature which determines the domain, the domain wall has two basic types: Néel wall and Bloch wall.

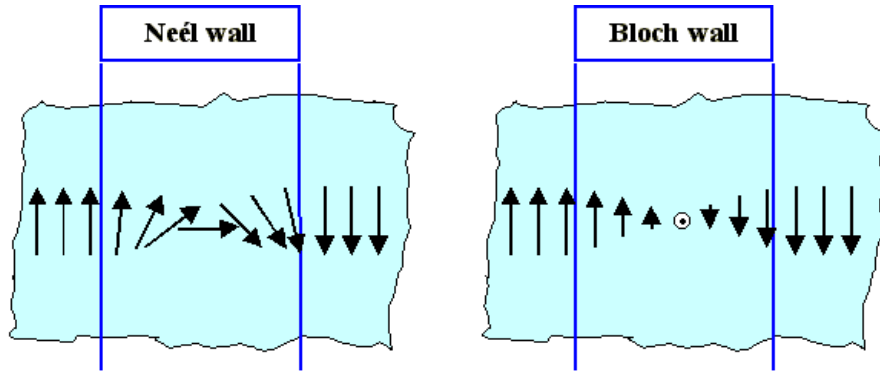


Fig. 16. Schematic diagrams of Néel wall and Bloch wall

The domain wall width and domain wall energy of 180° Néel wall and 180° Bloch wall are obtained as

$$\delta_{Ne'el} = \pi \sqrt{\frac{2A}{\mu_0 M_S^2}} = \pi d_s \quad (27)$$

$$\gamma_{Ne'el} = 4\sqrt{A \frac{\mu_0 M_S^2}{2}}$$

$$\delta_{Bloch} = \pi \sqrt{\frac{A}{K_1}} = \pi d_K \quad (28)$$

$$\gamma_{Bloch} = 4\sqrt{AK_1}$$

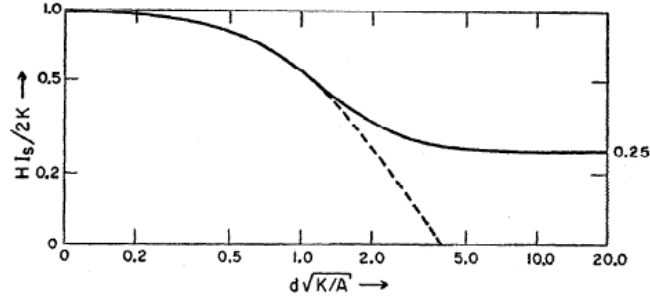


Fig. 17. The nucleation field (dashed) and coercive force (full curve) in terms of the coercive force of perfect material, as functions of the defect size, d . [23]

In many cases a magnetic material has a defect works as a source of the reversal domain nucleation, especially in the large scaled structure. Fig. 17 shows the coercive field as a function of the defect size. The larger defect results in less coercive force, because the magnetization process is no more controlled by propagation, but nucleation. Back to the switching fields as a function of the external field applying angle in Fig. 8, the switching field strength considering the inhomogeneity becomes much lower, particularly in low angles (Fig. 18). In both cases, the angular dependence of the switching field is similar to that of the coercivity due to domain wall pinning ($1/\cos\theta$) [24]. S stands for the reduced radius (R/R_0).

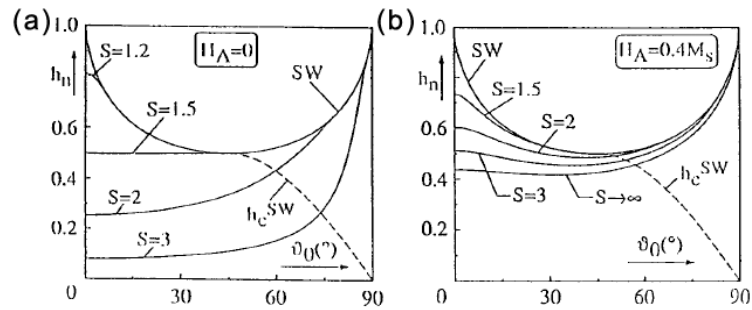


Fig. 18. Nucleation field of prolate spheroids (aspect ratio: 8) as a function of the field angle for (a) vanishing magnetocrystalline anisotropy (curling mode) and (b) for moderate uniaxial magnetocrystalline anisotropy.. The curve labeled SW gives the switching field due to the Stoner-Wohlfarth theory and the dashed line gives the corresponding coercivity [25].

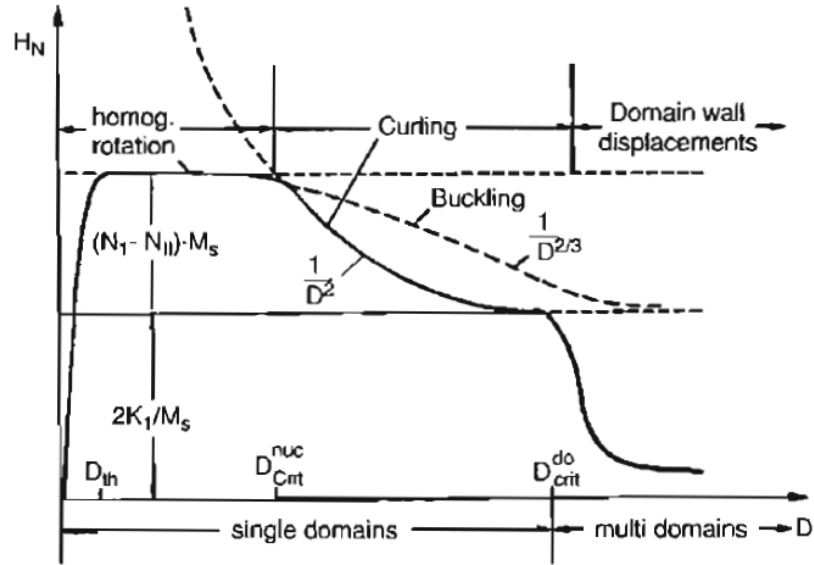


Fig. 19. Schematic representation of the coercive field as a function of the particle diameter D (solid line) perfect particle, and (dashed) imperfect particle [9].

The magnetic switching including homogeneous region to domain wall motion is summarized in Fig. 19. Above the critical size of superparamagnetism (D_{th}), the magnetization reversal mode of a given magnetic particle is varied by its dimensions, homogeneous rotation, curling and buckling, finally domain wall displacements. The nucleation field for reversal process is reducing as the reversal process becomes inhomogeneous. Please note that all previous reversal modes is quasistatistical process that the criteria are determined by energy minima.

(4) Precessional Motion

Precessional switching is the switching process occurs at short time scales, e.g. when the field is varied rapidly. If the field is applied in a very short time, the magnetization is reversed by magnetic torque rather than energy minimization. The torque is evaluated by the Landau-Lifshitz-Gilbert (LLG) equation [18],

$$\begin{aligned} \frac{d\mathbf{M}}{dt} &= -\gamma_0 (\mathbf{M} \times \mathbf{H}_{eff}) + \frac{\alpha}{M_S} \left(\mathbf{M} \times \frac{d\mathbf{M}}{dt} \right), \text{ or} \\ \frac{d\mathbf{J}}{dt} &= -\gamma (\mathbf{J} \times \mathbf{H}_{eff}) + \frac{\alpha}{J_S} \left(\mathbf{J} \times \frac{d\mathbf{J}}{dt} \right) \end{aligned} \quad (29)$$

where $\gamma_0 = \mu_0\gamma$, γ is the gyrometric ratio, 2.210175×10^5 m/As and \mathbf{H}_{eff} is the effective field obtained by the first derivation of total Gibbs free energy = 0 in Eq. (14),

$$\mathbf{H}_{eff} = \frac{2A}{J_S} \Delta \mathbf{u} + \frac{2K_1}{J_S} \mathbf{a}(\mathbf{J} \cdot \mathbf{a}) + \mathbf{H}_{ext} + \mathbf{H}_S. \quad (30)$$

In Eq. (29) α is the Gilbert damping constant.

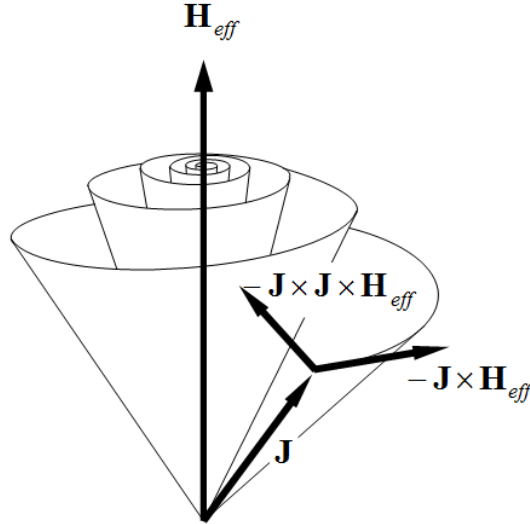


Fig. 20. Magnetic torque and damping applied on a spin \mathbf{J} .

The trajectory of precessional switching is estimated from the energy conservation. Assuming the magnet is saturated to positive x-direction, the total energy is

$$\frac{E}{\mu_0 M_S^2} = \frac{1}{2} (N_Z \mathbf{u}_z^2 - h_k \mathbf{u}_x^2) - h \mathbf{u}_y, \quad (31)$$

with

$$\mathbf{u}_x^2 + \mathbf{u}_y^2 + \mathbf{u}_z^2 = 1. \quad (32)$$

The h_k and h denote $2K_1/\mu_0 M_S^2$ and H_{ext}/M_S , respectively [26].

Here a coherent rotation is assumed that the exchange energy is neglected. N_z stands for the z-directional demagnetization field. From two equations above, the following equations are obtained. If the total energy is conserved in the whole procedure, the Landau-Lifshitz equation with damping constant $\alpha = 0$ becomes

$$\frac{d}{dt} \mathbf{u}_x = \gamma_0 M_S \mathbf{u}_z (N_Z \mathbf{u}_y + h) \quad (33)$$

$$\frac{d}{dt} \mathbf{u}_y = -\gamma_0 M_S \mathbf{u}_z \mathbf{u}_y (N_Z + h_k) \quad (34)$$

$$\frac{d}{dt} \mathbf{u}_z = -\gamma_0 M_S \mathbf{u}_x (h - h_k \mathbf{u}_y) \quad (35)$$

From the equations, the two equations below are obtained.

$$\mathbf{u}_x^2 = 1 - \frac{2h}{N_Z + h_k} \mathbf{u}_y - \frac{N_Z}{N_Z + h_k} \mathbf{u}_y^2 \quad (36)$$

$$\mathbf{u}_z^2 = \frac{2h}{N_Z + h_k} \mathbf{u}_y - \frac{h_k}{N_Z + h_k} \mathbf{u}_y^2 \quad (37)$$

Using Eq. (36) and (37), trajectories for precessional reversal are drawn.

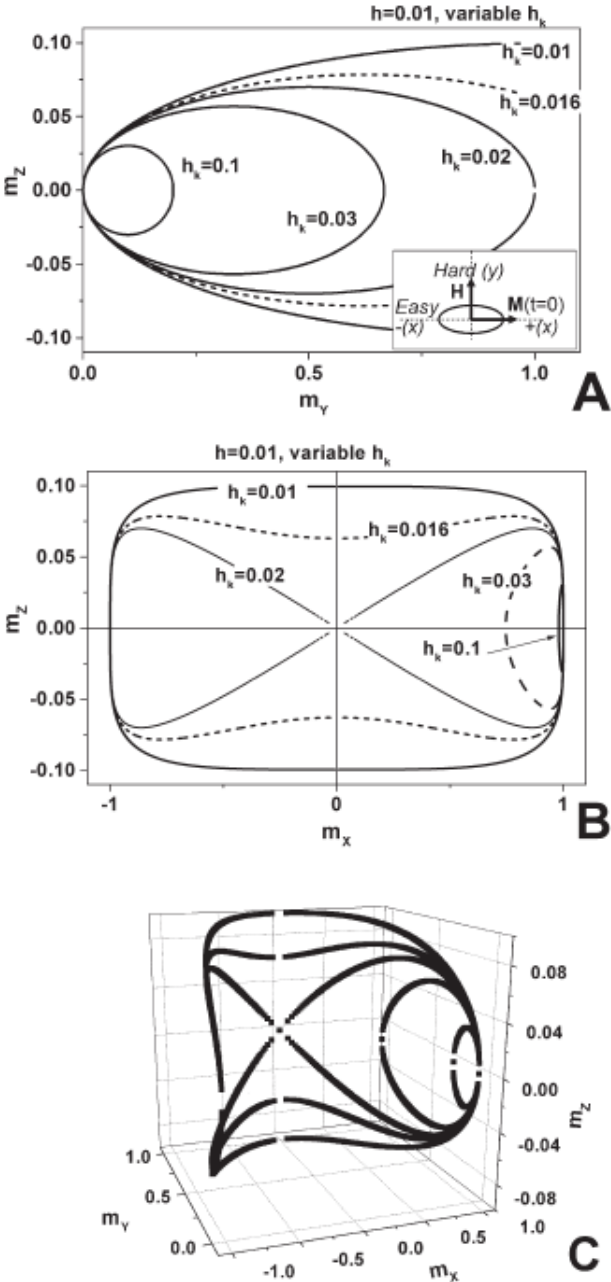


Fig. 21. Exact magnetization trajectory of a non lossy macrospin film of initial magnetization along x when subjected to a transverse field $h = 0.01$ applied along y , with $N_z = 1$. The uniaxial anisotropy is along x . The anisotropy field is varied from $h_k = 0.01, 0.016, 0.02, 0.03$ and 0.1 . The two later h_k values correspond to anisotropy-dominated trajectories. (a) Trajectory in the zy plane. (B) Trajectory in the (xz) plane. (c) Vector m (in the text, u) trajectory when initial magnetization is along x . Inset: Definition of the axes. The ellipse stands for the anisotropic macrospin [26].

1.3. Numerical Micromagnetics

(1) Introduction of numerical micromagnetics

Until the middle of 20th century, magnetic problems had to be treated by quantum mechanics in atomic scale or by Maxwell equation assuming simple magnetization state such as a saturated state. Supported by the description of the exchange energy by a continuum theoretical expression derived by Landau and Lifshitz [12], magnetic energy was able to be understood as a sum of several competing energy terms: Exchange energy, crystalline anisotropy energy, Zeeman energy and stray field energy [18, 27], as described in **Chapter 1.1**. Magnetoelastic energy [28-29], thermal fluctuation [30-31], eddy current [32-34], spin torque term [35-37] and microwave terms [38-39] are possible to be included for needs. In these days the development of the computer capabilities available makes it possible to use numerical methods to solve problems which had been unsolvable up to now. The numerical treatment of the micromagnetics requires a discrete representation of the continuous magnetization distribution. The discretization size is several nanometers, much larger than the atomic lattice constants. This is possible because of the exchange coupling, the spins are not varied significantly in a small dimension. The given magnetic model is discretized into small elements using finite difference method (FDM) and finite element method (FEM). In the discretized nodes or cells the effective fields are calculated, the magnetization is evaluated toward equilibrium using a torque from LLG equation (time integration) or the most stable state (energy minimization).

method	Author(s) and reference	Title of released program and the URL
FDM	Brown [18]	
	LaBonte [40]	
	Schabes and Bertram [41]	
	Nakatani et al. [42]	
	Scheinfein and Blue [43]	LLG http://llgmicro.home.mindspring.com/
	Berkov and Ramstöck [44]	MicroMagus http://www.micromagus.de/
	Oti [45]	
	McMichael and M. J. Donahue [46]	OOMMF math.nist.gov/oommf/
	Thiaville et al. [47]	
	Firastrau [48]	ST_GLFFT http://spintec.fr/spip.php?article333
FEM	Seshan and Cendres [49]	
	Fredkin and Koehler [50]	
	Bagneres-Viallix et al. [51]	
	Schrefl and Fidler [52]	FEMME www.suessco.com
	Ramstöck [53]	
	Hertel and Kronmüller [54]	
	Fischbacher et al. [55]	NMAG http://nmag.soton.ac.uk/
	Scholz et al. [56]	magpar http://www.magpar.net/
	Szabolics et al. [57]	feellgood [58]

Table 1. List of the various micromagnetic programs and their source.

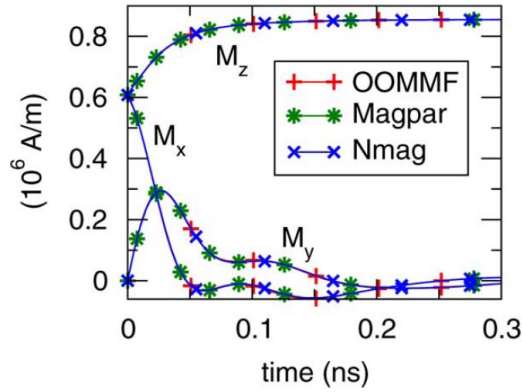


Fig. 22. Comparison of simulation packages for the bar example. Initial magnetization is $(M_x, M_y, M_z) = (0.707, 0, 0.707) \times 0.86$ MA/m. M increases over time, as the system tries to avoid strong magnetic effective surface charges on the long sides of the bar [55].

In many cases the numerical micromagnetic simulations show reliable results regardless of its method, as shown in Fig. 22 [55]. The OOMMF (FDM), Magpar (FEM) and Nmag (FEM) produce the same results for a given problem. However, the models with curved surfaces often make a deviation between the results owing to the edge steps in FDM models. Fig. 23 shows the sphere models for FDM and FEM calculations. The FDM model is subdivided into the cuboids with the same geometry, whereas the FEM models have small tetrahedra with irregular shape. In order to show the difference clearly, a rather large cubes are chosen to resolve the sphere. In an actual simulation, much smaller cell size are used to resolve geometry better [59].

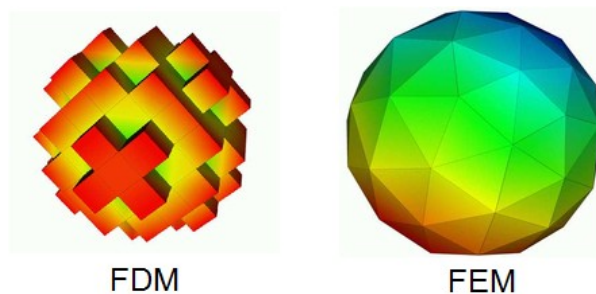


Fig. 23. Comparison of sphere models generated for FDM and FEM [59].

Fig. 24 shows an example of the discrepancy between FDM and FEM[60]. Vaysset et al. has performed a number of simulations on 60 nm-diameter spin-transfer oscillator in absence of application field, excited by a dc current. The results from macrospin model, FDM results with their own code [48] and FEM results, also from their own code [57]. The Finite Difference method and the Finite Element Method show almost identical results, except for a small range of current between 1.3×10^{11} and 1.7×10^{11} A/m². This difference has been proved to be due to a stationary spin wave induced by the staircase-like edge of the FD mesh.

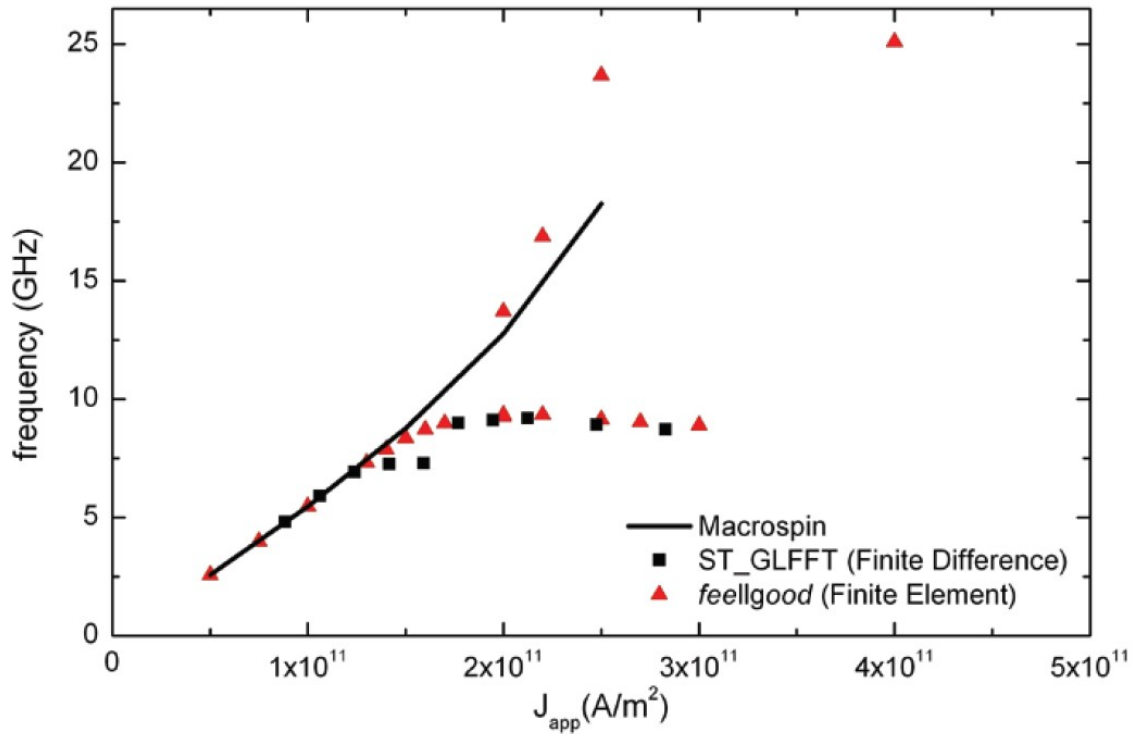


Fig. 24. Frequency vs. current density for Finite Difference simulations (black squares), Finite Element simulations (red triangles), and macrospin simulations (black line) [60].

(2) Finite Difference Method Micromagnetics

Finite difference method (FDM) is widely used to find approximate solutions of problems involving partial differential equations (PDEs). The basic idea is the approximation of the partial derivatives of a function f by finite different quotients in Cartesian Δx , Δy , Δz and time Δt .

$$f(x + \Delta x, y, z, t) = f(x, y, z, t) + \Delta x \frac{\partial f(x, y, z, t)}{\partial x} + \frac{(\Delta x)^2}{2} \frac{\partial^2 f(x, y, z, t)}{\partial x^2}. \quad (38)$$

A partial differential equation can be changed to a system of algebraic equations by replacing the partial derivations in the differential equation with their finite difference (FD) approximations. Fig. 25 shows a schematic of a given region, subdivided into FD elements. Using the algebraic equations given like Eq. (38) and boundary conditions, proper solutions at each node are obtained. In order to apply FD on micromagnetics, the field components in effective field (Eq.(30)) should be replaced with the followings.

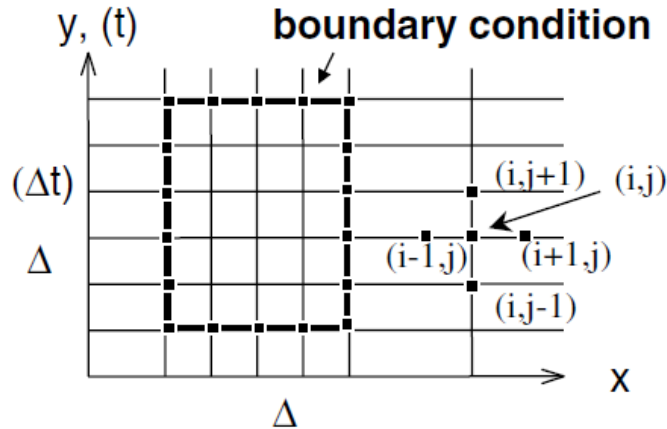


Fig. 25. Schematic discretization of a given region in the $(x,y)/(x,t)$ plane, subdivided into FD elements, in which the micromagnetic equations are satisfied [61].

$$\mathbf{H}_{exch} = \frac{2A}{\Delta x^2 M_S^2} \sum_{i \in NN} \mathbf{M}_i \quad (39)$$

where NN stands for the indices of the nearest neighbors. The calculation of the anisotropy is straightforward.

$$\mathbf{H}_{ani} = \frac{2K_1}{M_S^2} \mathbf{a}(\mathbf{J} \cdot \mathbf{a}) \quad (40)$$

The calculation of the stray field is calculated in this way. Within each computation cell, the magnetization is assumed to be homogeneous. In this case it is possible to calculate the demagnetization field analytically [62].

$$\mathbf{H}_s(\mathbf{r}) = \frac{\Delta x^3}{4\pi} \sum_i \left(\frac{\mu_i(\mathbf{r})}{|\mathbf{r} - \mathbf{r}_i|^3} - \frac{3(\mu_i(\mathbf{r}) \cdot (\mathbf{r} - \mathbf{r}_i)) \cdot (\mathbf{r} - \mathbf{r}_i)}{|\mathbf{r} - \mathbf{r}_i|^5} \right). \quad (41)$$

In many FDM micromagnetic packages the stray fields are treated by Fast Fourier Transformation (FFT) to reduce the computational power to deal with and shorten the calculation time [44].

(3) Finite Element Method Micromagnetics

Finite element (FE) method is a well established method, has been applied in many fields of computer aided science and engineering. In spite of the merit that arbitrary shapes are able to be dealt with, it requires the cost of a more complex mathematical background. At first, the model should be discretized into finite elements. Within these finite elements the solution of the problem is interpolated with polynomials.

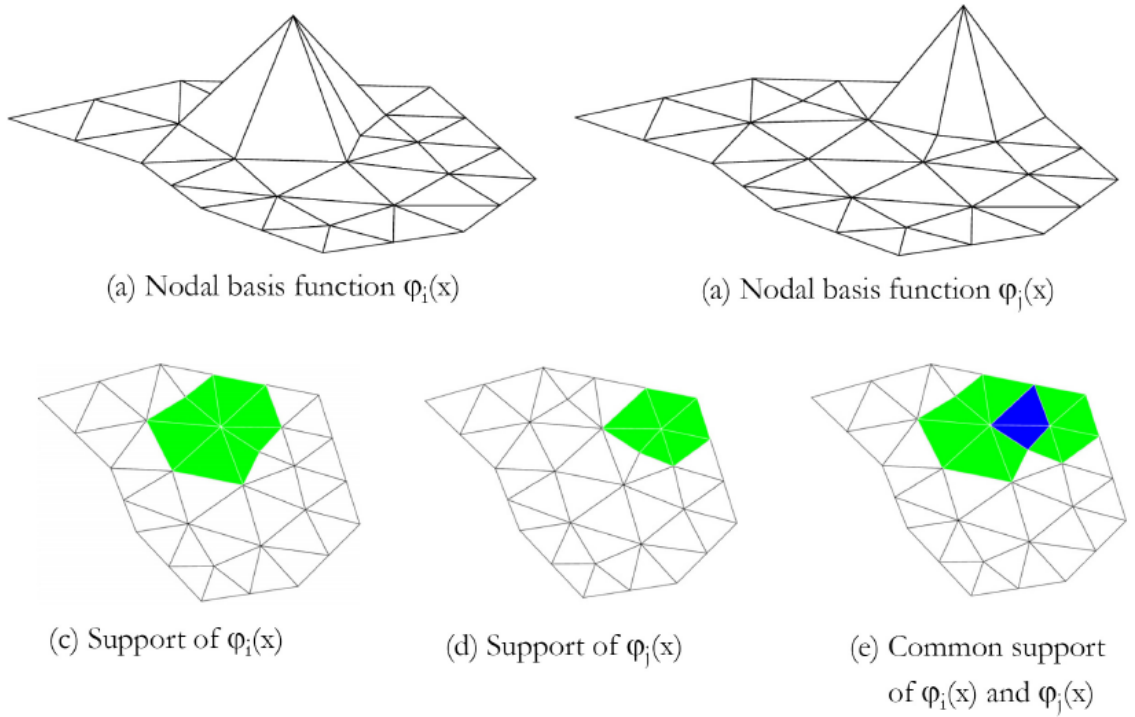


Fig. 26. Nodal linear basis functions and common support of two basis function.

Applying the finite element method to micromagnetism the magnetization $\mathbf{M}(\mathbf{r})$ is expanded with basis functions. In the finite element method the basis functions $\varphi_i(\mathbf{r})$ are chosen in such a way, that the support of each basis function (the region where $\varphi_i(\mathbf{r})$ is nonzero) is small. The support consists of only a few connected elements. The value of every basis function is 1 on one node and zero all the other nodes. (26)Fig. 26 gives an example for linear basis function in two dimensions. Only a small number of basis functions have a nonzero overlap.

The basis obey

$$\sum_{i=1}^N \varphi_i(\mathbf{r}) = 1. \quad (42)$$

and

$$\varphi_i(\mathbf{r}_j) = \delta(\mathbf{r}_j - \mathbf{r}_i). \quad (43)$$

where \mathbf{r}_i and \mathbf{r}_j denote the positions of the local node points i and j , respectively. N is the number of node points of the finite element mesh that coincides with the number of basis functions. Therefore for k -th element of \mathbf{M} we can write

$$M^k(\mathbf{r}) = \sum_{i=1}^N M_{S,i} u_i^k \varphi_i(\mathbf{r}). \quad (44)$$

$M_{S,i}$ is the polarization at the node point i . At a nodal point i the values of the reduced magnetic polarization $u^k(x)$ are given by the coefficients u_i^k .

Stray field calculation is a big burden for the computational resources. In order to make it efficiently, a hybrid boundary element method (BEM)/ FEM method are introduced by Fredkin and Koehler and implemented by Schrefl [15-16]. Here comes the stray field calculation process. According to the Maxwell's equation $\nabla \mathbf{B} = 0$ and the relationship between magnetic flux density \mathbf{B} , magnetic field strength \mathbf{H} , magnetization \mathbf{M} and magnetic polarization \mathbf{J} : $\mathbf{B} = \mu_0(\mathbf{H} + \mathbf{M}) = \mu_0 \mathbf{H} + \mathbf{J}$,

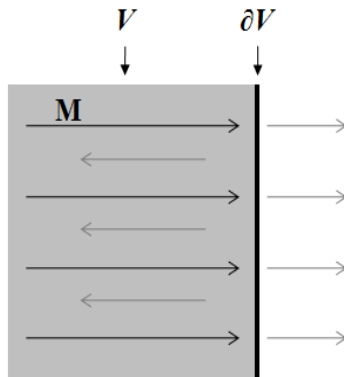


Fig. 27. A schematic diagram of the boundary of a magnetic model. V and ∂V stand for the volume domain and its boundary

$$\nabla \mathbf{B} = \mu_0 (\nabla \mathbf{H} + \nabla \mathbf{M}) = \mu_0 \nabla \mathbf{H} + \nabla \mathbf{J} = 0. \quad (45)$$

Consequently,

$$\nabla \mathbf{H} = -\nabla \mathbf{M} = -\frac{\nabla \mathbf{J}}{\mu_0}. \quad (46)$$

Using $\mathbf{H} = -\nabla \psi$, where ψ is the magnetic scalar potential,

$$\begin{aligned} \Delta \psi &= \nabla \mathbf{M} = \frac{\nabla \mathbf{J}}{\mu_0} \quad (\in \mathbf{V}, \text{ internal}) \\ \Delta \psi &= 0 \quad (\notin \mathbf{V}, \text{ external}) \end{aligned} \quad (47)$$

With boundary conditions at $\partial \mathbf{V}$,

$$\begin{aligned} \psi_{\text{int}} &= \psi_{\text{ext}} \\ (\nabla \psi_{\text{int}} - \nabla \psi_{\text{ext}}) \cdot \mathbf{n} &= \mathbf{M} \cdot \mathbf{n} = \frac{\mathbf{J}}{\mu_0} \cdot \mathbf{n}. \end{aligned} \quad (48)$$

In a actual hybrid BEM/FEM micromagnetic simulations the result of the boundary element method is stored as a form of boundary matrix B . At each step the Poisson equation in Eq. (47) is solved for a given distribution of the magnetic moments to receive the potential. Then the stray field is obtained from $\mathbf{H} = -\nabla \psi$ [63].

The stray field goes into the effective field, then LLG equation is calculated in every iteration step until the final time becomes smaller than the determined one, t_{final} . The micromagnetic simulation processes are drawn in Fig. 28 [64]. All micromagnetic simulation results in this manuscript is obtained from FEMME [65].

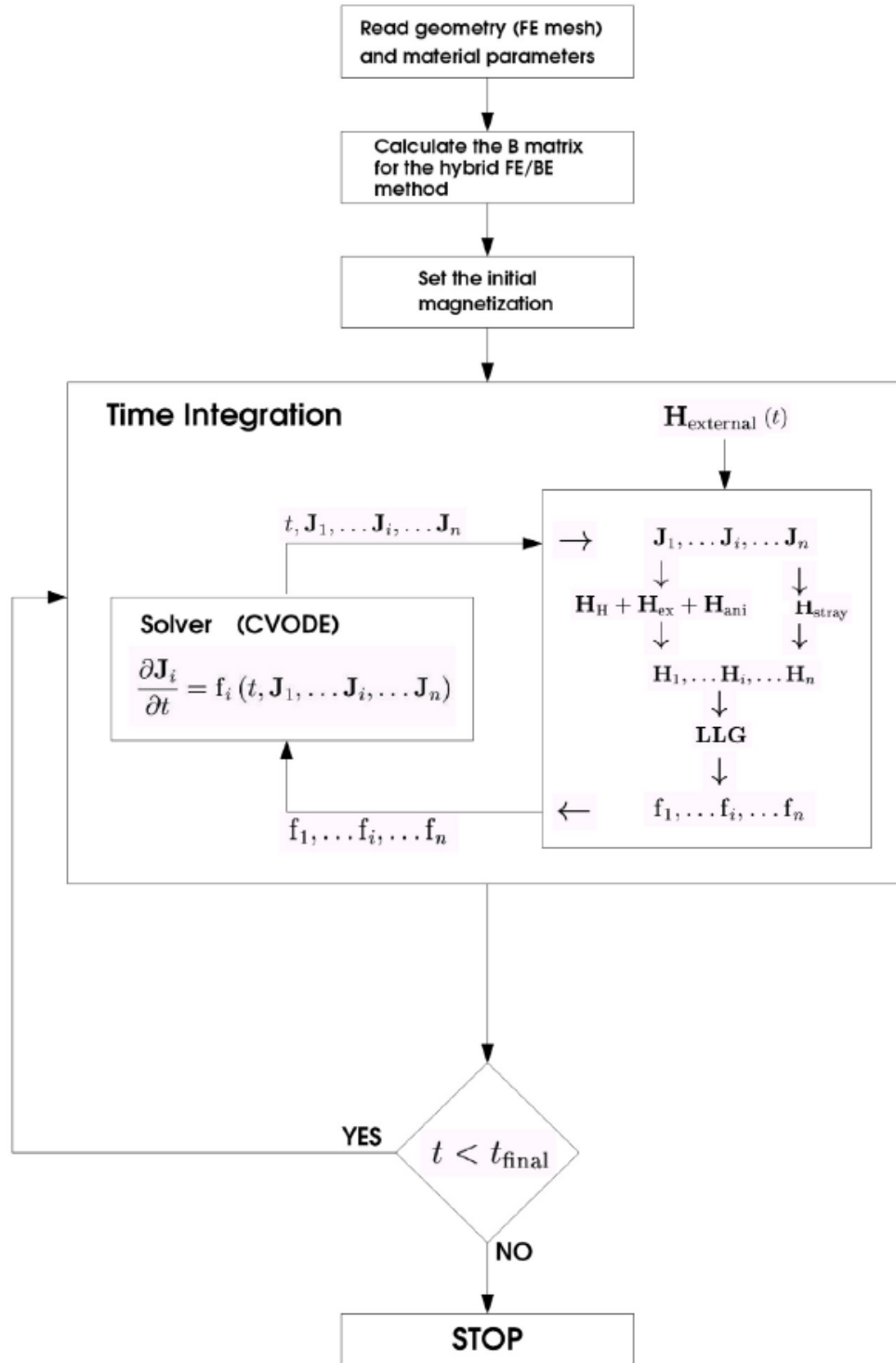


Fig. 28. Schematic of the simulation cycle of a typical finite element micromagnetic package such as MAGPAR [64].

(4) Energy barrier estimation : Nudged Elastic Band Method

A thermal stability of a magnetic bit is determined by the material parameters as well as the geometric factors, for example, the size. In the previous chapter we have looked through the magnetization reversal mode as a function of the magnetic particle diameter. The reversal by thermal fluctuation also follows one of the known magnetization modes such as coherent rotation or domain wall motion. In these two cases the height of the magnetic energy without external field is given by

$$\begin{aligned} E_{barrier} &= KV && \text{(coherent rotation)} \\ E_{barrier} &= 4F\sqrt{AK} && \text{(domain wall motion)} \end{aligned} \quad (49)$$

In this equation F stands for the cross-sectional area of the domain wall and V is the volume of the grain. The smaller one of the above energy barriers works as the effective one. The Eq. (49) is a good approach to roughly estimate the energy barrier, however, in many cases it is not sufficient to take into account the complex geometry of a bit composed of several kinds of materials. Berkrov [66] calculated the transition path of interesting single domain particles, minimizing the action along the path. He showed that a direct minimization of the action may also give paths through local maxima which have to be excluded. Therefore another way, so-called nudged elastic band (NEB) method is suggested by Henkelman and Jónsson to calculate minimum energy paths [67]. Starting from an initial guess for the path which connects two local minima of the system, a highly probable path is found moving the points along the path according to an algorithm which resembles tensioning an elastic band across a mountain. In micromagnetics we represent the magnetic states of a system by a set of magnetic moments. This corresponds

to the magnetization at the nodes of the finite element mesh, which is used to model the geometry and grain structure of the magnet. A sequence of magnetic states can be constructed in such a way as to form a discrete representation of a path from the initial magnetization state \mathbf{M}_i to the final magnetization state \mathbf{M}_f . The simplest case of the initial path is just a straight line interpolation in the configuration space between \mathbf{M}_i and \mathbf{M}_f .

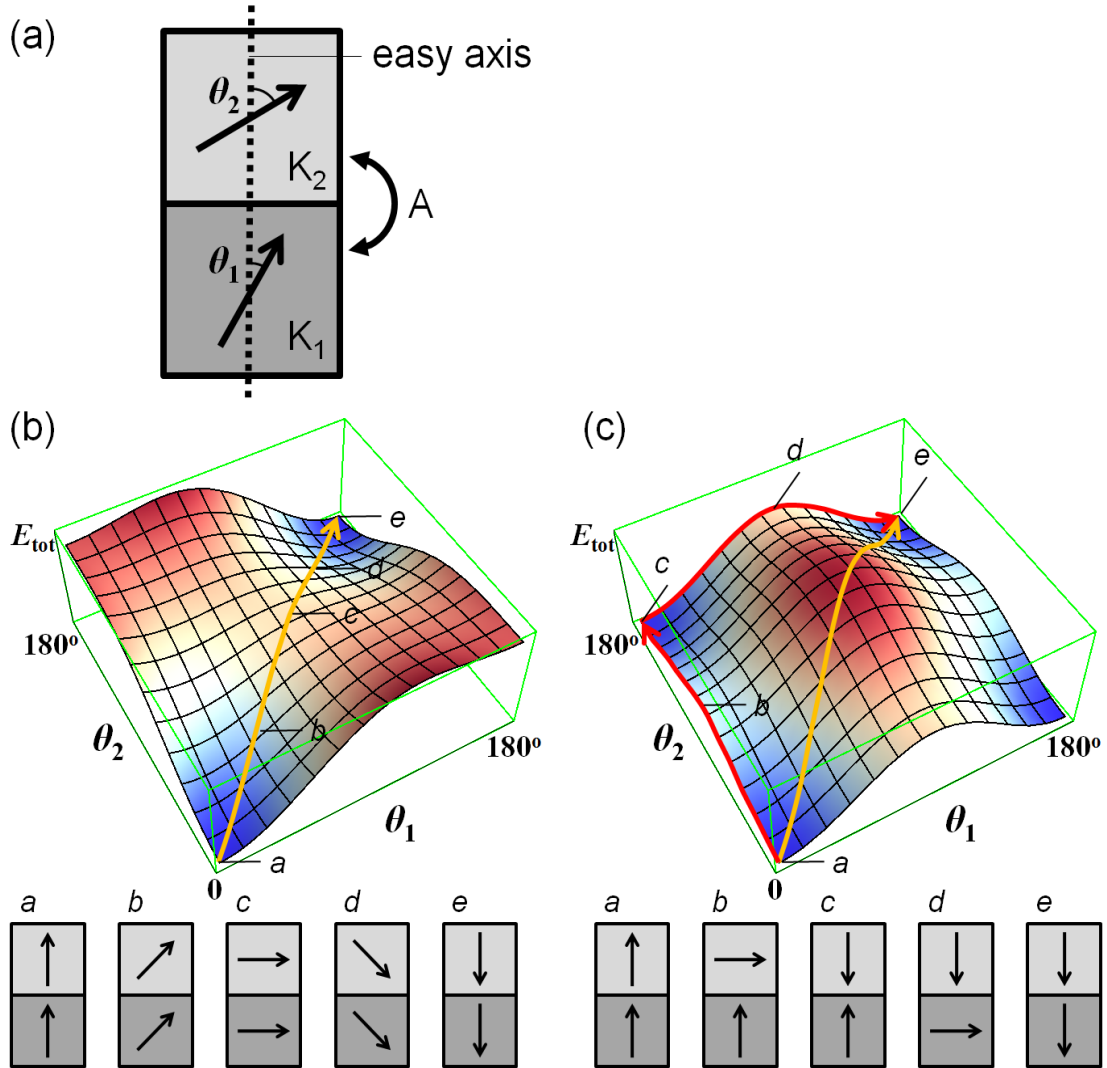


Fig. 29. (a) A schematic diagram of an exchange coupled relatively soft magnet on top and relatively hard one at bottom. They are exchange coupled with an exchange coefficient A . $K_1 = 2 \times K_2$. The energy landscape of their rotation process are shown for the contribution of exchange coupling is (b) strong and (c) weak. The amount of A in (b) is 100 times larger than in (c). Stray field interaction was neglected in all cases.

An initial path is assumed which connects the initial magnetization state $\mathbf{M}_i = \mathbf{M}_1$ with the final magnetization state $\mathbf{M}_f = \mathbf{M}_n$. A path is represented by a sequence of n images. The path is optimal, if for any image \mathbf{M}_k ($1 < k < n$) the gradient of the energy is only pointing along the path. Therefore the image of the optimal path has the following property

$$D = -\{\nabla E(\mathbf{M}_k) - (\nabla E(\mathbf{M}_k) \cdot \mathbf{t}) \cdot \mathbf{t}\} = 0 \quad \text{for } k = 1, n. \quad (50)$$

Here \mathbf{t} denotes the unit tangent vector along the path. For an optimal path the component of the energy gradient that is normal to the path is zero. The optimal path can be found using an iterative scheme. In each iteration step the images are moved in a direction parallel to the negative gradient of the energy and normal to the current path.

Fig. 29(a) shows an example of energy barrier determination. An exchange coupled structure is given, with crystalline anisotropies K_1 and K_2 ($K_1 = 2 \times K_2$), and exchange coefficient A between the two magnets. The spins inside of an individual magnet is perfectly coherent. If the exchange coefficient A is strong enough to overwhelm the exchange energy between two layers (Fig. 29(b)), the two layers are likely to reverse homogeneously: the thermal reversal path becomes the interpolation of the initial and final states, a straight line. The line (orange arrow) connecting from the initial state to the final state passes the saddle point at $\theta_1 = \theta_2 = 90^\circ$, the state that magnetization of the both layers are perpendicular to the easy axis. However, the interpolated initial path of the Fig. 29(c) passes the peak of the energy landscape. In this situation the discretized path points along the initial path has a torque to rotate its magnetizations.

Finally it passes two saddle points, the top and bottom layer is reversed independently (final path, red arrows). The reasonable switching mode of thermal fluctuation is obtained by applying this method on the micromagnetic simulations.

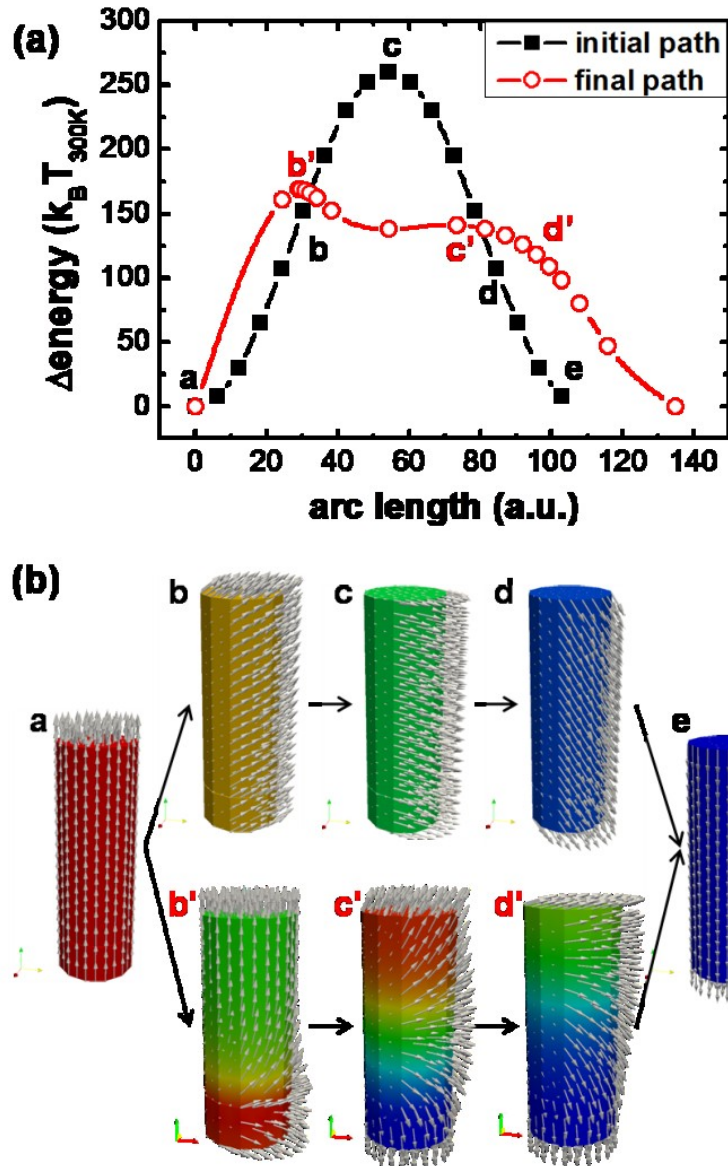


Fig. 30. (a) Energy along the initial path and final path. (b) Magnetization configurations of the magnetization along the initial (a-b-c-d-e) and the final (a-b'-c'-d'-e) path.

Fig. 30 shows an example of energy barrier calculation using NEB. The model was assumed as an exchange spring media composed of FePtCu hard layer and [Co/Pt]_N multilayer soft layer [68]. In order to find a optimized reversal path through minimum energy, we have prepared a cylindrical finite element model composed with 5nm thick FePtCu layer and 20 nm thick [Co/Pt]_N multilayer, with material parameters as following: crystalline uniaxial anisotropy constant $K_{U,FePtCu} = 1.4 \text{ MJ/m}^3$, $K_{U,[Co/Pt]} = 0.35 \text{ MJ/m}^3$, saturation polarization $J_{S,FePtCu} = 0.68 \text{ MJ/m}^3$, $J_{S,[Co/Pt]} = 0.63 \text{ MJ/m}^3$. The exchange coefficient A and interlayer exchange coupling A_{int} are set as 0.01 pJ/m. The easy axis is parallel to the z-axis, the direction of the height of the cylinder. In the initial state the magnetization is reversed by coherent rotation, therefore a saddle point is when magnetization vectors are rotated 90° to the easy axis. In the final state after 10000 iteration steps, the magnetization configurations are locally rotated from the initial state as shown in Fig. 30. The final path shows a domain wall motion. . As the reversal path is changed, the energy barrier path has changed its shape as well. In the coherent rotation reversal, the energy barrier was 260 $k_B T_{300K}$. After optimization the energy barrier is reduced to 169 $k_B T_{300K}$.

2. Inhomogeneous Writing Magnetic Fields for Magnetic Recording

2.1. Longitudinal Head Field

(1) Karlqvist Head

Magnetic field generated by a ring type head with a narrow air gap applied on a ferromagnetic recording layer with variation of the airgap, layer thickness and other influencing factors are studied by O. Karlqvist in 1954 [69]. Fig. 31 shows the illustration of the ring type recording head in his publication. The shape of the head is equivalent to the bent solenoid to make two surfaces at the end face each other with a small gap between them. Hence a strong magnetic flux path is generated near the gap. The flux paths at slightly beneath the head surface where the medium passes are roughly semi-circular in shape. Middleton et al. has suggested simple expressions along the semi-circular path neglecting the gap length $2g$ in Fig. 32, as shown in Eq. (51)~(54) [70].

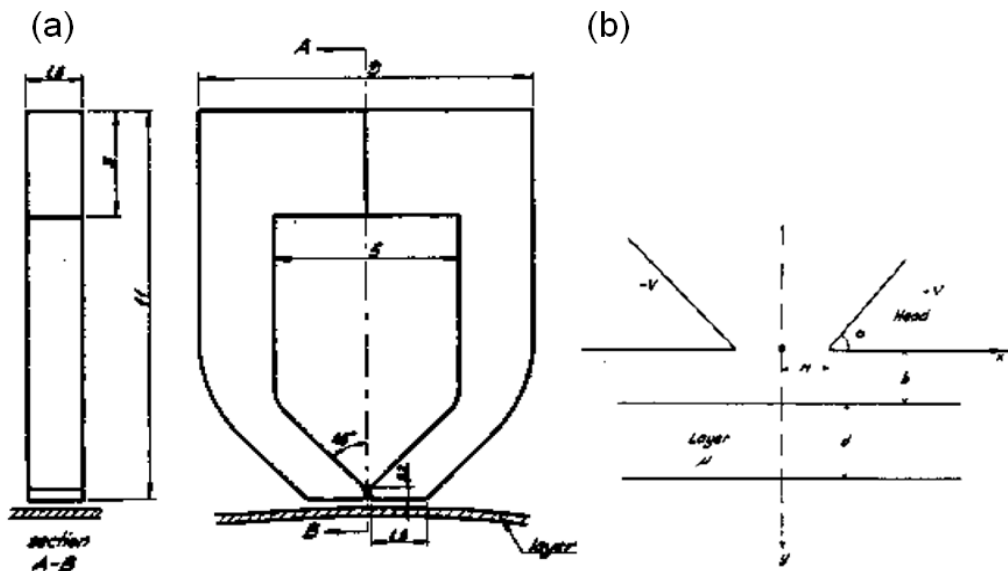


Fig. 31. (a) Sketch of the recording head. (b) The air gaps are exaggerated. [69]

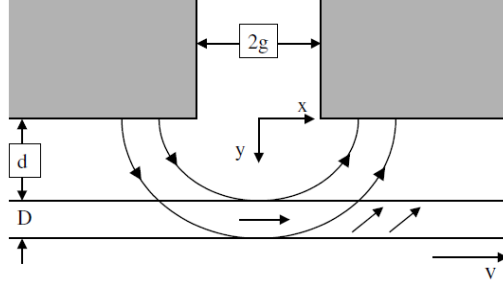


Fig. 32. Magnetization of a demagnetized medium prior to recording a transition [70].

$$H_t = \frac{I}{\sqrt{x^2 + y^2}} \quad (51)$$

$$H_x = \frac{Iy}{x^2 + y^2} \quad (52)$$

$$H_y = -\frac{Ix}{x^2 + y^2} \quad (53)$$

$$H_t^2 = H_x^2 + H_y^2 \quad (54)$$

H_t , H_x and H_y denote total field, longitudinal field and perpendicular field, respectively. The head field profile as a function of the distance is shown in Fig. 33. The longitudinal field has the maximum value at the middle of the gap.

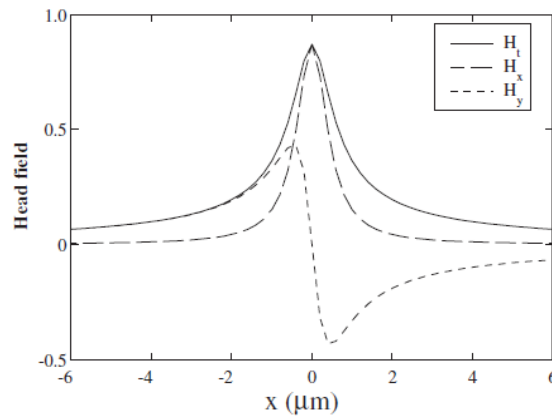


Fig. 33. Total head field H_t and its components H_x and H_y as functions of position below a recording head for $y = 0.15 \mu\text{m}$ [70].

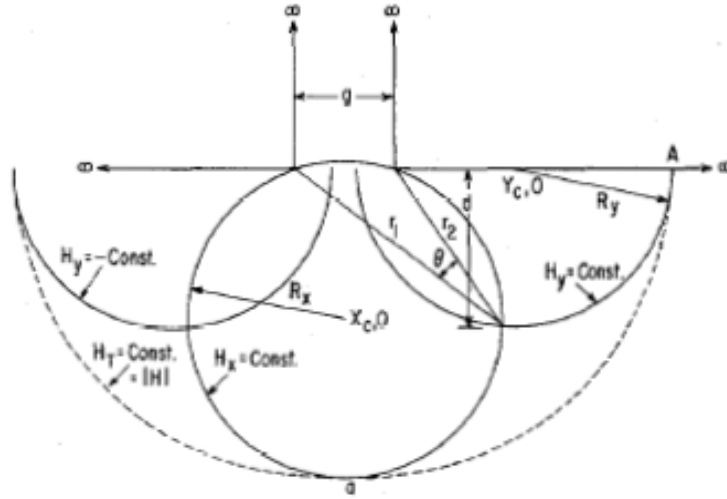


Fig. 34. Two-dimensional representation of the gap [71].

Here I stands for $n\eta$; n is the number of head turns, η is the head efficiency, i is the head current. The direction x and y are defined in Fig. 32.

A more rigorous treatment of the ring head field calls for a more sophisticated approach. Typically a conformal mapping technique is used to calculate the field in the close vicinity of the head gap [69, 71].

$$H_x = 2\rho \left(\tan^{-1} \frac{X_0 + g/2}{d} - \tan^{-1} \frac{X_0 - g/2}{d} \right) \quad (55)$$

$$H_y = \rho \ln \frac{(X_0 + g/2)^2 + d^2}{(X_0 + g/2)^2 - d^2} \quad (56)$$

In Eq. (55) and (56), g , X_0 and d denote the gap length, down track distance and magnetic film depth from the head base, respectively. ρ is the pole density, able to be scaled physically by changing current, number of turns of coil, etc.

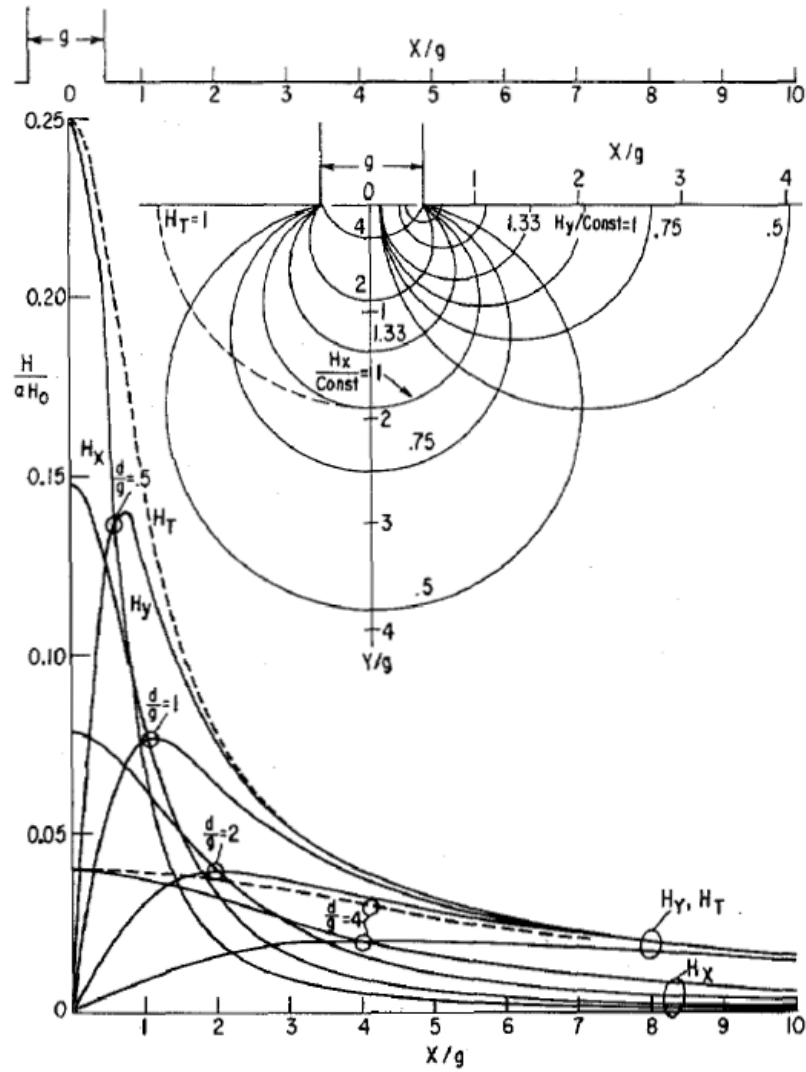


Fig. 35. Alternate representations of field configuration below gap [71].

(2) Lindholm Head

The head field generated from the ring type head with finite width is calculated by Lindholm in 1977 [72]. The 3-dimensional head field profiles were partly obtained at different boundary conditions, +x-limited semi-infinite, -x-limited semi-infinite and infinite in both directions as shown in Fig. 36(a) to (c), and then superimposed to build total head field strength. The conclusions are expressed in (57), as a form of summation in Equations (58)~(65).

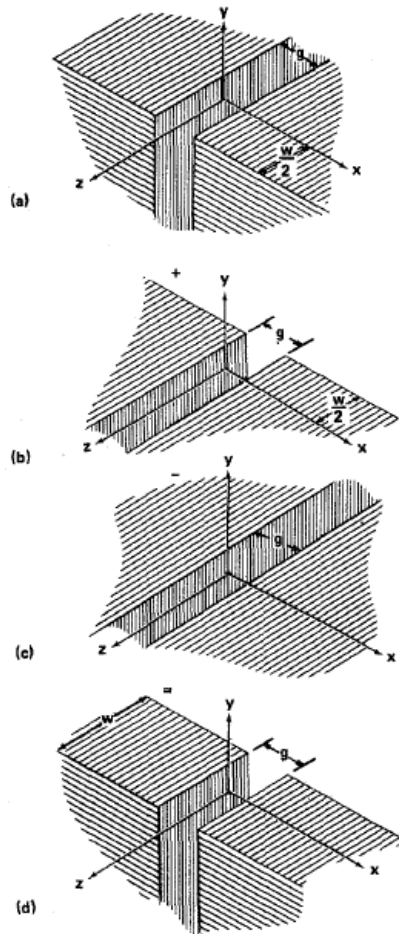


Fig. 36. Various boundary conditions to calculate the stray field partly. (a) +x-limited semi-infinite, (b) -x-limited semi-infinite, (c) infinite in both directions and (d) Superposition of wedges to obtain finite gap, finite width head [72].

$$H = H_1\left(x, y, z - \frac{w}{2}\right) + H_1'\left(x, y, z + \frac{w}{2}\right) - H_2(x, y, z) \quad (57)$$

The x, y, z components of the H_1 and H_2 are defined as following:

$$H_{1,x} = \frac{V_0}{\pi g} \left[\tan^{-1} \left(\sinh \left(\frac{2}{3} \sinh^{-1} \left(\frac{x+g/2}{\sqrt{y^2+z^2}} \right) \right) \right) / \sin \left(\frac{2\varphi}{3} \right) \right] - \tan^{-1} \left(\sinh \left(\frac{2}{3} \sinh^{-1} \left(\frac{x-g/2}{\sqrt{y^2+z^2}} \right) \right) \right) / \sin \left(\frac{2\varphi}{3} \right) \right] \quad (58)$$

$$H_{1,y} = \frac{V_0}{\pi g} \left[-4 \cosh \left(\frac{1}{3} \sinh^{-1} \left(\frac{x+g/2}{\sqrt{y^2+z^2}} \right) \right) \cos \left(\frac{\varphi}{3} \right) + \coth^{-1} \left(\frac{1}{3} \sinh^{-1} \left(\frac{x+g/2}{\sqrt{y^2+z^2}} \right) \right) \cos \left(\frac{\varphi}{3} \right) \right] + 4 \cosh \left(\frac{1}{3} \sinh^{-1} \left(\frac{x-g/2}{\sqrt{y^2+z^2}} \right) \right) \cos \left(\frac{\varphi}{3} \right) - \coth^{-1} \left(\frac{1}{3} \sinh^{-1} \left(\frac{x-g/2}{\sqrt{y^2+z^2}} \right) \right) \cos \left(\frac{\varphi}{3} \right) \right] \quad (59)$$

$$H_{1,z} = \frac{V_0}{\pi g} \left[-4 \cosh \left(\frac{1}{3} \sinh^{-1} \left(\frac{x+g/2}{\sqrt{y^2+z^2}} \right) \right) \sin \left(\frac{\varphi}{3} \right) + \coth^{-1} \left(\frac{1}{3} \sinh^{-1} \left(\frac{x+g/2}{\sqrt{y^2+z^2}} \right) \right) \sin \left(\frac{\varphi}{3} \right) \right] + 4 \cosh \left(\frac{1}{3} \sinh^{-1} \left(\frac{x-g/2}{\sqrt{y^2+z^2}} \right) \right) \sin \left(\frac{\varphi}{3} \right) - \coth^{-1} \left(\frac{1}{3} \sinh^{-1} \left(\frac{x-g/2}{\sqrt{y^2+z^2}} \right) \right) \sin \left(\frac{\varphi}{3} \right) \right] \quad (60)$$

V_0 stands for the potential, such as ρ in Eq. (55) and , (56) of Karlqvist head, and the parameter φ is defined as in H_1 .

$$\varphi = \begin{cases} \pi - \tan^{-1} \left(\frac{y}{z} \right) & (z \geq 0) \\ -\tan^{-1} \left(\frac{y}{z} \right) & (z < 0) \end{cases} \quad (61)$$

In H_1' , Eq. (58)~(60) are commonly used and only φ is differently defined as

$$\varphi = \begin{cases} \tan^{-1}\left(\frac{y}{z}\right) & (z \geq 0) \\ \pi + \tan^{-1}\left(\frac{y}{z}\right) & (z < 0) \end{cases} \quad (62)$$

The 3-directional field components in H_2 are defined as following.

$$H_{2,x} = \frac{V_0}{\pi g} \left[\tan^{-1}\left(\frac{x+g/2}{2}\right) - \tan^{-1}\left(\frac{x-g/2}{2}\right) \right] \quad (63)$$

$$H_{2,y} = \frac{V_0}{\pi g} \left[-\frac{1}{2} \ln\left(\left(\frac{x+g/2}{2}\right)^2 + 1\right) + \frac{1}{2} \ln\left(\left(\frac{x-g/2}{2}\right)^2 + 1\right) \right] \quad (64)$$

$$H_{2,z} = 0 \quad (65)$$

The head field profiles from the finite pole width are graphically shown in Fig. 37.

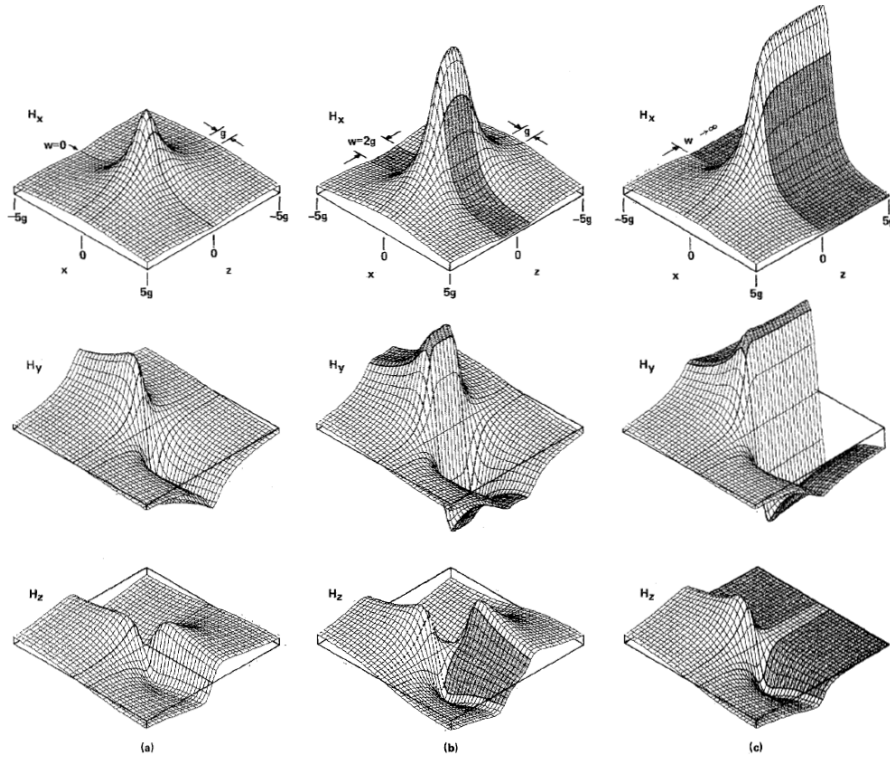


Fig. 37. Magnetic fields at $y = g/2$ for (a) zero width head, (b) finite width head, $w = 2g$, and (c) semi-infinite width head. Components are: longitudinal (H_x), vertical (H_y), and transverse (H_z) [72].

(3) Szczech Head

In 1986, T. J. Szczech published his head field calculation results for the case the leading pole and the trailing pole have finite pole lengths p and q , respectively [73-74]. The finite length of the writing head induces a undershoot of the head field, therefore the head field has a step-like profile at the edge of the heads, as if the Lindholm head has a sudden reduction of the writing head at the side wall of the writing poles. The schematic sketch of magnetic media and the head are shown in Fig. 38. In Szczech's publications the y coordinate stands for the perpendicular direction as Karlqvist's and Lindholm's does. The longitudinal head field component and perpendicular ones are described in Eq. (66) and (71), respectively. The factor Q is to be calculated using the distance from the gap center, as in Eq. (67). The parameters from A to L were found by fitting to finite different calculations: $A = 0.835$, $B = 0.0433$, $C = 0.512$. The deep gap field H_S is defined as Eq.(70). The details and the values of the parameters are listed in Eq. (72)~(79) [73].

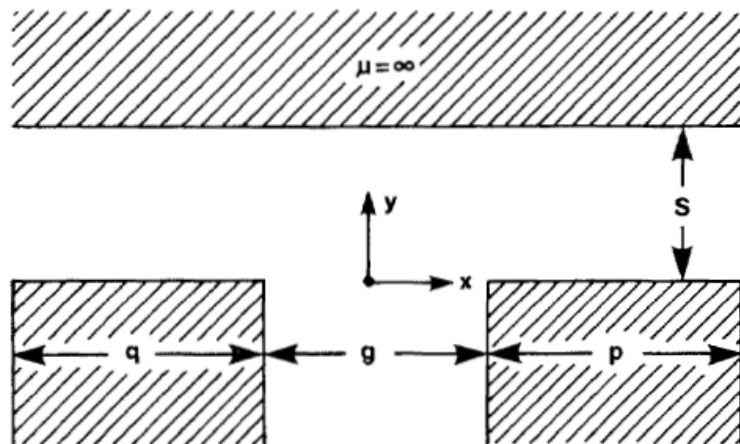


Fig. 38. Geometry for the head design with a finite pole lengths [74].

$$\begin{aligned}
H_x(x,y) = & \frac{H_S}{\pi} \left\{ \frac{Qy_1B}{C} (x_1^2 + y_1^2 + C^2) \ln \left(\frac{C+0.5}{C-0.5} \right) + Qx_1y_1B \ln \left(\frac{y_1^2 + (0.5-x_1)^2}{y_1^2 + (0.5+x_1)^2} \right) \right. \\
& \left. - \left(QB(x_1^2 - y_1^2 - C^2) - A \left(\tan^{-1} \left(\frac{0.5+x_1}{y_1} \right) + \tan^{-1} \left(\frac{0.5-x_1}{y_1} \right) \right) \right) \right\} \\
& + \frac{H_S D}{(x_1 - E(0.5 + p_1))^2 + y_1^2} \left\{ \frac{y_1}{2\pi} \ln \frac{((1-E)(0.5+p_1))^2}{(0.5-x_1+p_1)^2 + y_1^2} \right. \\
& \left. - (x_1 - E(0.5 + p_1)) \left(0.5 - \frac{1}{\pi} \tan^{-1} \left(\frac{0.5-x_1+p_1}{y_1} \right) \right) \right\} \\
& + \frac{H_S F}{(x_1 + G(0.5 + q_1))^2 + y_1^2} \left\{ \frac{y_1}{2\pi} \ln \frac{((1-G)(0.5+q_1))^2}{(0.5+x_1+q_1)^2 + y_1^2} \right. \\
& \left. - (x_1 + G(0.5 + q_1)) \left(0.5 - \frac{1}{\pi} \tan^{-1} \left(\frac{0.5+x_1+q_1}{y_1} \right) \right) \right\}
\end{aligned} \tag{66}$$

where

$$Q = \frac{1}{\left\{ \left(y_1^2 + (x_1 + C)^2 \right) \left(y_1^2 + (x_1 - C)^2 \right) \right\}}, \tag{67}$$

$$q_1 = 0.99 \frac{q}{g}, \tag{68}$$

$$\text{and } p_1 = 0.99 \frac{p}{g}. \tag{69}$$

The p_1 and q_1 are introduced to obtain better fitting results.

$$H_S = H_x(0,0), x_1 = \frac{x}{g}, y_1 = \frac{y}{g} \tag{70}$$

$$\begin{aligned}
H_y(x, y) = & -\frac{H_S}{\pi} \left\{ \frac{Qx_1B}{C} (x_1^2 + y_1^2 + C^2) \ln \left(\frac{C+0.5}{C-0.5} \right) \right. \\
& + 2Qx_1y_1B \left(\tan^{-1} \left(\frac{0.5+x_1}{y_1} \right) + \tan^{-1} \left(\frac{0.5-x_1}{y_1} \right) \right) \\
& \left. - \frac{1}{2} (QB(x_1^2 - y_1^2 - C^2) - A) \ln \left(\frac{y_1^2 + (0.5-x_1)^2}{y_1^2 + (0.5+x_1)^2} \right) \right\} \\
& - \frac{H_S I}{(x_1 - J(0.5 + p_1))^2 + y_1^2} \left\{ y_1 \left(0.5 - \frac{1}{\pi} \tan^{-1} \left(\frac{0.5-x_1+p_1}{y_1} \right) \right) \right. \\
& \left. + \frac{(x_1 - J(0.5 + p_1))}{2\pi} \ln \frac{((1-J)(0.5+q_1))^2}{(0.5-x_1+q_1)^2 + y_1^2} \right\} \\
& - \frac{H_S K}{(x_1 + L(0.5 + q_1))^2 + y_1^2} \left\{ y_1 \left(0.5 - \frac{1}{\pi} \tan^{-1} \left(\frac{0.5+x_1+q_1}{y_1} \right) \right) \right. \\
& \left. + \frac{(x_1 + L(0.5 + q_1))}{2\pi} \ln \frac{((1-L)(0.5+q_1))^2}{(0.5+x_1+q_1)^2 + y_1^2} \right\}
\end{aligned} \tag{71}$$

The coefficients D to L are found to be as follows.

$$D = 0.004 \frac{P}{g} + 0.086, \tag{72}$$

$$E = 0.9, \tag{73}$$

$$F = 0.004 \frac{q}{g} + 0.086, \tag{74}$$

$$G = 0.9, \tag{75}$$

and

$$I = 0.004 \frac{P}{g} + 0.086, \tag{76}$$

$$J = 0.9, \tag{77}$$

$$K = 0.004 \frac{q}{g} + 0.086, \quad (78)$$

$$L = 0.9. \quad (79)$$

Eq. (66) has the terms about the contributions of the leading pole (3rd and 4th lines) and trailing one (5th and 6th). Their contributions are able to be scaled by multiplying *undershoot factor*.

The comparison between the analytic equations above and the experimental results are shown in Fig. 31. Fig. 31(a) shows the longitudinal (x -directional) component, and Fig. 31(b) shows the perpendicular (y -directional) one. The experimental and analytic ones show very nice agreement each other.

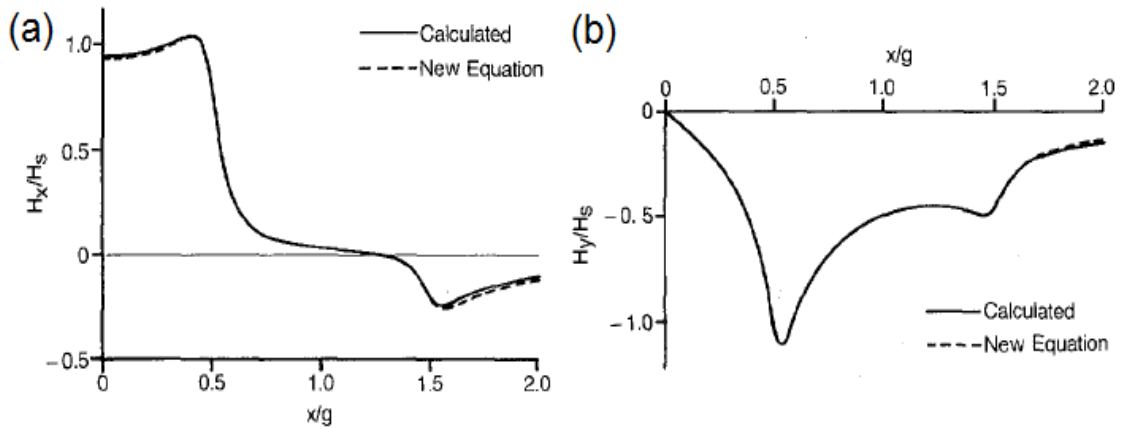


Fig. 39. (a) Comparison of exp. plot of H_x vs. x and plot from Eq. (66) with $g = p = q = 1$, $y = 0.063$, $D = F = 0.09$, and $E = G = 0.9$. (b) Comparison of exp. plot of H_y vs. x and plot from eq. (71) [73].

(4) Comparison of ring type heads

The head field profiles of the Karlqvist, Lindholm, and Szczech heads are summarized in Fig. 40. The upper figures denote the longitudinal (blue) and perpendicular (red) head field strength along the down track distance. In all models the head gap is defined as 200 nm. The finite head width is assigned only for the Lindholm head as 150 nm, the finite head length of $p = q = 100$ nm in Szczech head is with a light gray. The gap region is marked with a yellow color, the finite head length in Szczech head is with a light gray. Szczech field profiles have the maximum longitudinal and perpendicular components strength at very edge of the head gaps, whereas the Karlqvist and the Lindholm head have the strongest longitudinal component at the gap center. The undershoot factor in Szczech field determines the negative longitudinal field very outside of the head poles.

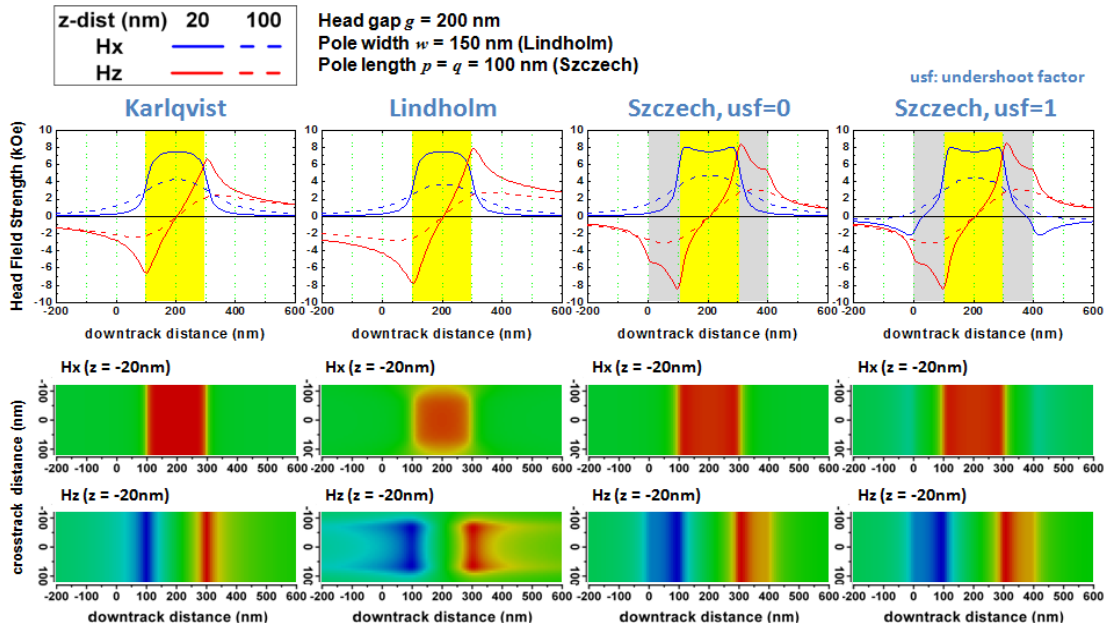


Fig. 40. Comparison among the ring type head field, Karlqvist, Lindholm and Szczech. The undershoot factor of the Szczech head is varied between 0 and 1. In above figures, the strength of the down track field component is marked as blue, and the one of the perpendicular one is red.

The figures located at the below of Fig. 40 shows the head field strength on the plane parallel to recording media surface. Red indicates the 10 kOe, and blue -10 kOe. The Szczech field profiles show clear ranges of the leading and trailing edges. All heads except for Lindholm head has infinite head width, therefore the head field profiles are not depending on the crosstrack directions. Due to the limited head width, the longitudinal component of the Lindholm is not as strong as others. The color indicating the field strength is blurring out at the parts closer to the air gap and the head width edges. The perpendicular component is maximized at the head width edges, but also blurred out in all directions.

2.2. Perpendicular Head Field

(1) Single Pole Tip (SPT) Head

Perpendicular magnetic recording technology has been rising since the grain size of longitudinal media became so small that they cannot support a domain structure. Perpendicular recording media are composed of the grains of which easy axes of the particles are oriented perpendicularly to the film plane. Therefore the concept of perpendicular recording head has suggested as a form of the single pole tip head [3]. The ring type heads produce writing field between the air gap where the magnetic flux density in the outside is maximized. For the perpendicular recording, for the purpose of generating magnetic field perpendicular to the plane, a straight solenoid with a high saturation magnetization core material is used as a writing head. Due to its geometry, this type of head is called as single pole tip (SPT) head, often referred as single pole type head. The magnetic field of a magnetic element with a uniform magnetization set up according to the distribution of magnetic surface poles. Khrizroev and Norpoth have derived the equations from the saturated magnet. The magnetic field from the SPT head was calculated by their suggestions in [75-76].

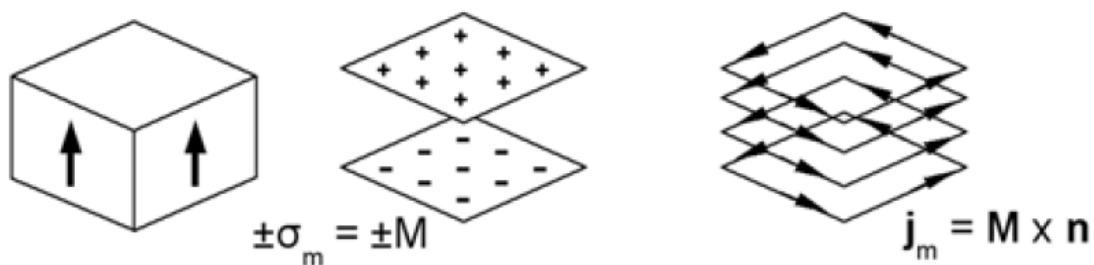


Fig. 41. Representation of prismatic magnet, by magnetic surface poles and equivalent surface currents of uniform magnetization along the z-axis

A cuboid ferromagnet of which x , y , z are ranged in between $[0,a]$, $[0,b]$ and $[0,c]$, respectively with uniform magnetization along the z -axis is prepared as Fig. 41. This situation equals two rectangular sheets at a distance c with homogeneous magnetic charge densities $\pm M_S$ or an equivalent electric current density $M_S \mathbf{x} \times \mathbf{n}$ circulating around the lateral surface, respectively. From the charge integrals, the magnetic field strength out of the saturated magnet is derived as in Eq. (80)~(82). Similar equations are also derived by Schabes, Engel-Herbert and Hesjedal et al [11, 62].

$$H_x(x, y, z) = \frac{M_S}{4\pi} \ln \left\{ \frac{\sqrt{\alpha^2 + (z-c)^2} \left(\beta + \sqrt{\alpha^2 + \beta^2 + z^2} \right)}{\sqrt{\alpha^2 + z^2} \left(\beta + \sqrt{\alpha^2 + \beta^2 + (z-c)^2} \right)} \right\} \Bigg|_{\alpha=x-a}^{\alpha=x} \Bigg|_{\beta=y-b}^{\beta=y}, \quad (80)$$

$$H_x(x, y, z) = \frac{M_S}{4\pi} \ln \left\{ \frac{\sqrt{\beta^2 + (z-c)^2} \left(\alpha + \sqrt{\alpha^2 + \beta^2 + z^2} \right)}{\sqrt{\beta^2 + z^2} \left(\alpha + \sqrt{\alpha^2 + \beta^2 + (z-c)^2} \right)} \right\} \Bigg|_{\alpha=x-a}^{\alpha=x} \Bigg|_{\beta=y-b}^{\beta=y}, \quad (81)$$

$$H_z(x, y, z) = \frac{M_S}{4\pi} \left\{ \arctan \left(\frac{\alpha \cdot \beta}{(z-c)\sqrt{\alpha^2 + \beta^2 + (z-c)^2}} \right) - \arctan \left(\frac{\alpha \cdot \beta}{z\sqrt{\alpha^2 + \beta^2 + z^2}} \right) \right\} \Bigg|_{\alpha=x-a}^{\alpha=x} \Bigg|_{\beta=y-b}^{\beta=y}. \quad (82)$$

(2) SPT Head With Soft Underlayer (SUL)

The performance of the SPT is enhanced if accompanied with soft underlayer (SUL). Soft underlayer. The SUL belongs physically to the medium and magnetically to the head. Fig. 42 sketches a cross section through the medium and the head structure along the center of a track, $y = 0$. As in the previous session on SPT, x stands for the downtrack direction, y the cross-track direction and z for the perpendicular direction. The writing occurs at the main pole and the flux path is closed through the SUL and the return pole. The resulting field configuration of the system of pole and SUL can be best understood using the principle of image charges. For an ideal SUL, the head field can be calculated using the principle of images: one can image of the charge distribution of the pole. The image surface is the surface of the SUL. As shown in Fig. 42 on the right, the imaging procedure reverses the sign of the magnetic charges, but not the direction.

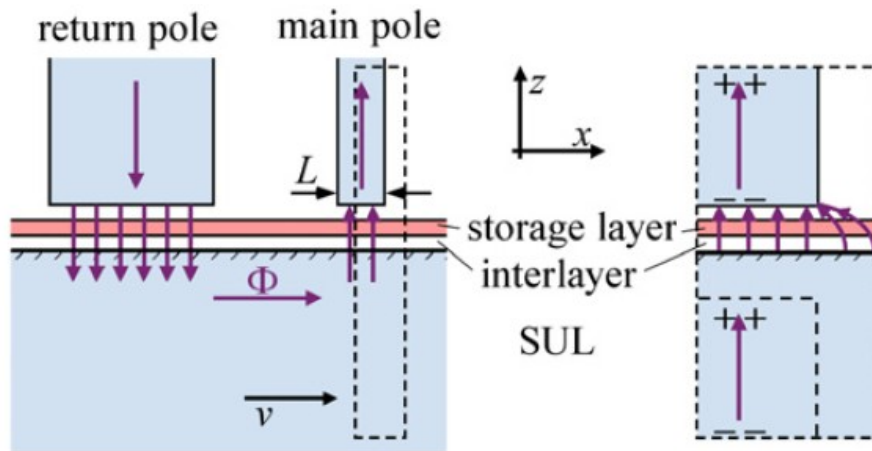


Fig. 42. Overview of the perpendicular recording geometry with a SUL. The figure on the right shows a blow-up of the dashed rectangle where the final recording occurs. The effect of the SUL can be thought of as an additional image pole that is located in the SUL, thus forming a ring head turned sideways. For all pictures, it is assumed that the medium moves and the head is at rest [3].

2.3. Writing Head Fields Summary

Fig. 43(a) shows the schematic diagrams of Lindholm, SPT and SPT with SUL prepared for our micromagnetic simulations. For the purpose of quantitative comparison of the write heads, a standard value describing head field strength is required. In our works we set the midpoint of the air gap (in Lindholm) or head base (SPT and SPT with SUL), where the perpendicular head field component (Lindholm) and the longitudinal one (SPT and SPT with SUL) vanishes. The field strength at this point is called ‘deep gap field’ for Lindholm head, and ‘base field’ for SPT and SPT with SUL. The head fields from the fields are able to be scaled by controlling the current of number of coil turns.

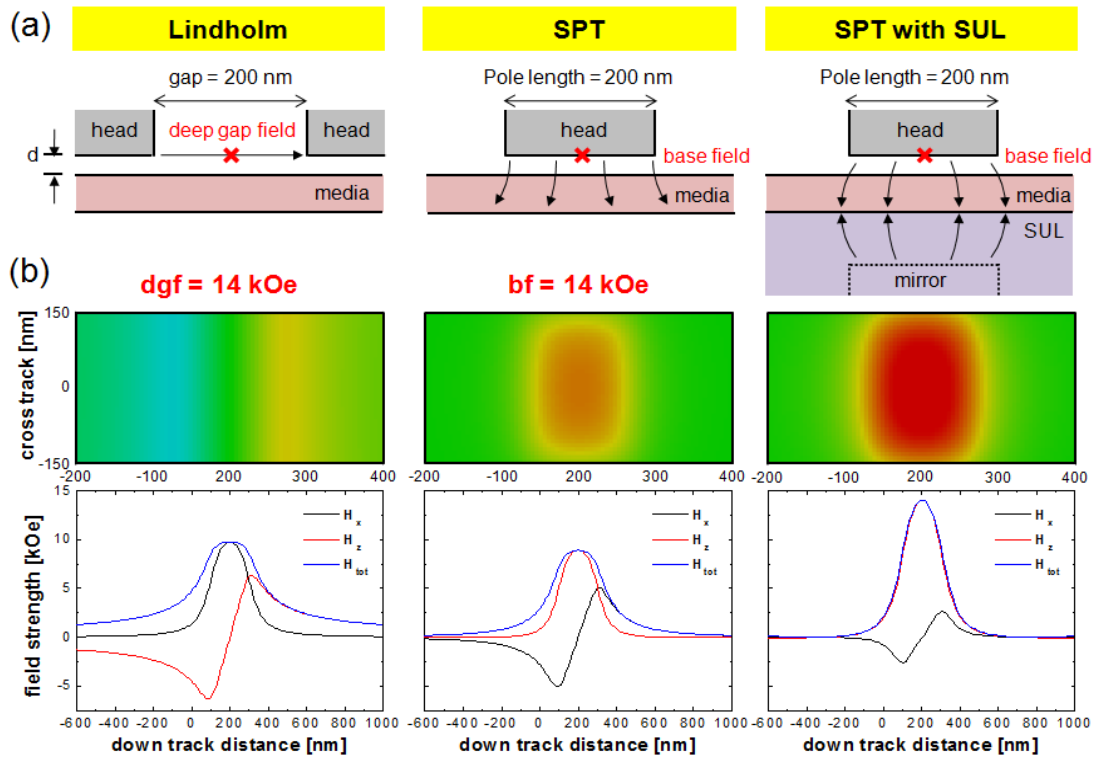


Fig. 43. (a) Schematic diagrams of Lindholm, single pole tip (SPT) and SPT with soft underlayer (SUL). The small cross presents the position where the deep gap field (in Lindholm head) and base field (in SPT and SPT with SUL) are defined. (b) Writing head field strength on xy plane (above) and head field strength along down track distance. H_x and H_z stands for the down track direction and perpendicular direction, respectively. H_{tot} is total field strength resulted from H_x and H_y .

Fig. 43(b) represents the writing head field strength on x (downtrack)- y (crosstrack) plane as color code (above) and longitudinal field strength (H_x) and perpendicular field strength (H_z) with total field strength (H_{tot}) (below), for the case of head to media distance d is 20 nm. In order to compare the field profiles of the heads quantitatively, the deep gap field and base field are fixed as 14 kOe. Very wide(6 μm) width is taken for the Lindholm head, and only the center was taken. The head edge effect is neglected therefore it can be regarded as a Karlqvist head. In Fig. 43(b), the Lindholm head and the SPT head show quite different profiles in xy plane owing to the different head geometries and field profiles along the down track distance. It is noticeable that the strength of the Lindholm head and SPT head is similar to each other, only difference is that the longitudinal field of the Lindholm head is close to the perpendicular one in SPT head. If the SPT head is accompanied with SUL, the perpendicular component is much stronger and the longitudinal component is much less than the SPT head without SUL.

3. Advanced Recording Media

3.1. Introduction: Recording Materials and Exchange Spring Scheme

(1) Trilemma

The increasing demand in high-density recording media has led to the requirement for recording media with smaller grains to keep the signal to noise ratio (SNR). In this case the magnetic energy stored in a single bit decreases because the energy is expressed as a form of product of the crystalline anisotropy K and volume V , KV . The energy competes against the thermal energy $k_B T$ and must be large enough to prevent spontaneous magnetization reversals, which then lead to thermal decay and eventually superparamagnetism. Accordingly a hard magnetic material with large K , such as (Co, Fe)Pt $L1_0$ phase [77-79].

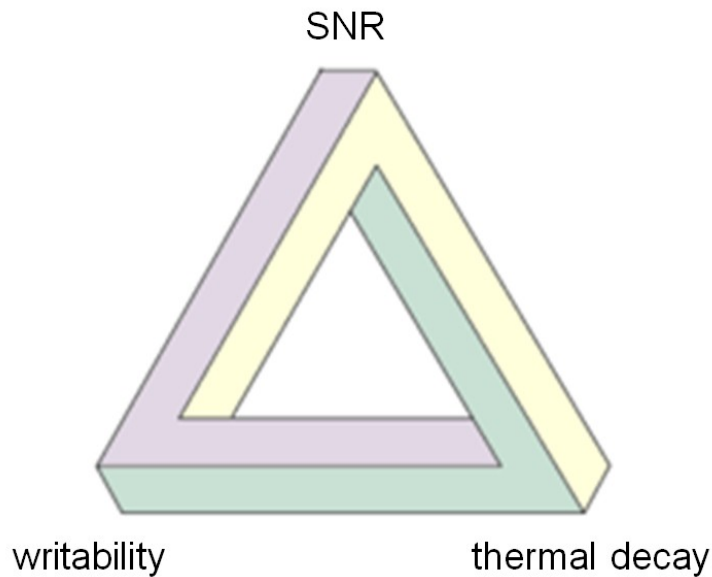


Fig. 44. The trilemma of magnetic recording: achieving high medium SNR requires the utilization of small grains. Small grains have energy barriers (KV) that are too small to ensure thermal stability of the recorded information. An increase in the anisotropy energy density K increases the required write field beyond the capability of available head materials.

Increasing K generally goes along with an increase in the anisotropy field and a higher magnetic field is required to switch the magnetization. Head fields are limited by the material that can be used to fabricate the poles, and the maximum obtainable saturation magnetization is that of CoFe with $\mu_0 M_S = 2.4$ T [80]. Therefore, the design space is either limited by thermal decay, writability, and insufficient SNR as shown in Fig. 44. In any case, one is left with a choice between ‘equally undesirable options’, which is, by definition, a *trilemma*. In this sense, any advances to further evolve magnetic recording can be regarded as a means to break or to postpone the trilemma.

There are a numerous approaches to overcome the trilemma, most of the concepts for advanced recording media is based on perpendicular recording, not only for the granular media and bit patterned media for hard disk drives [3, 81], but also for the magnetic tape recording media [82-83]. The perpendicular recording technique is accompanied with heat assisted recording [84], microwave assisted recording [85], and percolated recording [86-87]. In the following chapters we are going to represent the experimental studies including microstructure investigation and micromagnetic simulations based on the experimental findings.

(2) Writing Process

We have two ways for performing writing process in micromagnetic simulations. One is the fully integrated magnetic recording, and the other one is using precomputed field box method. In fully integrated magnetic recording, all parts working on the writing process are prepared as finite element models, their interactions are considered [88].

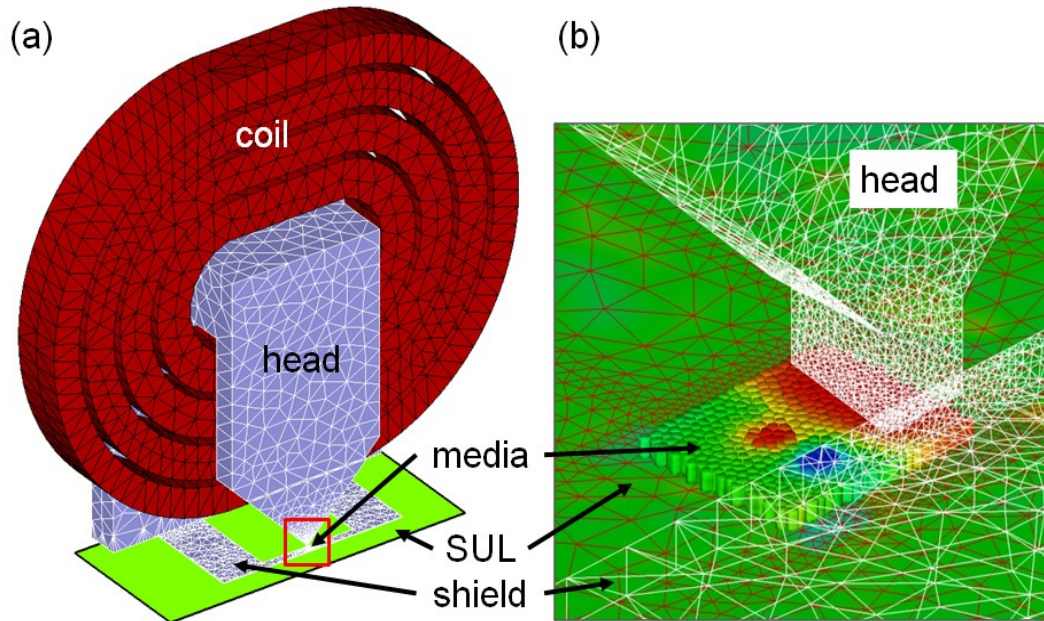


Fig. 45. Finite element models for fully integrated perpendicular magnetic recording. (a) The writing module is consisted of coil, head (with shield, optionally), SUL and media. The writing head pole tip with media is enlarged in (b). The media is placed very below writing head.

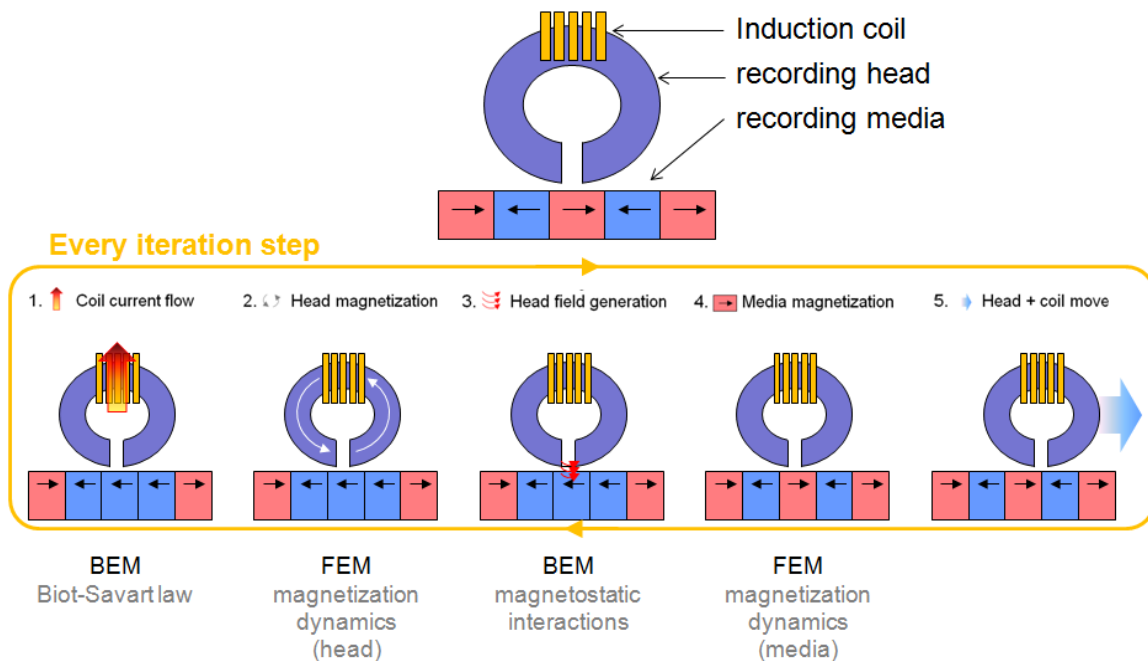


Fig. 46. Fully integrated micromagnetic writing simulation processes.

- Using fully integrated micromagnetics

The finite element models for fully integrated recording process are shown in Fig. 45, with the procedures in Fig. 46. The coil, head, SUL and media models are prepared with the proper dimensions. (1) At the beginning of the simulation a current is applied on the coil model, then magnetic field applied on the writing head is generated by Biot-Savart law. (2) The field applied on the writing head magnetizes the pole tip, (3) which induces magnetic field onto the media. (4) The magnetic recording media exposed to the head field responses. If the magnetic field is sufficient to magnetize the bit, the magnetization reversal occurs. (5) The head and media model, precisely speaking, the field generated by writing head moves to the down track direction in every time step. The 5 steps described above is repeated in every iteration steps. The fully integrated micromagnetics enables us to consider the interaction between head and media. It also makes it possible to consider a delayed head field profile due to the time taken for head magnetization and eddy current effect [32-33, 89]. However it requires a big amount of computational resources and takes relatively long time. Therefore, in many cases, the precomputed field box method is used in many cases.

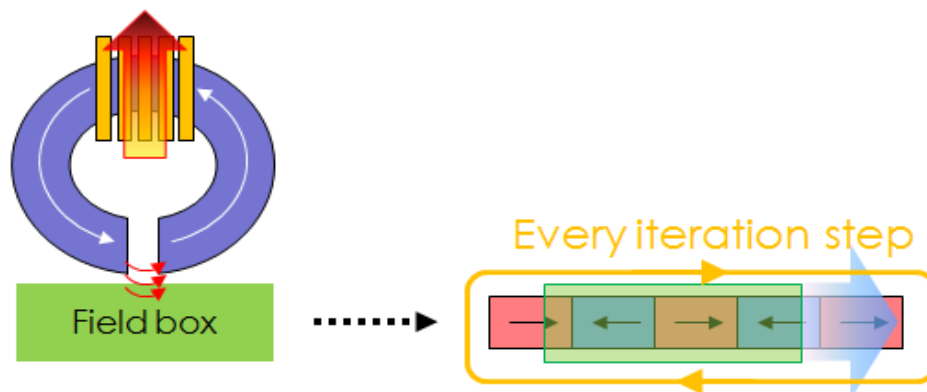


Fig. 47. Writing process using precomputed field box.

- Using precomputed field box

The precomputed field box is not precise as fully integrated micromagnetic simulation. However, it provides an efficient way to simulate writing processes. The writing process using precomputed head field is shown in Fig. 47. The first step is same to the fully integrated micromagnetics. The current applied on the coil induces magnetization of the writing head, which resulted in the write head field. In this method the writing field is not directly applied on the media model, but stored in a 3-dimensional field box. This precomputed field box is stored as an independent file. When the writing simulation is performed, the field box is read and applied onto the media file, accompanied with the movement in accordance with the head field profile. The field strength in precomputed field is determined by the *scale factor* multiplied on it. Physically the scale factor denotes the scaled current density, magnetic potential on the write head surfaces, and/or scaled saturation magnetization of the pole tip material referred in Eq. (51)~(82). The field box method has merits compared with the fully integrated micromagnetic simulations as following.

- (1) Computational resources: Since the field box method deals with only a part of the whole model, it requires much less physical memory than the fully integrated method.
- (2) Repetitive simulations: Once a field box is produced, it represents the head and coil model. In repetitive simulations, the field box is able to be used instead of the head and coil models. It also saves time, especially in the recording simulations.

(3) Applying analytic field profiles: Without field box method, in recording simulation we should use a numerical head field or prepare another input code in micromagnetic solver itself for analytic head field, i.e. Karlqvist head [69].

(3) Read Back Process

As in writing process, the micromagnetic simulation for read back process has two main options: fully integrated micromagnetics and using precomputed field box method. For read back simulations, the precomputed field box method has two ways: (1) So called ‘imprint’ method: A field box is created above the media, along the recording media track. The stray field data is stored in the field box. The magnetization changes of the read head element is detected as a read back signal while it moves inside of the field box. (2) Using reciprocity theorem, a field box is generated by the read head model, and it is applied onto the media. According to the reciprocity theorem, the product of magnetic field from media and magnetization of read head model is equivalent to the product of magnetic field from read head model and magnetization of media [8].

$$\int_{\Omega} \mathbf{H}_{\text{media}}^{\text{stray}} \cdot \mathbf{M}_{\text{reader}} d\Omega = \int_{\Omega} \mathbf{H}_{\text{reader}}^{\text{stray}} \cdot \mathbf{M}_{\text{media}} d\Omega \quad (83)$$

The interaction energy (ΔE_{inter}) between the field box and the written bit is regarded as the read back signal, therefore the unit of the signal is energy [J] or energy density [J/m^3].

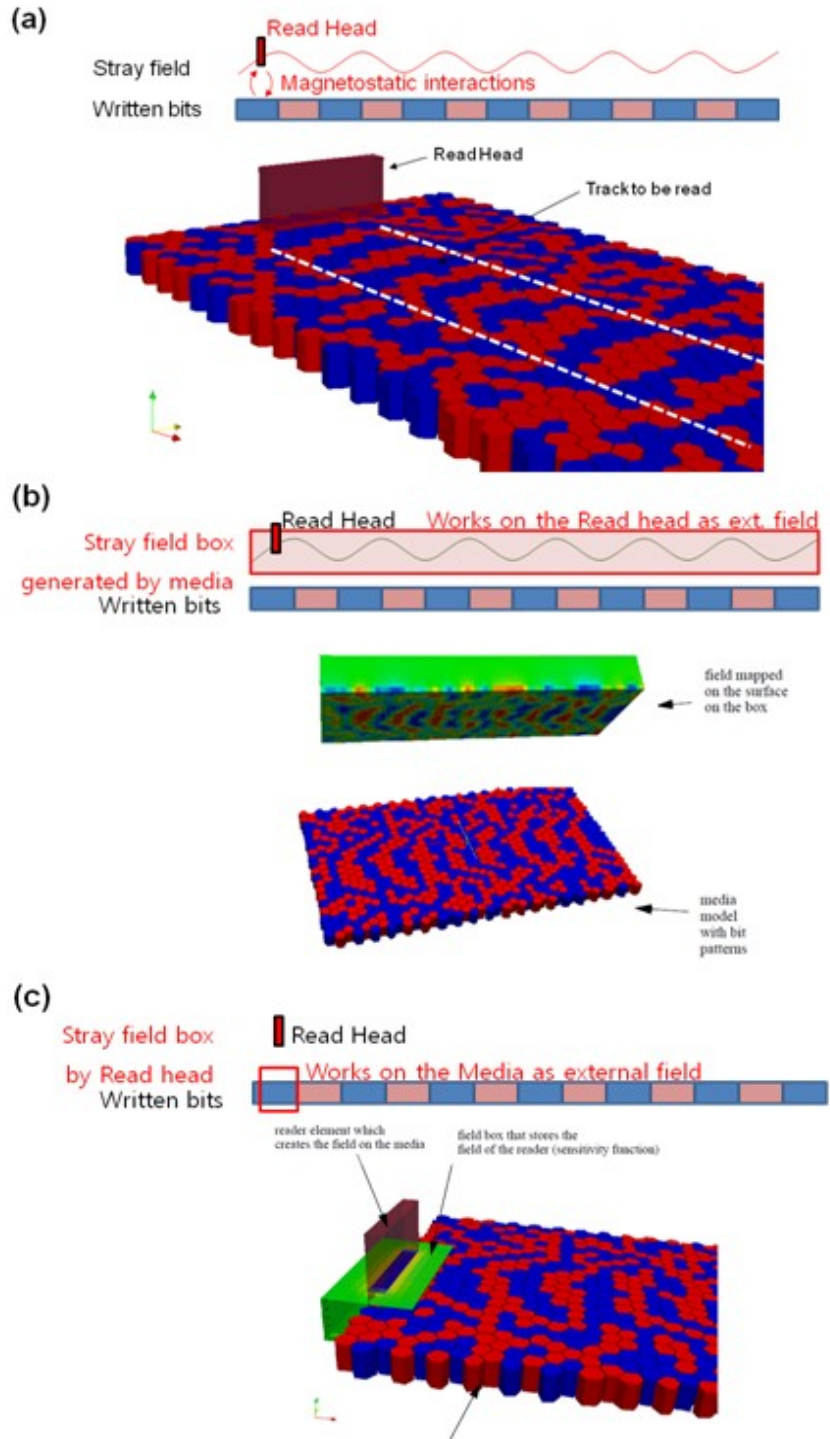


Fig. 48. Three methods of the read back process. (a) Direct read back calculation using fully integrated micromagnetic simulation. (b) Field box calculation of the written bits on media, “imprint”. (c) Using reciprocity theorem.

A double Szczech head is chosen for the read head model, considering the effect of the shields placed in front and rear of the read head element. Fig. 49 shows the procedures to build it, with 5 nm thick free layer, shield length $p = q = 100$ nm and the shield to shield distance = 100 nm. (1) magnetic field between left shield and free layer and (2) free layer and right shield are generated independently, and (3) the two field profiles are summed into total field. The total field is the sensitivity function, its strength as a function of downtrack distance and distance from head base is shown below.

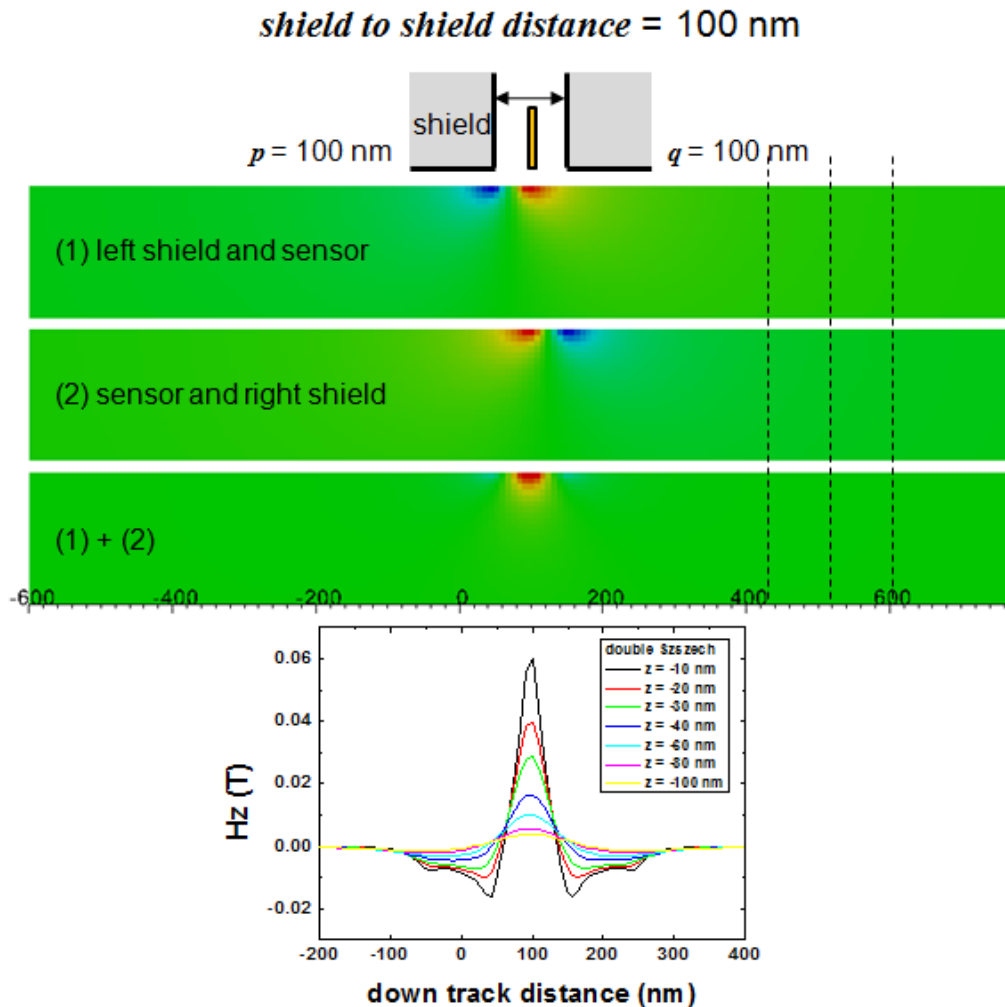
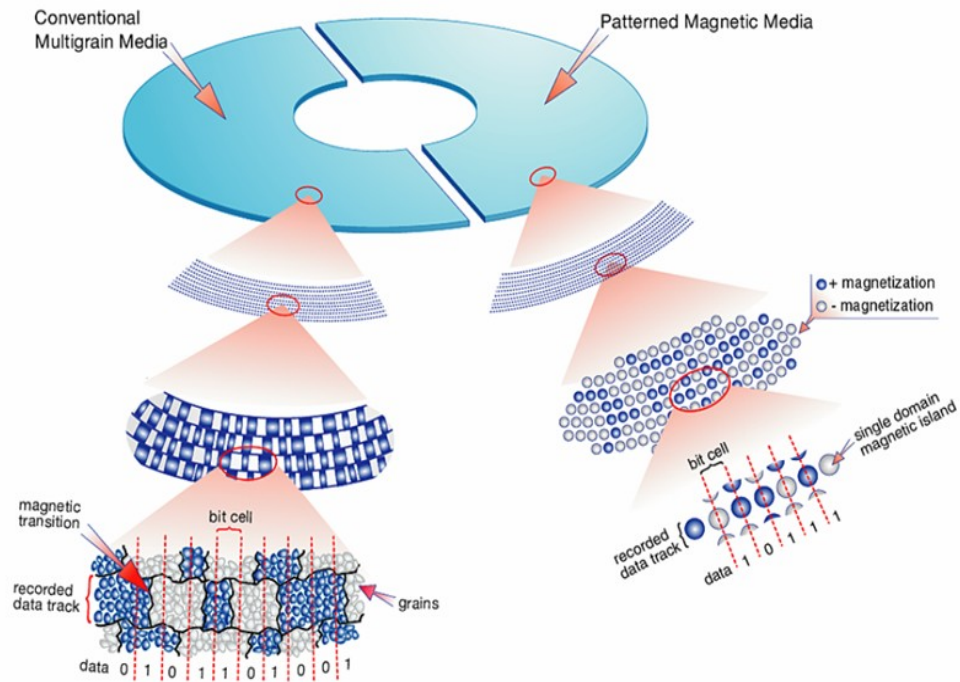


Fig. 49. The procedure to build double Szczech head field for analytic read head model.

3.2. Bit Patterned Media (BPM)

(1) BPM Designed for High Density Recording

Bit patterned media is one of the promising candidates of the future recording system to overcome trilemma [90]. In these days bit patterned media (BPM) has been studied very intensively to achieve recording densities greater than the one obtained for a conventional granular perpendicular magnetic recording[81]. The bits are physically separated, therefore they are exchange decoupled. The exchange isolation permits stable recording in denser recording media [91]. The individual bit of the BPM is defined as a single domain grain. A reduction of bits dimensions to smaller than the critical size is obtained by ion beam lithography[92-93], electron beam lithography[94] or nano imprint[95]. The process suggested by Hitachi GST is shown in Fig. 51.



© 2004 Hitachi Global Storage Technologies

Fig. 50. Comparison between conventional multigrain media media and bit patterned media [96]

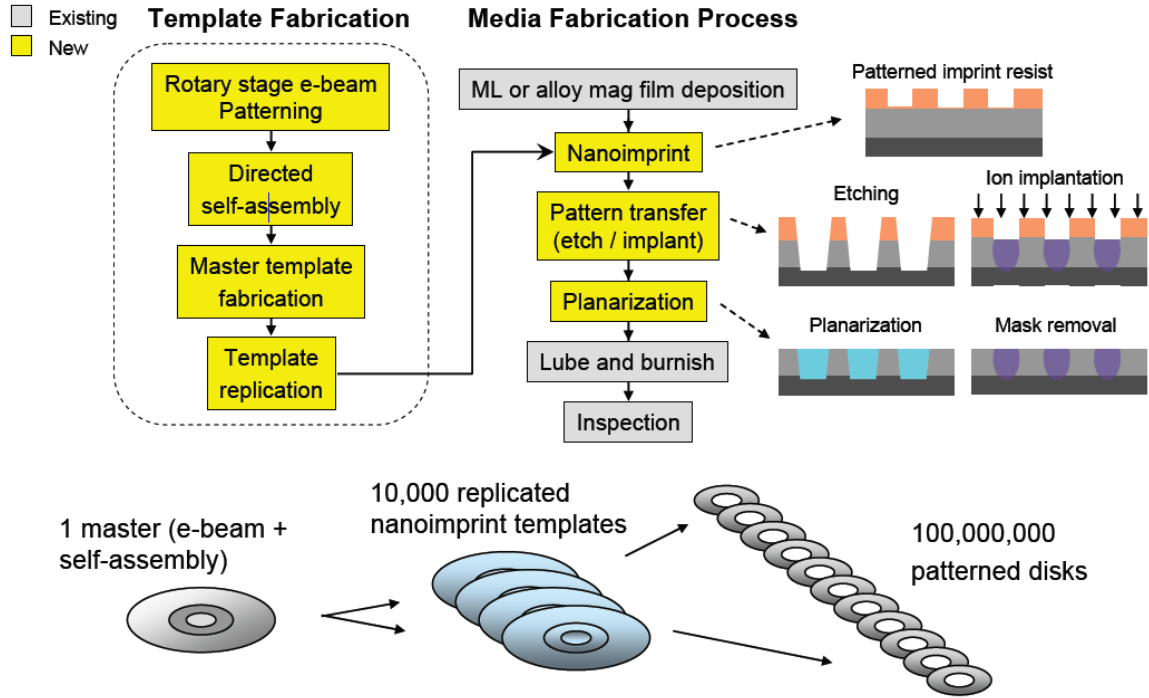


Fig. 51. Patterned media: fabrication overview [97]

From the viewpoint of the patterning, BPM presents an extreme challenge to lithography because of the aggressive feature and the tight size/spacing sigma requirements to achieve the high-density magnetic recording, such as 1Tdot/in.² of which pitch corresponds to 25 nm [98-99]. BPM applications require more aggressive targets than the semiconductor industry, and the latter will not provide a lithography solution in time for BPM based on the roadmap. However, compared to the semiconductor industry, the good news is that BPM patterning only requires a single mask step with no critical alignment requirements. The combination of e-beam direct writing with imprint lithography appears to be the only possible choice for this application at this moment. These two disciplines will have to work together to meet the needs of BPM technology[100].

(2) Contributions on Switching Field Distribution (SFD)

It is known that the BPM media have a broader switching field distribution (SFD) as compared with the continuous film of the same material[101-102]. This outcome is caused by the bit size distribution and the inhomogeneous magnetic properties – an easy axis alignment, diversions of a crystalline anisotropy, partial damages on the bits during the fabrication processes. However, it is not easy to quantify the contribution of the individual SFD source in experiments, because measured SFD is a result of the superposition of all contributions[103-105]. For the purpose of finding the contribution of the individual SFD source, we perform micromagnetic simulations varying easy axis orientation, anisotropy distribution or bit sizes separately. The micromagnetic results were based on and compared with the experimental study.

The $L1_0$ chemically ordered, (001) textured, 5nm thick FePtCu alloy was prepared. Foremost, FePt(4.4 nm)/Cu(0.6 nm) was deposited on a thermally oxidized Si (001) substrate. Subsequently, RTA treatment was applied at 600°C for 30 s in N_2 atmosphere[106-107]. As grown specimen was subjected a magnetometry measurement by means of the superconductive quantum interference device (SQUID). A perpendicular uniaxial anisotropy (K_1) of 0.55 MJ/m³ and a saturation magnetization (M_S) of 770 kA/m were found. After measurement the bit patterned structure was prepared. First Ta was deposited on the top of FePtCu continuous film. The 30 nm bit patterns were formed on it using block copolymer with nano imprint and subsequent CF_4 etching of the Ta layer. Finally FePtCu BPM is prepared by Ar^+ ion milling processes. Fig. 52(a) and Fig. 52(b) show the final FePtCu nanostructures (period = 60 nm, dot size = 30 nm) which maintain

the initial perpendicular magnetic anisotropy. The bits are in a magnetically exchange decoupled and single-domain ground state. As it is shown in Fig. 52(c), a drastic increments in switching field from 0.96 kOe to 5.05 kOe and absolute SFD from 0.51 kOe to 5.16 kOe are found after patterning. In this paper, the switching field is defined as the field at which the derivation of the hysteresis curve is maximized. While the absolute SFD is a difference between the fields where the magnetization reversal process is initiated (1 %) and finalized (99%). The relative SFD is defined as the absolute SFD divided by the switching field.

The microstructure of the BPM was investigated using field emission gun scanning electron microscopy (FEG SEM) FEI Quanta 200, and transmission electron microscopy (TEM) FEI Tecnai F20. The TEM specimen was prepared using dual beam focused ion beam (DBFIB) FEI Quanta 200. The size distribution of the FePtCu BPM was obtained by the particle detection on the SEM plan view image analysis shown in Fig. 53(a). The mean diameter was 29.95 nm and the standard deviation was 2.2 nm, corresponding to 7.36% of the mean value. The side view (cross sectional view) of the bit array is shown in Fig. 53(b). The irregularity of the bit thickness and spacing on the figure results from the selected TEM sample area as indicated with a white bar in Fig. 53(a). High resolution TEM image accompanied with the Fast Fourier Transformation (FFT) image in Fig. 53(c) confirms that the FePtCu bit has a $L1_0$ phase of which c axis is perpendicular to the plane. The cross sectional view also demonstrates that the bit has a truncated cone shape resulted from the experimental procedures[108].

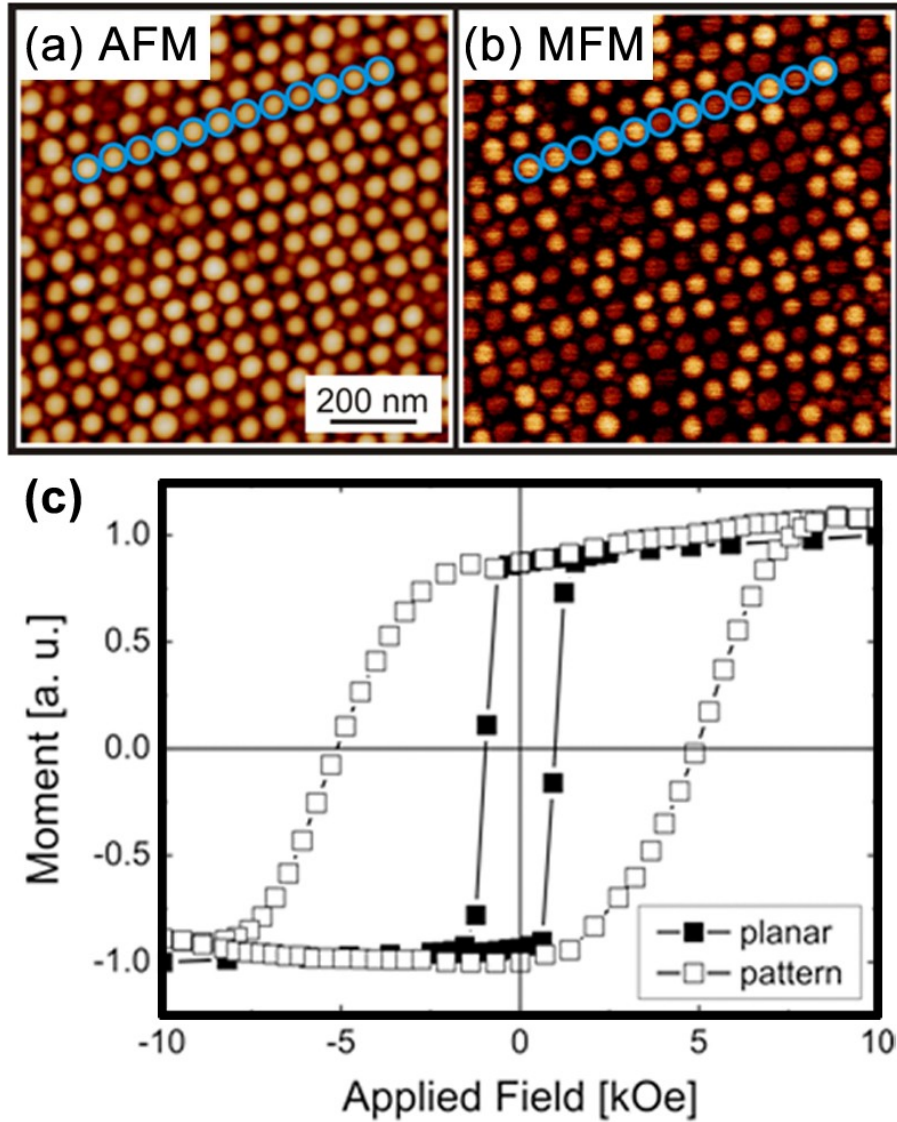


Fig. 52. (a) AFM and (b) corresponding MFM image of the patterned area (dot size = 30 nm, pitch = 60 nm). The sample is in the demagnetized state and one row of nanostructures is highlighted for comparison. (c) Kerr magnetometry of the continuous planar film (solid) and the patterned media (open).

Based on the TEM results, the finite element models were prepared (Fig. 53(d)), with a diameter of the bottom plane D varied from 16 to 44 nm, whereas that of the top plane was set to 60% of D . The misorientation θ was varied up to 5° of full-width at half-maximum (FWHM), whereas the crystalline anisotropy constant K_1 was modified up to

10% of standard deviation. Both sets of values were Gaussian distributed. From the XRD experiment the FWHM of the FePtCu BPM was found to be $2.7 \pm 0.3^\circ$. In this session all simulations were performed on a single bit in order to exclude magnetostatic interactions between the bits [103, 108-109].

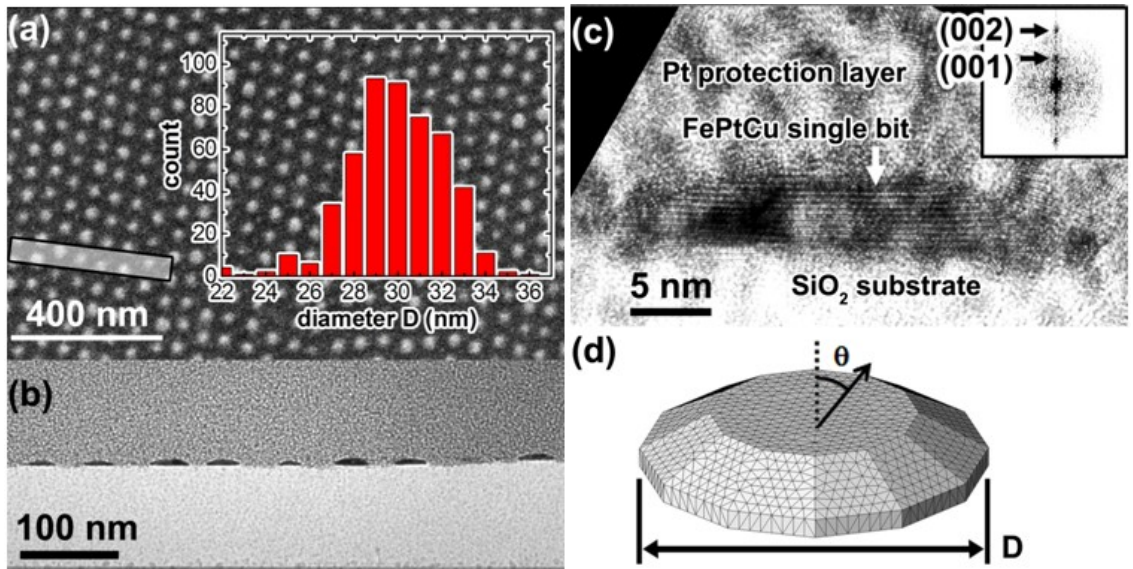


Fig. 53. Electron microscopy image of the FePtCu bits. (a) Top view SEM image with a size distribution. (b) Cross sectional TEM image. (c) High resolution TEM image of a single bit. The inset image is the FFT of the lattice fringes. (d) FEM model of a bit with a diameter D and misorientation of the easy axis θ .

From angular dependency simulations on a standard model ($K_1 = 0.6 \text{ MJ/m}^3$, $\theta = 0$, $D = 30 \text{ nm}$), the Stoner-Wohlfarth curve for a coherent reversal process was found (not shown). In all following simulations the external field was applied perpendicular to the film plane, with a tilting angle of 0.01° . Since the magnetization of the bit is reversed by a Stoner-Wohlfarth coherent rotation, the crystalline anisotropy K_1 and the misorientation θ play the most important roles in switching field determination. The switching fields obtained for a field applied along an angle of 0.01° are summarized in Fig. 54. Fig. 54(a)

shows the switching fields proportional to K_1 whereas the slope from the micromagnetic simulation is smaller than $2/M_S$, the case of the anisotropy field $H_k = 2K_1/M_S$. The switching fields become smaller as the misorientation θ increases (Fig. 54(b)). The switching field is drastically reduced by a small misorientation. However, as the misorientation further increases, the reduction of the switching field became smaller, it converges in the given range of $\theta < 12^\circ$. A stronger tendency of the convergence is found for lower K_1 , for the case of the contribution of the self demagnetization field is larger. If the crystalline anisotropy increases, the switching field approaches to the Stoner-Wohlfarth fields as a function of the misorientation θ [110].

The contribution of the self demagnetization field caused by the bit shape is clarified in the size dependency tests in Fig. 54(c). As the diameter increases, the switching field is decreasing owing to the demagnetization factor increment along the easy axis. Since the diameters of the bottom and top planes are varied while the bit thickness is fixed, the side wall angle becomes smaller as the bit enlarges. According to the study of Kalezhi et al[108], the side wall angle and the bit size independently contribute to the switching field: The switching field gets weaker as the side wall angle shrinks and also as the bit diameter enlarges. Consequently the switching field reduction shown in Fig. 54(c) is the superposition of the two contributions. Please note that the slope of the line connecting the switching fields hardly changes as the K_1 is varied. Such behavior still appears even if the K_1 is 1.8 MJ/m^3 (not shown). That means the contribution of the size variance is independent of the K_1 and θ , contributions as described in the micromagnetic Gibbs free energy equation [18]. For the same reason, the

relative SFD due to the size distribution is kept reduced as the material with a stronger K_1 is used.

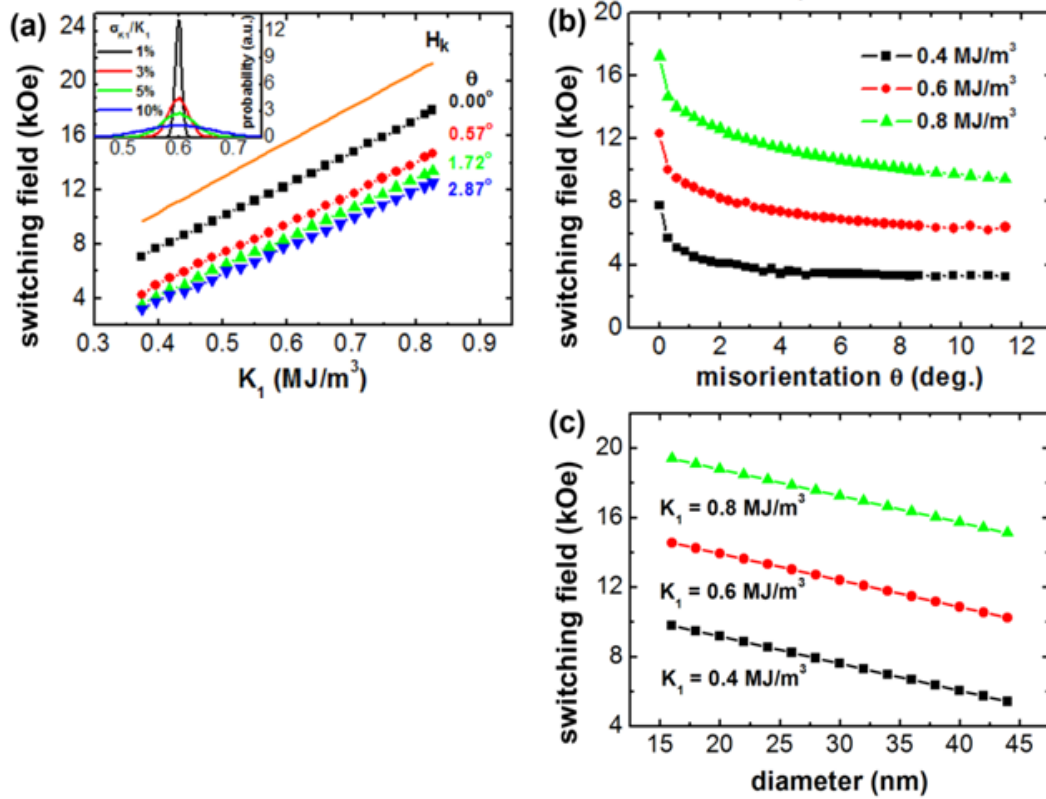


Fig. 54. Switching fields as a function of the (a) crystalline anisotropy K_1 compared with anisotropy constant $H_k = 2K_1/M_S$ the (b) misorientation θ . The inset in (a) shows the Gaussian distribution of K_1 , and the attached numbers on the lines denotes the misorientation θ , and (c) the bit diameter D for the cases of $\theta = 0$. In (a) and (b) the bit diameter D is fixed as 30 nm.

The switching field distribution is obtained as follows. Under the variance of a property in a certain range, the switching field is varied as shown in Fig. 54. Due to the fact that the properties have a Gaussian distribution in the range, the switching probability in the external field is possible to be calculated using the relationship between the property and the switching field. Fig. 55 shows the switching probability as a function

of the external field strength, contributed by each sources of the switching field distribution. When a property is varied, all the other properties are kept as the standard values described above. In order to find out the relationship between the external field strength and bit switching probability, a cumulative distribution is applied. The absolute and relative SFDs are written on the bar graphs.

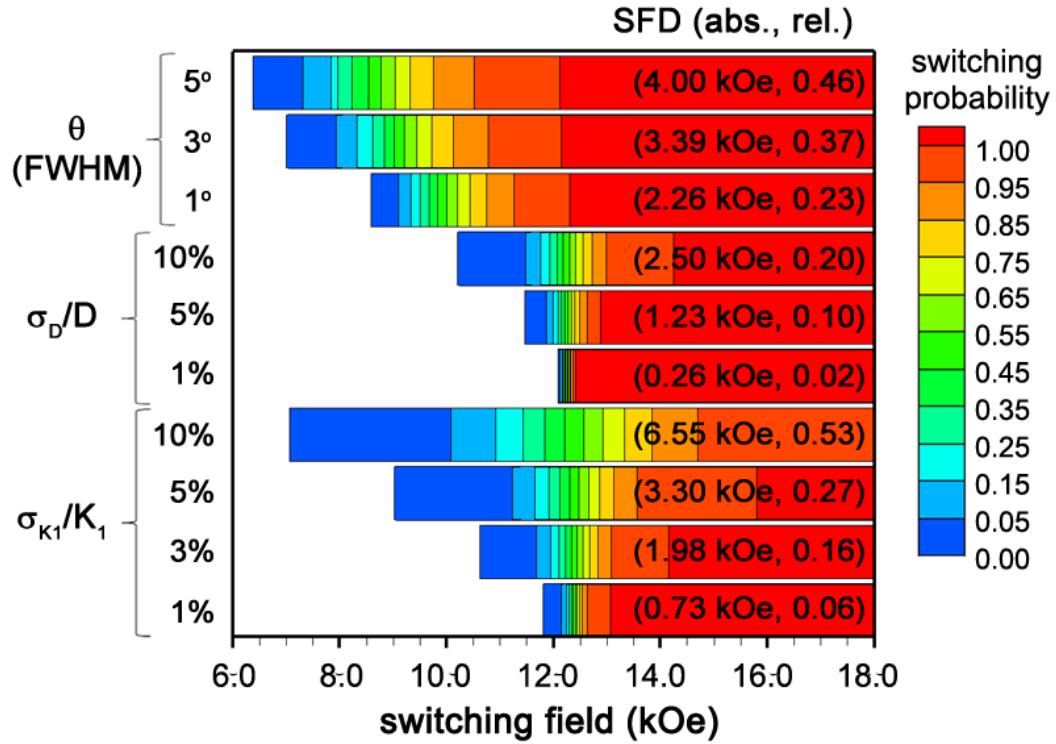


Fig. 55. Contributions of the misorientation θ , bit diameter D , and the K_1 deviation σ_{K_1}/K_1 on the switching field distribution. The absolute (SFD, in kOe) and the relative (SFD/ $H_{sw,avg}$, dimensionless) are written on each bar which represents the cumulative switching probability.

The K_1 and size distribution contributes on the SFD linearly, up to 0.53 ($\sigma_{K_1}/K_1 = 10\%$) and 0.20 ($\sigma_D/D = 10\%$). The K_1 distribution influences on the SFD more than twice than the size distribution related to the contributions of the crystalline and shape anisotropy, proportional to M_S^2 . The misorientation has a square root relationship with

SFD. As discussed above, the SFD increases with a small θ . Comparing to the experimental results $\theta_{\text{FWHM}} = 2.7^\circ$ and $\sigma_D/D = 7.36\%$, it can be approximated that the contribution of the misorientation and size distribution on the relative SFD are 35% and 15%, respectively. The contribution of σ_{K_1}/K_1 is not considered because it was hard to be obtained by experimentally.

In conclusion, the contributions of the diversion of the crystalline anisotropy, bit size and the easy axis orientation on the SFD were studied separately based on the experimentally prepared FePtCu $L1_0$ single phase BPM. Micromagnetic simulation results revealed that the deviation of the intrinsic properties is stronger than that of the geometric properties.

(3) BPM Material Design: Exchange Spring BPM

In order to solve the writability issue on hard magnet such as FePt L1₀ phase, the concept of exchange spring media was suggested aiming to reduce the switching field of a hard magnetic layer [111]. A grain of such a medium consists of a soft part in which reversal nucleates and a hard part which provides stability. These systems switch by nucleation and a domain wall motion, where the switching field is reduced due to the lower nucleation field of the soft layer and thus a lower field is required to push the domain wall across the interface between the soft and hard parts (pinning field) [9]. Moreover, the exchange spring concept can also be extended to other innovative future magnetic recording schemes such as bit patterned media (BPM) aiming to extend the magnetic storage density beyond 1Tbit/inch² [112].

The switching field of the exchange spring media is determined by the larger one between the nucleation field H_{nucl} and the pinning field H_{pin} as follows

$$H_{nucl} = \frac{2K_{soft}}{J_{S,soft}} + \frac{1A\pi^2}{2t_{soft}^2 J_{S,soft}} \quad (84)$$

$$H_{pin} = \frac{2K_{hard}}{J_{hard}} \frac{1 - \frac{K_{soft}}{K_{hard}} \frac{A_{soft}}{A_{hard}}}{\left(1 + \sqrt{\frac{A_{soft}}{A_{hard}} \frac{J_{soft}}{J_{hard}}}\right)^2} \quad (85)$$

$$= \frac{2K_{hard}}{J_{hard}} \frac{1 - \frac{K_{soft}}{K_{hard}}}{\left(1 + \sqrt{\frac{J_{soft}}{J_{hard}}}\right)^2} \quad (\text{if } A_{hard} = A_{soft}) \quad (86)$$

(4) Writing on Exchange Spring BPM with a Moving Writing Head

In order to realize the magnetization reversal of a very hard layer such as FePt L1₀, we have introduced the exchange spring scheme to bit patterned media. As D. Suess and R. H. Victora have suggested the exchange composite structures [113-115], switching field reduction is reported by many researchers [116-117]. However, the reported FePt L1₀ phase based exchange spring media still requires higher switching fields than current recording head can apply [116]. We focused not only preparing an exchange spring structure to simply reverse FePt L1₀ phase, but also the reducing the switching field to be applied by the recording head. According to Klemmer and Weller the anisotropy field of the FePt L1₀ phase is large as much as 11.7 T [77, 118], which is not able to be achieved by write head. A possible way to reverse FePt L1₀ phase is to utilize the exchange spring structure. In order to reduce the pinning field defined in Eq.(86) lower than 1.7 T, a material of which $K_1 \geq 2.81 \text{ MJ/m}^3$ is required as a “soft” magnet. Even though the material is used, its nucleation field is still too large that another soft layer is requested. Consequently, a graded media is recommended to reverse FePt L1₀ structure [119].

Material	Crystalline Anisotropy K_1 (MJ/m ³)	Saturation Polarization J_s (T)	Saturation Magnetization M_s (kA/m)	Anisotropy Field $\mu_0 H_k$ (T)
Co ₉₀ Cr ₁₀ [120]	0.42	1.19	947	1.53
FePtCu L1 ₀	2.00	1.1	875	6.13
FePt L1 ₀	4.00	1.2	955	8.38

Table 2. Material parameters for trilayer exchange spring media.

- Influence of the head excitation position and write head field strength

In order to find the influence of the head excitation position relative to the bit position and write head field strength, a trilayer exchange spring media structure is prepared. The structure is supposed to be composed of 5nm thick FePt L1₀ phase hard layer, 5 nm thick FePtCu L1₀ intermediate layer, and 10 nm Co₉₀Cr₁₀ alloy as a soft layer. The material parameters of the materials are summarized in Table 2. The material parameters of the FePtCu L1₀ and FePt L1₀ phases are obtained experimentally by the research group of Manfred Albrecht in Chemnitz University of Technology.

At first, the exchange spring media was exposed to homogeneous external magnetic field with varying field applying angle. The analytically calculated nucleation field of the soft layer is 14.1 kOe, and the pinning fields between the layers are 6.85 kOe and 5.46 kOe, respectively. Therefore it can be expected that the switching field would be determined by the largest value, the nucleation field. The nucleation field H_{nucl} , switching field H_{SW} and the coercive field H_C are summarized as a function of the field applied angle Fig. 56(b), from the demagnetization curves shown in Fig. 56(a).

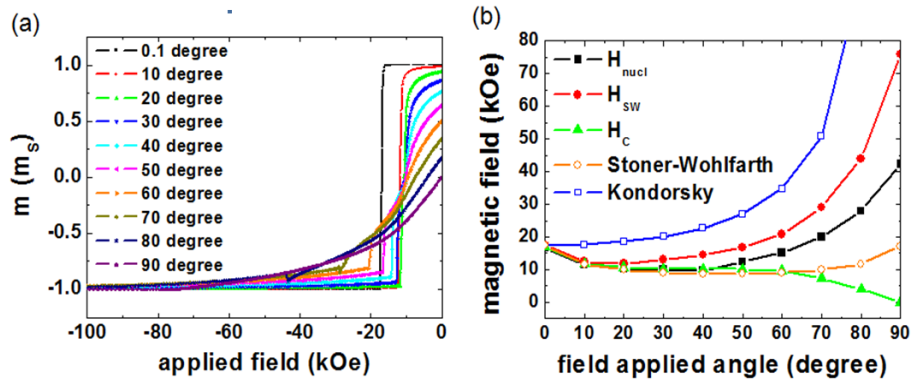


Fig. 56. (a) Magnetization curves with various field applying angle. (b) Nucleation field (square), switching field (circle) and coercive field (triangle) as a function of the field applied angle. The Stoner-Wohlfarth coherent rotation curve and the Kondorsky curves are presented for comparison.

The nucleation field and the switching field are defined as $m/m_S = 0.95$ and -0.95 , respectively. The smallest switching field was obtained as 11.8 kOe, 16% lower than the analytically estimated value. The switching field reduction is resulted from the reduction of the nucleation field. Since the soft layer has a small K_1 to form a reversal domain, it tends to be switched by a coherent rotation following the Stoner-Wohlfarth curve. As revealed in Fig. 56(b), the nucleation field is the closest one to the Stoner-Wohlfarth fields. Once the switching process is initiated, the switching field process is converted to the domain wall motion, therefore the switching curve becomes closer to Kondorsky curve. From the static field application results it seems that the switching field of a structure is simply determined by the material parameters of the recording media. However, if the dynamic external field is applied, it becomes another story. In order to find out the magnetization response on the realistic head field, a head field generated from the single pole tile head with soft underlayer as shown in Fig. 57(a) is applied. The field was initially turned off, but initiated in 0.1 ns to certain strength. The field strength was modulated by multiplying a scale factor (sf) on the head field profile. Fig. 57(a) is the case of the $sf = 1$, of which maximum field strength is 1 T very below the head base. The head field strength is decayed as the distance from the head base becomes larger. The head field was turned off at the beginning, and initiated in 0.1 ns. The magnetization switching behavior was studied in different bit position from -10 to 55 nm. The bit position was defined as defined as the relative position from the trailing edge of the write head to the bit center. For example, if the bit position is 0 nm, the bit is placed very below the trailing edge.

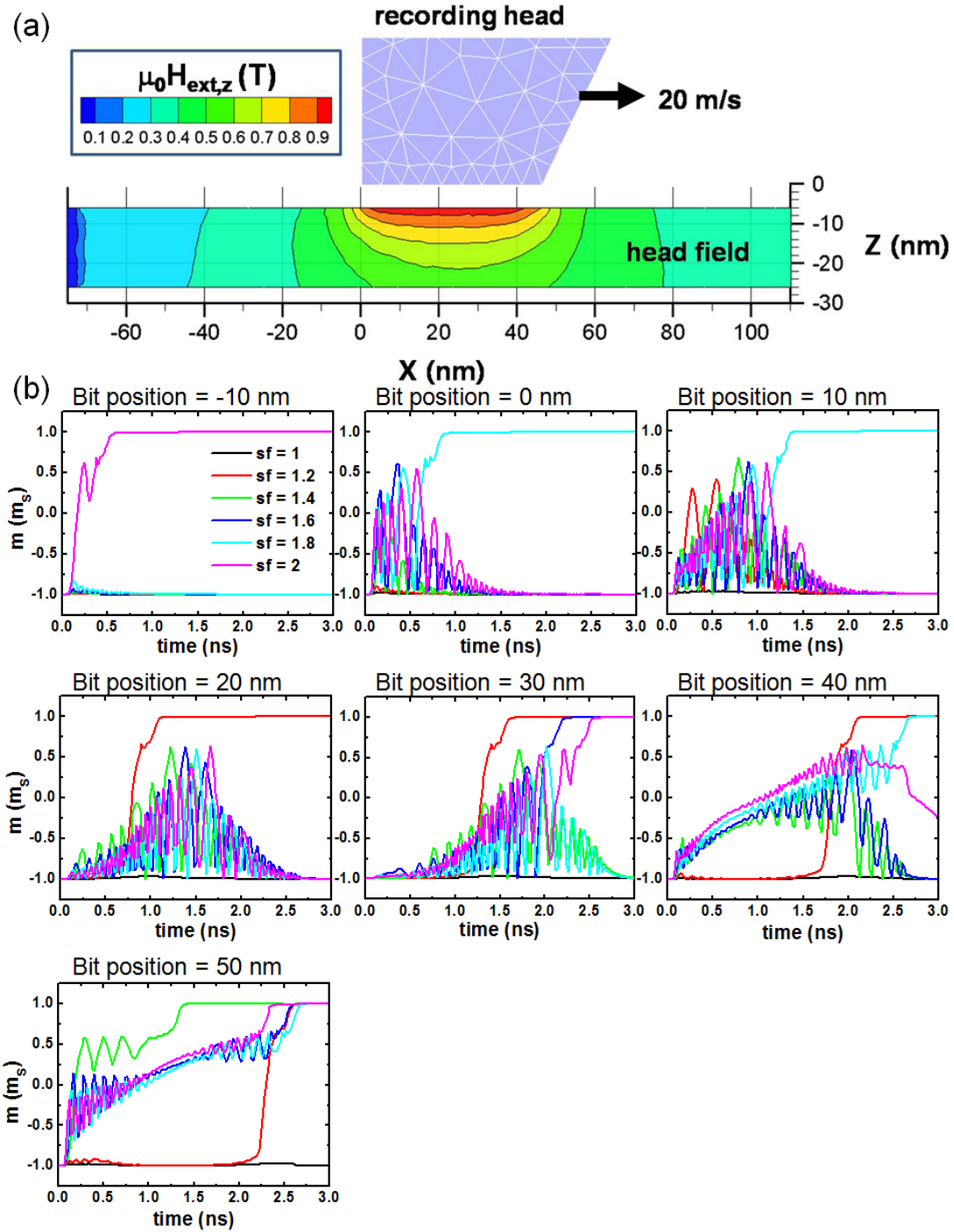


Fig. 57. Magnetization processes from dynamic micromagnetic simulations with TUCH-03, in the cases of grain position varied from 20 to 55 nm. (a) Initial positions of the recording head and grains for each cases, (b) scale factor application as a function of time, (c) Magnetization behaviors of the grain, in a given position and scale factor.

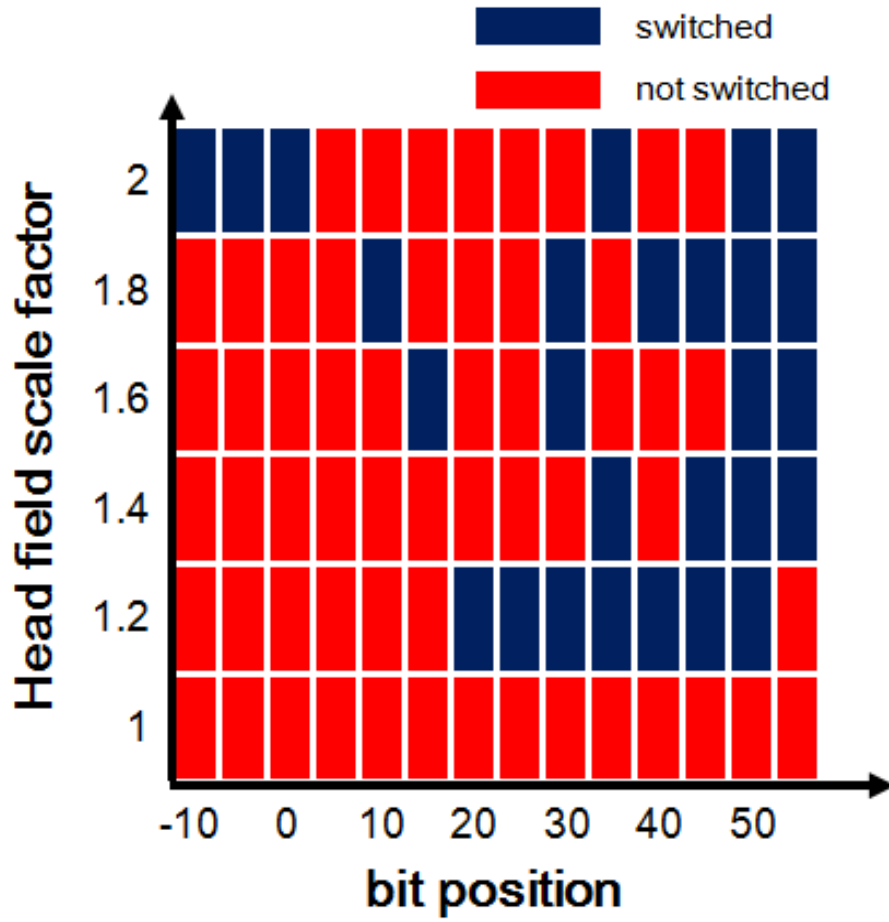


Fig. 58. Phase diagrams of successful switching events (blue), as a function of the grain position and head field scale factor.

- Effective Head Field Gradients in Exchange Spring Media

Areal densities in the magnetic recording industry have successively increased over the last several years during the shift to perpendicular recording. The single pole type (SPT) writing head was developed to generate stronger fields and sharper head field gradients and effect higher recording densities for media that have small grains and high magnetocrystalline anisotropy. One particular limit of high-density recording is transition jitter[121] that originates from head field gradients, granularity of the media, and the switching field distribution of individual grains. Miura et al.[122] and Goldberg et al.[123] reported a correlation between head field gradient and transition jitter. Goldberg et al.[123] proposed that a strong effective field gradient is required to reduce transition jitter, because it correlates with transition jitter and is independent of the geometric parameters.

The head field gradient has been studied by varying geometric parameters³, tilting the write field angle [80, 124], and experimentally analyzing the head field with atomic force microscopy (AFM)[125]. Under ideal head field gradients, perfect transitions are obtained if the granular media possesses no switching field distribution. Transition jitter is also affected by the structure of the multilayer recording media. Due to the gradually decaying head field depth profile, the position of the hard and soft magnetic material within the grain strongly influences switching behavior. In this section, we report the effective head field gradient and changes that occur in various magnetic media. Traditionally, the head field gradient is measured in a plane that is parallel to the media surface, at a certain distance from the air-bearing surface (ABS). This approach works

perfectly if the grains switch by uniform rotation. Exchange spring media, introduced to increase signal-to-noise (SNR) ratios and thermal stability, however, do not reverse uniformly. In exchange spring media, nucleation and expansion of a reversed domain are expected to constitute the most probable switching mechanism.

To understand the effects of head field gradient on granular media, a 3-dimensional head field profile was simulated using a hybrid finite element method and boundary element method, implemented in the FEMME software package [126]. By computing the position of the bit transition Δp as a function of the media anisotropy K for different structures, we show that the relationship $\partial\Delta p/\partial K$ provides a measure of effective head field gradient. To determine the exact position of the transition compared with the write head position, a write head model and a 20-nm-thick recording media model were simulated. The writing head moved 1 nm above the media at a velocity of 20 m/s. The pole tip ($J_S = 2.4$ T, $M_S = 1.91$ MA/m) had a width of 20 nm and a length of 45 nm. The write current was 50 mA. We computed the write fields of the recording head without shields (Fig. 59(a)). Instead of simulating grains that had realistic shapes and diameters, we created an array of grains. The basal plane of each grain was 0.9 nm x 0.9 nm, and the center-to-center distance was 1 nm with a thickness of 20 nm. Each ideal grain was discretized into tetrahedral finite elements. The chain was located at the center of the head (y -coordinate = 0), parallel to the down track direction. No exchange or magnetostatic interactions were allowed between neighboring grains. Notably, the grains do not represent real media but were used to probe the exact position of the transition, providing a measure of effective head field gradient.

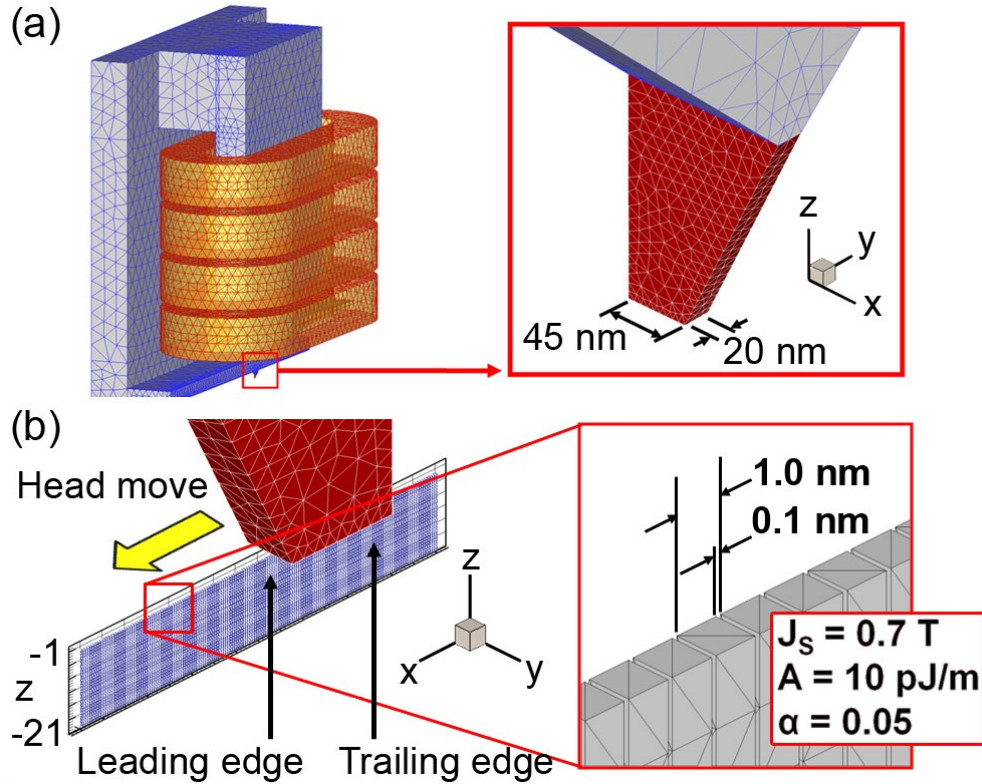


Fig. 59. (a) Finite element model and schematic of the recording head with coil. (b) The decoupled grains are shown with the recording head model. The saturation magnetic polarization is $J_s = 0.7 \text{ T}$, exchange constant $A = 10 \text{ pJ/m}$, and the Gilbert damping constant $\alpha = 0.05$. The initial trailing edge position is $x = 0 \text{ nm}$ at $t = 0 \text{ ns}$.

The setup of the simulation was as follows: we first chose the initial coordinates of the trailing edge on the recording head and the media to be located at $x=0$, and the head field = 0 T. After 0.1 ns, the head field reached a maximum of 1.4 T (using a linear ramp), having moved 2 nm, as shown in Fig. 60a and Fig. 60b. The maximum head field gradient was 0.1 T/nm at the trailing edge. The uniaxial crystalline anisotropy constant K_{hard} was varied up to K_{max} , the maximum anisotropy constant that allowed the media to be switched under a given head field profile. The structure of the media was classified by the number of layers of the models—i.e., a single, bi-, or trilayer medium.

	Bilayer	Trilayer 1a	Trilayer 1b	Single Phase	Trilayer 2b	Trilayer 2a
K_{\max} (MJ/m ³)	0.83	0.91	0.74	0.41	0.50	0.62
$\partial\Delta p/\partial(K_{\text{hard}}/K_{\max})$ (nm) @ $K_{\text{hard}}/K_{\max} = 1$	4.93	7.11	6.71	12.62	25.94	22.67
E_{barrier} ($k_B T_{300K}$) @ $K_{\text{hard}}/K_{\max} = 1$	65.14	61.72	61.50	45.78	42.39	42.05

Table 3. Comparison of K_{\max} , first derivative of Δp , and Energy barrier at 300 K and $K_{\text{hard}}/K_{\max} = 1$.

The single phase medium possessed a uniform crystalline anisotropy of K. The bilayer system was composed of a 10-nm-thick bottom layer with a high crystalline anisotropy K_{hard} , coupled to a 10-nm-thick top layer, for which $K_{\text{soft}} = 0.4 \times K_{\text{hard}}$. For the trilayer system, we studied 4 cases in which the total thickness was kept at 20 nm; see Fig. 61a. Each system was composed of a 10-nm-thick layer and 2 5-nm layers with the following anisotropy values: $K_{\text{soft}} = 0.4 \times K_{\text{hard}}$, $K_{\text{inter}} = 0.6 \times K_{\text{hard}}$, and K_{hard} , which was varied from 0.4 to 1.0 K_{\max} ; see Table 3. The intermediate layer was included to reduce the pinning field between the soft and hard layers and maintain thermal stability [9, 119].

For exchange spring media that possessed a magnetically hard bottom layer compared with a single phase medium, K_{\max} increased by more than 2-fold (as seen in Table 3). As the head passed over the grains, a reversal began near the leading and trailing edges, because the write field had a significant in-place component. Depending on the media, the cell reversed by quasiuniform rotation (single phase medium and trilayer media with a magnetically hard upper layer) or nucleation and successive domain

wall propagation from the top to the bottom of the media (in bilayer and trilayer media with a magnetically soft upper layer). The switching process and the position of the bit transition Δp are illustrated in Fig. 60.

The bit transitions Δp for all structures are plotted in Fig. 61 as a function of the normalized anisotropy $K_{\text{hard}}/K_{\text{max}}$ (Fig. 61(b)). The comparison of Δp and $\partial\Delta p/\partial K$ is shown, fitted with a negative exponential curve. The first derivative of the curve is the change of Δp that was induced by the distributions of the granular anisotropy $K_{\text{hard}}/K_{\text{max}}$. The higher first derivative implies that the same amount of relative anisotropy dispersion leads to wider transition jitter. The first derivatives of the graphs in Fig. 61(b) are shown in Fig. 61(c). For all structures, $\partial\Delta p/\partial(K_{\text{hard}}/K_{\text{max}})$ became smaller with increases in $K_{\text{hard}}/K_{\text{max}}$. Hence, independent of the type of structure that is used, K_{max} is recommended as the optimal design, because it has the highest effective write field gradient. In comparison, the $\partial\Delta p/\partial(K_{\text{hard}}/K_{\text{max}})$ factor for the structures suggests that to maximize the effective head field gradient in the bilayer and trilayers, the high anisotropy layer should be at the bottom. The origin of the small $\partial\Delta p/\partial(K_{\text{hard}}/K_{\text{max}})$ in such structures is attributed to the reversal mechanism. In exchange spring media and trilayered systems, the nucleation first forms at the top of the grain when the head field exceeds the nucleation field. If a magnetic multilayer structure possesses a weak pinning field between the layers compared with the nucleation field, a successful reversal is determined by successful domain formation. If the soft layer is exposed to the stronger head field (i.e., a position closer to the pole tip), an easier reverse domain nucleation will result even though the magnetic hard layer is under a weaker field (i.e., further from the pole tip).

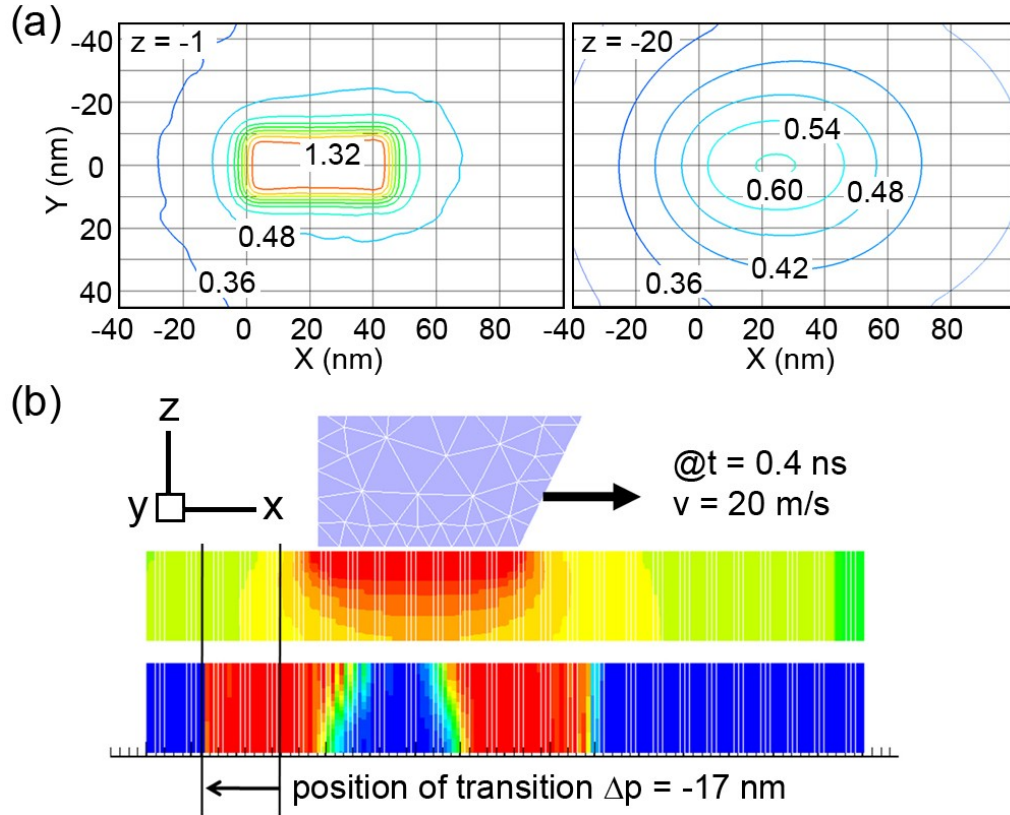


Fig. 60. (a) Head field profile on xy plane at $z = -1$ nm (left) and $z = -21$ nm (right). The attached numbers on the contour denote the z -component of the head field. (b) Transient state of the recording simulation ($t = 0.4$ ns) of a single phase medium with $K_{\text{hard}} = 0.2$ MJ/m³. The position of the head (8 nm), the head field gradient, and the magnetization status of the media of the same are shown after 0.4 ns.

Consequently, a high head field gradient is only required to be close to the pole tip, with the hard layer positioned at the bottom. The region in which a high field gradient is required is determined by the nucleation volume.

In contrast, the single phase perpendicular recording media, reversing by homogeneous rotation, requires a large head field gradient. This must be located in the down track direction and over the entire thickness of the media. This model is supported by simulations in which the reversal mode is constrained to a homogeneous rotation using a large exchange constant, $A = 1000$ pJ/m. In Fig. 61c, the black line (X symbols),

where $A = 1000$ pJ/m, is higher than that of the single phase medium, where $A = 10$ pJ/m. A more homogeneous rotation, induced by the higher exchange constant, results in a smaller effective head field gradient. The smallest $\partial\Delta p/\partial(K_{\text{hard}}/K_{\text{max}})$, which is the largest effective head field gradient, was achieved by the exchange spring media. The $\partial\Delta p/\partial(K_{\text{hard}}/K_{\text{max}})$ of the trilayer (2a) and (2b) that had the hardest layer at the top of the structure showed the least effective head field gradient. These media structures reversed almost homogeneously, similar to the single phase medium, due to the creation of a large nucleation field by the hard layer at the top. To compare the effective head field for the extreme cases, we took the values at $K_{\text{hard}}/K_{\text{max}} = 0.9$ of $\partial\Delta p/\partial(K_{\text{hard}}/K_{\text{max}}) = 8$ nm and $\partial\Delta p/\partial(K_{\text{hard}}/K_{\text{max}}) = 30$ nm for the bilayer and trilayer (2d), respectively. If the anisotropy constant in the grains is varied by 10%, the transition is $8 \times 10\% = 0.8$ nm (bilayer) and $30 \times 10\% = 3$ nm (trilayer 2b), which corresponds to a reduction in jitter by 70%.

The reversal mechanism also influenced thermal stability. Thermal stability of the tested structures was estimated by the analytical equation

$$E_{\text{barrier}} = \min\left(4F\sqrt{AK_{\text{hard}}}, K_{\text{avg}}V\right) \quad (87)$$

where F is the cross sectional area of the grain, K_{avg} is the average anisotropy constant within a grain, and V is the volume of an individual grain. The former term corresponds to domain wall reversal through the thickness, and the latter is due to coherent rotation. As shown in Fig. 61(d), the structures that had a higher measured effective head field gradient possessed a larger energy barrier by up to 50%. The comparison of the effective

head field gradient and thermal stabilities between the media types at $K_{\text{hard}}/K_{\text{max}}$ is summarized in Table 3.

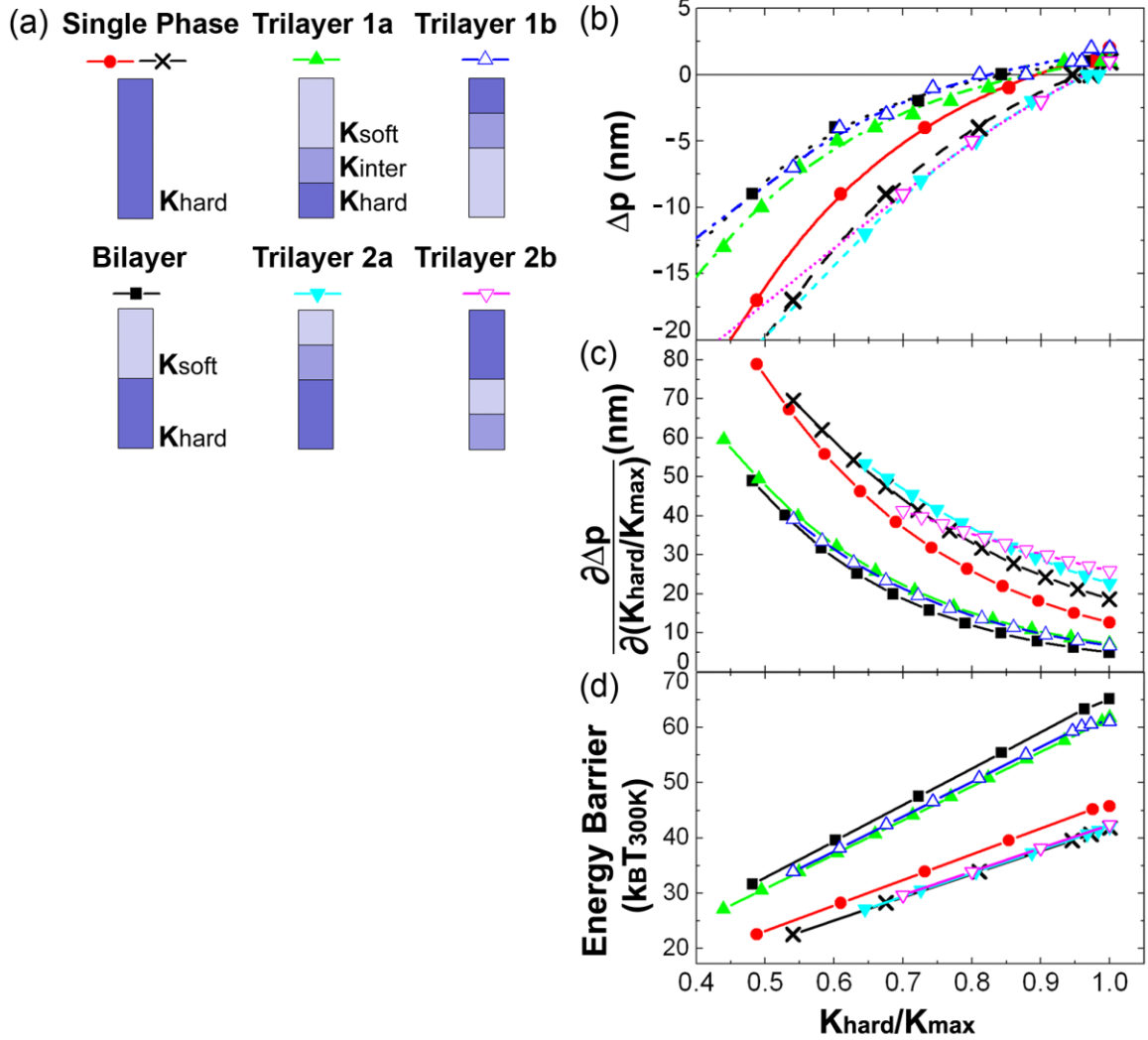


Fig. 61. (a) Schematic of the investigated media models (K_{hard} colored dark blue, K_{soft} light blue) (b) The displacement of the bit transition Δp as a function of the normalized anisotropy constant, $K_{\text{hard}}/K_{\text{max}}$ is shown for all media. The data were fitted using a negative exponential curve. (c) The first derivate of (b) as a function of the normalized crystalline anisotropy $K_{\text{hard}}/K_{\text{max}}$. (d) The energy barrier of the models as a function of $K_{\text{hard}}/K_{\text{max}}$.

In summary, we found that the head field gradient was not required to be high throughout the entire thickness of the media. The head field was only required to be large enough to switch the soft layer if position in the upper section of the grain, allowing switching by domain nucleation and propagation. The bilayer and trilayer (1a and 2a) exhibited larger effect head field gradients compared with the single phase medium. The thermal stability was also enhanced by 50% in exchange spring media, corresponding to an enlarged head field gradient. These results provide design specifications for increasing the density and stability of recording media.

(5) FePtCu L1₀ / [Co/Pt]_N Exchange Spring Media

Even though many theoretical studies are available dealing with the optimization of exchange spring media [116, 127-128], only few experimental attempts on the realization of FePt-based exchange spring media are reported in literature [129-130]. These studies are mostly limited to exchange spring media revealing an isotropic orientation of the easy axis of magnetization. In this session we present the formation of an exchange spring media combining hard magnetic FePtCu alloy films with softer Co/Pt multilayers. In order to study the thickness dependence of the soft layer on the magnetization reversal process of the exchange spring media, the number of bilayers, N , in the [Co/Pt] _{N} multilayer stack was varied. Moreover, the interlayer exchange coupling between the soft and hard films was modified by using rapid thermal annealing (RTA). These studies were accomplished by micromagnetic simulations providing routes for improving the exchange spring media performance.

- Experiments (by TU Chemnitz, Germany)

Hard magnetic L1₀ ordered Cu-alloyed FePt films with strong (001) texture was prepared by a two-step process, following the route presented by Yan et al.[106]. The first step is to prepare a L1₀ chemically ordered and (001) textured FePtCu hard layer. A 0.5-nm-thick Cu layer and a 4.5-nm-thick FePt layer were sequentially sputter-deposited on a thermally oxidized Si(100) substrate at room temperature. After the deposition, the samples were removed from the vacuum chamber, transferred to a separate RTA setup and annealed to 600 °C for 30 seconds in N₂ atmosphere in order to form the L1₀ ordered

FePtCu phase with (001) texture. Then, an additional $[\text{Co} (0.28 \text{ nm}) / \text{Pt} (0.76 \text{ nm})]_N$ multilayer-stack was deposited on top of the FePtCu layer at room temperature (Fig. 62). A series of exchange spring samples were prepared by varying the number of $[\text{Co}/\text{Pt}]$ bilayers in the stack, N , from 5 to 25. In order to enhance the interlayer exchange coupling between the layers, this specimen (as-prepared) was additionally processed by RTA to 450°C for 10 seconds (RTA treated).

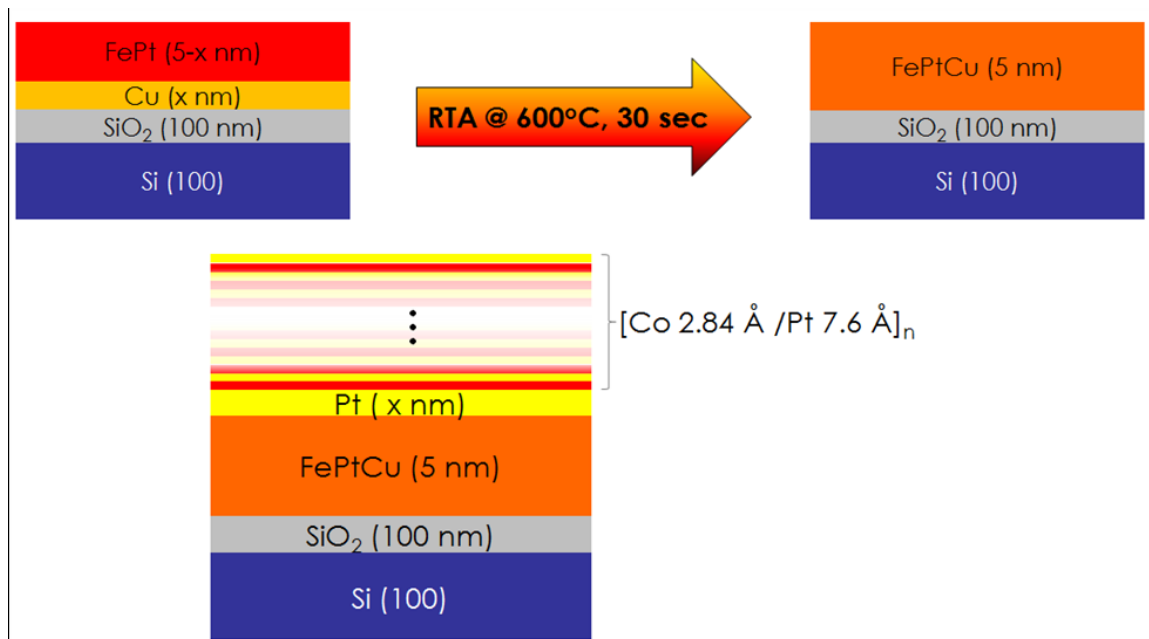


Fig. 62. Schematic sketch of (upper) FePtCu layer formation and (lower) FePtCu/ $[\text{Co}/\text{Pt}]_N$ exchange spring media structure.

In addition, reference samples with only the $[\text{Co}/\text{Pt}]_N$ multilayer films grown directly on SiO₂(100nm)/Si(100) substrates were prepared. SQUID characterization of the reference samples shows the presence of the out-of-plane easy axis of magnetization for the samples with $N > 5$. The samples with out-of-plane easy axis have a saturation

magnetization M_S^{soft} of about 0.63 T and a uniaxial magnetic anisotropy constant K_{soft} varying from 0.30 to 0.44 MJ/m³ with increasing number of bilayers similar to results reported in literature [131-133].

The growth of [Co/Pt]_N multilayers on FePtCu films results in two-step hysteresis loops when measured along the easy axis (out-of-plane) direction (Fig. 63b-d, solid symbols). The presence of well separated switching events for the hard and soft layer reveals that the interlayer exchange coupling between the two layers is weak compared to the pinning field that is defined as a field required to initiate the magnetization reversal process in the hard layer. In this case, when the magnetization of the soft layer is fully reversed at low field, a domain wall is pinned at the interface between the soft and hard layer. The domain wall pinning is depending on the interlayer exchange coupling and need to be pushed into the hard layer. Interestingly, the switching field of the hard layer is systematically reduced with increasing number of bilayers as summarized in Fig. 64. This proves that the nucleation process in the hard layer depend also on the integral magnetic properties of the soft layer as the interlayer exchange coupling is assumed to be not affected by the increased number of bilayers. Note that the switching field, $\mu_0 H_0$, given in Fig. 64, was defined as the maximum of the derivative dM/dH (inset in Fig. 63b), which is close to the coercive field.

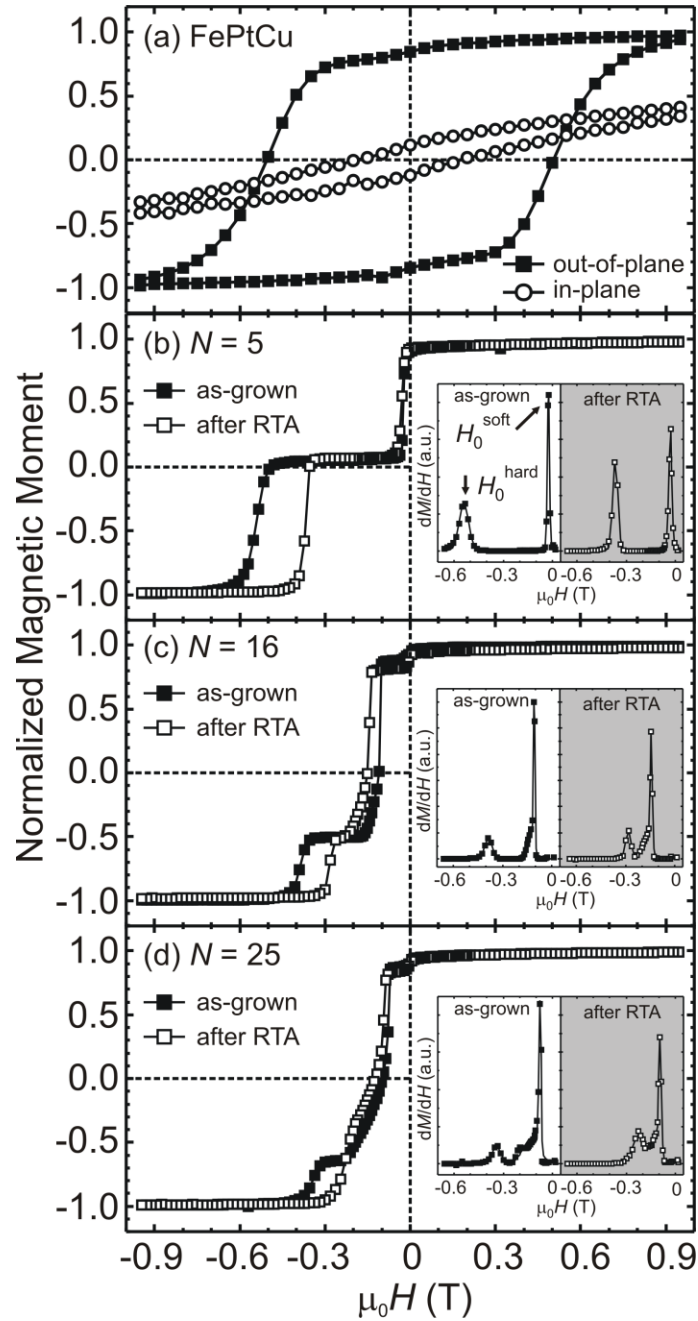


Fig. 63. (a) SQUID hysteresis loops of a hard magnetic FePtCu alloy film measured in the out-of-plane and in-plane geometry. (b-d) Series of out-of-plane hysteresis loops taken on FePtCu/[Co/Pt]_N samples with different bilayer number N (solid symbols) and after a RTA process (open symbols). The insets in (b-d) represent the first derivative of the hysteresis loops revealing the evolution of the switching field distribution as well as switching field of the hard and soft layers.

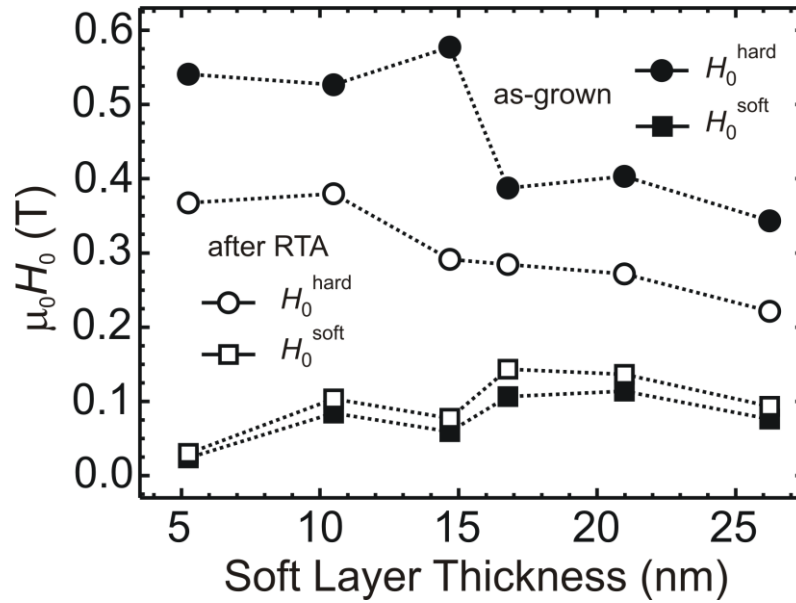


Fig. 64. Switching field dependence of the hard and soft layers as function of the soft layer thickness (solid symbol), and after applying a RTA process (open symbols).

Another important observation is that the switching field distribution of the hard layer is drastically narrowed by adding a soft layer. A similar effect was recently reported by Sbiaa et al. [134] on exchange coupled Co/[Co/Pd] stacks.

But not only the switching field of the hard layer is affected by the presence of a soft layer, it was turned out that the hard layer also influences the switching field of the soft layer. The evolution of the switching field of the $[\text{Co/Pt}]_N$ multilayer stacks with increasing bilayer number is presented in Fig. 64 as well. However, here the situation is more complicated as the magnetic properties of the soft layer vary with bilayer number N . First, a steady increase of the coercive field was found with increase of the number of bilayers in the stack from 5 to 16, but then levels off for larger bilayer numbers. The latter can be attributed to an increase of the amount of structural defects with bilayer

number affecting the Co/Pt interface quality and thus resulting eventually in an overall reduction of the magnetic anisotropy [131-133]. In addition, we observed an increase of the saturation field of the soft layer (see Fig. 63) which is mainly related to the intrinsic properties of the Co/Pt multilayer films where specific domain patterns (i.e. bubble domains) are stabilized with increasing bilayer number [135-136]. Furthermore, the exchange coupled hard layer will have an impact on the switching field of the soft layer which is attributed to the magnetic hardening of the soft layer via interlayer exchange coupling which will be discussed in more detail in the micromagnetic simulation part.

To influence directly on the interlayer exchange coupling between the hard and soft layers, an additional RTA step (450°C for 10 sec) was applied to the FePtCu/[Co/Pt]_N sample series to induce intermixing at interface. The corresponding out-of-plane hysteresis loops are included in Fig. 63 (open symbols). It is important to mention that the applied RTA process does not affect the magnetic properties of the hard layer at all, however, the atomic diffusions are supposed to be initiated at the interface therefore the change of interlayer exchange coupling as well as the magnetic anisotropy at the interface are expected. Similar to the previous observation on the as-grown samples (Fig. 63, solid symbols), two-step hysteresis loops are observed for samples with $N \leq 16$. However, a pronounced further reduction of the switching field, $\mu_0 H_0^{\text{hard}}$, is achieved that indicates the improved interlayer exchange coupling after the RTA process (Fig. 64). At the same time, the switching field of the soft layer increases compared to the initial exchange spring media. It is important to note that the anisotropy field of the exchange spring media after the RTA process is still 4.4 T which is only slightly lowered compared to the

single FePtCu alloy layer (4.5 T). The latter confirms that the presence of the soft magnetic layer does not degrade the thermal stability of the hard magnetic layer as was originally suggested by Suess et al. [111].

- Microstructure Investigation

As a collaboration with TU Chemnitz, we have investigated the microstructures of an exchange spring media composed of FePtCu hard layer and [Co/Pt]_N soft layer by nanoanalytical electron microscopic investigations. Comparing the as grown specimen with a specimen treated by rapid thermal annealing (RTA), the switching field of the FePtCu single phase specimen is enlarged, whereas that of the FePtCu/[Co/Pt]_N exchange spring structure was reduced. From experiments, the switching field reduction by RTA treatment was observed. TEM investigations were performed on the as-prepared and RTA treated specimen using a FEI TECNAI F20 with a field emission gun operated at 200 keV equipped with an annular scanning-TEM (STEM) detector and an energy dispersive spectroscopy (EDS) detector. The energy filtered TEM (EFTEM) experiments were carried out using a Gatan Image Filter (GIF) system. Both plan-view and cross-section TEM samples were prepared by a conventional method: mechanical polishing with SiC paper followed by 4 kV Ar⁺ ion milling process. The ion milling process was finalized by 1 kV to reduce the ion beam damages.

The plan-view BF images and their corresponding selective area diffraction patterns (SADP) are shown in Fig. 65. After RTA treatment, stronger Moiré fringes appear and the SADPs are turned from circles into arcs, which means that the film texture

development of the (001) FePtCu L1₀ and (111) [Co/Pt] multilayer was strengthened after RTA treatment. The diffraction rings of the as-prepared specimen and the RTA treated one are shown in Fig. 65(c) and Fig. 65(d), respectively. The rings show the typical ring spacing associated with face-centered-cubic (fcc) Pt structure overlapped with the face-centered-tetragonal (fct) FePtCu structure. Both structures have very strong (111) and (200) rings located very closely to each other. The presence of the FePtCu (110) ring proves that the FePtCu layer is exhibiting the L1₀ phase. The (111) rings reveal a double-ring structure consisted with those from FePtCu and Pt [137-138]. Due to the implementation of copper, the lattice parameters of FePtCu are found to be $a = 0.3895$ nm and $c = 0.3580$ nm. As expected, these values are different from those of the known lattice parameters of the binary FePt L1₀ phase, $a = 0.3852$ and $c = 0.3713$ nm [106, 139]. After RTA treatment, the lattice parameters slightly change to $a = 0.3894$ nm and $c = 0.3582$ nm, which is in the error range of the setup.

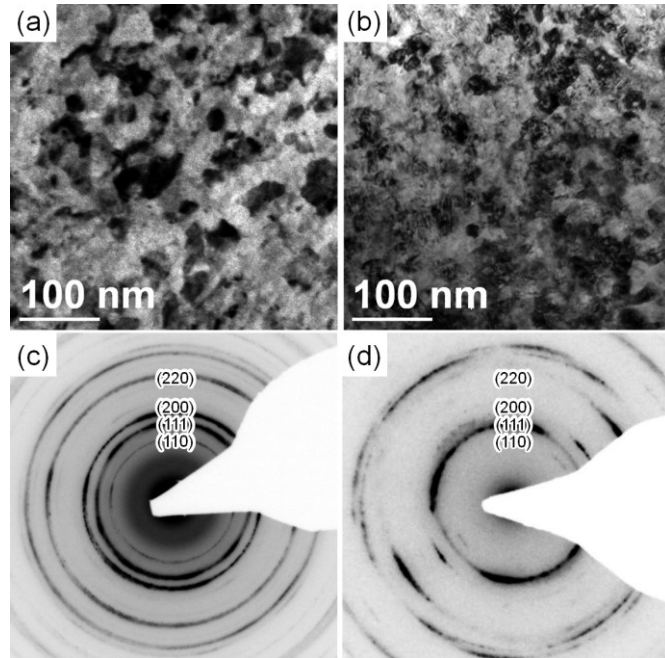


Fig. 65. Bright field images of the (a) as-prepared and (b) RTA treated FePtCu/[Co/Pt]₁₆ exchange coupled composite, with selective area diffraction patterns of (c) as-prepared and (d) RTA treated specimen.

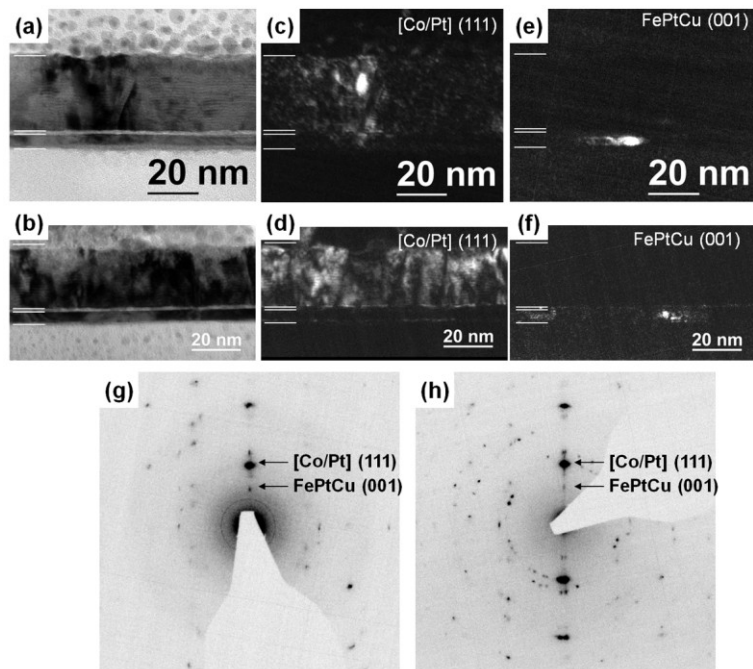


Fig. 66. Cross sectional images of as-prepared (a, c, e) and RTA treated (b, d, f) specimens with their SADPs (g, h), respectively. (c) and (d) shows the dark field images of [Co/Pt] (111), and (e) and (f) shows the dark field images of FePtCu (001).

Since our specimens are composed of many layers, it is not easy to distinguish the individual grains of the FePtCu layer from those of the [Co/Pt] multilayer by plan-view images. Hence, the crystal structure of the grains can be understood by the cross-sectional SADP analysis. Fig. 66 shows the bright field images and dark field images of as-prepared and RTA treated specimens with its corresponding SADPs. The bright field images clearly show the FePtCu hard layer and [Co/Pt] multilayer with a thin bright interlayer between them. From the energy filtered TEM (EFTEM) experiment shown in Fig. 4(e), the interlayer is found to be an iron oxide layer possibly formed when the sample was removed from the vacuum chamber to ambient condition. In the dark field images of the as-prepared specimen the interlayer belongs to the [Co/Pt] multilayer, not to the FePtCu hard layer. RTA treatment turned it to be fct structure as shown in Fig. 66(f), with a very sharp crystal structure transition to the [Co/Pt] (111) surface normal in the soft layer at the hard/soft phase boundary as found in Fig. 66(d). The RTA treatment induced change in the crystal structure is more evident in high resolution TEM (HRTEM).

In Fig. 67(a), the HRTEM image of the as-prepared specimen, the interlayer has a crystal structure close to one of the Co/Pt multilayers with a (111) normal. On the other hand, in Fig. 67(b), the lattice fringes of the interlayer are very similar to that of the FePtCu hard layer. This change is also observed by the reduced fast Fourier transform (FFT) images. The ordered fct structures show bright spots in the direction perpendicular to the surface normal, as indicated with long arrows. However, the disordered (111) textured fcc-like structures show distorted hexagonal spot patterns. Since the RTA process was performed only for 10 seconds, usually it is considered that the time was not

enough to induce phase transformation from disordered state to ordered state[140]. Nevertheless recently it is reported that phase transformation is reinforced under appropriate residual stress and/or strain [141]. The presence of the fct ordered phase under the oxide layer might have applied adequate stress to induce phase transformation during RTA treatment.

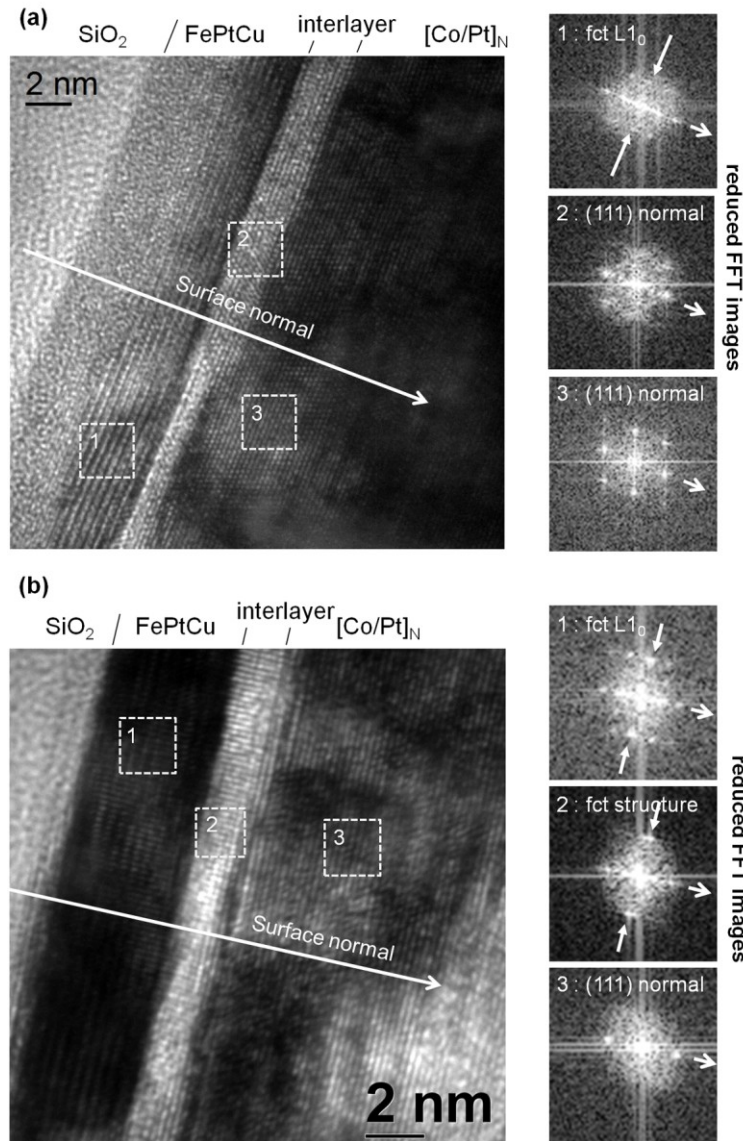


Fig. 67. High resolution cross sectional images of the (a) as-prepared and (b) RTA treated specimen. The reduced FFT images are corresponding to the squares marked on the high resolution images.

In order to find out the changes of the chemical compositions near the interface, EDS line scans were performed on STEM mode as shown in Fig. 68. A part of Co/Pt multilayer of the as-prepared specimen is lost during the TEM sample preparation process. All EDS line scan data are normalized to find out relative changes as a function of the position on the specimen. Since the intensity of the EDS spectrum and HAADF signal is also sensitive to the thickness, we should be very careful in the analysis of the EDS spectra. The HAADF signal amplitudes are decaying in the [Co/Pt] multilayer as the position is going further from the substrate in the as-prepared specimen and vice versa in the RTA treated specimen. These dependencies are thought to be related to the influence of TEM sample thickness. A certain amount of Fe and Co diffusion into the opposite layer is observed, but it happened in both specimens that it is hard to tell that more Fe and Co atoms are diffused by RTA treatment. Therefore, Fe and Co diffusion seem not to be sufficient evidences to explain the enhanced interlayer exchange coupling by RTA treatment. Please note that the Cu diffusion into the Co/Pt multilayer after RTA treatment is predominant compared with the Fe spectrum in the same region. Since the Cu atoms might also play an important role in enhancing FePt L1₀ ordering, Cu diffusion gives another explanation for us why interlayer crystallization was achieved by RTA treatment[106].

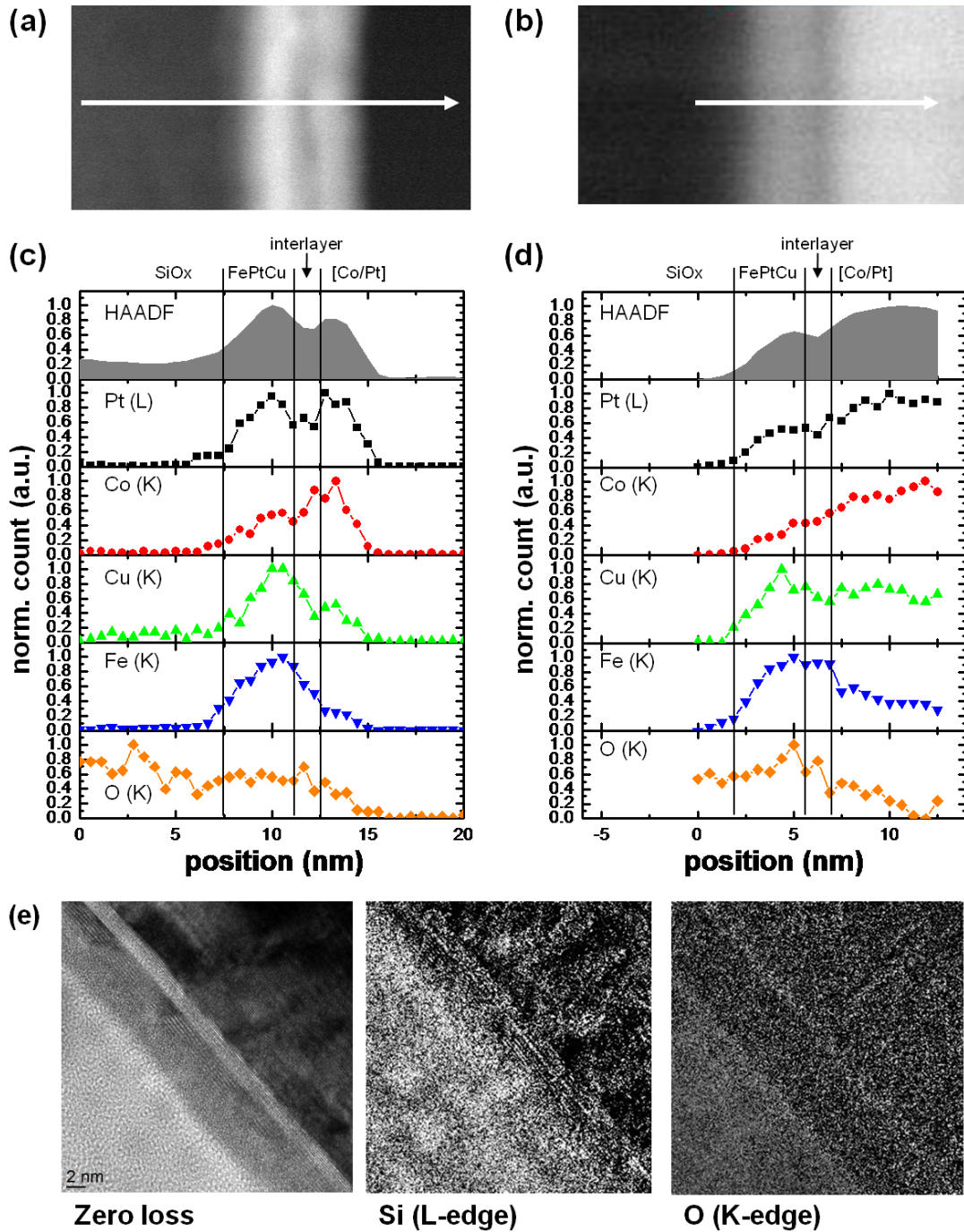


Fig. 68. Chemical analysis results using (a~d) EDS line scan on STEM and (e) EFTEM element map. (a) and (c) are the STEM HAADF image of as-prepared specimen, where (b) and (d) are those of RTA treated one.

- Micromagnetic Simulations

In order to get a better understanding of the coupling phenomena in the complex exchange spring media system, micromagnetic simulations were performed using a finite element model for a two-layer stacked cylindrical nanostructure with a diameter of 10 nm (Fig. 69a). Note that as we consider a single nanostructure instead of a continuous layer, the propagation of the magnetic domain walls in lateral direction is not taken into account. The magnetic properties of the model structure were taken from experimental data using $M_S^{\text{hard}} = 0.68$ T, $M_S^{\text{soft}} = 0.63$ T, and $K_{\text{hard}} = 1.4$ MJ/m³. The thickness of the hard layer was fixed to 5 nm where that of the soft layer is varied from 0 to 25 nm. The magnetic anisotropy of the soft layer K_{soft} was varied from 0.3 to 0.5 MJ/m³ to account for the modification of magnetic anisotropy with varying number of bilayers as observed experimentally. The bulk exchange constant was set to 10 pJ/m for both layers while the interlayer exchange constant, A_{int} , was varied between 0.01 and 10 pJ/m including the magnetostatic interaction between the two layers. The external field was applied by a rate of 0.1 GHz with a Gilbert damping constant $\alpha = 0.1$, which is slow enough to suppress precessional switching.

The magnetization curves obtained from the micromagnetic simulations for two different values of K_{soft} , 0.3 and 0.35 MJ/m³, are shown in Fig. 70a and Fig. 70b, respectively. The interlayer exchange constant A_{int} was set to 2 pJ/m, which corresponds to 20 % of the bulk exchange constant. In both cases $\mu_0 H_0^{\text{hard}}$ is substantially reduced by introducing an exchange coupled soft layer which further decreases with increase of the soft layer thickness as observed experimentally (Fig. 63). By increasing the magnetic anisotropy of the soft layer, the two-step reversal behavior vanishes forming a single step

reversal (Fig. 70b). Therefore, the experimentally observed reversal behavior of the exchange spring media can be attributed to the magnetic hardening of the multilayers with increasing bilayer number. In addition, a series of hysteresis loops was simulated for various interlayer coupling strengths A_{int} keeping $K_{\text{soft}} = 0.3 \text{ MJ/m}^3$ fixed (Fig. 70b). The switching field of the soft and the hard layer as a function of the interlayer exchange coefficient was analytically explained by Richter and Dobin [142]. The analysis of the shape of the hysteresis loops shows that with increasing interlayer exchange coupling ($A_{\text{int}} \geq 3 \text{ pJ/m}$) the switching field $\mu_0 H_0^{\text{hard}}$ of the hard layer is further reduced while the soft layer becomes gradually harder, until the bilayer structure starts to reverse as a single layer. A similar behavior was found experimentally after the RTA process which is expected to induce a stronger interlayer coupling (Fig. 63).

To cover the full dependence of the switching field of the hard layer on the interlayer exchange coupling strength and the thickness of the soft layer using $K_{\text{soft}} = 0.4 \text{ MJ/m}^3$ and $K_{\text{hard}} = 1.4 \text{ MJ/m}^3$, the switching field, $\mu_0 H_0^{\text{hard}}$, was calculated and the results are summarized in the contour map of Fig. 70c. The data include the already discussed special cases presented in Fig. 70a and Fig. 70c. For a weak interlayer exchange coupling ($A_{\text{int}} \leq 0.3 \text{ pJ/m}$), the soft layer thickness does not influence the switching field of the hard layer. However, $\mu_0 H_0^{\text{hard}}$ drops substantially with the increase of the coupling strength. Hereby, the hysteresis loops show a gradual transition from a two-step loop to a single-step one as expected. The transition boundary separating the two cases is marked with a dashed line, which depends on the magnetic anisotropy of the soft layer.

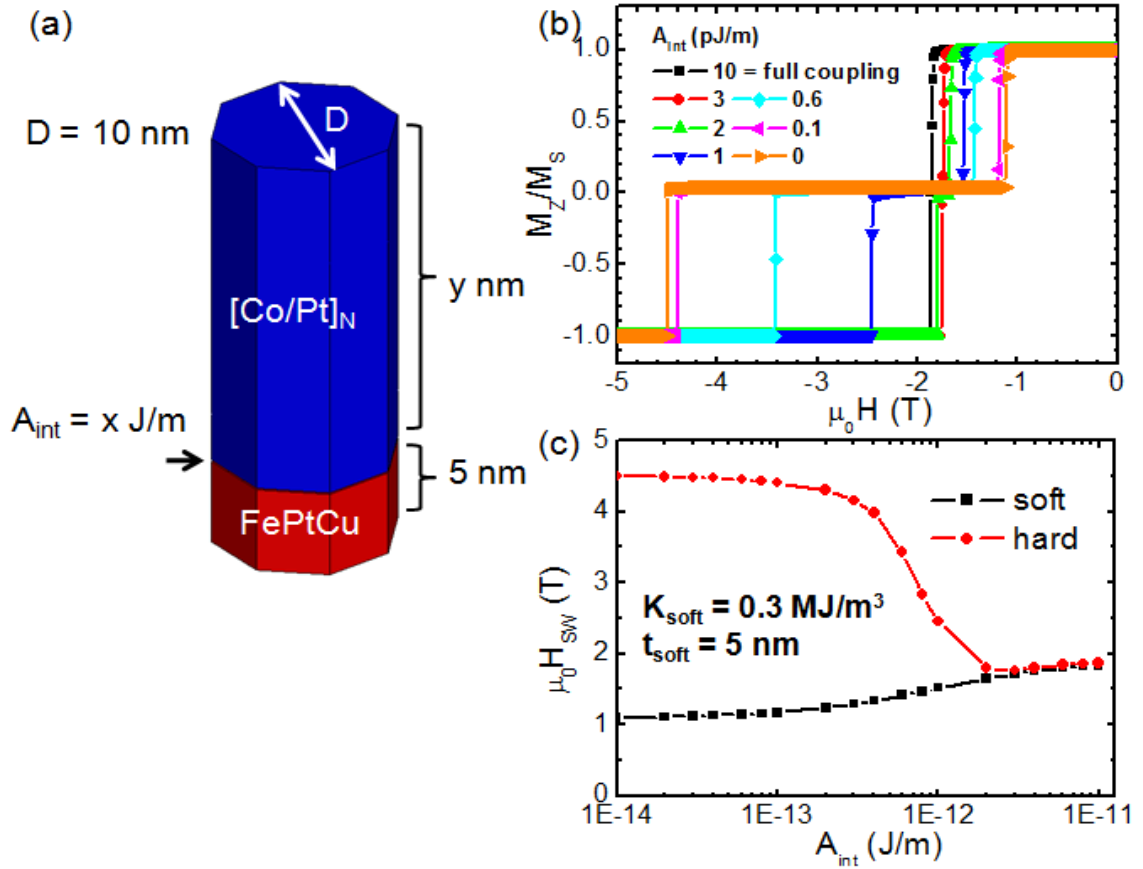


Fig. 69. (a) Finite element model for micromagnetic simulation. (b) M-H curves with varied interlayer exchange constants, A_{int} , keeping $K_{\text{soft}} = 0.3 \text{ MJ/m}^3$ and $t_{\text{soft}} = 5 \text{ nm}$ fixed. (c) Switching field of the soft and hard layer as a function of the interlayer exchange constant.

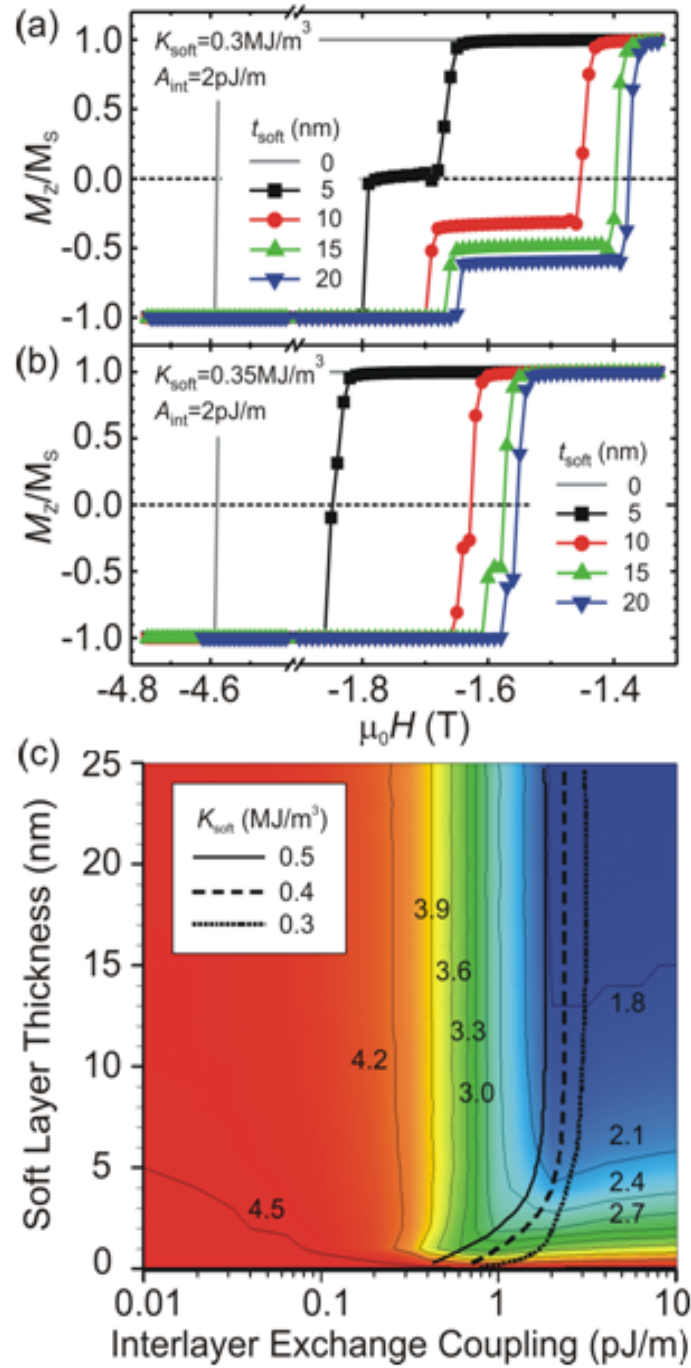


Fig. 70. Calculated M-H curves of exchange spring media using different soft layer thicknesses, t_{soft} , for (a) $K_{\text{soft}} = 0.3 \text{ MJ/m}^3$ and (b) $K_{\text{soft}} = 0.35 \text{ MJ/m}^3$. (c) Contour map of the hard layer switching field $\mu_0 H_0 \text{hard}$ as a function of the interlayer exchange constant and the soft layer thickness keeping $K_{\text{soft}} = 0.4 \text{ MJ/m}^3$ fixed. The phase boundary between the two-step loop to a single-step reversal of the EEC media is marked with a dashed line. Phase boundaries for $K_{\text{soft}} = 0.3 \text{ MJ/m}^3$ (dotted line) and 0.5 MJ/m^3 (solid line) are also shown.

- Conclusion

In conclusion, we realized an exchange spring media which consist of a hard FePtCu alloy film and softer $[\text{Co/Pt}]_N$ multilayer stack revealing an out-of plane easy axis of magnetization. We demonstrated experimentally that the switching field could be efficiently reduced by increasing the thickness of the soft magnetic layer. In addition, an applied RTA process performed on the FePtCu/ $[\text{Co/Pt}]_N$ stack enhances directly the interlayer exchange coupling and thus reduces further the switching field of the hard layer. From the microstructure investigation using TEM, it was found that a gentle RTA treatment has changed two main features of the microstructures: one is the crystalline structure of the iron oxide interlayer, and the other is the Cu diffusion into the soft layer. The iron oxide interlayer has transformed from a fcc-like structure with (111) surface normal into a fct-like structure with (001) surface normal texture. This phase transformation is believed to be enhanced by the residual stress in the interlayer and the Cu diffusion. The performed micromagnetic simulation study has clearly revealed the key ingredients to reduce the switching field in an exchange spring media: (i) Enhancement of the interlayer exchange coupling, which can be further adjusted by proper insertion of interlayers forming a graded media; and (ii) employing thicker soft layers with adjusted magnetic anisotropy which reduces the domain nucleation field of the soft layer. These aspects are of great importance for the design point of exchange spring media.

(6) FePt L1₀ / FePt A1 Graded Media

A FePt L1₀ phase based exchange coupled composite and graded media has been suggested to achieve the areal density beyond 1 Tbit/in² with still high thermal stability [111, 113]. The suggested structure of graded media is a stack of thin magnetic layers of which magnetic properties, mainly anisotropy constant is gradually reduced to lower the nucleation field[9]. Since the concept of the graded media has published, there have been many experimental demonstrations, for example, FePt(L1₀)/Fe, FePtCu/[Co/Pt]_N, FePt-TiO₂/CoPt-TiO₂ and FePt/CoPt systems [78, 107, 116, 143-144]. The switching fields of the systems were reduced to half of the hard magnet by introducing the soft layer, however, the theoretically predicted reduction by a factor of 10 with less than 20 nm of graded layer has not achieved yet [111, 119]. The researchers have tried to solve the problem by interface mixing using post-annealing [78, 107, 116, 143]. In its stead we have proposed a new concept of graded media: single material but various phases, utilizing phase transition process. In this chapter we are going to present the microstructures and micromagnetic simulation results of the FePt L1₀/A1 graded media.

According to the phase diagram of Fe-Pt alloy, Fe_xPt_{1-x} alloy has two stable structures when x is close to 0.5: one is disordered fcc A1 phase, the other is ordered fct L1₀ phase (Fig. 71). They have different material parameters: $a_{L10} = 0.3852\text{nm}$, $c_{L10} = 0.3713\text{ nm}$ and $a_{A1} = 0.382\text{ nm}$ [106, 145-146]. In Fig. 71 the fcc phase is supposed to be appeared if only the temperature is higher than 1300 °C in bulk specimen. But if the FePt film is grown on substrate by film deposition methods, for example, DC magnetron sputtering, fcc phase is formed on Si substrate at room temperature and fct phase is

obtained on MgO substrate if the temperature is high enough. The temperature for fct phase growth on MgO substrate is found to be 700°C [147]. According to Hsiao et al, the degree of ordering is decreasing as the substrate temperature decreases. It is known that FePt L₁₀ is the representative hard magnet whereas the fcc structure has a very low crystalline anisotropy [77, 148-149].

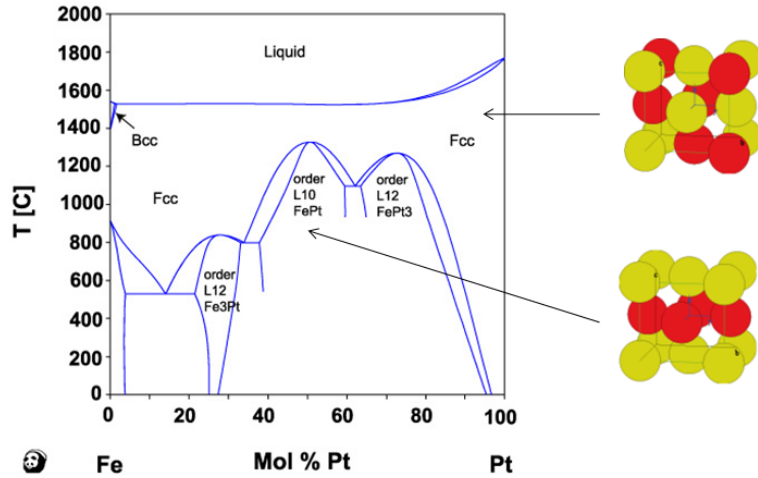


Fig. 71. Phase diagram of FePt. L₁₀ ordered phase is to be formed if the portion of Fe and Pt are comparable [150].

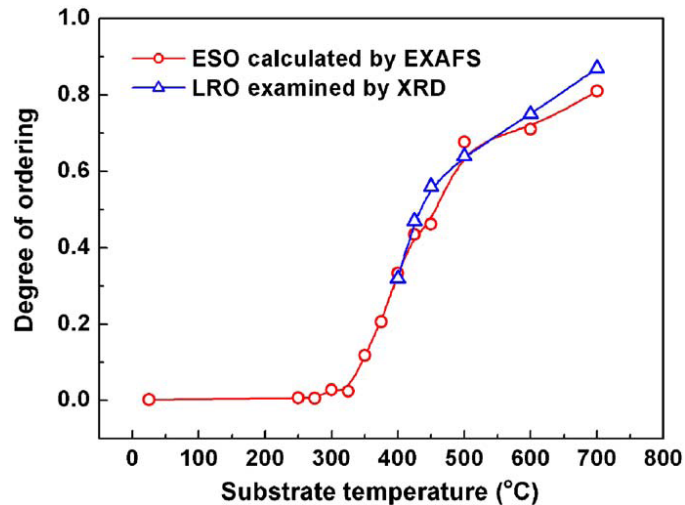


Fig. 72. calculated ESO curve using Fe edge of EXAFS showing the variation of ESO versus substrate temperature. The results of ordering parameter examined by XRD are superimposed [147].

- Experiments with XRD analysis (by NCSR “D”, Greece)

We have worked with (001) textured MgO substrates on which FePt can be grown with (001) orientation, i.e., with the c-axis, the easy anisotropy axis, of the tetragonal phase perpendicular to the film plane. At first a single phase L1₀ FePt layer with high coercive field H_c and perpendicular to the film plane magnetic anisotropy was deposited on the MgO substrate at 700 °C. The next step was the growth of the graded L1₀ to A1 FePt layer on top of the magnetically hard L1₀ FePt layer. This is done by keeping the same sputtering conditions except that the substrate temperature was varied during deposition from 700 down to 280 °C. This produces a monotonic gradient of the anisotropy constant through the thickness of the layer. Here we report on the structural and magnetic properties of these hard/graded ESM. Our results show that the switching field of the composite media is significantly reduced compared with those of the single hard phase media, verifying the theoretical calculations.

We have used a Cooke magnetron sputtering system with an Ar pressure of 3 mTorr and a base pressure of 5×10^{-8} Torr. The first step was the growth of a hard layer with perpendicular magnetic anisotropy. To this end we used (001) textured MgO substrates, on which an 11.5-nm-thick layer of FePt is deposited. The transformation of as-deposited magnetically soft (A1) FePt cubic phase to the tetragonal phase (L1₀) is carried out by deposition of the FePt layer at $T_D = 700$ °C. Under these deposition conditions FePt can be grown with (001) orientation [151], ensuring that the easy axis of magnetization, which coincides with the crystallographic c-axis, is perpendicular to the film plane.

The next step was the growth of the graded layer on the hard layer, which gradually becomes softer as the deposition temperature is reduced. The substrate temperature affects the structural transformation of FePt and thus changes the chemical order parameter. The magnetic anisotropy of FePt is strongly correlated with the crystal structure, so any change of chemical order should produce a corresponding change of the anisotropy field through the thickness of the layer. It is through this mechanism that we control the samples' magnetic characteristics. After the deposition of the hard layer (thickness of 11.5 nm) at 700 °C, the graded layer is deposited by ramping the substrate temperature from an initial temperature $T_{DI}=700$ °C to a final temperature T_{DF} which varies from 600 to 280 °C. The deposition continues uninterrupted throughout the whole process.

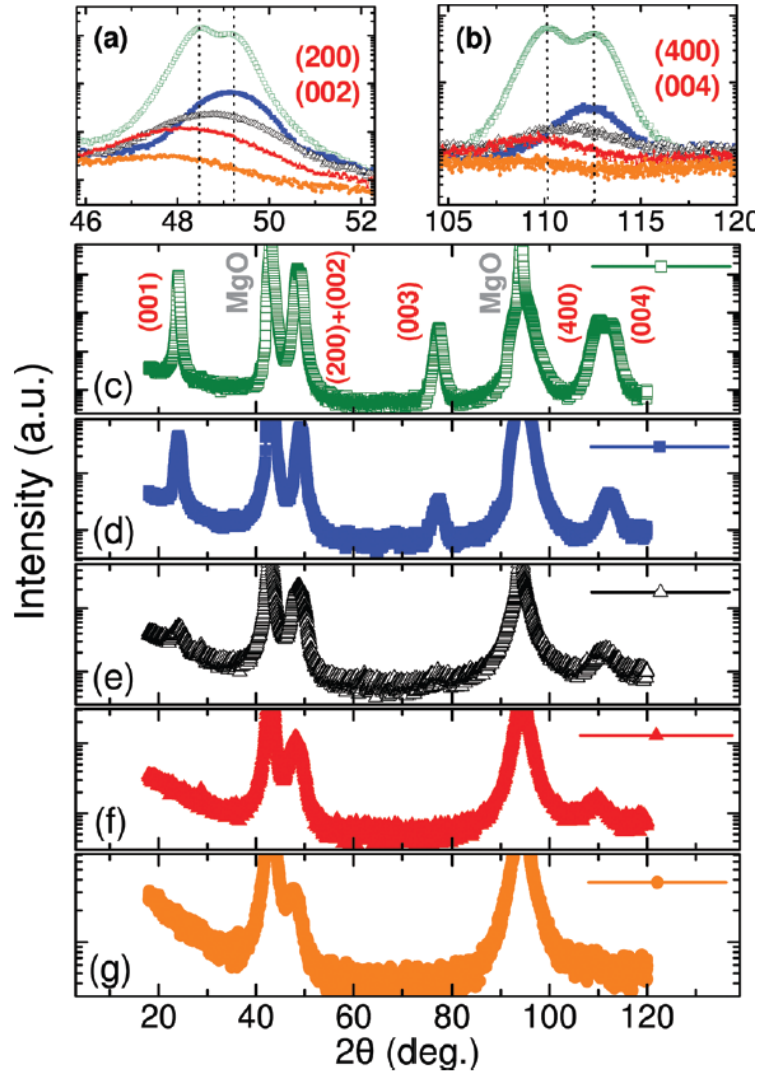


Fig. 73. (a) Magnifications of the double diffraction peaks (200) and (002) and (b) the (400) and (004) diffraction peaks of the hard(11.5 nm)FePt(L1₀)/graded(30 nm)FePt(L1₀ to A1) composite; dotted lines indicate the positions of the peaks. X-ray spectrum of (c) hard(11.5 nm)/graded(30 nm) composite and 5 nm single layers deposited at different temperatures (d) 600, (e) 450, (f) 300 °C, and (g) RT.

Except for the substrate deposition temperature T_D , the growth conditions were identical with those used for the hard layer deposition. X-ray diffraction spectra and rocking curves were collected with a SIEMENS D500 powder diffractometer using Cu K_α radiation. Magnetization measurements were performed with a Quantum Design

superconducting quantum interference device magnetometer. For the AFM studies we used an NT–MDT company scanning probe microscope in semicontact mode.

In order to obtain a better knowledge of the formation of the hard/graded system of FePt, we first examined single FePt layers with a thickness of 5 nm deposited at different temperatures (Fig. 73). The as-deposited FePt forms in the cubic phase with (200) texture. For samples annealed at temperatures lower than 400 °C, the (400) fundamental peak appears, in addition to the (200) peak, indicating that FePt remains in fcc structure, but with improved texture, as rocking curve measurements verify (Fig. 74). At 450 °C we observe the (001) reflection, which is present only for the tetragonal phase of FePt. Also there is a significant shift of the (200) and (400) reflections to higher angles, to the positions of the (002) and (004) superlattice reflections. Both observations reveal that the transformation to the tetragonal phase has initiated. At higher deposition temperatures one more superlattice peak, (003), is observed. Rocking curves showed that the film growth is highly oriented (Fig. 74), with the desired (001) texture. AFM investigations (Fig. 75) reveal columnar growth of the hard layer with a grain size of the orders of 100 and 40 nm for the 11.5 and 5 nm films, respectively.

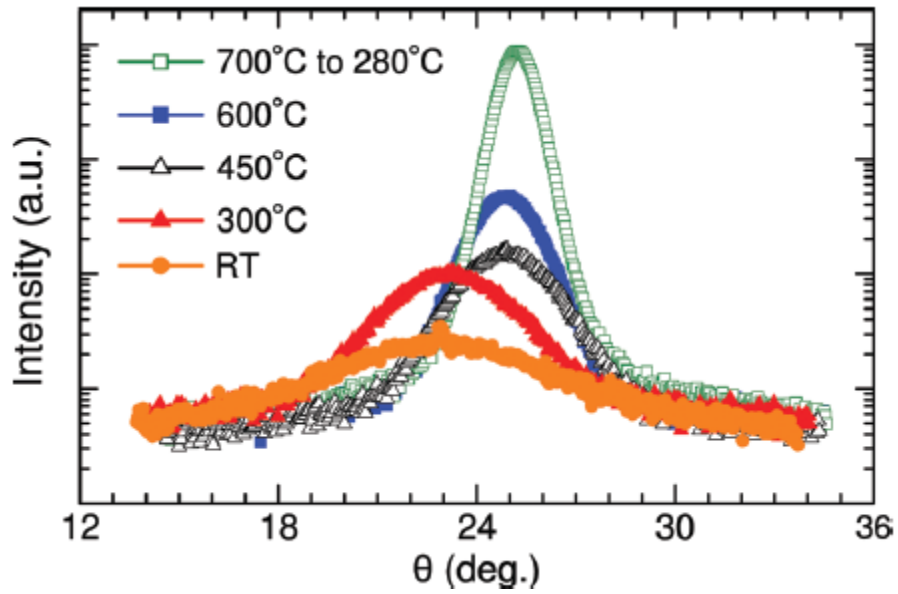


Fig. 74. (002) Rocking curves of hard(11.5 nm)FePt(L_1) / graded(30 nm)FePt(L_1 to A_1) composite (solid squares) and (200) rocking curves of 5nm single layers deposited at layers deposited at different temperatures 600 °C (open squares), 450 °C (open triangles), 300 °C (solid triangles), and RT (solid circles). The scale of intensity axis is logarithmic.

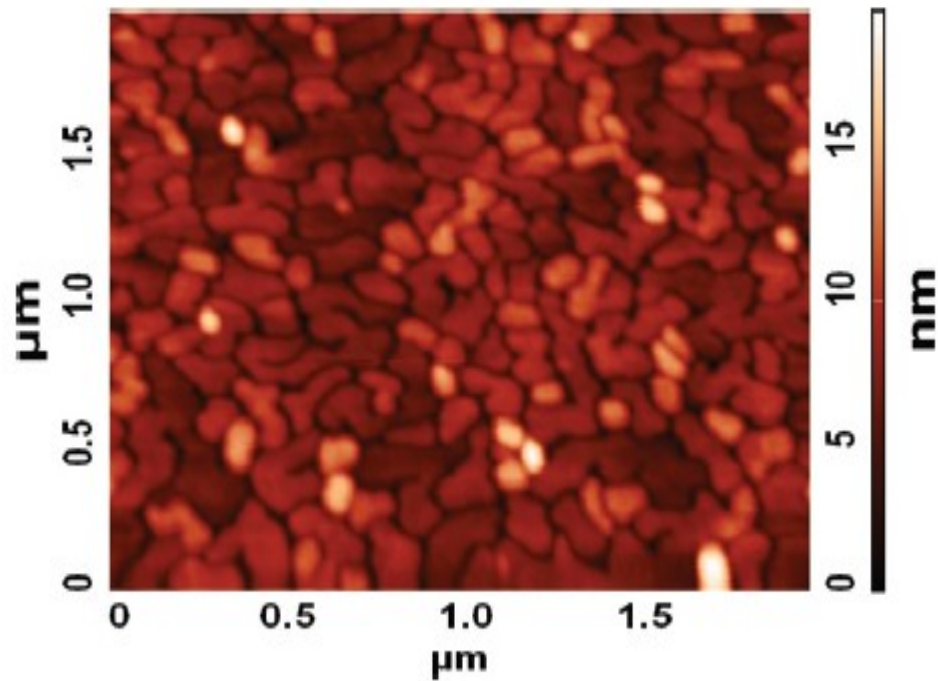


Fig. 75. AFM image of 11.5 nm single hard FePt (L_1) layer deposited at 700 °C.

After the deposition of the graded layer, the texture of the same (001) reflections as those of the hard layer appear. When a thick graded film is deposited, i.e., a thickness $t_g = 30$ nm, at much lower deposition temperatures than the initial temperature of 700 °C, two additional reflections to those of (002) and (004) are observed, as shown in Fig. 73(a) and Fig. 73(b). These peaks correspond to the (200) and (400) fundamental reflections of the A1 phase, revealing a gradual change of the crystal structure from L1₀ to A1. The full-width at half-maximum of all peaks measured by the rocking scans is approximately 1°, indicating a highly oriented film. Typical hysteresis loops of hard(11.5 nm)/graded(t_g nm) exchange spring media and the single hard layer 11.5 nm deposited at 700 °C are shown in Fig. 76. The loops in all cases were measured with the external field perpendicular and parallel to the film plane. We have to emphasize that the coercive field of the hard layer alone is 34 kOe, with the easy magnetization axis shown to be normal to the film plane. The same findings hold for all hard/graded FePt systems described here.

Fig. 77 illustrates the dependence of the coercive field H_c of the hard/graded system on the thickness of the graded layer t_g . In the range $8 \text{ nm} < t_g < 12 \text{ nm}$ the coercive field of the composite is considerably lower than the initial hard layer value of 34 kOe. The coercivity is actually lower than 10 kOe, making the system suitable for magnetic recording applications.

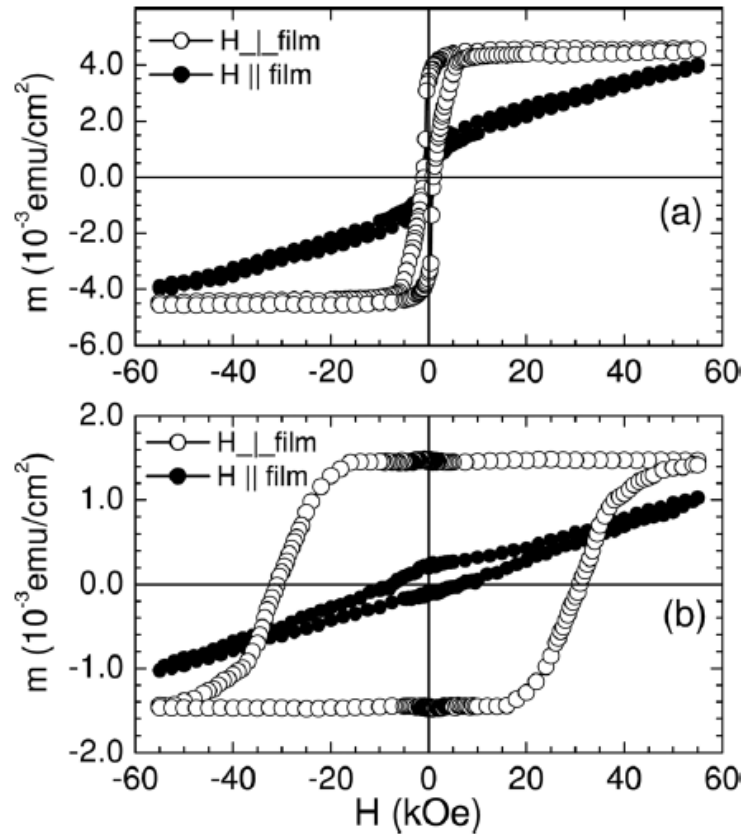


Fig. 76. (a) Hysteresis loops with field parallel (solid symbols) and perpendicular (open symbols) to the film plane of hard(11.5 nm)/graded(12 nm) composite deposited at varying temperature from 700 to 420 °C and (b) a single hard layer 11.5 nm deposited at 700 °C.

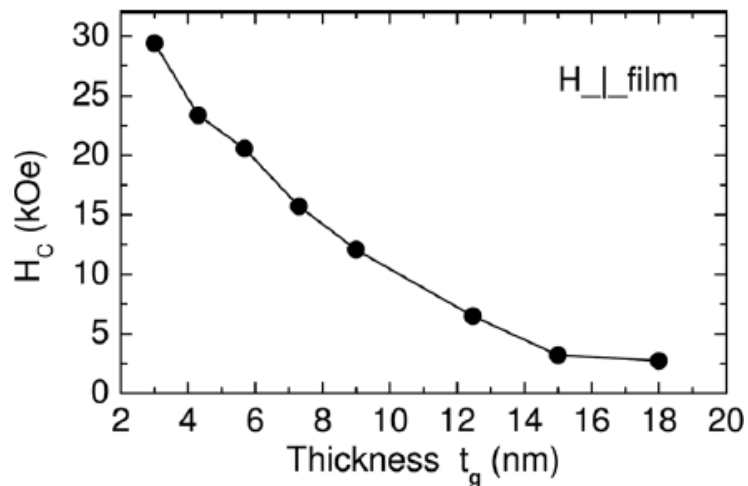


Fig. 77. Dependence of the coercive field H_c of hard(11.5 nm)/graded(t_g nm) system on the thickness of the graded layer t_g .

- Microstructure Investigation using TEM

It is known that the microstructure of FePt alloy is varied by substrate and deposition temperature and stress applied on the substrate [138, 141, 146-147, 152-154]. In this chapter we are going to present the microstructure of FePt films on MgO substrate in various temperatures. TEM samples for FePt films deposited on MgO (001) substrate fabricated by NCSR “D” were prepared using conventional method: sequential SiC paper grinding, diamond sheets polishing, and finally thinned by PIPS. The reason of using conventional method is that the aim of the study is to find out atomic resolution images. Therefore we have chosen the way to minimize damages on the microstructures. At the beginning, we are going to represent a single phase FePt grown on MgO substrate under a single temperature.

1. FePt film grown at 200°C

The cross section images and selective area diffraction images of FePt film grown at 200°C was shown in Fig. 78. The thickness of FePt film is about 17 nm. From the dark field (DF) imaging on the cross section view, most of the film is found to be FePt L₁₀ phase. The selective area diffraction pattern (SADP) on the cross section view reveals that FePt L₁₀ phase exists in the film, however, the presence of A1 phase is not clearly shown due to the overlapping of the peaks with the ones from L₁₀ phase, as shown in Fig. 78(d). In order to find a better evidence for the phase composition, high resolution TEM (HRTEM) image was taken for the cross section, and analyzed using

reduced FFT technique (Fig. 79). The lattice fringes of MgO are clearly shown to from atomic images. FePt grown on top of it is found to be two-phase state. One is $L1_0$ phase found at site 1, with lattice parameters $a = 0.394$ nm and $c = 0.386$ nm. In this case the c/a becomes 0.980 which is close to the known values for bulk FePt $L1_0$ phase, $a = 0.385$ nm and $c = 0.371$ nm, then c/a is 0.964 [155]. Disordered fcc A1 structure was found at site 2, with lattice parameters of $a = c = 0.386$ nm, which also agrees with the bulk value $a = c = 0.382$ nm [155].

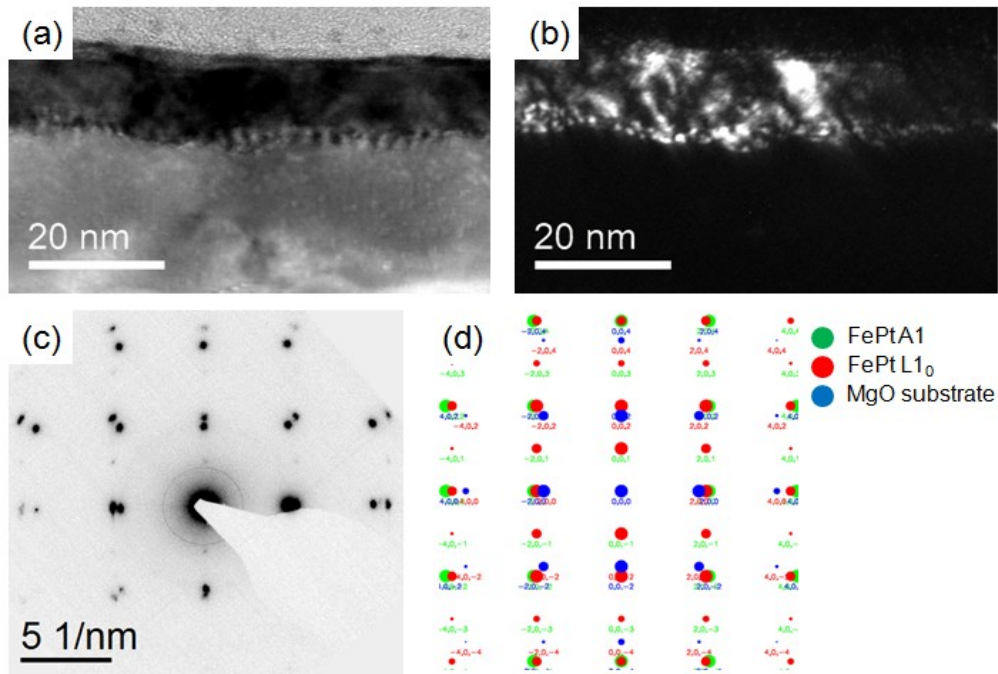


Fig. 78. Cross sectional (a) bright field (BF) image and (b) dark field (DF) image of FePt $L1_0$ (001) plane. Selective area diffraction image (a) taken experimentally and (d) simulation results for the case of FePt A1 phase and FePt $L1_0$ phase coexist.

It is an interesting feature that $L1_0$ phase is found even in the specimen prepared at 200°C . Judged by the fact that the $L1_0$ phase is grown on top of the A1 phase, it is supposed that the formation of A1 phase has reduced the residual stress applied on the

growing film which resulted in a condition for FePt L1₀ phase growth [141]. The interface between MgO substrate and FePt film was not very sharp. Fig. 78(a) shows a wavelike contrast at the substrate/film boundary. HRTEM of the interface has revealed that there are misfit dislocations due to the lattice parameter misfits. As described above, our FePt A1 phase has a lattice parameter of 0.386 nm whereas the MgO substrate has a value of 0.4217 nm. Therefore there is about 10 % of misfit which induced dislocations shown in Fig. 80. Dislocations are marked with yellow arrows.

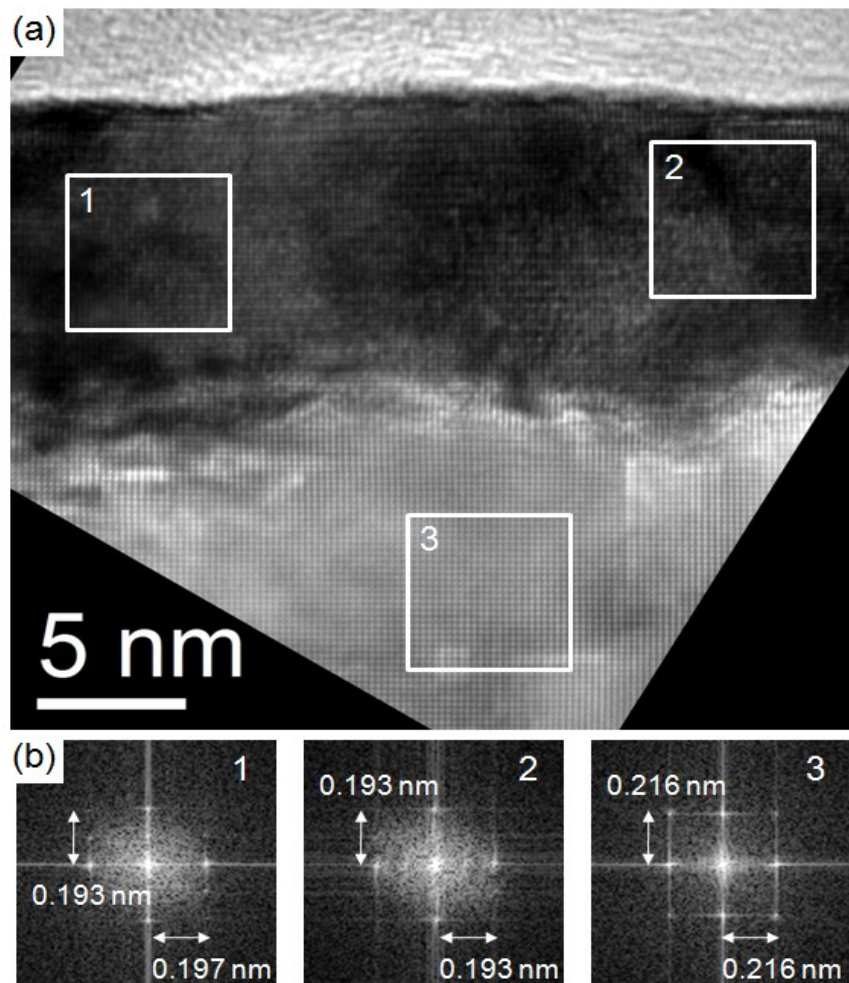


Fig. 79. (a) High resolution TEM (HRTEM) image of FePt film grown at 200°C. (b) Reduced FFT images of each parts in (a). The numbers assigned on each figures correspond to the site marked in (a).

2. FePt film grown at 500°C

Another FePt film deposited at substrate temperature of 500°C was investigated. The relatively low magnification TEM image and its diffraction pattern are shown in Fig. 81. The film has an island-like structure, whereas the specimen grown on 200°C has a continuous film structures. The thickness of the film was measured as about 17 nm. From the selective area diffraction pattern, the peaks correspond to FePt L₁₀ structure are detected. The structure analysis was performed in detail using HRTEM and reduced FFT images (Fig. 82). In Fig. 82, the crystal structure of FePt film grown at 500°C was revealed as L₁₀ phase, at least, mostly.

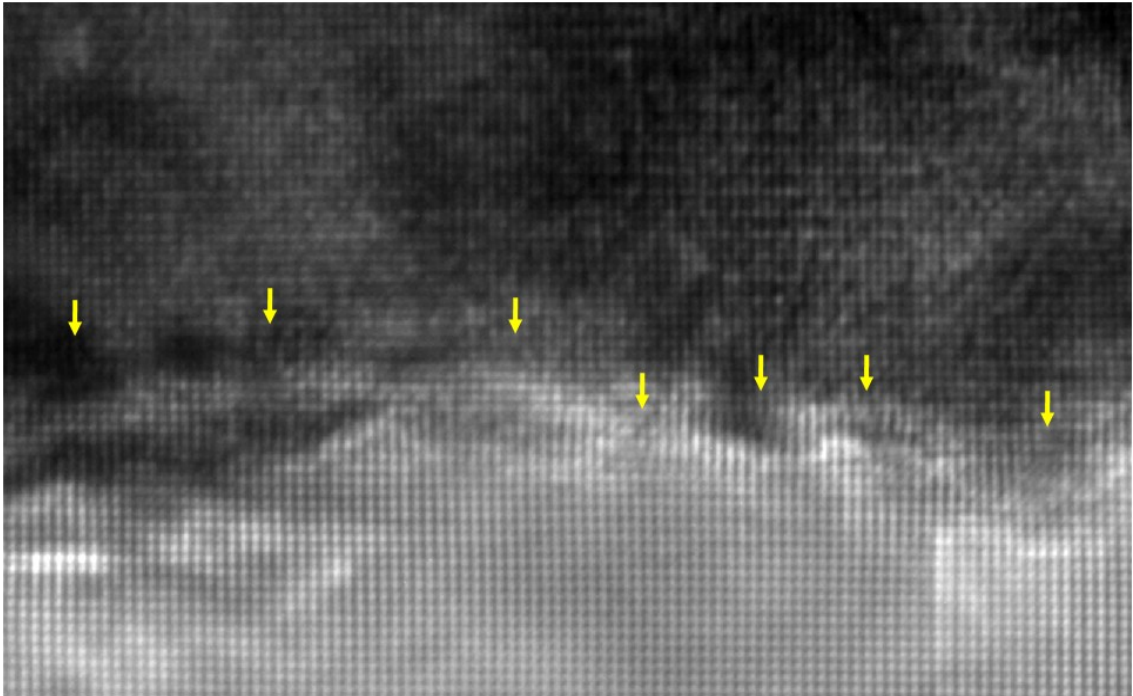


Fig. 80. HRTEM image at the interface between MgO substrate and FePt film.

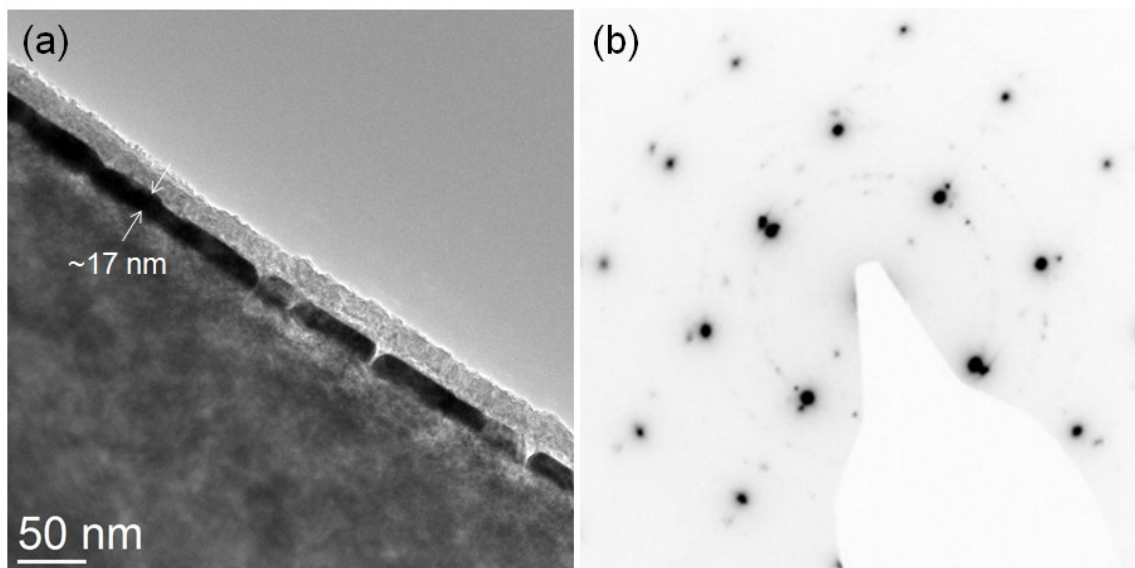


Fig. 81. (a) Relatively low magnification TEM BF image and (b) selective area diffraction pattern.

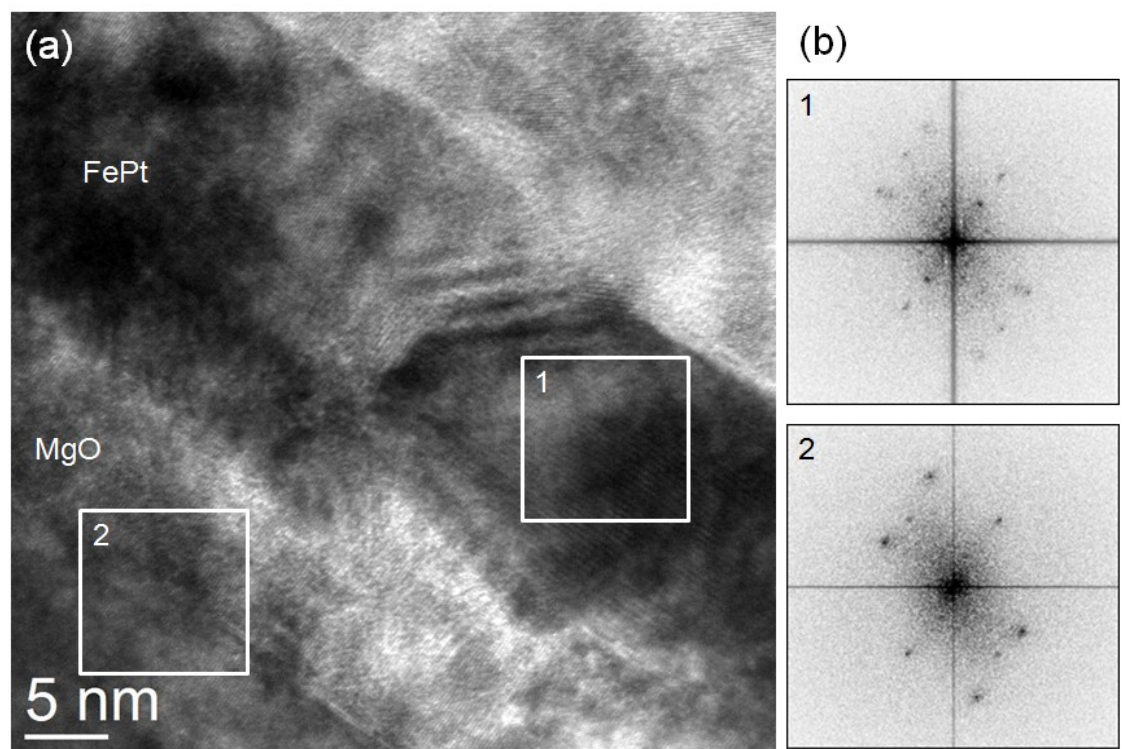


Fig. 82. (a) HRTEM image of the FePt film grown at 500°C, and (b) reduced FFT results of the site 1 and 2.

3. FePt film grown at graded temperature 700 ~ 600°C

Before starting sessions about the microstructures of FePt film prepared under graded temperature, the double diffraction phenomenon should be understood. Double diffraction occurs when a diffracted beam traveling through a crystal is rediffracted either within the same crystal or when it passes into a second crystal. If the initial diffraction vector of the beam is \mathbf{g}_1 and it is rediffracted by reflection \mathbf{g}_2 , then the resultant diffraction vector of the double-diffraction beam is $(\mathbf{g}_1 - \mathbf{g}_2)$. If \mathbf{g}_2 is not an allowed reflection in the first crystal, the double-diffraction beam is characteristic of neither the first nor the second crystal [156].

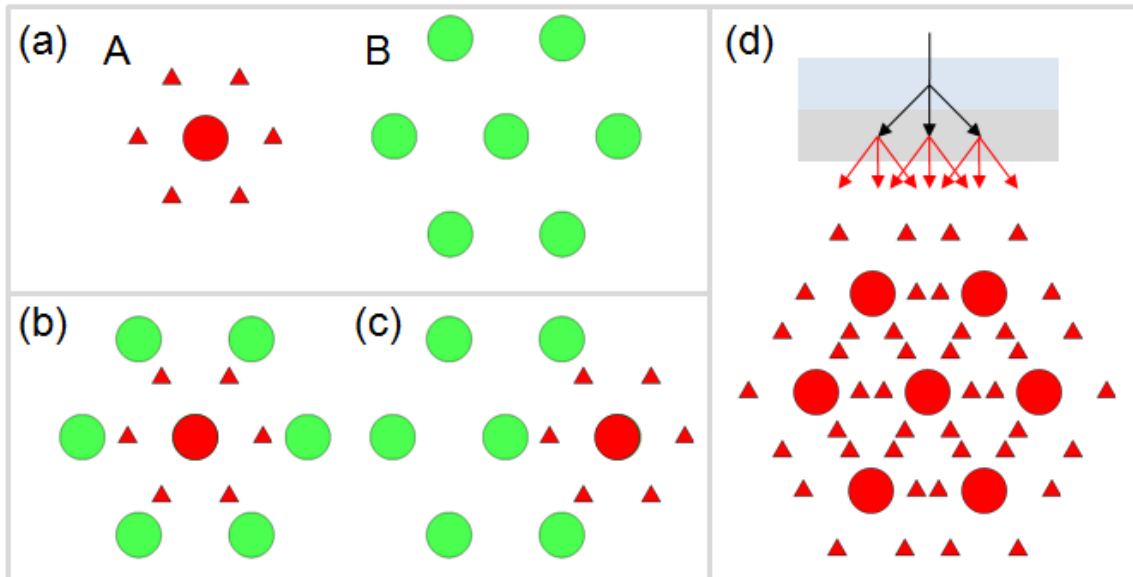


Fig. 83. (a) Diffraction patterns of crystal A and B. (b) Overlapping of the diffraction pattern of A and B for the case of both crystals are diffracted by the common incident beam. (c) Overlapping of the diffraction pattern of A and B for the case of the diffraction of crystal A was occurred by a diffracted beam of crystal B. (d) Schematic diagram of double diffractions.

An example of double diffraction is shown in Fig. 83. Let us assume that there are crystal structure A and B, of which diffraction patterns are as Fig. 83(a). If the crystals coexist, the diffraction pattern appears as a form of overlapped image of them. In many cases, only the incident beam is strong enough to induce diffraction on the other crystal. Therefore diffraction pattern such as Fig. 83(b) is observed. However, for the case of the two crystals exhibit epitaxy, the first diffracted beams also induce second diffractions on the second crystal (double diffraction) such as shown in Fig. 83(c). In experiment we observe the overlapped diffraction patterns from all available sources, hence the diffraction pattern becomes complicated (Fig. 83(d)).

Electron microscopy investigation has performed on FePt $L1_0$ /graded media, of which $L1_0$ phase is deposited at 700°C whereas the temperature for the graded media deposition was varied from 700°C to 600°C . The thickness of the $L1_0$ layer and the graded layer are designed to be 11.5 nm and 10 nm, respectively. Fig. 84 shows the electron microscopy results. The plan view SEM image (Fig. 84(a)) reveals that the shape of the FePt islands is strongly determined by the MgO substrate orientation. The edge of the islands are parallel to (100) and (010) directions of the substrate. The specimen is polished to be a TEM specimen, of which plan view images are shown in Fig. 84(b) and (c), with its SADPs (Fig. 84(d)). Due to the double diffractions, the SADP has a complicated structure of spot patterns. A number of satellite spots are pointed around the main ones.

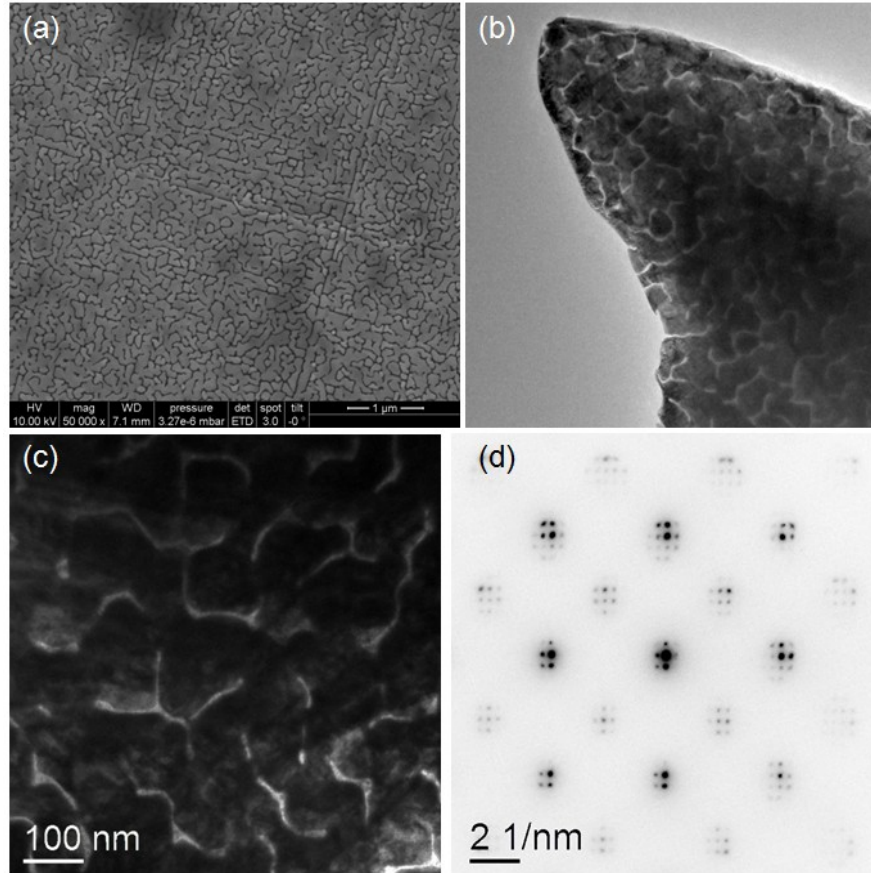


Fig. 84. (a) SEM plan view image of the FePt L10/graded (700°C → 600°C). TEM plan view bright field images (a) relatively lower magnification and (b) relatively high magnification. (d) electron diffraction pattern with a double diffraction.

Cross sectional TEM samples are prepared to observe distribution of the L10 and A1 phases in a bit. Fig. 85 shows (a) bright field image and (b) selective area diffraction patterns comparing with simulation. The experimentally obtained SADPs agree well with the simulations results. The L1₀ phase and A1 phase in FePt films are found by dark field images. In Fig. 85(c) and (d), the bright field represents the A1 phase and L1₀ phase obtained from (2,0,2) and (2,0,1), respectively. By comparing two dark field images, A1 phase is found near the top surface whereas L1₀ phase are located at the inside of the bits. For the purpose of verification, HRTEM images are obtained as shown in Fig. 86(b). The

presence of $L1_0$ and $A1$ phases are proved by reduced FFT images (Fig. 86(c) and (d)). The z-directional lattice parameters are measured as $c_{A1} = 0.380$ nm and $c_{L1_0} = 0.386$ nm. The boundary between the two phases is found by recognizing HRTEM images. Interestingly, the interface is found to be very rough that the height of the $L1_0$ chimney into $A1$ matrix is up to 6 nm. The rough interface structure instead of gradual lattice parameter modification was predicted by Misumi et al. [157]. According to his study using Monte Carlo simulation taking advantage of ab initio method, if the growth temperature is slightly lower than critical temperature for $L1_0$ phase formation, $L1_0$ and $A1$ phases are tend to be co-exist with a few nanometers distance between themselves.

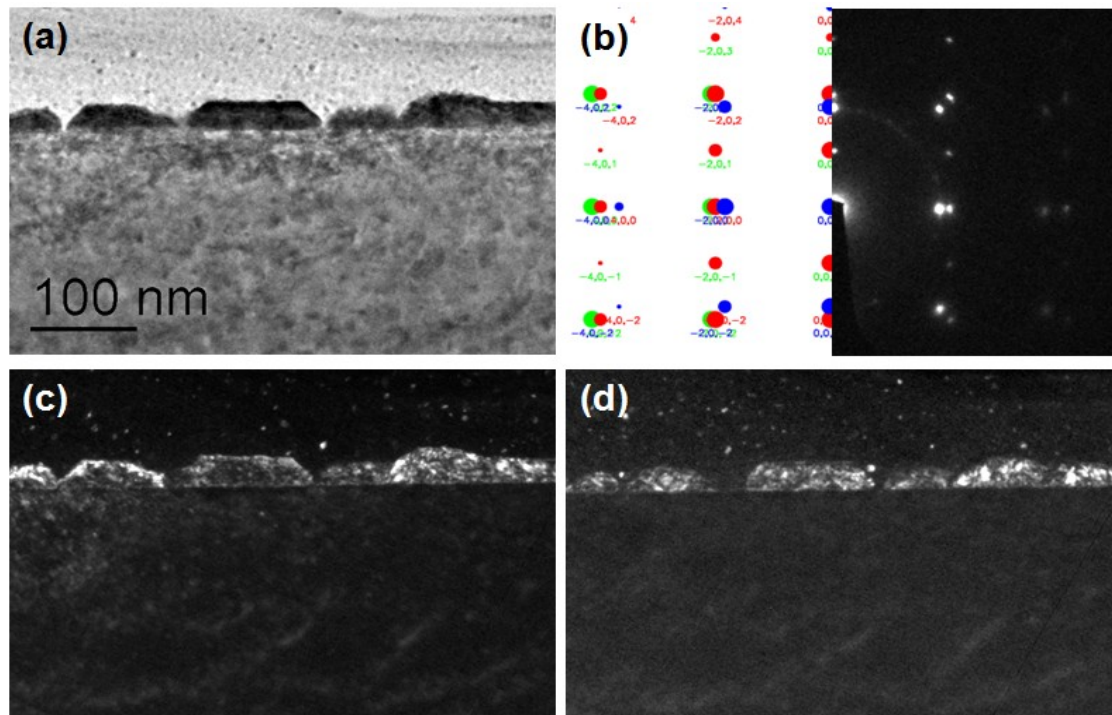


Fig. 85. Cross sectional (a) bright field image and (b) selective area diffraction patterns, comparison between simulation (left) and experiment (right). (c) and (d) represents the dark field images corresponding $A1+L1_0$ (2,0,2) and $L1_0$ (2,0,1), respectively.

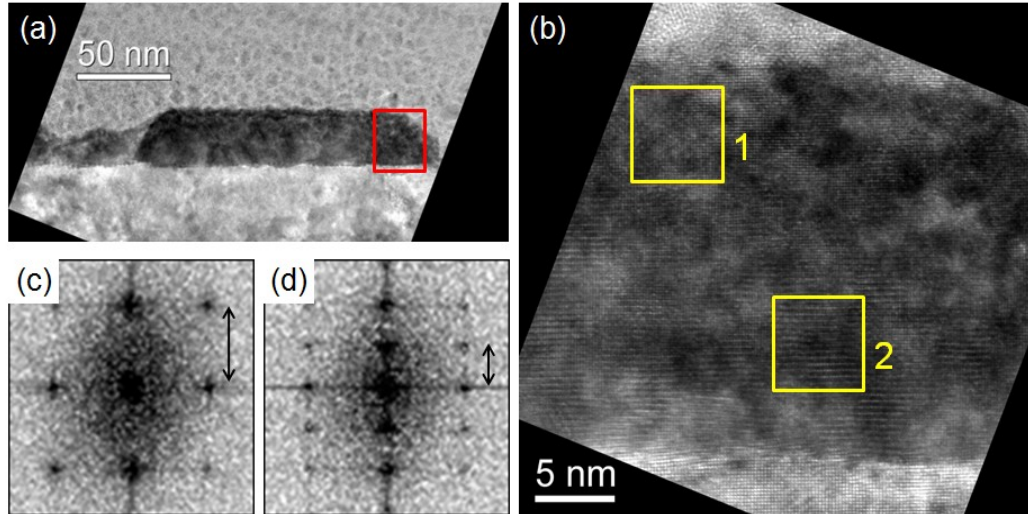


Fig. 86. (a) Cross section image of a single bit and (b) HRTEM image of the marked site in (a). (c) and (d) are the reduced FFT results of site 1 and 2, respectively. The distances marked with an arrow in each figure are (c) 0.190 nm and (d) 0.386 nm, corresponding to (002) and (001) distance of A1 phase and $L1_0$ phase, respectively.

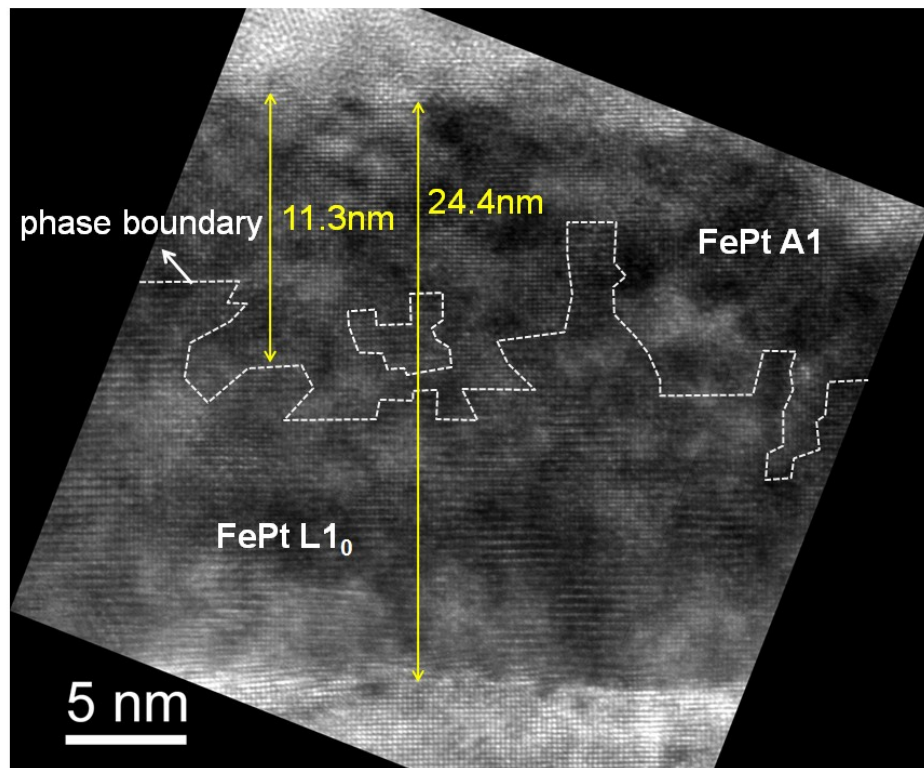


Fig. 87. $L1_0$ phase and A1 phase with the phase boundary between them judged by HRTEM images. The average thickness of the $L1_0$ phase and A1 phase are found to be 13.1 nm and 11.3 nm, respectively.

4. FePt film grown at graded temperature 700 ~ 450°C

In order to find out the influence of the cooling rate on the microstructure of FePt graded layer, the specimen with a structure of MgO (001)/FePt L1₀ (@700°C, 11.5 nm)/FePt graded (@700°C → 450°C, 10 nm) is prepared. Since the temperature reduction is 250°C whereas the previous case is 100°C, the temperature reduction rate was higher by a factor of 2.5. Fig. 88(a) shows the SEM plan view image. The most remarkable difference between the one of the graded media finalized at 600°C is the island shape. Unlike the island shapes shown in Fig. 84(a), the grains deposited in lower temperatures has little coincidence between the grain boundary direction and the film orientations. The irregularity of the grain shape is also proved in TEM bright field images in Fig. 88(b) and Fig. 88(c). In spite of the apparent difference, the SADPs show the same structure compared with the previous one.

The cross section investigation results are shown in Fig. 89. Fig. 89(a) shows the bright field image and Fig. 89(a) its SADP. The spot patterns show clear existence of L1₀ phase. The dark field images corresponding FePt L1₀ + A1 (002), FePt L1₀ (001) and MgO (002) are shown in Fig. 89(b), (c) and (d), respectively. In Fig. 89(b), most of the top layer and also many part of the inside respond to the peak L1₀ + A1 (002) whereas the peak L1₀ (001) phase is found mostly inside of the specimen. The finding is verified by HRTEM image shown in Fig. 90. FePt L1₀ phase occupies most of the bottom part of the specimen, and A1 phase near the top surface. The interface between the two phases is much less rough than the case of the graded media finalized at 600°C. The interface is

very flat, including a couple of unclear structures. In the structures, the lattice fringe is not clear that if the site is $L1_0$ phase or A1 phase. The smooth interface explains the reason why the specimen finalized at 450°C has a higher switching field (9.624 kOe) than that of the specimen finalized at 600°C (4.0 kOe). In our micromagnetic simulations the rough interface between the hard/soft phases reduces the pinning field effectively, by providing wedges as reversal domain nucleation sites [158].

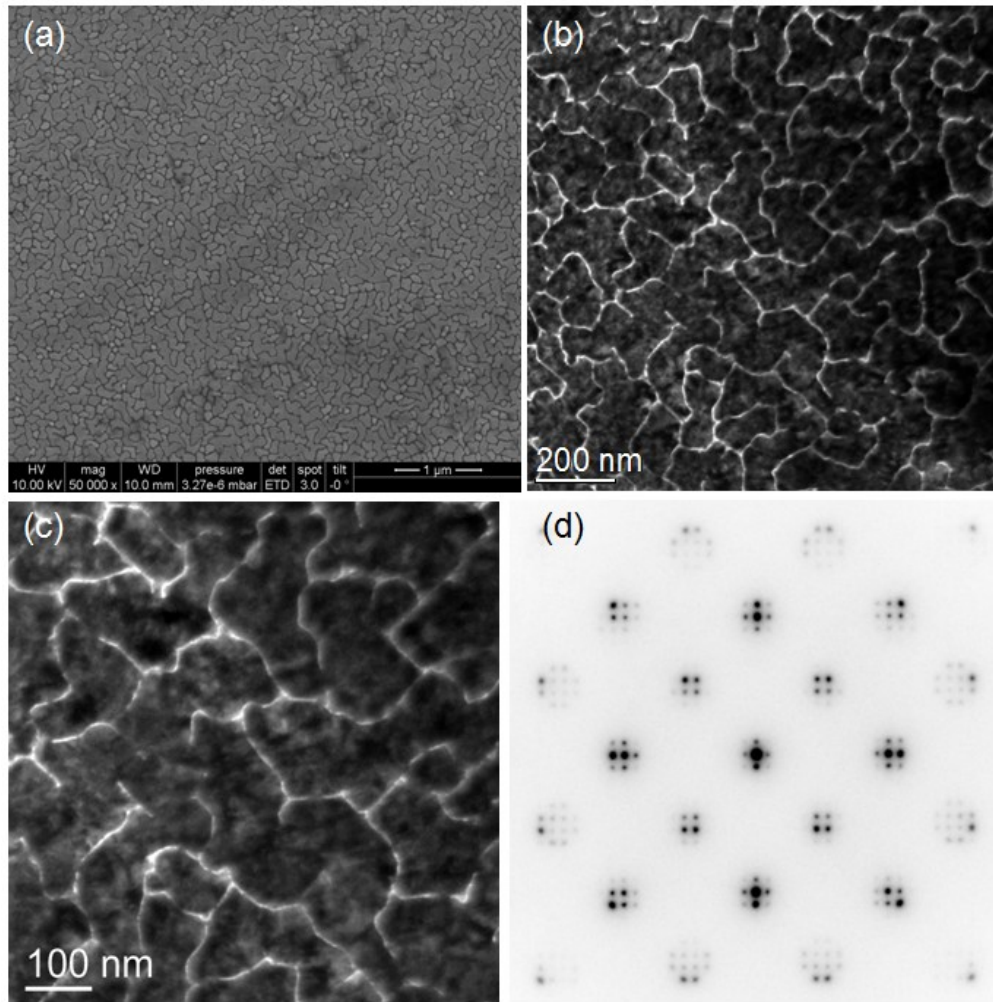


Fig. 88. (a) SEM plan view image of the FePt $L1_0$ /graded ($700^\circ\text{C} \rightarrow 450^\circ\text{C}$). TEM plan view bright field images (a) relatively lower magnification and (b) relatively high magnification. (d) Electron diffraction pattern with a double diffraction.

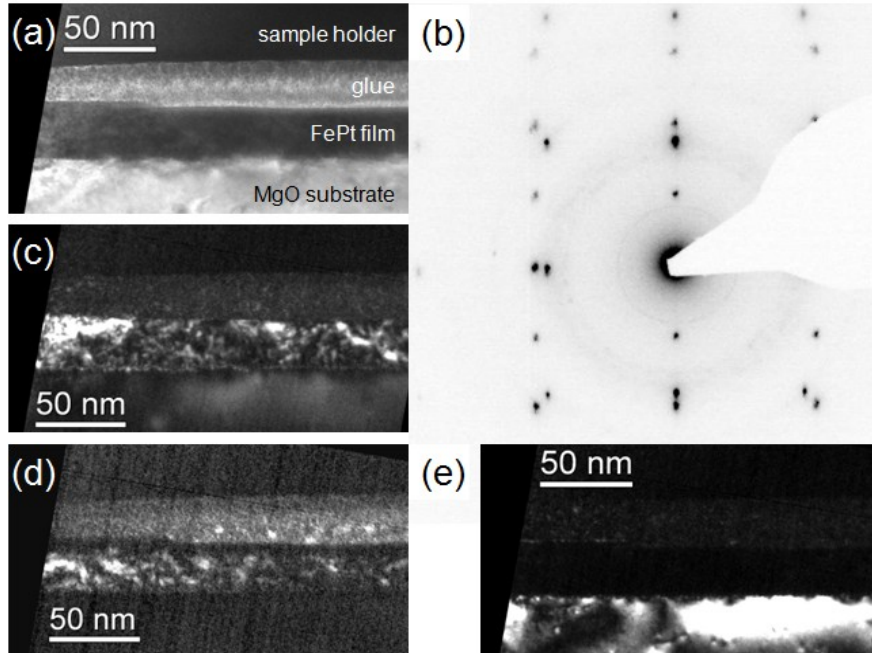


Fig. 89. Cross sectional (a) bright field image and (b) selective area diffraction patterns. (c) and (d) represents the dark field images corresponding $A1+L1_0$ (0,0,2) and $L1_0$ (0,0,1), respectively.

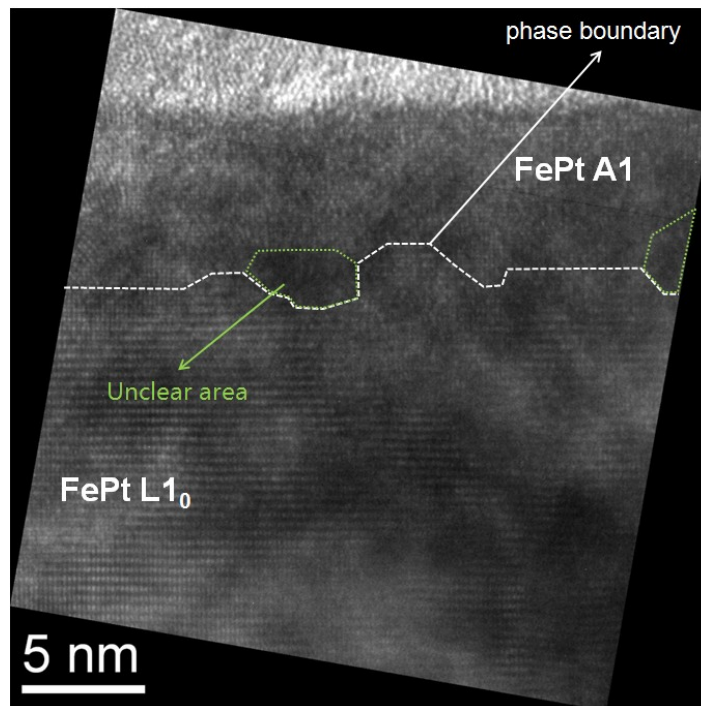


Fig. 90. $L1_0$ phase and A1 phase with the phase boundary between them judged by HRTEM images. Regions of which structure was hard to judge were found near $L1_0/A1$ interphase boundary.

5. FePt film grown at graded temperature 700 ~ 262°C

Finally, a graded media with much thicker graded layer (designed to be 37.5 nm), finalized at 262°C is prepared. Due to the low final temperature and thickness, the film totally lost the alignment of the island edges along the crystal directions of the substrate. Fig. 91(a) shows the plan view SEM image. Very little alignment of the grain boundaries are observed on it, as well as TEM plan view images in Fig. 91(b) and Fig. 91(c). In higher magnification image (Fig. 91(c)), Moiré patterns aligned on the (001) and (010) directions are visible. The period of the moiré pattern is measured as 2.70 nm, however, the value does not correspond to the moiré pattern periodicity p between any phases in the specimen. The calculated moiré pattern period p if there is no lattice rotation between them is determined by the equation $p = d_1 d_2 / |d_1 - d_2|$ [156]. The moiré pattern period from the FePt L1₀ phase and FePt A1 phase is supposed to be 19.01 nm ($a_{L10} = 0.394$ nm and $a_{A1} = 0.386$ nm), from FePt A1 phase and MgO is supposed to be 4.2 nm ($a_{MgO} = 0.425$ nm and $a_{A1} = 0.386$ nm) and from FePt L1₀ phase and MgO is supposed to be 5.4 nm. In its stead, the moiré pattern period corresponds to the distances between the satellite peaks generated by double diffractions shown in Fig. 91(d). That means the moiré pattern is also a resultant of double diffraction.

The cross section TEM investigation is performed to find out the phase distribution as before, the results are shown in Fig. 93. The L1₀ (001) peak was responded only at the bottom side of the film as expected and the boundary between the L1₀ and A1 phases is found very rough. The rough interphase boundary is clearly seen in Fig. 92(d).

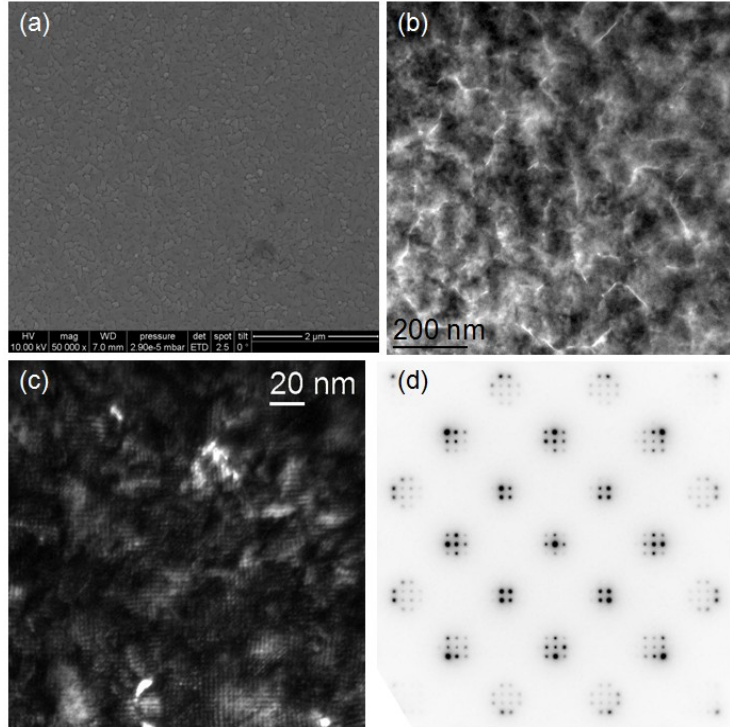


Fig. 91. (a) SEM plan view image of the FePt L10/graded (700°C → 262°C). TEM plan view bright field images (a) relatively lower magnification and (b) relatively high magnification. (d) Electron diffraction pattern with a double diffraction.

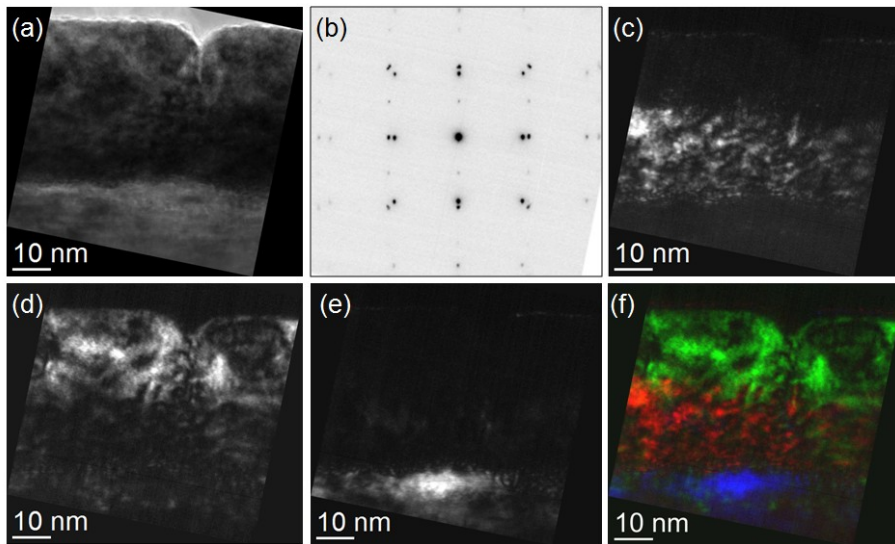


Fig. 92. Cross sectional (a) bright field image and (b) selective area diffraction patterns. (c), (d) and (e) represents the dark field images corresponding Al+L1₀ (0,0,2), L1₀ (0,0,1) and MgO (0,0,2), respectively. (f) The dark field images are overlapped to figure out the interfaces between the phases.

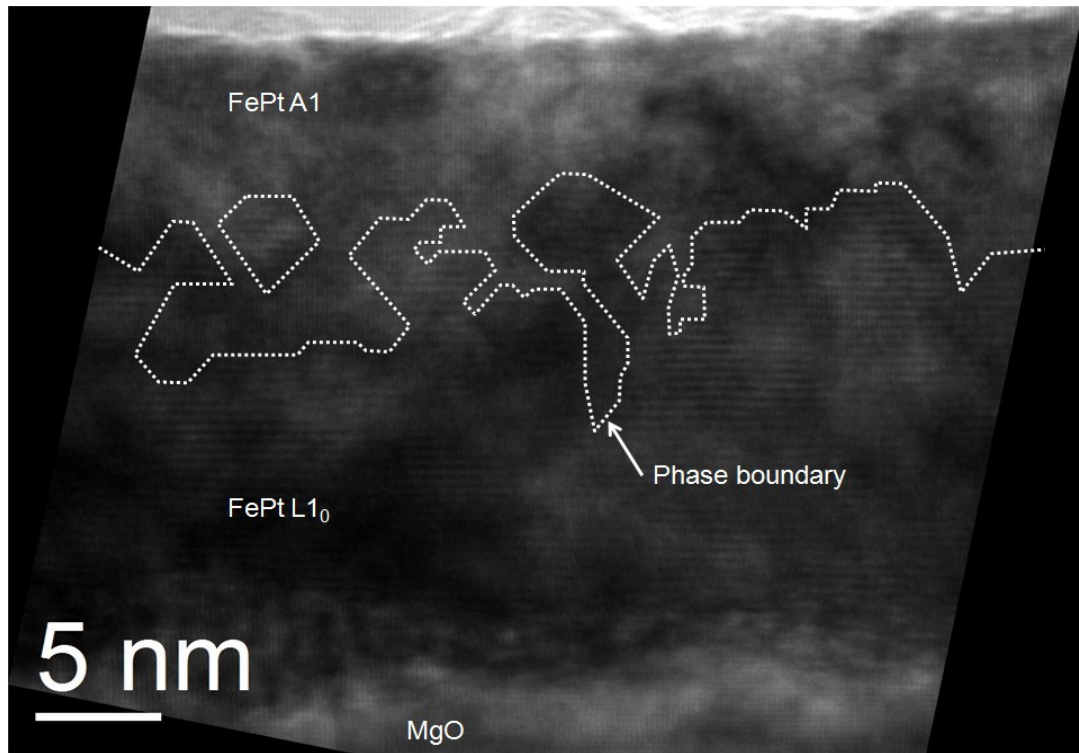


Fig. 93. L₁₀ phase and A1 phase with the phase boundary between them judged by HRTEM images.

Direct phase observation through HRTEM image shown in Fig. 93 reveals a complicated phase boundary between FePt L₁₀ phase and A1 phase. The thickness of the hard layer, graded layer and soft layer are found to be 8.38 nm, 10.49 nm and 5.46 nm, respectively. The measured total thickness is 24.33 nm, which is much thinner than the designed one: 49.0 nm. The top layer is probably lost during the sample preparation. The reversal domain wall width is going to be contracted when it passes through the rough interface, averaged by the portion of the L₁₀ and A1 phases.

- Micromagnetic Simulations

In this chapter we are going to focus on the analysis of the switching behaviors of the FePt graded media, and expand the idea to possible structures of the media. For micromagnetic simulations the following material parameters are taken from the hysteresis loops and previous study of J. Filder [148]: $M_{S,A1} = 796 \text{ kA/m}$, $M_{S,L10} = 1257 \text{ kA/m}$, $K_{1,A1} = 0.1 \text{ MJ/m}^3$ and $K_{1,L10} = 5.0 \text{ MJ/m}^3$.

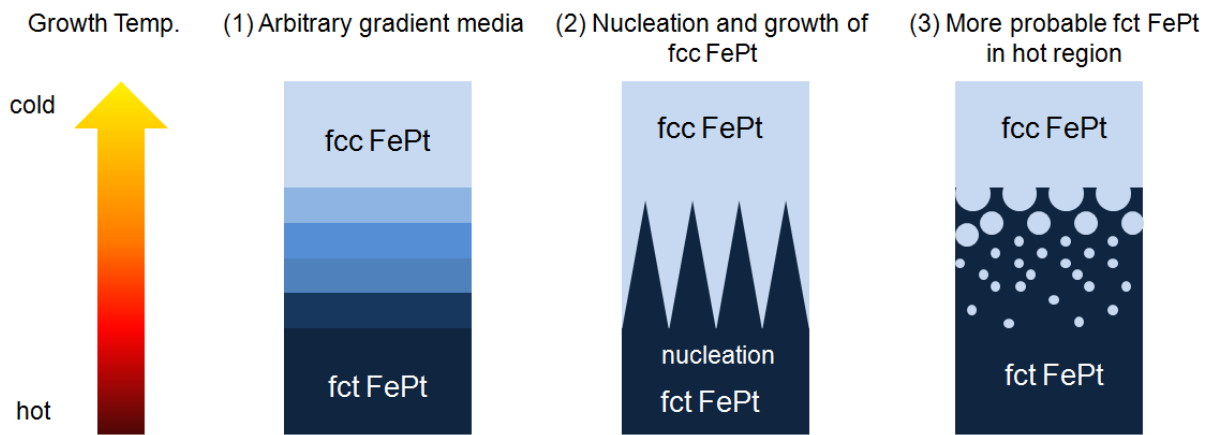


Fig. 94. Probable structures of FePt graded media. For the cases of (1) lattice parameters are gradually decreasing, as well as material parameters, (2) fcc phase is formed by nucleation and growth mechanism and (3) FePt phase is formed more probably in lower temperatures.

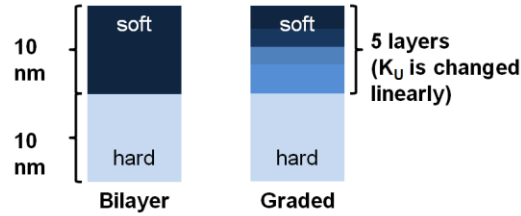
Prior to electron microscopy investigations, we have thought of the possible structures of FePt graded media deposited in decreasing substrate temperature, as shown in Fig. 94. The first structure, (1) arbitrary gradient media, is prepared supposing that the lattice parameters are gradually changing. From the study of Yan and Berry [106, 153], it is found that the additional Cu changes the lattice parameter of the FePt $L1_0$ structure which not only induces easier phase transformation, but also reduces crystalline anisotropy. The structure (1) is prepared following that hypothesis. The second structure,

(2) nucleation and growth of fcc FePt was prepared based on the phase diagram of FePt shown in Fig. 71. In the phase diagram, there are only two stable phases for Fe₅₀Pt₅₀. From the fact, it can be assumed that fcc phase is nucleated at a certain temperature, and grows as the deposition temperature decreases. In this model the degree of ordering stands for the portion of fcc and fct phases. The third model, (3) more probable fct FePt in hot region is prepared under a similar assumption with (2). As the temperature lowers the formation of fcc phase is more probable. The only difference between (2) and (3) is that the fcc phase is not continuously formed. Since the 2nd and 3rd model have the same physical background, micromagnetic simulations will be focused on (1) and (2) only.

Fig. 95 shows the structures of the stacked graded media and phase graded media. For simplicity the thickness of the hard layer and the graded layer are fixed as 10 nm whereas the phase profile in the graded layer is varied. In the Graded media of the Stacked Graded Media, the graded layer has 5 layers of which individual thickness is 2 nm. In the layers K_U is varied linearly, the top layer has the property of the soft phase. Since the models are to briefly evaluate performance of the two structures, the model size is set as 10 nm x 10 nm. The material parameters are also briefly set, $M_{S,hard} = M_{S,soft} = 1592$ kA/m, $K_{U,hard} = 4$ MJ/m³. The crystalline anisotropy of the soft phase was varied from 0 to 0.8 MJ/m³. The hysteresis curves are shown in Fig. 96. For the case of bilayer, the switching field is determined by the pinning field between two phases. At the beginning of the reversal process the soft layer starts to be reversed, and then the hard layer reverses if the applied field exceeds the pinning field. In Graded media and G-01, the hard layer reverses more smoothly than Bilayer. For the case of G-03, which has the

least hard phase portion in graded layer, shows hysteresis curves of those shape is in between those of the Bilayer and G-01.

Stacked Graded Media



Phase Graded Media

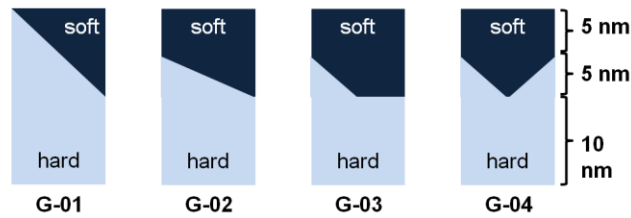


Fig. 95. Schematic structures of the stacked graded media and phase graded media. Bilayer structure is included in the category of stacked graded media. Phase graded media is varied for 4 cases with various shapes of interface.

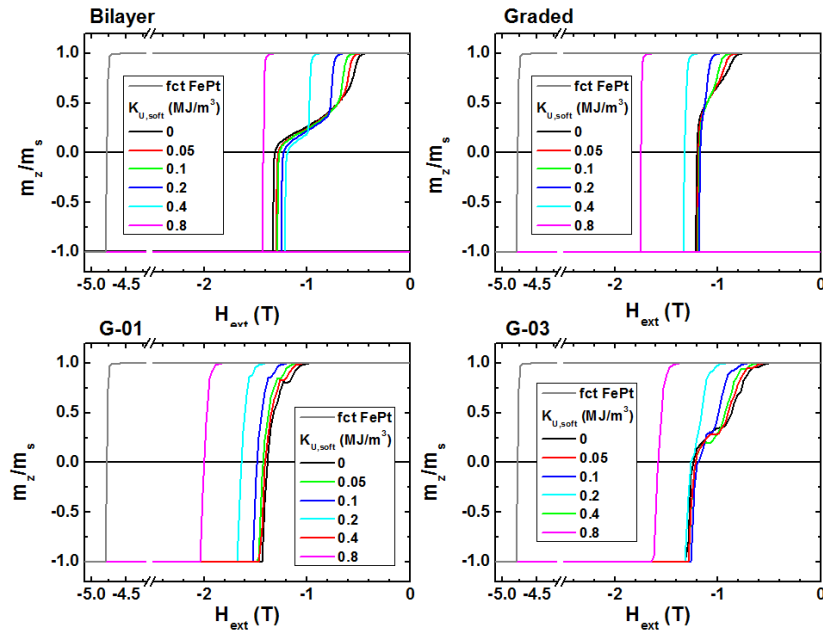


Fig. 96. Hysteresis curves of the bilayer, graded, G-01 and G-03 media. The crystalline anisotropy of the soft layer is varied from 0 to 0.8 MJ/m³. The hysteresis curves are compared with that of fct FePt single layer.

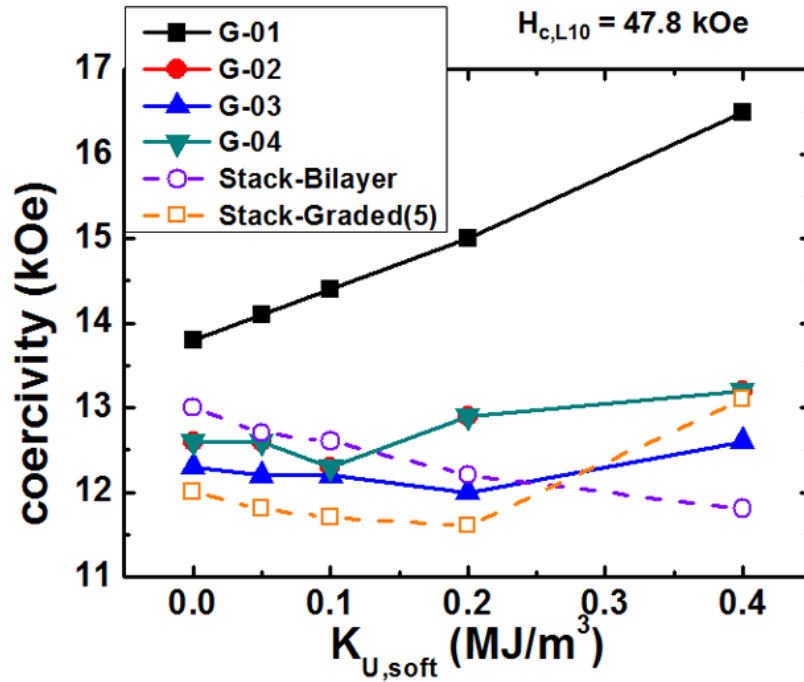


Fig. 97. Summary of coercivities of the Stacked Graded Media and Phase Graded Media.

The coercivities of the Stacked Graded Media and Phase Graded Media are summarized in Fig. 97. The coercivity of the G-01 is linearly increasing as the crystalline anisotropy of the soft layer increases. But in all other cases coercivity is in range between 11.5 to 13 kOe, corresponding to 24 to 27 % of the coercivity of single L₁₀ phase, respectively. It is remarkable that the phase graded media of G-02 to G-04 shows performance comparable to Graded Media in Stacked Graded Media. One more interesting feature is that the G-02 and G-04 show exactly same coercivity in spite of different interface profile. If a graded media is able to be fabricated using only two materials, it would be a great achievement in development of the magnetic recording media. The suggested structure of graded media is a stack of thin magnetic layers of which magnetic properties, mainly anisotropy constant is gradually reduced to lower the

nucleation field[9]. Since the concept of the graded media has published, there have been many experimental demonstrations, for example, FePt(L1₀)/Fe, FePtCu/[Co/Pt]_N, FePt-TiO₂/CoPt-TiO₂ and FePt/CoPt systems[78, 107, 116, 143-144]. The switching fields of the systems were reduced to half of the hard magnet by introducing the soft layer, however, the theoretically predicted reduction by a factor of 10 with less than 20 nm of graded layer has not achieved yet[111, 119]. The researchers have tried to solve the problem by interface mixing using post-annealing [78, 107, 116, 143].

A good news for the FePt L1₀/A1 graded media is that Murayama et al. has reported the nucleation of the L1₀ phase inside of the A1 matrix as a function of the annealing temperature [159], and similar results were shown by Monte Carlo simulations [157]. They revealed that the L1₀ and A1 phase co-exist at the temperature lower than the critical L1₀ formation temperature T_C , with a nanoscale rough interface between them. Based on the finding that the performance of the graded media is able to be achieved using only two phases if they have an inclined interface between them, one step advanced models are prepared to study magnetization behaviors of the phase graded media in detail.

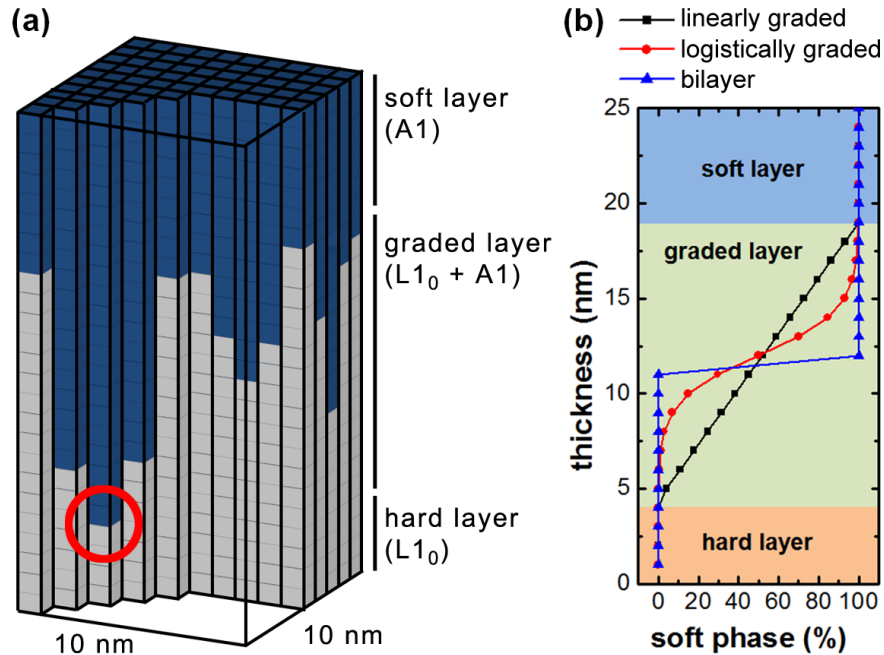


Fig. 98. (a) The phase graded media model for the case of the linear phase transformations with 15 nm thick graded layer. (b) Phase profile comparison between the linearly, logarithmically graded media and bilayer. The bilayer consists of only hard and soft layers.

Finite element (FE) models for micromagnetic simulations on phase graded media were prepared as 25 layers of 10 nm by 10 nm plane of which thickness is 1 nm. Each layer is composed of 1 nm³ cubic units as shown in Fig. 98(a). The switching field of FePt L1₀/A1 graded media has been reduced by gradually decreasing deposition temperature [160]. The TEM investigation of such prepared specimen has revealed very well separated L1₀ and A1 phases. In order to reflect the experimental results, the degree of ordering of the FePt alloy at a certain layer was taken as the portion of the hard phase in the soft phase matrix. The structure of the “phase graded media” in the FE model was prepared as following. At the early stage of the graded media growth, the substrate

temperature is supposed to be higher than the critical phase transformation temperature (T_C) to make only $L1_0$ hard phase (hard layer). When the temperature is reduced to T_C , The A1 phase starts to nucleate at some certain points as marked with a red circle in Fig. 98(a). The distance between the nucleation sites were fixed to 5 nm. As the temperature decreases as the thickness increases, the portion of the A1 phase in a layer is increased to reach 100% at the low deposition temperature (T_f) [147]. The set of layers deposited between T_C and T_f is named as “graded layer”, because the portion of the two phases is gradually changing in this range. In this paper the linear and logistic profiles of the A1 phase were applied to describe the portion of the hard and the soft phase as shown in Fig. 98(b). The logistic curve is similar to the degree of ordering for the case of the substrate temperature was linearly controlled [141]. The thickness of the graded layer (t_g) was varied from 9 to 21 nm, whereas the hard layer thickness was fixed to 4 nm. Once the temperature is lowered below T_f that no $L1_0$ phase is formed any more, the layers deposited later than this is only composed of A1 phase (soft layer). Rickman and Tong [161-162] have reported that the evolved grain structure is strongly influenced by not only the nucleation mode of the second phase, but also the microstructure of the first phase. However, in this study, the grain structure of the phases was neglected to focus on the influence of the graded layer structure.

Stacked graded media models were prepared to be compared with the phase graded media. In this paper the stacked graded media are named as ‘averaged stacked graded media’, because the magnetic property of the individual layer of the stacked graded media was determined by averaging those of the phase graded media as shown in

Fig. 99(a), $K_i = K_{\text{hard}} p_i + K_{\text{soft}} (1 - p_i)$ and $M_{S,i} = M_{S,\text{hard}} p_i + M_{S,\text{soft}} (1 - p_i)$ where p_i is the portion of the hard phase at i th layer. Also, the L1₀/A1 bilayer structure was introduced for comparison. The thickness of the soft layer (t_{soft}) of the bilayer was also varied from 9 to 21 nm, therefore the hard layer thickness of the bilayer was varied from 16 to 4 nm. The magnetic properties of the hard phase and the soft phase are given as following [148, 160]: crystalline anisotropy $K_{\text{hard}} = 5 \text{ MJ/m}^3$, $K_{\text{soft}} = 0.1 \text{ MJ/m}^3$ and saturation magnetization $M_{S,\text{hard}} = 1257 \text{ kA/m}$, $M_{S,\text{soft}} = 796 \text{ kA/m}$. The exchange constant $A = 10 \text{ pJ/m}$ is assigned for both phases and also for the interphase exchange coupling between the L1₀ and A1 phases. The typical finite element mesh size was 0.5 nm to resolve the domain structure accurately. The field was applied at an angle of 0.01° with respect to the easy axis (thickness direction), with a field rise time of 0.1 T/ns. The energy barrier of the given model was calculated by the nudged elastic band method. The maximum number of iteration step was set to 7000, but the optimum path was found in much less steps.

Fig. 99(b) shows the switching field of the various graded media compared with the bilayer. It is known that the switching field is determined to be the smaller one of the nucleation field H_{nucl} in Eq. (84) and the modified maximum pinning field $H_{p,\text{max}}$ as following [9, 119].

$$H_{p,\text{max}} = \left(\frac{1}{\partial z} \frac{\partial E(z)}{2M_S(z)} \right)_{\text{max}} = \left(\frac{2}{\partial z} \frac{\partial \sqrt{AK(z)}}{M_S(z)} \right)_{\text{max}} \quad (88)$$

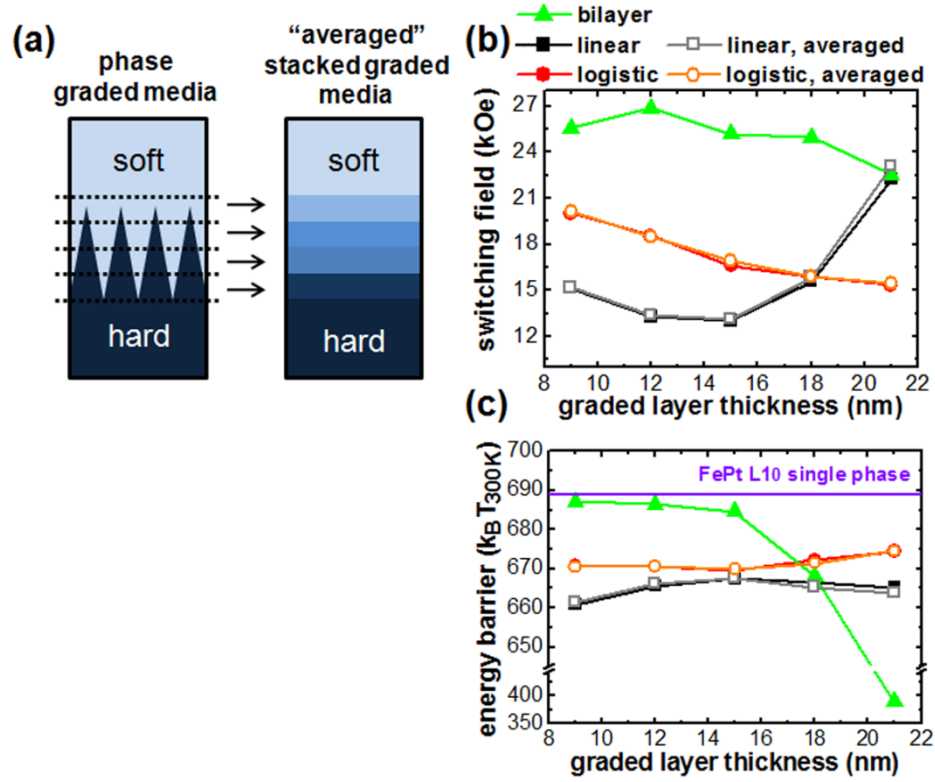


Fig. 99. (a) Schematic structure of the phase graded media and averaged stacked graded media. (b) Comparison of the switching field between the graded media and the bilayer. (c) Minimum Comparison of the energy barrier as a function of the graded layer thickness. (For the bilayer, the x axis in (b) and (c) describes the thickness of the soft layer.)

In Eq.2 z stands for the distance from the bottom to the top of the media. Since the sum of the graded layer thickness and the soft layer thickness is fixed as 21 nm, the soft layer becomes thinner as the graded layer gets thicker. That means that the maximum pinning field $\mu_0 H_{p,\max}$ is increasing in thinner graded layer regardless of the phase profile type, whereas the nucleation field $\mu_0 H_n$ behaves the opposite way. As a result, the switching field of the model with a linear phase transition has a minimum value at $t_g = 15$ nm. The case of logistic transition shows different behaviors. Owing to the tails near the graded/soft layer interface, the nucleation field is much reduced compared to the case of

linear transitions whereas the maximum pinning field is enlarged. Hence the switching field of the logistic profile is determined by the maximum pinning field which is larger than in the linear case. The switching field of the logistic profile is linearly decreasing as a function of the graded layer thickness even in the case that there was no soft layer ($t_g = 21$ nm) as shown in Fig.2b. Considering that the bilayer shows almost constant value of 24 kOe determined by the pinning field between $L1_0$ and A1 phase, the switching field of the graded media was reduced up to 13 kOe (linear, $t_g = 15$ nm), which is 50 % of the bilayer and 16 % of the FePt $L1_0$ single phase media (79 kOe), respectively. The phase graded media also show a very high energy barrier larger than $660 k_B T_{300K}$, close to the value of the FePt $L1_0$ single phase as shown in Fig. 99(c).

It should be noted that the switching fields and the energy barriers of the phase graded media show a good agreement with the averaged stacked graded media. In order to explain this interesting behavior, simple thin 2-dimensional-like platelet models of the phase graded media and average stacked graded media were prepared as shown in Fig. 100(a) for better observation of domain wall motion. The two models show similar reversal curves and domain wall motions as well in Fig. 100. Initially, local magnetization reversal found in the A1 phase propagates into the tip of $L1_0$ phase when the external field reaches 12 kOe, which is only half of the pinning field between $L1_0$ and A1 (Fig. 100(b)-A). In Fig. 100(b)-(B~D), once a part of the $L1_0$ phase has been switched, the reversed area is easily expanded under small additional external field because there is no pinning field in the phase.

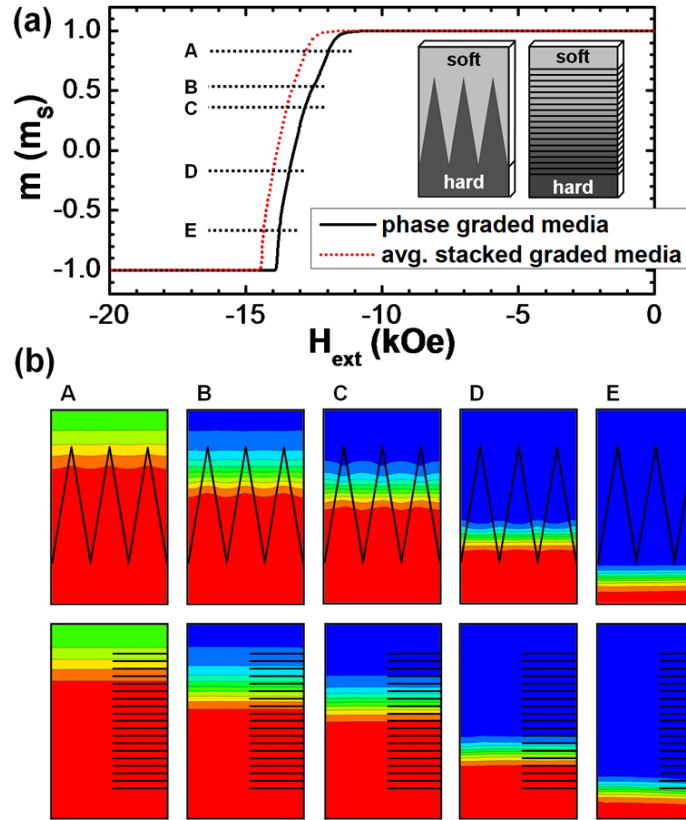


Fig. 100. (a) Magnetization reversal of two-dimensional simplified models. (b) Magnetization configuration of the domain wall motion at the marked points on the demagnetization curve. The material boundaries of the advanced stacked graded media are marked only right half, for better visibility.

The amount of the additional field is determined by the additional domain wall energy (Eq.2) owing to the increased portion of the hard layer in the domain wall. Increment of the domain wall energy by grown portion of hard layer Δp_i is calculated by $\Delta K_i = K_{\text{hard}} \Delta p_i + K_{\text{soft}} (1 - \Delta p_i)$, which is exactly the same way the material properties of the average stacked graded media are determined. Therefore the switching field of the phase graded media is close to that of the average stacked graded media. Please note that the domain wall widths of the phase graded media are close to the ones in the averaged

stacked graded media as well. Finally the reversal process finishes when the domain wall penetrates the hard layer (Fig. 100(b)-E). There might be a concern about the switching field distribution owing to the irregular distribution of the wedge tip positions. The probable switching field distribution was estimated using platelet models with a 15 nm linear phase transition similar to the one shown in Fig.3, but only three wedges between them. The center wedge tip position was varied from -3 nm to +3 nm of its original coordinate toward the easy axis direction. From the simulations very small switching field difference of 0.4 kOe was found (not shown).

The difficulty of development of stacked graded media is that the coherent growth of the N^{th} layer correlated with the previous layer on the magnetic properties is required in every layer. In the present work we present a phase graded media with a rough interphase boundary. We have demonstrated that the phase graded media appear the same features as stacked graded media. Creating a rough interface between a hard and a soft magnetic phase is feasible for reduction of the switching field. The work described in this session was published in Applied Physics Letters [158].

3.3. Particulate Media

(1) Introduction

The areal recording density for magnetic tape recording based on the particulate media has been increased enormously, 42% annually in the past few years. In 2007, 6.7 Gbit/in² areal density was achieved [163] and in 2011, 29.5 Gbit/in² areal density was released [6]. One of the causes for obtaining high areal densities was the application of densely packed hexagonal barium ferrite (h-BaFe) platelets, which have many advantages over metal particles (MP): chemical stability, high coercivity, and small particle size [164-167]. The small aspect ratio of the h-BaFe particles enables themselves to be easily aligned by applying of an external field during the coating procedure on the polymer tape [168]. The 6.7 Gbit/in² and 29.5 Gbit/in² writing and read-back processes were performed using randomly oriented h-BaFe media. However, as h-BaFe particles have been originally suggested for perpendicular media, recent results reveal a higher signal-to-noise ratio (SNR) when the media particles are aligned to a certain direction [169-170]. Basically, SNR depends on the quality of the writing and the reading process, as well as on the media quality itself. Since the tape recording media are mostly used as backup media and should be easily removed from the head block, the head to media distances are not as stationary as in the case of hard disk media. The mechanical fluctuation of the media to head distances has a possibility to affect on the read and write processes [171]. In this study we have investigated the SNR performance as a function of the write and read head to media distance, for differently oriented h-BaFe particulate media with a constant packing density of 40 %.

(2) Hexagonal BaFe (h-BaFe) Particulate Media

- Writing Performance as a Function of Head to Media Distance

The average diameter and thickness of the hexagonal (h)-BaFe platelet are given as 21 nm and 7 nm, respectively, with volume distribution of 25% according to experimental observations [172]. The microstructural models as input for the micromagnetic simulation of the h-BaFe particulate media were prepared by an implementation of the Lubachevsky-Stillinger packing algorithm [173]. The packing process was started from a pre-defined aspect ratio of 3:1 (diameter to thickness), preferred orientation (mean azimuth angle $\langle\theta\rangle$ and mean polar angle $\langle\varphi\rangle$) and degrees of spatial misorientations (standard deviation of the angles, $\Delta\theta$ and $\Delta\varphi$) with Gaussian distribution (Fig. 101a). The particles started to grow from the randomly distributed seed points until the spatial packing density reaches about 40 %, which reproduces the experimental results [169]. The microstructural models of the particulate media models are shown in Fig. 101b. As input parameters for the micromagnetic simulations we used a mean saturation magnetization $M_S = 0.345$ T and a mean uniaxial crystalline anisotropy $K = 1.25 \times 10^5$ J/m³ with a standard deviation of 20 % [174]. Due to the anisotropic shape of the h-BaFe particles, the linear packing densities were determined by the particle alignment as shown in Fig. 101b. Three types of particulate media models, named as #L (longitudinally oriented), #R (randomly oriented), and #P (perpendicularly oriented) are prepared (see Table 4). The magnetic storage layer consisting of approximately 3000 h-BaFe platelet has a length of 1300 nm, a width of 200 nm and a thickness of 100 nm. The $\Delta\theta$ and $\Delta\varphi$ of #L and #P are set to 30°. The #R media was prepared as a perpendicularly

oriented one with $\Delta\theta = \Delta\phi = 60^\circ$, following the experimental observations that the h-BaFe particles are self-aligned during the coating procedures. The hysteresis loops for applied homogeneous external field are shown in Fig. 101c and Fig. 101d. According to the hysteresis loops, the chosen $\Delta\theta$ and $\Delta\phi$ values lead to squarenesses and coercivities which are close to experimental data as shown in Table 4 [169, 175-176].

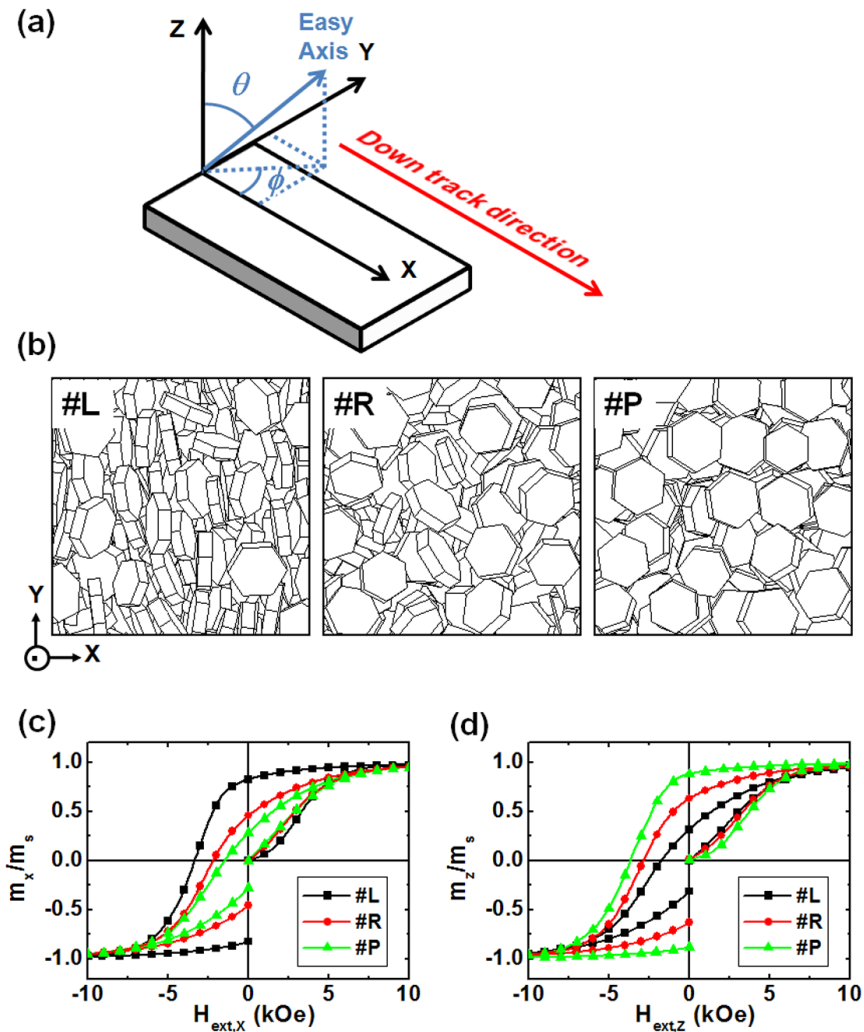


Fig. 101. (a) Coordinate system of our simulations. X axis is corresponding to the down track direction of magnetic tape recording media, where y and z axes are the cross track direction and the perpendicular direction, respectively. (b) Top view 100 nm x 100 nm sized images of the longitudinally (#L), randomly (#R), and perpendicularly (#P) oriented media. (c) Hysteresis loops of the models, under homogeneous longitudinal field. (d) Hysteresis loops of the models, under homogeneous perpendicular field.

Model		#L	#R	#P
Preferred orientation	$\langle\theta\rangle$	90°	0°	0°
	$\langle\phi\rangle$	0°	0°	0°
Misorientation (standard deviation)	$\Delta\theta$	30°	60°	30°
	$\Delta\phi$	30°	60°	30°
Squareness ratio	Longitudinal	0.824	0.456	0.280
	Perpendicular	0.315	0.629	0.880
Coercivity (Oe)	Longitudinal	3334	2182	1464
	Perpendicular	1726	2834	3655

Table 4. Geometric and magnetic properties of particulate media models. $\langle\theta\rangle$ and $\langle\phi\rangle$ are the mean values of azimuth angle θ and polar angle ϕ , respectively.

Our finite element numerical micromagnetic software code enables us to solve the Landau-Lifshitz-Gilbert equation of motion for the magnetization of an entire magnetic device [61, 177]. The finite element simulations are based on the hybrid boundary element method [16]. In the case of magnetic recording simulations, the input are the data of the detailed microstructure of the recording media, the geometry of the write head, the layer stack and shield geometry of the read head, the intrinsic properties and the current wave form of the write current, etc. Macroscopic properties like current waveform, read-back voltage, transition jitter are input/output of a multiscale simulation that treats the functional behavior of a recording system while taking into account the microscopic magnetization processes during recording and read back. The matrix compression technique is used for fast multiplication of matrices arising from the boundary element method, which is used to calculate the interaction fields between the write head and the storage media [178-179]. A 3-dimensional writing field box of Karlqvist ring type head field with a 200 nm gap between two poles is generated for writing simulations [69]. The Karlqvist head field box moved along the down track direction of the particulate media

with 6 m/s velocity, alternating its signs in every 10 ns. Consequently a pattern of 20 alternating bits with a length of 60 nm is written on each model, corresponding to 423 kfc. For reliable SNR analysis the recording process has been repeated by shifting the phase of the write head current by $\frac{\pi}{2}$, which moves the bit transition area from the previous simulations by 30 nm. The particulate media with different current phase is considered as a new recording process, because the read back signals are detected by different particles those have same magnetic properties except for their alignments.

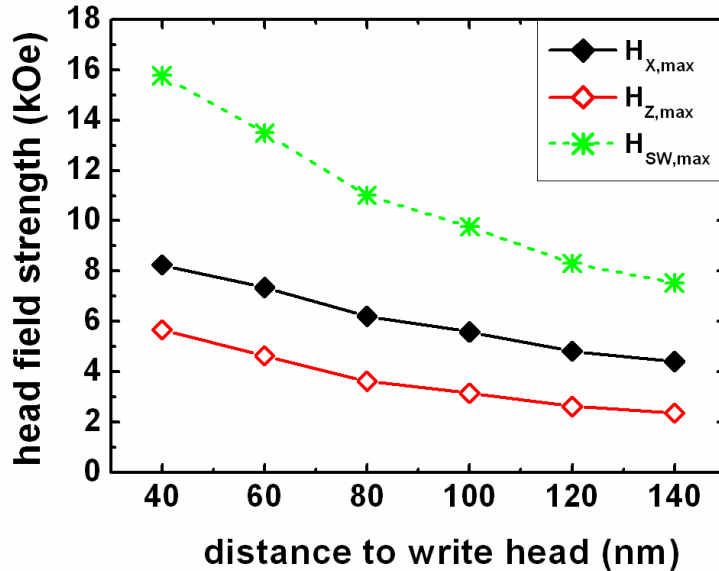


Fig. 102. Maximum x- and z-directional Karlqvist head field components and Stoner-Wohlfarth switching field $H_{SW} = \left(H_x^{\frac{2}{3}} + H_z^{\frac{2}{3}} \right)^{\frac{3}{2}}$.

Fig. 102 shows the maximum longitudinal (x) and perpendicular (z) components of the Karlqvist head field. For a writing head to media distance of 40 nm, the maximum values of the components are 8.3 and 5.7 kOe, respectively. Comparing the coercive

fields of Table 4, these fields are strong enough to magnetize the h-BaFe particles in x- or z-directions. The magnetization reversal process of a particle is also determined by the angle between its easy axis and the external field vector. The h-BaFe particles are supposed to be reversed by coherent switching following Stoner-Wohlfarth (SW) equation, due to their small size and magnetic parameters [8]. The maximum SW switching fields H_{SW} are shown in Fig. 102 as a function of the z-directional perpendicular distance from the head. The maximum head field decays when the head to media distance is increased. The maximum SW switching field for a head to media distance of 140 nm is about half of the one of 40 nm. Nevertheless the SW switching field is still twice stronger than the coercive fields (Table 4).

From Fig. 103, a schematic writing process and the final states of the written bits are shown. For all cases the bits are written with the write head to media distance d_{write} of 40 nm. As it is observed in the Fig. 103b, the #L media is written rather more longitudinally than perpendicularly where #R and #P media are perpendicularly than longitudinally written, according to the distributions of the easy axis of the h-BaFe platelets. Direct analysis of the magnetization vectors on each finite element node reveals that #R media has comparable longitudinal and perpendicular components, where #L has a two-fold stronger longitudinal magnetization component than the perpendicular one as shown in Fig. 105b and Fig. 105a, respectively. #P shows a stronger perpendicular magnetization component than the longitudinal one, as revealed in Fig. 105c.

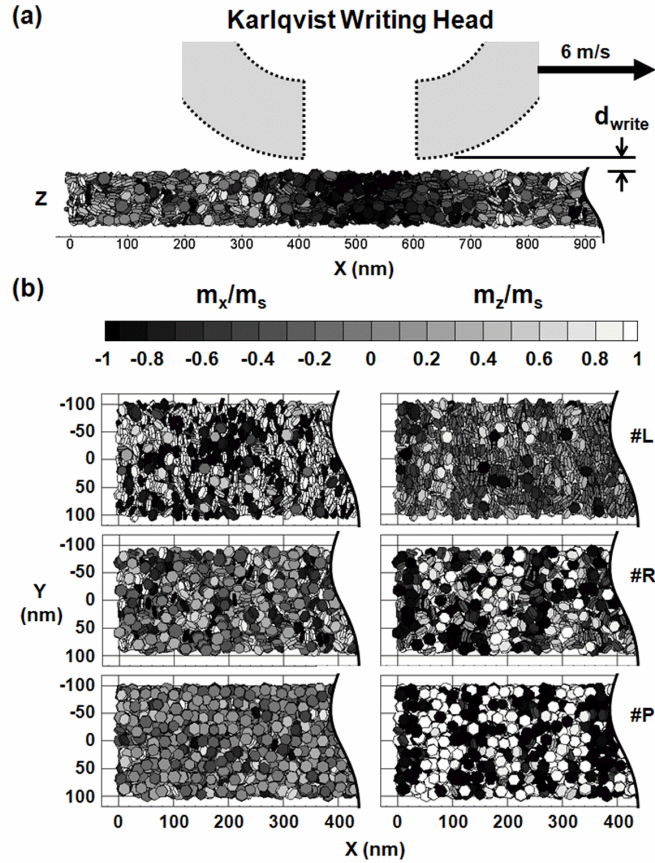


Fig. 103. (a) Schematic diagram of the writing process. The d_{write} denotes the distance between the Karlqvist writing head and media. (b) x- and z-directional magnetization components of the media, when $d_{write} = 40$ nm.

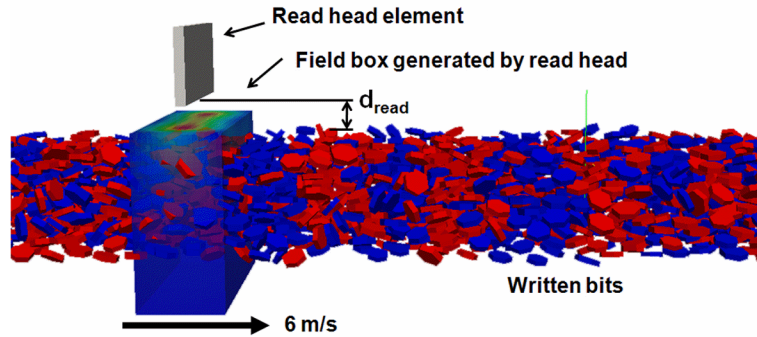


Fig. 104. Read-back process using reciprocity theorem. The field box generated by the read head is passing through the media with a given read distance. The interaction between the field box and the written bits induces the changes of the magnetic interaction energy, which is regarded as the read back signal.

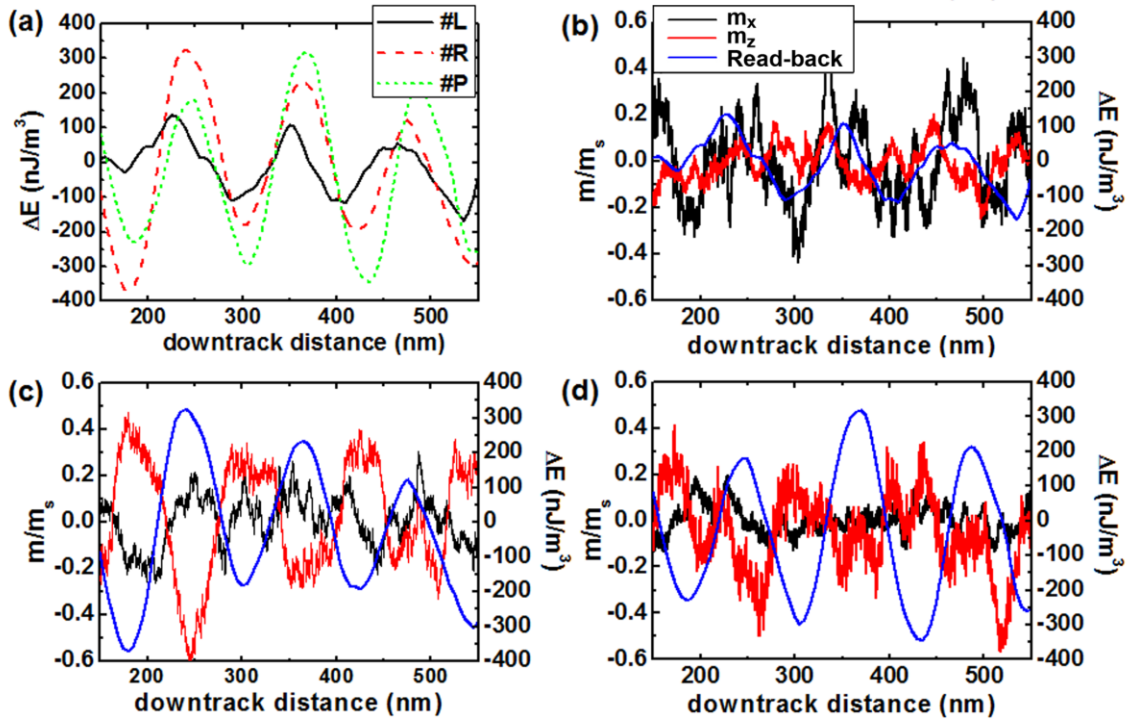


Fig. 105. (a) Read-back signals of the bits written on a part of #L, #R and #P media. The x- and z-directional magnetization components of the bits written on the (b) #L media, (c) #R media and (d) #P media, with the read-back signal of the same area.

For the read-back process simulation, there are three options: (1) Direct calculation of the magnetostatic interactions between the read head model and the magnetization of the individual particle. (2) Calculation of the total magnetization of the read head model, during its movement inside of the precomputed stray field box originated by the media. (3) Using the reciprocity theorem [8], the magnetic interaction energy calculation between the media and the field box generated by the read head model. In this study we have used the reciprocity theorem to save the computational resources and calculation time [34]. A permalloy block assuming the free layer of the giant

magnetoresistance (GMR) sensor with 10 nm thick (down track direction, x), 150 nm long (cross track direction, y) and 80 nm wide (perpendicular direction, z) without shields is taken into account. The stray field box generated by the read head model was moved along the written bits through the media as shown in Fig. 104. This leads to the magnetic interaction energy changes which regarded as a read-back signal. A read-back signal with 60 bits is prepared by connecting three signals consisting of 20 bits, each created by an individual phase-shifted writing simulation. A pair of 60-bit read-back signals is also prepared by arranging the signals in different order. The difference of the conjugate signals which are originated from the different arrangement of the media, is defined the media noise. Related to this, the auto-correlation SNR (AC-SNR) is obtained in time domain as following

$$SNR = 10 \log_{10} \frac{Var_{signal}}{Var_{noise}} = 20 \log_{10} \frac{\sigma_{signal}}{\sigma_{noise}} \quad (89)$$

where the Var and σ states the variance and standard deviation, respectively [180].

It should be noted that in the high frequency range like 423 kfcf, the time domain method underestimates the SNR compared with the frequency domain method. Therefore the SNRs shown in this paper are only used for comparison between different conditions. In order to study the SNR performance, the distances from head to media, d_{write} and d_{read} were varied from 20 nm to 100 nm. Fig. 105a shows the read-back signals as a change of magnetic energy, unit of energy density from #L, #R and #P media, for the case of d_{write} and d_{read} are 40 nm. The x- and z-component of the Karlqvist writing head field have magnetized the particulate h-BaFe platelets along their easy axis. The magnetization of

the particle mainly contributes to the read-back signal detection. The signal obtained from #L media is advancing in phase by $\frac{\pi}{2}$ than #P. The #R media also showed a little phase shift compared with the #P media. In order to study the origin of the phase shift, we have investigated the x- and z-directional magnetization components of #L and #P media as shown in Fig. 105b and Fig. 105c. For the case of #L media, the read-back signal is following the x-directional magnetization whereas the z-directional magnetization is randomly distributed. In contrary, the read-back signal of the #P media inversely follows the z-directional magnetization curve in general. The inverse behavior comes from the definition of the read-back signal. Since the stray field box used for read-back process is generated by the read head module saturated in +z-direction, the negatively (-z) written bits were detected by an increase of the magnetic interaction energy and the positively (+z) written bits were detected by a decrease.

Read-back simulation results of the written bits on various write distances are shown in Fig. 106. As the write head to media distance d_{write} is increased from 20 nm to 100 nm, the signal amplitude of the #L media is nearly unchanged, whereas the amplitude of the #R and #P media is gradually decreased to 69 % and 81 % of the maximum value, respectively. The change of the SNR as a function of the write distance is remarkable. Generally the SNR is decreasing as the write distance is increasing. Comparing the SNRs between the cases d_{write} is 20 to 100 nm, the reduction is about 30 % in all cases. An interesting feature was found on #L and #P media, at $d_{\text{write}} = 40$ nm. Contrary to the others, the SNR of the #L media is increasing when d_{write} is increasing from 20 to 40 nm. Therefore the case of $d_{\text{write}} = 40$ nm is the optimum distance for the #L media, but also

the least favorable write distance for the #P media. The local minima and maxima seem to be originated from the interactions between particle orientation and Karlqvist head field profile. During the write process, the total acting field, consisted of longitudinal field component maximized at the center of the head (at $x = 500$ nm in Fig. 103a) and the perpendicular component maximized at the edge of the poles (at $x = 400$ and 600 nm in Fig. 103a) interact with the orientation of the particles. The interaction determined by the type of the media and the distance between the write head to the media causes the changes of SNRs according to the given write distances. In most cases the #P media show the best SNR performance and the #R media show the worst. The results are in good agreement with the experimental studies [169].

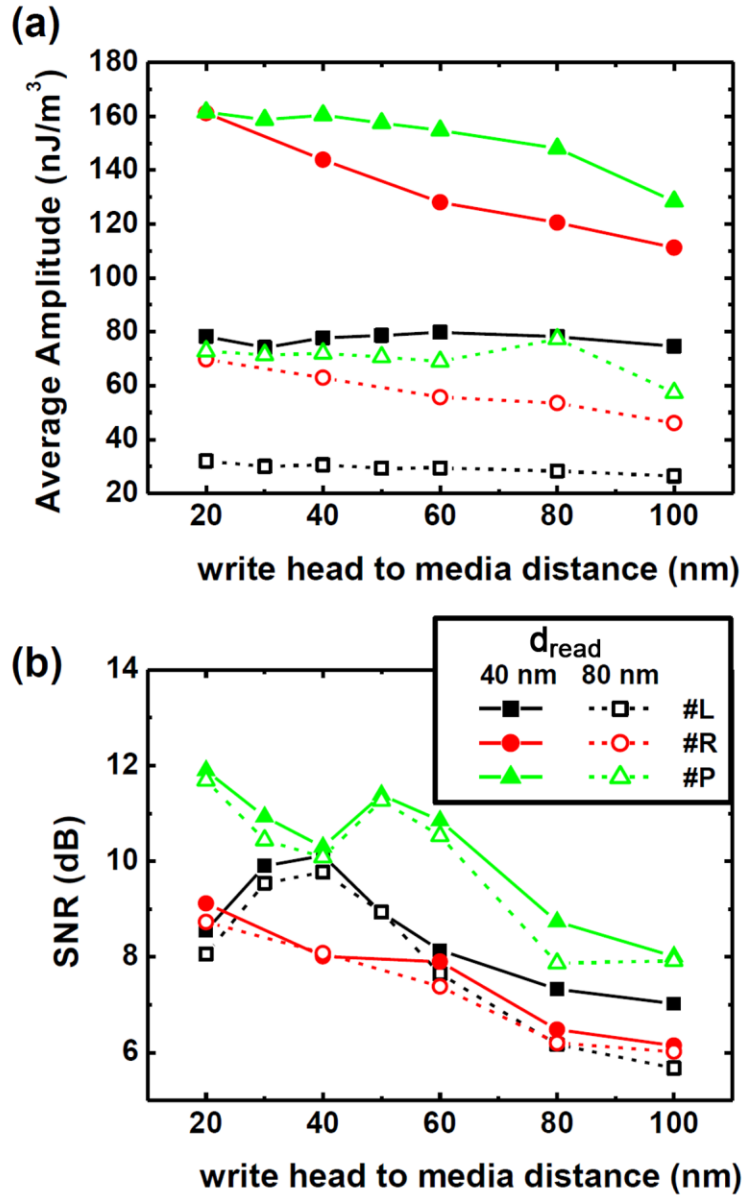


Fig. 106. Read-back signal properties of the bits written in fixed read head to media distances. The average amplitude of the (a) signal and the (b) SNR as a function of the write head to media distance.

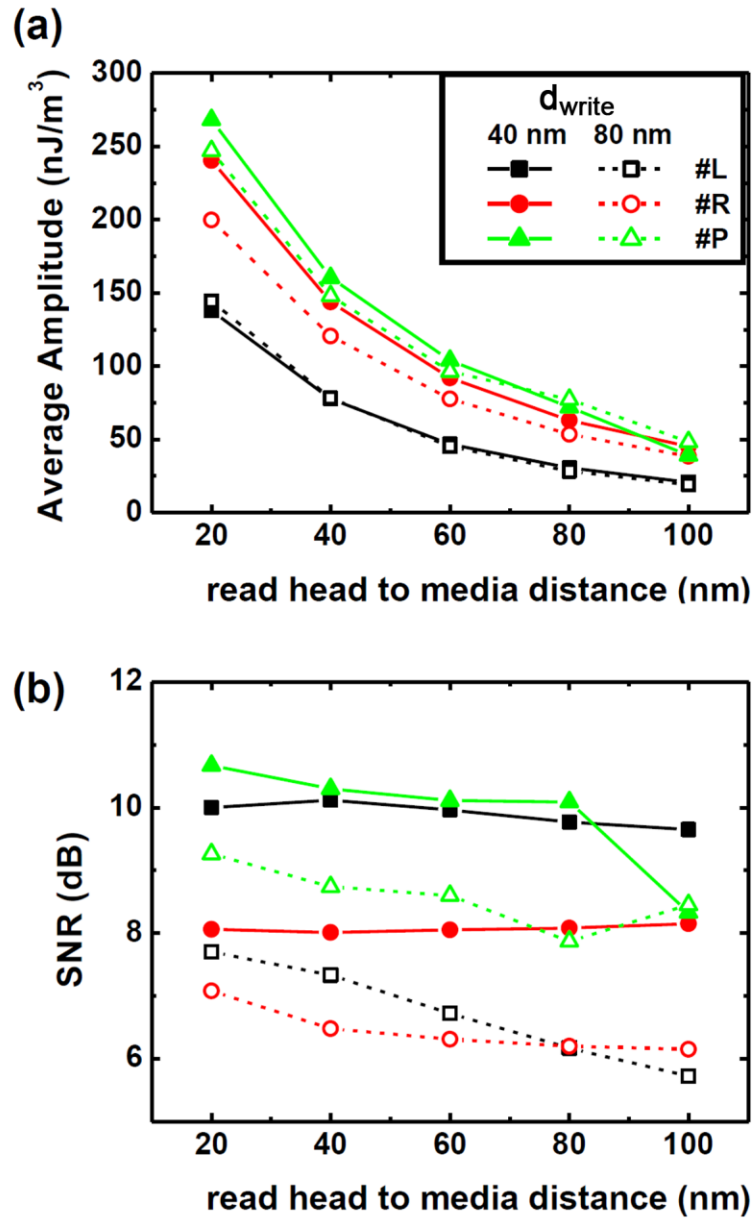


Fig. 107. Read-back signal properties of the bits written in fixed write head to media distances. The average amplitude of the (a) signal and the (b) SNR as a function of the read head to media distance.

The signal amplitude and the SNR dependency on the read head to distance d_{read} are studied in more detail and are shown in Fig. 107a and Fig. 107b. The write distance d_{write} is fixed at 40 and 80 nm and the read distance d_{read} is varied. The signal amplitude is inversely proportional to the distance d_{read} , regardless of the write distance d_{write} . The #R and #P media which have a larger perpendicular component show a stronger signal than the #L media as observed in Fig. 106. The read head more strongly reacts on the perpendicular than the longitudinal component of the media stray field by a factor of 2. However, the SNR behaves differently as shown in Fig. 107b. For the case of $d_{\text{write}} = 40$ nm, the SNRs are independent of the read head to media distance d_{read} . The strong SW switching field explains, why the SNR performance was independent of the read distance if d_{write} is 40 nm. In this case, the strongly aligned media, #P and #L have similar SNR performances to each other, about 2 dB higher than #R media, as also revealed in Fig. 106(b). But for the case of $d_{\text{write}} = 80$ nm, the reduction of the SNR is found in all kinds of media, whereas the #L media reveal the strongest SNR decay for increasing d_{write} . The SNR of #L media is reduced up to 4 dB for the distance for $d_{\text{read}} = 100$ nm, which is an even lower SNR than that of #R. At $d_{\text{write}} = 80$ nm, the SNR reduction of #P and #R from when $d_{\text{read}} = 20$ to 80 nm are less than 1 dB, which is much smaller than the case of increasing write distance.

Considering underestimation by time domain method, SNR analysis was performed in a frequency domain on the best case, #P at $d_{\text{write}} = 20$ nm and $d_{\text{read}} = 40$ nm, and the worst case, #L at $d_{\text{write}} = 100$ nm and $d_{\text{read}} = 80$ nm to clarify the recording quality of the h-BaFe platelets. In Fig. 108, the Fast Fourier Transform (FFT) filtered signal and

noise are shown in the frequency domain. The bit density of 423 kfcf corresponds to 0.0083 nm^{-1} in the signal spectrum, and is marked by an arrow. The best (#P) and the least favorable (#L) SNR values are 24.4 dB and 14.62 dB, respectively. The International Magnetic Tape Storage Roadmap of INSIC have recommended for advanced magnetic tape recording that the broadband SNR is 16.7 dB when the bit length is 63 nm [181]. From the frequency domain SNR results of this paper, it is shown that the value suggested by INSIC is achieved in most cases as long as the read head to media distance is kept in a range, less than 80 nm.

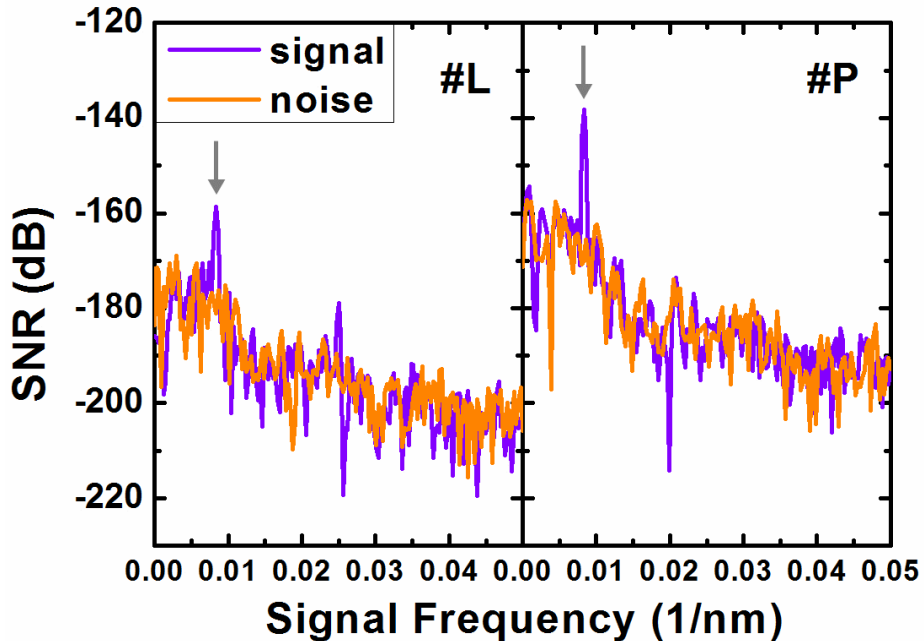


Fig. 108. The SNR as a function of the signal frequency, of the #L media at $d_{write} = 100 \text{ nm}$ and $d_{read} = 80 \text{ nm}$ (left) and of the #P media at $d_{write} = 20 \text{ nm}$ and $d_{read} = 40 \text{ nm}$ (right). The signal frequency of 0.0083 nm^{-1} corresponding 423 kfcf is marked with arrows

In this session we have studied the read-back performance of advanced h-BaFe platelet tape recording media, as a function of the recording head to media distance using

micromagnetic simulations and SNRs obtained in the time domain. Our results have predicted the experimentally verified results, in which the mechanical fluctuation would reduce or enhance the signal amplitude and SNR, according to the distance from media to head. The fluctuation of the media to the read head more strongly affects on the signal amplitude than on the SNR, whereas that of the write head to media does on the SNR. Since the fluctuation of the media to the write head distance is crucial for SNR, the operation of the media on the write head should be controlled precisely. Comparing the h-BaFe media types by its orientation, the #P media is found to be the best oriented media structure. Considering the underestimation of the SNR calculated in time domain, additional SNR analyses were performed in frequency domain. The frequency domain results suggest that the h-BaFe platelets produce enough SNR to be applicable for the next generation tape recording media.

- Writing Performance under Various Writing Heads

From the previous sessions it was found that the h-BaFe particulate media shows a better performance if the particles are perpendicularly aligned. In this session, we tried perpendicular head field onto the randomly oriented (#R) and perpendicularly oriented (#P) h-BaFe media to study the recording quality as a function of various writing heads. We have introduced SPT head to apply perpendicular head field more efficiently than conventional longitudinal head, i.e. Lindholm head. Moreover, the influence of the soft underlayer (SUL) was also employed. Fig. 109 shows the cross section parallel to the xz plane of the field box which contains the writing head fields.

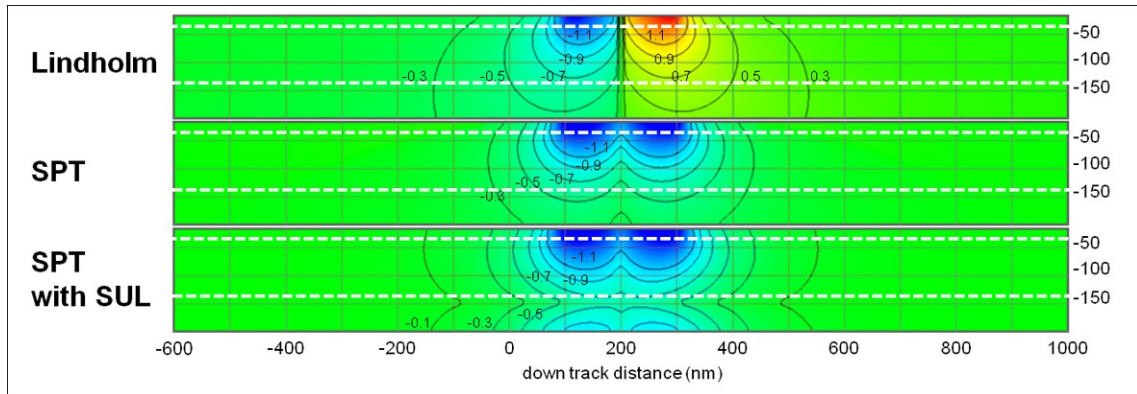


Fig. 109. Head field profiles of the Lindholm head, SPT head without SUL and SPT head with SUL. The dashed line indicates the position of h-BaFe media is supposed to be placed. The numbers attached on the isolines show the strength of the Stoner-Wohlfarth field in Tesla.

The SPT head was assumed as a saturated magnetic pole with dimension of 200 nm long along the down track direction by 300 nm wide along the cross track direction, and the SUL was supposed to behave as a perfect mirror image of the SPT. Head field from the SPT was calculated following the permanent magnet approximation [75-76]. In Fig. 109 the h-BaFe particulate media is to be placed between the white dashed lines, the head to media distance is 20nm and the media thickness is 60 nm. The colors and isolines correspond to the Stoner-Wohlfarth field strength, because the h-BaFe particles are supposed to be reversed by coherent rotation. Since the isolines have a regular step of 0.2 T, the dense lines indicate the larger head field gradient. It is found that the Lindholm head field disperses at the bottom, whereas the SPT head field does less. When SUL is introduced, the strong head goes deeper than before. In this case the isoline indicating 0.7 T reaches at the bottom of the media. The writing field boxes shown in Fig. 109 are applied on the media model to perform writing simulations. The processes are shown in Fig. 110, with written bit structures resulted from the three types of writing head fields.

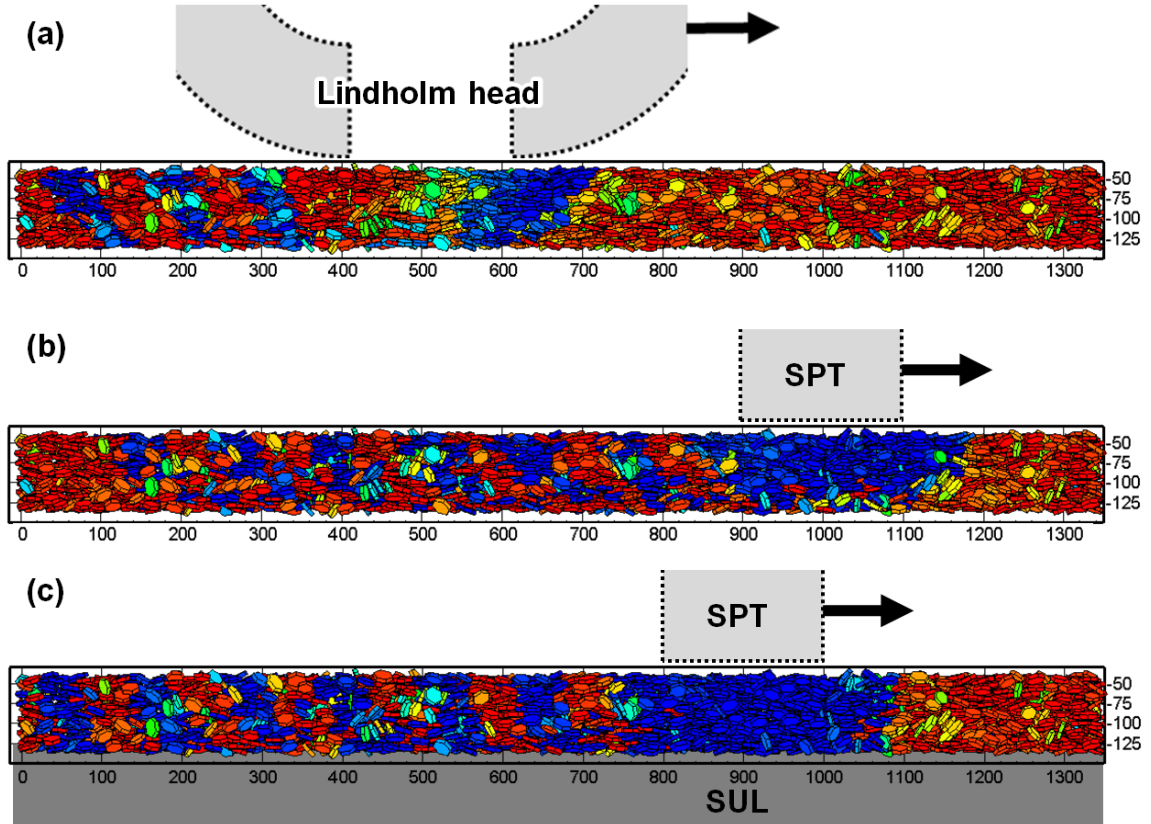


Fig. 110. Snapshots of the writing processes using (a) Lindholm head, (b) SPT head without SUL and (c) SPT head with SUL.

In all cases the head movement velocity was fixed as 20 m/s, with a fixed deep gap field or base field of 14 kOe. The bit structures shown in Fig. 110(a) and (b) reveal that the bit transitions resulted from the Lindholm and SPT head are clearly inclined to the media surface with an angle of 40°. However, the SPT with SUL head results in much steeper bit transitions, about 60° (Fig. 110(c)). The quality of writing is estimated by arctangent curve fitting, using the following equation (90).

$$m_z = b \arctan \frac{x - x_0}{a} + y_0 \quad (90)$$

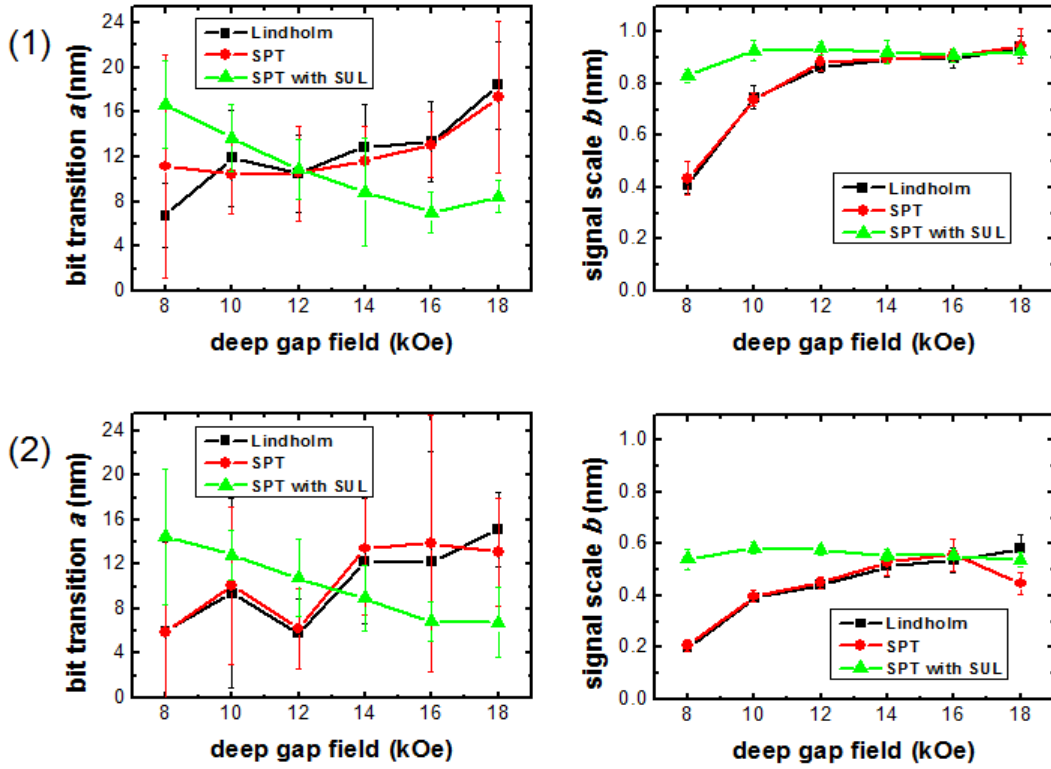


Fig. 111. Bit transition parameter a and signal scale b for (a) #P media and (b) #R media. The volume distribution $\sigma_v/V = 50\%$.

In Eq. (90), the a stands for the length of bit transition, and b for the signal scale. For the good writings a should be small and b should be large. The bit transition parameters and signal scales are summarized in Fig. 111. For Lindholm and SPT head, the bit parameter is increasing as the deep gap field (base field) increases. However, for the cases of SPT head is accompanied with SUL, the bit transition gets smaller as the stronger base field is applied. The SPT head with SUL has another good performance: the signal scale is close to the saturated value even in small deep gap field. The superior performance of the SPT head with SUL is resulted from the deeply penetrating writing fields. It is also found that in all cases the perpendicularly aligned particulate media (#P)

is better than the random one (#R). The performance of the h-BaFe particulate media is finally estimated by signal to noise ratio (SNR). The Lindholm, SPT head, SPT head with SUL are applied with a fixed deep gap field (base field) of 14 kOe. The linear density is varied in 300, 400 and 500 kfc. The SNRs estimated by fast Fourier transformation (FFT) of 18 μm read back signal are summarized in Fig. 112. The performance of the SPT head without SUL is comparable with that of the Lindholm head. The lower SNR of SPT head than Lindholm head seems to be resulted from the weak depth-penetrating head field. As shown in Fig. 110, the SPT head without SUL could not write on the bits at the bottom of the media. But using the SPT head with SUL solved the problems. The deep-penetrating strong head field has increased the SNR up to 30 %, for the case of 20 m/s velocity on the #R media, by introducing SUL.

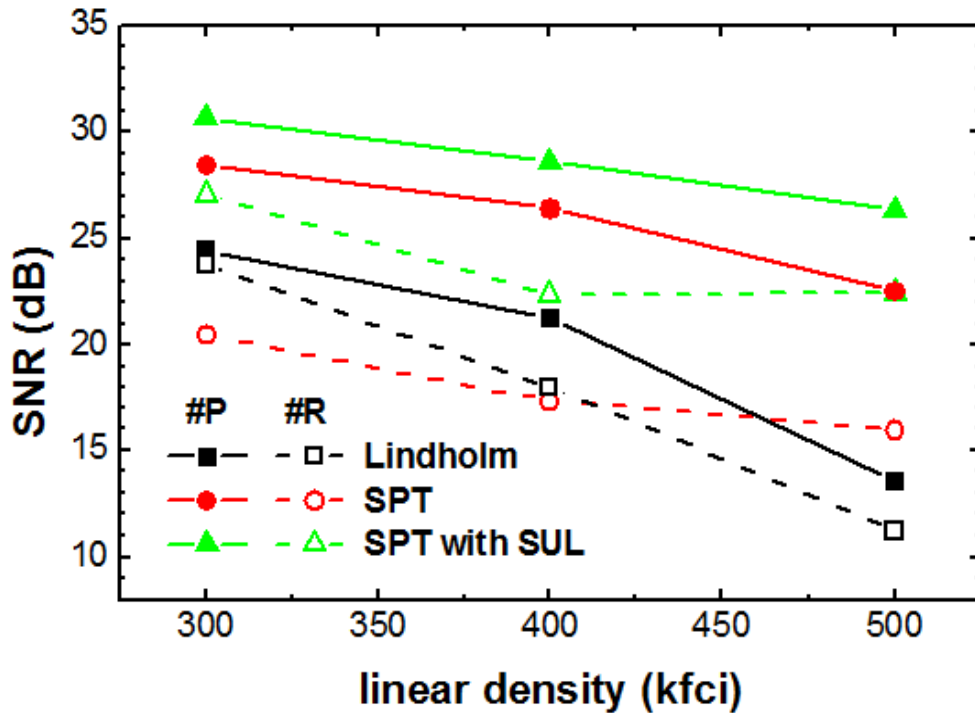


Fig. 112. Signal to noise ratio (SNR) of #P and #R h-BaFe particulate media written with Lindholm, SPT, and SPT head with SUL, in various linear densities.

3.4. Sputtered Film

Sputtering is the technique to activate ions to cause bombardments on the target material, for thin-film deposition process, etching and material analysis. The inert gas, i.e. Ar, is hit by an accelerated free electron. The electron transfers kinetic energy to a couple of electrons of the Ar atom therefore it becomes an Ar^+ ion. At this point the positively charged ions are accelerated into the negatively charged electrode striking the surface and blasting loose electrode material and more free electrons by energy transfer. The additional free electron feed the formation of ions and the continuation of the plasma. All the while free electrons find their way back into the outer electron shells of the ions thereby changing them back into neutral gas atoms.

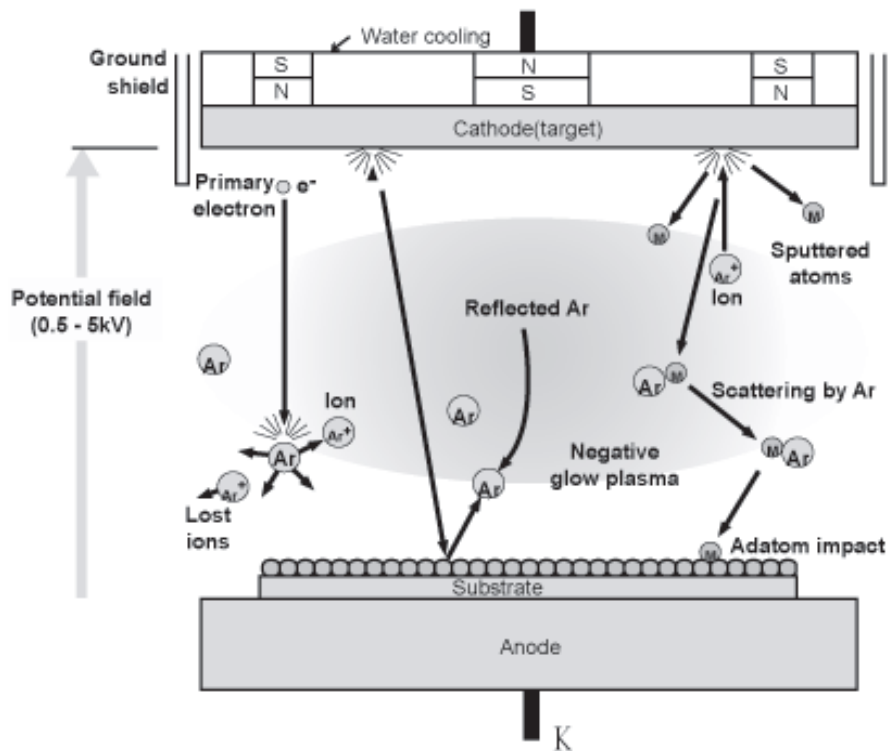


Fig. 113. Schematic diagram of the sputtering mechanism in the constraint chamber [182].

Due to the laws of conservation of energy, when these electrons return to a ground state, the resultant neutral gas atom gas gained energy and must release the same energy in the form of photon. The photons are the reason the plasma appears to be glowing. The efficiency of the sputtering is enhanced in magnetron sputtering shown in Fig. 113. If the magnets are provided behind the target, the stray fields between the magnetic poles restrict the distribution of the free electrons near the target, consequently the ionization and neutralization of the Ar atoms occurs much more frequently.

If two targets are applied on the sputtering system and the substrate is at aside of the gap between the targets, this technique is called Facing Target Sputtering (FTS) [183]. FTS has advantage for deposition of tape media compared to conventional DC magnetron sputtering. By FTS, damage-less deposition can be achieved even on a few-micrometer plastic base film at room temperature without a cooling system, since the plasma is trapped between two targets by the DC magnetic field and is never in contact with the substrate [184-186].

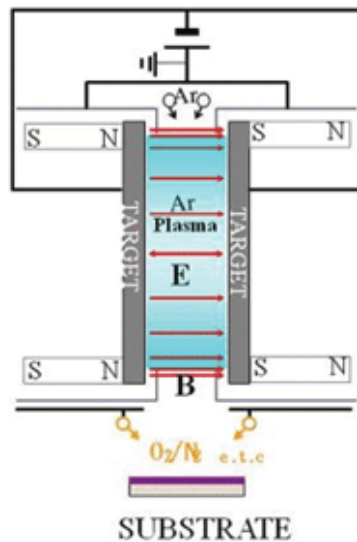


Fig. 114. Schematic diagram of the Facing Target Sputtering (FTS).

(1) CoCrPt-SiO₂ Granular Media

- Modeling from TEM Image

There are two ways to generate finite element models in batch process. The first one is using a Voronoi cell construction [187-188]: Seed points are randomly distributed on space, but only 2-dimensional plane in our case, then the points which has the same distance to the nearest points are collected as boundaries. This method is called as Voronoi tessellation, named after a mathematician who has suggested the method in 1907. The other way is to use image processing techniques on TEM image. Finite element model of the granular model is able to be directly taken from plan view TEM image, owing to the fact that the grains are deposited as a single layer on top of the seed layer. Fig. 116 shows an example of the grain detection process using image processing techniques. The CoCrPt-SiO₂ image was imported from the work done by Park et al [189]. The imported image is to pass thresholding filter to distinguish the grain and the boundaries. In the given image the grains are darker than the boundaries. The image is inverted that the grains became white, and the boundaries black.

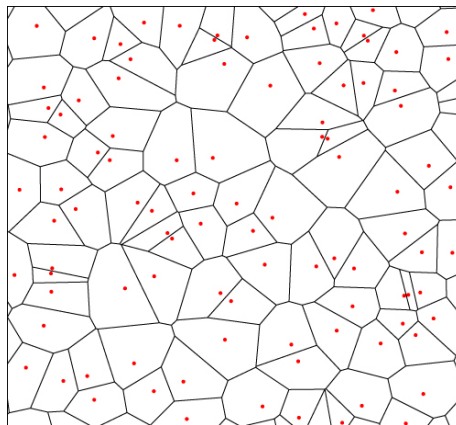


Fig. 115. Voronoi tessellation of a set of point particles. Voronoi cells are convex and their edges join at trivalent vertices [187].

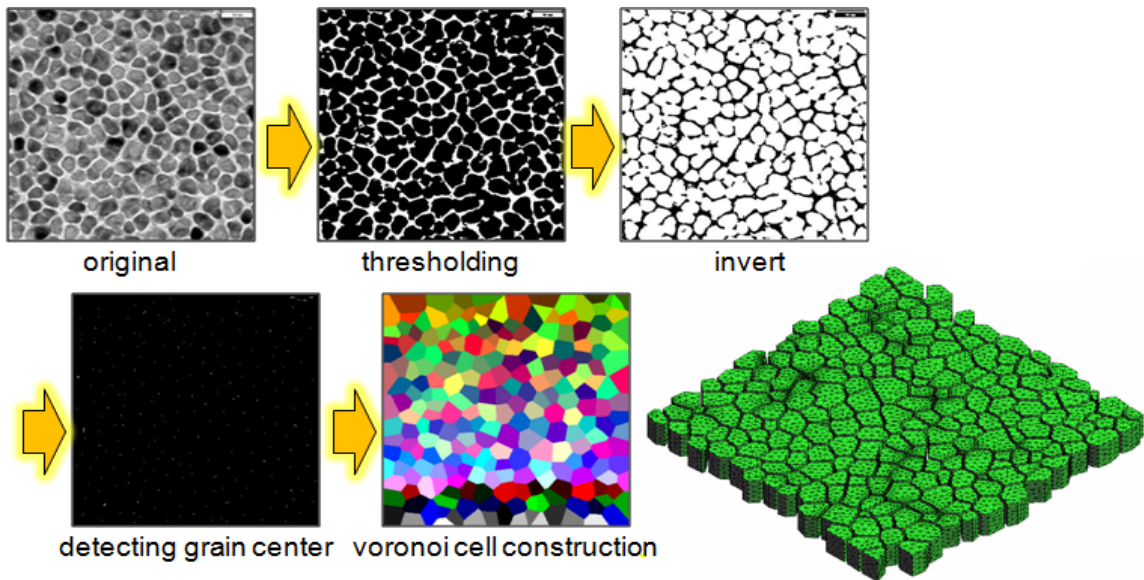


Fig. 116. Procedures for image process for grain detection to build finite element models.

It was for the purpose of using distance transformation [190]. The distance transformation is applied on every single pixel on the image, which finds the smallest distance to the back pixel. Therefore the grain boundary will be zero, and the grain center will have the local maximum. Through two-dimensional differentiation, the local maximums are able to be found and set as the seed point of Voronoi cell construction. Finally the finite element models are able to be prepared using the voronoi cell constructions and given grain boundary thickness. The advantage of this method is that the real microstructure is able to be directly imported to calculate the realistic magnetic behaviors of the given structure. There is a similar try but get the one step advanced microstructure importing process suggested by Itagaki et al [191-192]. They have developed a program to analyze a high resolution TEM image lattices to define high angle grain boundaries. But due to the limitation of the inspection area, it is not easy to get a statistics from a micrometer-sized region with that method.

- Recording Performance

CoCrPt-SiO₂ granular media deposited on thermally oxidized SiO₂ or glass amorphous substrate has been suggested and actually used as a magnetic recording media for hard disk drives owing to its suitable magnetic properties and small grain size less than 10 nm [120, 189, 193]. As magnetically harder materials are required for the hard disk drives, the CoCrPt ternary alloys seem to be fading away. However, CoCrPt-SiO₂ sputtered film on Aramid film is suggested as an advanced tape recording media and 45 Gbit/in² areal density is achieved recently [184-186]. Finite element models describing CoCrPt-SiO₂ media are prepared based on the works done by Matsunuma et al [186, 194]. A granular media composed of 8400 grains (1800 nm long, 200 nm wide) with 6 nm of grain diameter and 2 nm of grain boundary thickness and 18 nm thick film is prepared. Based on the XRD results performed by Matsunuma's group ($\Delta\theta_{50} = 13.8^\circ$), the deviation of the grains' easy axis are set as 10°. The uniaxial crystalline anisotropy K_U and saturation magnetization M_S are set as 250 kJ/m³ and 450 emu/cc, respectively.

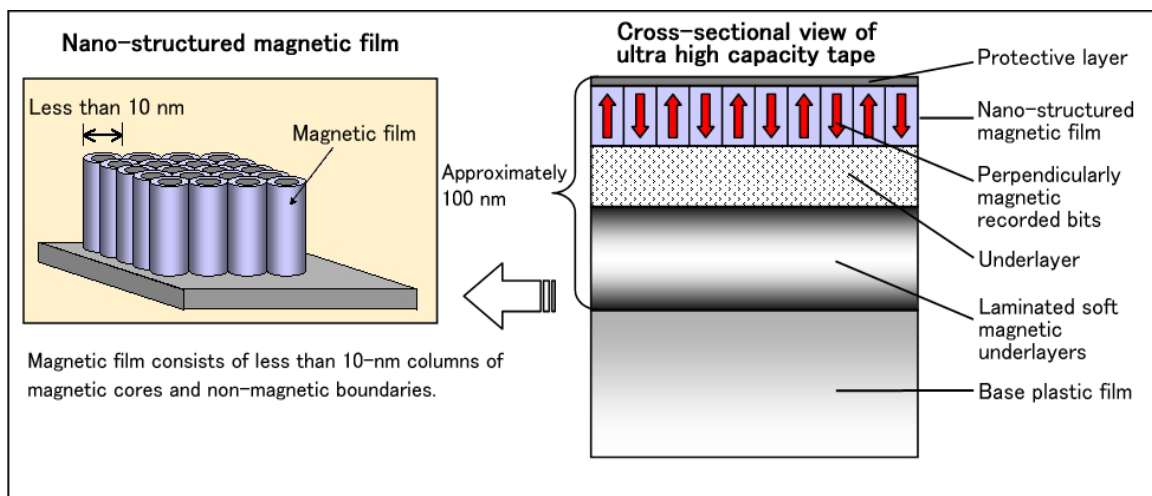


Fig. 117. Schematic diagram of CoCrPt-SiO₂ sputtered media prepared by face target sputtering [194].

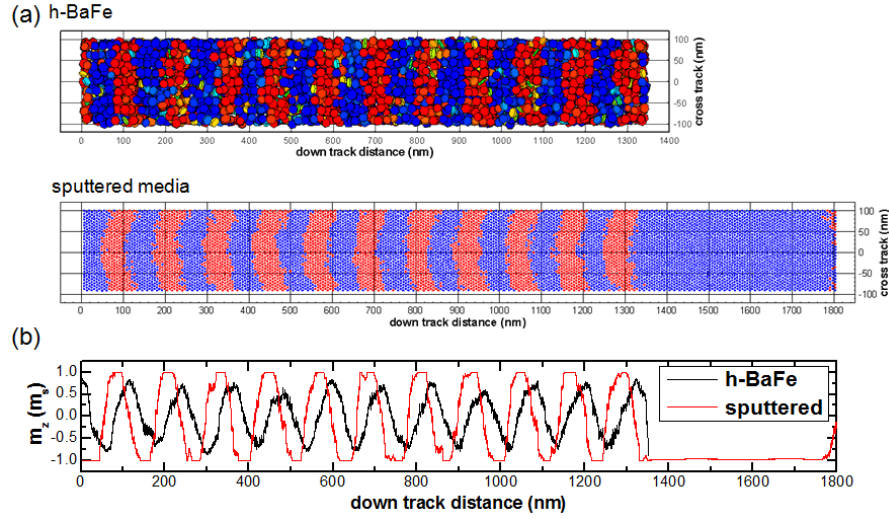


Fig. 118. (a) Plan view of the written bit states of perpendicularly aligned (#P) h-BaFe media, and the CoCrPt-SiO₂ sputtered media. The bits are written using SPT head with SUL, with a head to media distance $d = 40$ nm. (b) Perpendicular magnetization component of the two media as a function of down track distance. The black line indicate the written bit states of h-BaFe media, and the red one is for the sputtered one.

The written bits on the sputtered media with a bit density of 423 kfcI are shown in Fig. 118(a), compared with that of the h-BaFe particulate media. The writing head velocity was 20 m/s, with a head to media distance 40 nm. In both cases the SPT head with SUL is applied as a writing head. It is clearly shown that the bit transition is determined by the particle or grain size, with a writing head width especially for the case of the sputtered media. The bit transition curvatures due to the limited SPT head width are observed. From the analysis of the perpendicular magnetization component in Fig. 118(b), the bit transition parameter of the h-BaFe particulate media and the CoCrPt-SiO₂ sputtered media are found as 19.87 nm and 7.89 nm, respectively. It should be noted that the bit transition parameter of the sputtered media is mainly resulted from the finite writing head width. If the SPT head had a wider width, the bit transition parameter should have been much reduced.

(2) [Co/Pt]_N Percolated Media

The storage capacity of hard disk drives is mainly governed by the physical size of one information bit. In conventional hard drives, the recording medium consists of weakly magnetically coupled grains. To increase the storage density and thus the storage capacity, a reduction of the grain size is required to keep the signal-to-noise ratio low. However, such a reduction has a lower boundary, the superparamagnetic limit [81], at which the magnetic information becomes thermally unstable. New concepts to overcome this issue are under investigation. One approach, called bit patterned media (BPM), consists of ordered arrays of magnetic nanostructures, where one bit of information is represented by one single nanostructure [195]. Although the concept of BPM is considered to be promising to extend the areal storage density beyond 1 Tbit/inch², versatile manufacturing methods to produce BPM have to be developed [196-198]. To realize such a BPM system, arrays of nanostructures with periods below 25 nm have to be fabricated, which is rather challenging.

In this regard, an alternative concept of a recording medium referred to as percolated perpendicular medium (PPM) has been recently introduced [86, 199]. This medium consists of an exchange coupled magnetic film with densely distributed nonmagnetic defects acting as pinning sites for magnetic domain walls. In this scheme, the continuous exchange coupled film satisfies the criteria of thermal stability of the bit, while the densely distributed pinning sites ensure relatively smooth bit-boundary transitions.

According to results reported by Zhu and Tang [199], the application of PPM results in a significantly lower bit transition length parameter and transition position jitter compared to conventional granular perpendicular media, even with randomly distributed pinning sites, however, a uniform distribution of the pinning sites reduces both parameters even further. Thermal stability of PPM in the region away from domain walls should not be an issue, as the thermal stability is mainly given by the exchange coupling in the continuous film, if the nucleation field for a reverse domain is significantly larger than the demagnetization field [87]. However, thermal stability of a data bit is determined by the energy barrier against moving a domain wall out of the pinning sites. It was shown by Zhu and Tang, that the energy barrier reaches a maximum when the thickness of a Bloch domain wall is about twice the size of the pinning site [87]. However, this result was obtained for varying the domain wall width by changing the exchange parameter of the planar film, which is of little practical relevance. By increasing the amount of pinning sites and their size, the resulting length of a domain walls in the system is reduced and so is the energy stored in the domain wall.

Although a detailed theoretical description of PPM is provided in literature, there are only a few experimental realizations of a percolated perpendicular medium. In one example, evenly distributed nonmagnetic defects in a magnetic matrix were achieved by co-deposition of magnetic material (CoPt and FePt alloys) with nonmagnetic oxides (MgO, SiO) [200-201]. Another example concerns the direct deposition of Co/Pt multilayers onto anodized alumina substrates resulting in the formation of PPM with evenly distributed pinning centers [202-204]. In this case, the pores serve as pinning sites

for the domain wall propagation due to the variation of the magnetic parameters and magnetic film thickness around the perimeters of the pores. Furthermore, CoPt alloy films with perpendicular magnetic anisotropy were grown on SiO₂ nanoparticle arrays with particle sizes as small as 10 nm [205-206]. The peculiar magnetization reversal behavior was attributed to the specific structure of the cap array where the pinning of domain walls was suggested to occur at the intersections between particles acting as defects. Brombacher et al. [207] recently presented another approach, based on the pinning of magnetic domain walls in Co/Pt multilayer films on nonmagnetic defects given by plasma etched polystyrene particles with initial diameters of 180 nm. The etched particles with a resultant size of about 40 nm act as nucleation and pinning sites for magnetic domain walls.

Here, we concentrate on the realization of PPM by deposition of Co/Pt multilayer films with out-of-plane easy axis of magnetization on nanopatterned inorganic substrates. Such stable, highly ordered nanopatterns of various oxides are prepared by simple chemical solution deposition using commercial block-copolymers. Compared with top-down techniques, this method is cheap, scalable, and gives high reproducibility without expensive, specialized equipment [152, 208-209]. Recently, we have shown the magnetization reversal in Co/Pt multilayer films deposited on ZrO₂ membranes with a perforation size of 67 nm and a period of 110 nm [210]. The performed study showed an effective pinning of magnetic domain walls on the inhomogeneities given by the positions. However, with respect to the possible application as recording media, templates with smaller periods are required. In the present work, we concentrate on the

magnetic domain wall pinning in Co/Pt multilayer films grown on ZrO₂ membranes with a perforation size of 17 nm and a period of 34 nm. We show by performing micromagnetic simulations that magnetic exchange coupling between the materials deposited into the perforations and the surrounding magnetic film is an important issue that might limit the performance of this type of PPM.

- Experiments (by TU Chemnitz, Germany, CNRS, France and SuperSTEM Laboratory Daresbury, UK)

Nanoperforation structure was fabricated with ZrO₂ deposition on Si wafer by dip coating using a withdrawal speed of 0.5 mm/s and at a temperature of 40°C, and very low relative humidity. The layer was then heated up to 500°C for 5 minutes to decompose the organic part and ensure the crystallization of the ZrO₂ [208-209, 211]. Fig. 119 shows a representative plane-view SEM image of the ZrO₂ membrane revealing an assembly of nanoperforations homogeneously dispersed on the substrate. Quantitative analysis was accomplished by conventional image processing technique giving an average perforation diameter of 17 nm and an average centre-to-centre distance of 34 nm.

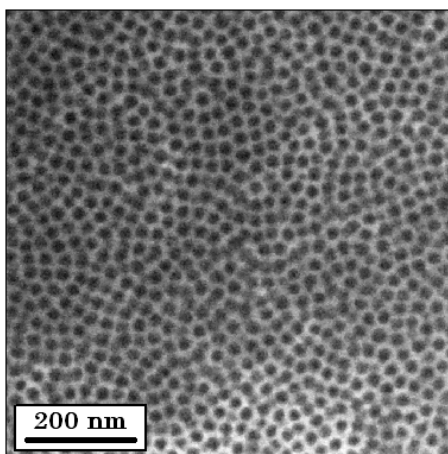


Fig. 119. SEM image of the as-prepared ZrO₂ nanoporated membrane.

These so prepared ZrO₂ membranes with nanoporations were used as a template for the following deposition of magnetic Co/Pt multilayer films. Using dc-magnetron sputter deposition (Ar⁺ sputter pressure: 8.2×10^{-3} mbar) at room temperature, a 4.8-nm-thick Pt seed layer was deposited onto the substrates followed by 8 repetitions of the bilayer Co(0.28 nm)/Pt(0.76 nm) and a Pt cover layer of 1.91 nm nominal thickness to prevent oxidation of the system. In addition, a reference sample grown directly on a planar SiO₂(100 nm)/Si(100) substrate was prepared. Superconductive quantum interference device (SQUID) characterization of the reference sample shows the presence of an out-of-plane easy axis of magnetization with a uniaxial magnetic anisotropy constant K_U of about 3×10^5 J/m³ and a saturation magnetization M_S of about 0.6 T.

The morphology of the Co/Pt multilayer stack with respect to the underlying nanoporated template plays an important role in the magnetic coupling between the

material within the nanoporations and the surrounding film. Therefore, in the following a detailed description of the structural properties of the samples after the deposition of the metal film will be presented.

Structural characterization of the samples after Co/Pt multilayers deposition was performed using the C_s -corrected SuperSTEM I at the SuperSTEM Laboratory Daresbury (UK) in high-angle annular dark field (HAADF) mode. The micrographs in Fig. 120 reveal a cross-sectional view of the sample. Different parts of the sample can be distinguished: silicon substrate (bottom), natural SiO_2 layer, ZrO_2 layer and multilayer stack. In the polycrystalline metal film, the pure platinum layers (seed and cover layer) appear brighter than the multilayer part. The alternating contrast in the multilayer area corresponds to the Co/Pt bilayers. The zirconia layer was found to be polycrystalline with smooth height variations in the planar part of the film. In addition, the depth of the perforations in the zirconia layer is about 8 nm, reaching through almost the complete thickness of the layer (about 10 nm).

The side walls of the perforations have different shapes (Fig. 120): on the one hand side, perforations with steep or even negatively inclined side-walls (i.e. bottom wider than top) cause an abrupt height change in the metal layer (Fig. 120(a)). In addition, positively inclined side-walls with a small step are observed (Fig. 120(c)). In that case, the step in the zirconia layer again results in an abrupt height change of the multilayer stack. However, along the inclination, the magnetic film follows the smooth variation in the substrate morphology and therefore bends down towards the perforation, preserving the multilayer structure along the inclination (Fig. 120(b)). Due to the interfacial origin of

perpendicular magnetic anisotropy in Co/Pt multilayers, their growth onto positively inclined side-walls might result in a tilt of the easy axis of magnetization [193, 203].

The thickness of the Pt seed layer and the thickness of the multilayer stack with respect to the perforation depth was chosen in a way not to create any physical connection between the magnetically active parts in the nanodots and the surrounding film, as it might cause magnetic exchange coupling. In the case of step edges in the magnetic stack (Fig. 120(a)), a clear separation between the multilayers in the nanodots and the surrounding film was observed leading to magnetic exchange decoupling. However, at the locations with positively inclined side-walls (Fig. 120(c)), the reduced height of the steps results in a partial connection of the magnetic parts and thus in exchange coupling. The strength of this coupling might be reduced compared to the continuous film due to the disturbance of the multilayer structure at the connection area.

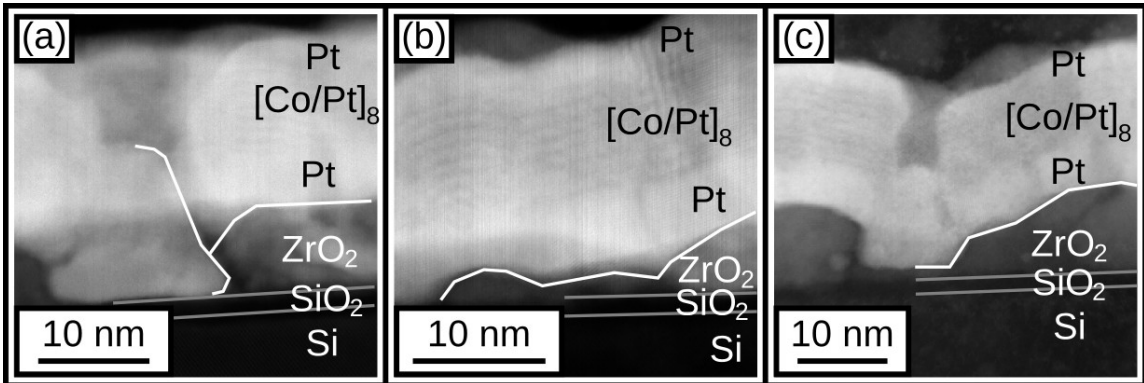


Fig. 120. TEM micrographs of the sample after Co/Pt multilayer deposition. The components of this film can be distinguished in the images as indicated. The multilayer structure is visible. The different types of edges in the zirconia layer and magnetic layer stack are (a) step edge, (b) inclined edge, and (c) combination of a small step and an inclination (right side of the perforation).

The integral magnetic properties of the samples grown on nanoporous membranes were characterized using polar magneto-optical Kerr effect (MOKE)

magnetometry with a focused beam operating at a wavelength of 670 nm. The orientation of the applied magnetic field with respect to the sample normal, θ , can be varied between 0° (perpendicular to the substrate plane) and 90° (in the substrate plane) without changing the polar detection geometry thus allowing to perform an angular dependent measurement. The hysteresis loop taken at $\theta = 0^\circ$ shows full remanence, with a coercive field of about 2 kOe (Fig. 121). Please note that assuming the presence of two distinct magnetic subsystems (nanodots and surrounding film), a double-step hysteresis loop is expected and was observed in the case of Co/Pt multilayers deposited onto nanoporations with an average size of 67 nm [210]. However, a single-step loop was measured by MOKE in agreement with the expected (partial) magnetic exchange coupling.

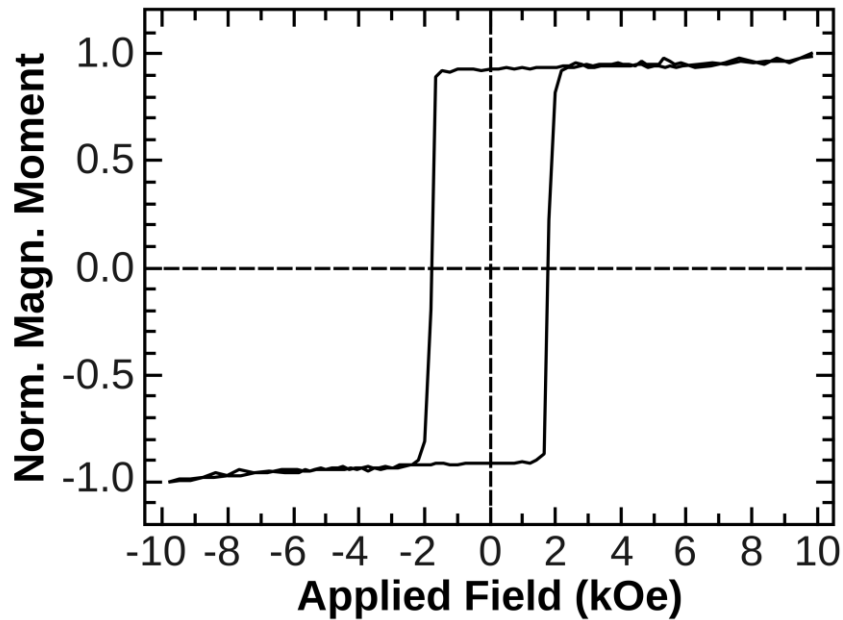


Fig. 121. Polar MOKE hysteresis loop taken at $\theta = 0^\circ$.

To study the magnetization reversal behavior, a series of remanence curves was measured using MOKE by first saturating the sample and then exposing it to a reverse magnetic field. The series of remanence curves taken at different angles θ is shown in Fig. 122(a). The remanence curve taken at $\theta = 0^\circ$ reveals a similar shape to the hysteresis loop indicating that the magnetization reversal process observed in an applied field is irreversible. The increase of the angle θ substantially influences the switching field (Fig. 122(a)). Please note that the switching field $H_{SW}(\theta)$ is defined analogous to the coercive field by $H_{SW}(\theta) = H(\theta, M = 0)$, where M is the remanent magnetic moment. The angular dependence of the switching field shows Kondorsky-like behavior, which is indicative of a depinning process of 180° domain walls in a material with uniaxial anisotropy, however with a substantial delay at high angles (Fig. 122(b)). In this respect, it is important to mention that the Kondorsky model [24] is derived in the assumption that the quality factor $Q (= K_U/K_{shape})$ is infinitely large, which is true for rather hard magnetic materials. For the Co/Pt multilayers under study the estimation for the quality factor gives a value of $Q \approx 2.1$. In this case the influence of the demagnetizing fields on the reversal behavior of the film is expected to alter the angular dependence of the switching field. Ghidini et al. [212] have recently presented an analytical formalism to account for finite values of Q . The best fit of the experimental data in the frame of the Ghidini model is shown in Fig. 122(b) (dotted line). The fit was achieved for $Q = 2.6$ assuming the internal critical threshold for irreversible switching of 2 kOe (switching field), and supports the assumption of domain wall depinning as the decisive coercivity mechanism.

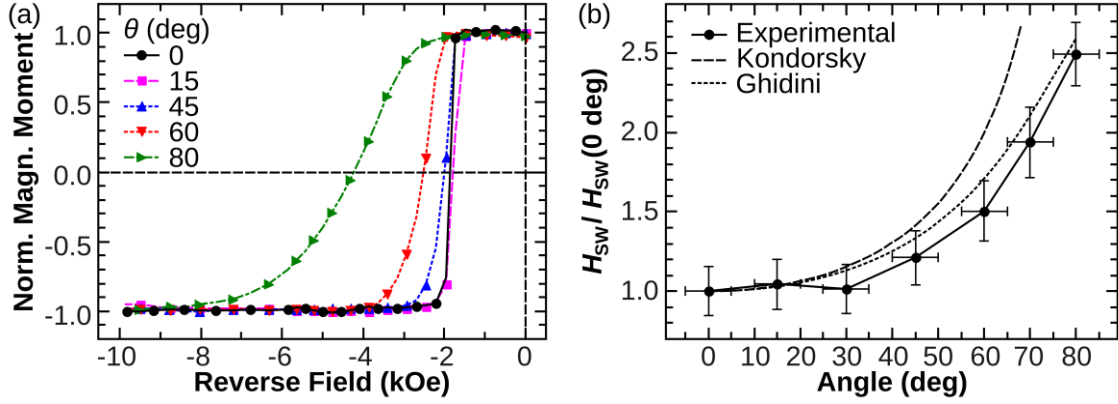


Fig. 122. (a) Remanence curves taken at different θ . (b) Angular dependence of the switching field. The Kondorsky-like [Kondorsky 1940] [24] behavior (dashed curve) and the fit according to Ghidini [212] (dotted curve) with a quality factor of $Q=2.4$ have been plotted for comparison.

To visualize the depinning process, an in-field MFM study has been performed using a home-built in-field MFM stage [213], working with the lift mode, which allows one to gain magnetic and topographic information at the same time. The study of pinning of magnetic domain walls in the system was performed starting from an ac-demagnetized state [203]. The evolution of the magnetic domain pattern is shown in Fig. 123. The MFM images show that an initial increase of the magnetic field up to 1.2 kOe results in only minor changes of the shape of the magnetic domains (some of them are marked in Fig. 123(a-d)). The length scale of these changes of the order of 30 nm and multiples and the resulting shape of the domains suggests motion of the domain wall from one nanoporation to another. However, due to the limited resolution of the MFM setup, it is not possible to judge whether the pinning of domain walls takes place on the positions of the nanoporations (period of 34 nm). Further increase of the magnetic field above 1.2 kOe results in a rapid vanishing of magnetic domains (not shown). The MFM images were used to construct an initial curve of the magnetization (Fig. 123(e)) by considering

the ratio, m , between the areas with a magnetization pointing parallel (S_p) and antiparallel (S_a) to the moment of the MFM tip: $m = (S_p - S_a)/(S_p + S_a)$. In a magnetic field of up to 1.2 kOe the magnetization only slowly increases with increasing the applied field. At 1.2 kOe a sudden rise of the magnetization can be observed, afterwards saturation is reached at about 1.8 kOe. The relatively weak increase of m at fields smaller than 1.2 kOe is an indication of the domain wall pinning in the system [202, 214-215].

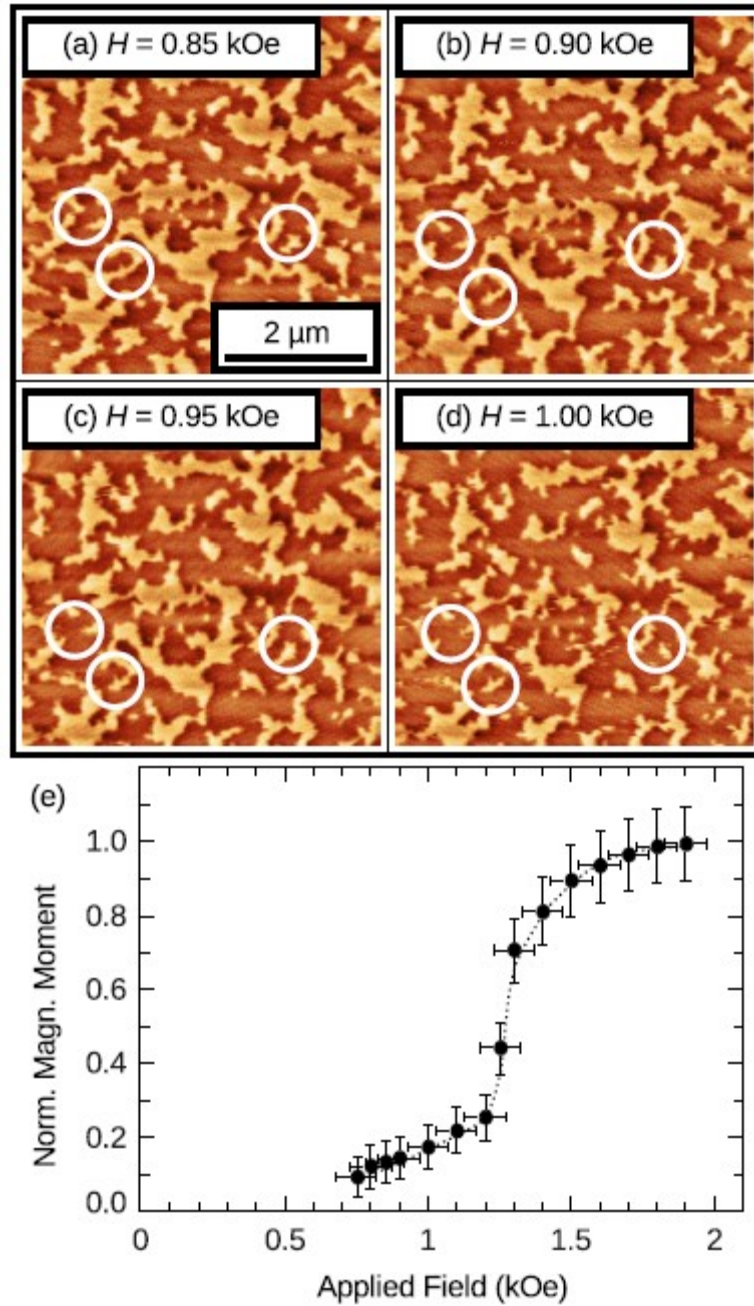


Fig. 123. ((a)–(d)) In-field MFM images of Co/Pt multilayers grown on a ZrO_2 nanoporated membrane. The applied field is indicated in the respective panel. The measurement is started from an ac-demagnetized state. The scale bar in panel (a) applies to all panels. (e) Initial magnetization curve of Co/Pt constructed from the analysis of the MFM images. The dotted line is a guide to the eye.

To follow the displacement of magnetic domain walls in more details, high resolution MFM (hr-MFM) imaging of a single magnetic domain was carried out using a Nanoscan hr-MFM with a spatial resolution of the magnetic data of about 10 nm. This high resolution is achieved under vacuum and by operation in non-contact mode. The obvious drawback is that no topographic information is recorded which could be used to correlate the change of the shape of a domain to some topology. The modification of the shape and size of the magnetic domain in an applied external magnetic field is shown in Fig. 124. In agreement with the discussion above, an increase of the applied magnetic field up to 1.25 kOe does not result in a significant change in the shape of the magnetic domain (Fig. 124(a-c)). In a field of 1.50 kOe, the pinning threshold is overcome and part of the domain is switched (Fig. 124(d)). The reversal results in the formation of elongated features (Fig. 124(e), enlarged in Fig. 124(g)). Remarkably, the length of these features measured along the perimeter of the domain are integer multiples of (34 ± 2) nm. Combined with the fact that such small features are not favorable in highly exchange coupled Co/Pt films with a low amount of pinning and nucleation sites, we attribute the stabilization of those features to the pinning of domain walls on the structural inhomogeneities provided by the nanoperforated template. Further increase of the applied field leads to the complete switching of the domain (Fig. 124(f))

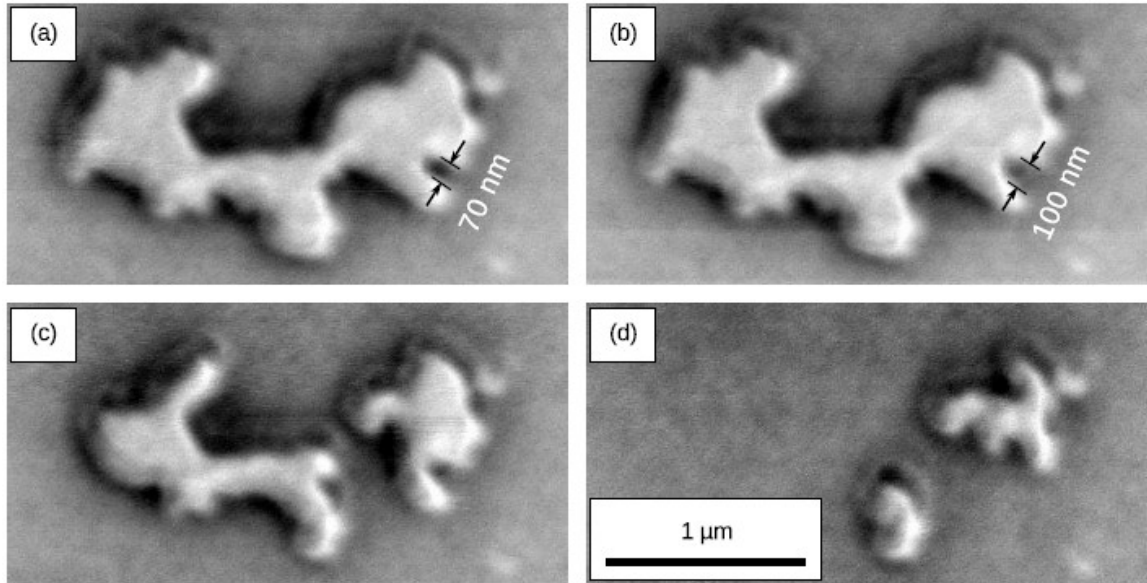


Fig. 124. High-resolution in-field MFM images taken on the sample in various applied fields: (a) 0.50 kOe, (b) 1.00 kOe, (c) 1.50 kOe, (d) 1.75 kOe. At fields below 1.50 kOe, only slight changes in the domain configuration are observed ((a), (b)). At higher fields, domains vanish rapidly ((c), (d)) by forming elongated features, which are not favorable in a film with a low number of pinning sites. The scale bar in panel (d) applies to all panels. The displacement of the domain wall indicated in panel (a) and (b) of about 30 nm is in good agreement with the period of the underlying nanoporated ZrO_2 template (34 nm).

- Micromagnetic Simulations on Pinning/ Depinning Behavior

To better understand the pinning behavior of magnetic domain walls in a complex system consisting of magnetic nanodots surrounded by a continuous magnetic film, a series of micromagnetic simulations was performed. Please note that all previous theoretical studies on PPM were done on exchange coupled magnetic films with holes acting as pinning sites. Our system is different due to the presence of magnetic nanodots in the holes allowing for magnetostatic as well as exchange coupling between the magnetic nanodots and surrounding film. Therefore, the micromagnetic model was adopted to account for these coupling effects. In the following we present a comparison of magnetic domain wall pinning in systems with and without nanodots.

Finite element (FE) micromagnetic simulations using the simulation package FEMME [216] were performed. The size of the FE model was $280 \times 280 \times 8 \text{ nm}^3$ with nanoporations of a diameter of 18 nm and a period of 32 nm. The 8-nm-thick magnetic nanodots were positioned 4 nm lower than the film. The magnetic parameters were adopted from the experiments. Following the discussion above, reduced exchange coupling between the nanodots and the surrounding film is expected. However, since the exchange coupling coefficient between the film and a nanodot, A_{int} , could not be determined experimentally, it was systematically varied from 0 to 100% of the exchange coefficient of the planar film, $A_{\text{film}} = 1 \times 10^{-6} \text{ ergs/cm}$. Please note that this exchange parameter between the planar film and the nanodots should be treated as an effective one as the real topography of the magnetic film near the nanoporations (including tilt of the easy axis of magnetization due to inclination of the side walls) is not accounted for in the

model. The exchange coefficient and anisotropy constant within the nanodots was taken to be the same as for the continuous film. In order to access the depinning field of a domain wall, the magnetic configuration shown in Fig. 126(a) was considered. The depinning field H_d is defined as the field required to move a domain wall from the initial position. The depinning field was very precisely determined, by comparing changes of the magnetization curve and magnetic energies. As the first step of the depinning field determination, external field strength was reduced regularly as Fig. 125(a), to confirm if the domain wall is depinned or not. Once H_d is overcome, fields as small as 20 Oe are sufficient to move the domain wall to the position of the next pinning site. The latter case is well described in literature [86, 199]. Fig. 125(b) shows the magnetization curve for the case of $A_{int} = 0$. At a certain external field marked with an arrow, the magnetization is drastically reduced. The field is to be defined as a depinning field, but, precise definition of it is not easy. Therefore we investigated the sum of exchange energy density (e_{exch}) and anisotropy energy density (e_{ani}). Since the length of the domain wall is increasing as the domain wall is about to escape from pinning, the $e_{exch} + e_{ani}$ rises. The $e_{exch} + e_{ani}$ drops as soon as the domain wall is pinned to other nanopertorations. The comparison of the $e_{exch} + e_{ani}$ with magnetization curve is shown in Fig. 125(c). The local maximum of the $e_{exch} + e_{ani}$ coincides with the drop of magnetization.

Please note that the contribution of the demagnetization field is somewhat arbitrary, because it strongly depends on the specimen size and the specific magnetic domain configuration of the film, thus, the demagnetization field is not taken into account.

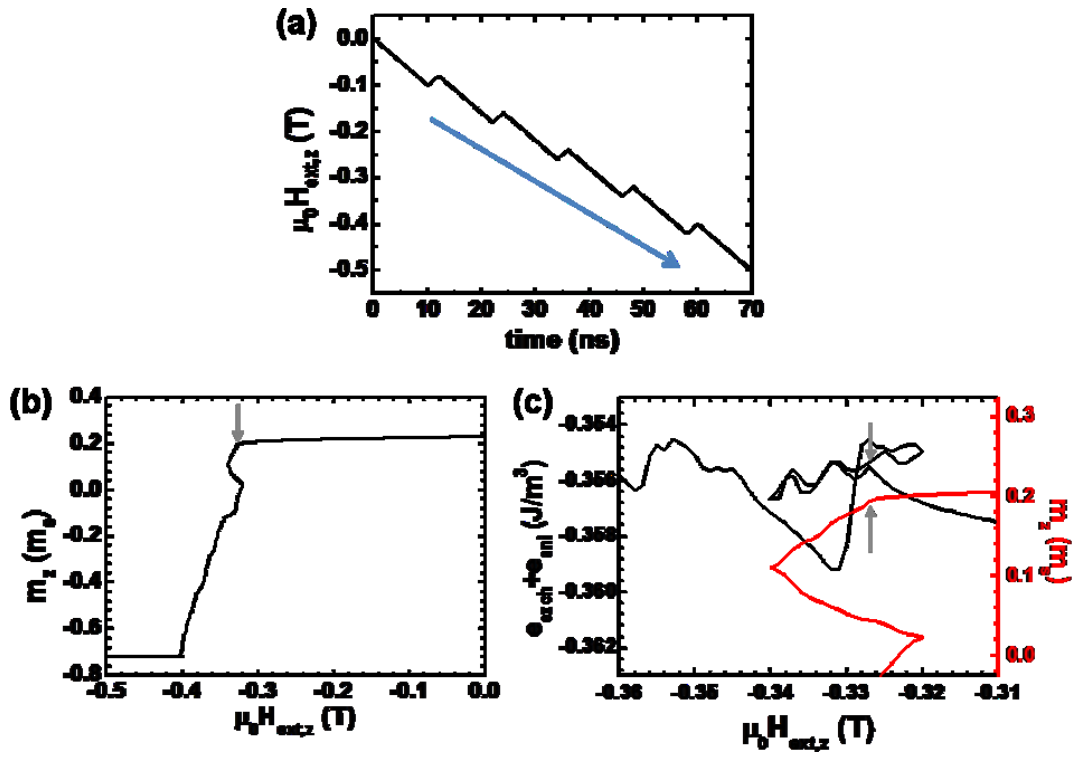


Fig. 125. (a) Applied field profile for domain wall motion as a function of time. (b) Magnetization of the PPM model as a function of applied field, for the case of $A_{\text{int}} = 0$. (c) Sum of exchange energy and anisotropy energy ($e_{\text{exch}} + e_{\text{ani}}$) compared with the detailed magnetization shown in (b).

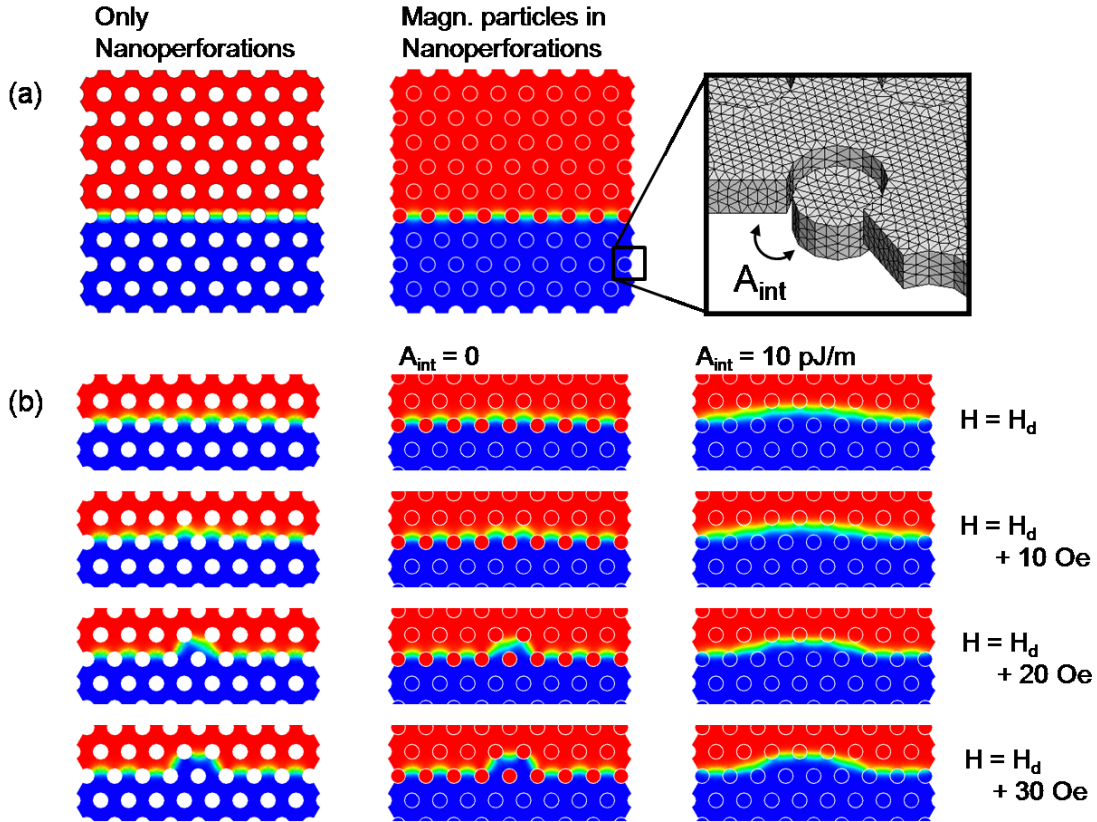


Fig. 126. (a) Initial magnetization states for two types of PPM (b) Domain wall displacement in increasing applied field H .

The simulation data showed that the domain wall pinning behavior highly depends on the exchange parameter A_{int} . As shown in Fig. 126(b), when the magnetic nanodots are fully decoupled from the surrounding magnetic film ($A_{int} = 0$), the pinning behavior is exactly the same as that of the PPM without nanodots. The magnetic state of the nanodots is not affected by the domain wall motion in the continuous film: the dots reverse their magnetization by a coherent rotation process at much higher fields, of about 17 kOe. On the contrary, when nanodots and surrounding film are perfectly coupled ($A_{int} = 10 \text{ pJ/m}$), the system behaves like a continuous film in spite of the difference in

morphology (the nanoparticles are located 4 nm below the geometric level of the planar film). In this case, the domain wall is not pinned but passes through the nanodots.

When $A_{\text{int}} = 0$ (no exchange coupling between planar film and nanodots), the value of $H_d = 3.26$ kOe for the depinning field is obtained for the PPM with magnetic nanodots, being the same as if no nanodots were present in the system. As A_{int} is increased from 0 to 0.1 pJ/m (which corresponds to 1% of the exchange coupling constant of the planar film), a larger depinning field H_d is required as the unswitched domain configuration in the nanodots stabilizes the pinned domain wall. As a result, H_d increases linearly with A_{int} in the range of $0 < A_{\text{int}} < 0.1$ pJ/m (Fig. 127). It is important to mention that such an increase of the depinning field cannot be observed in a simulation of conventional PPM, i. e. for simple nanoperforations (Fig. 127, dashed and dotted line): The effect is a peculiarity of the system with an additional source of exchange energy acting against the external magnetic field and thus influencing the domain wall propagation. The possibility to tune the depinning field by changing the exchange coupling between magnetic material inside the nanoperforations and surrounding exchange coupled film is of great importance as a higher depinning field allows for enhanced stability of the written information bit. However, the $H_d(A_{\text{int}})$ dependence exhibits a maximum at $A_{\text{int}} = 0.1$ pJ/m, as due to the increased exchange between the nanodots and the surrounding film the magnetic domain wall can propagate into the particle and thus the entire system behaves like an exchange coupled continuous film ($H_d = 0$ when $A_{\text{int}} = A_{\text{film}} = 10$ pJ/m).

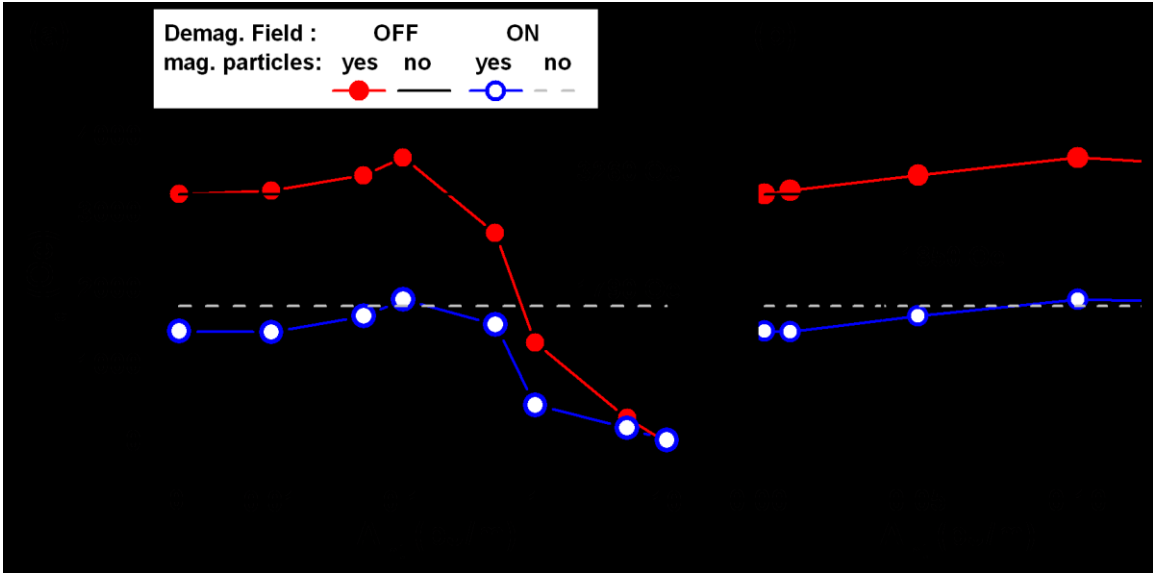


Fig. 127. (a) Depinning fields H_d of the percolated media as a function of the intergranular exchange coupling constant A_{int} between magnetic nanoparticles and film. The attached numbers are the pinning fields of the media without magnetic particles. (b) The range $0 < A_{int} < 0.1$ pJ/m is enlarged with a linear scale of A_{int} . Please note that the key applies for both panels of the figure.

Accounting for the demagnetization field results in a reduction of the depinning field H_d by about a factor of 2 for all coupling coefficients A_{int} (Fig. 127). Fig. 128 displays the nucleation and saturation fields for the PPM with and without nanodots as a function of A_{int} . Contrary to the large influence of the exchange between the film and magnetic particles on the depinning field, in the assumed model with hard nanodots, the coupling is essentially without effect on the saturation field of the planar film and shows only a slight increase in the nucleation field of the planar film as A_{int} becomes larger. This is due to the strong field required for the nucleation of the inverse magnetic domain in the dots compared to the depinning field (Fig. 127 and Fig. 128). The nucleation field is more than 5 kOe larger than H_d . The nucleation field slightly increases as A_{int} becomes

larger, but the saturation field is found to be independent of the exchange coupling between the magnetic film and the nanodots (Fig. 128).

Moreover, it is important to note that with an increase of the exchange coupling between the nanodots and the surrounding film the transition from double-step to a single-step hysteresis loop is observed. For the experimentally determined magnetic properties, single-step hysteresis loops were found in the simulation for all A_{int} larger than 5% of A_{film} . On the other hand, the value of A_{int} cannot be significantly larger than this value, as this would lead to a clear decrease of the depinning field which is not observed experimentally. This reduced coupling is in line with the assumptions drawn on the basis of the structural investigation of the magnetic layer.

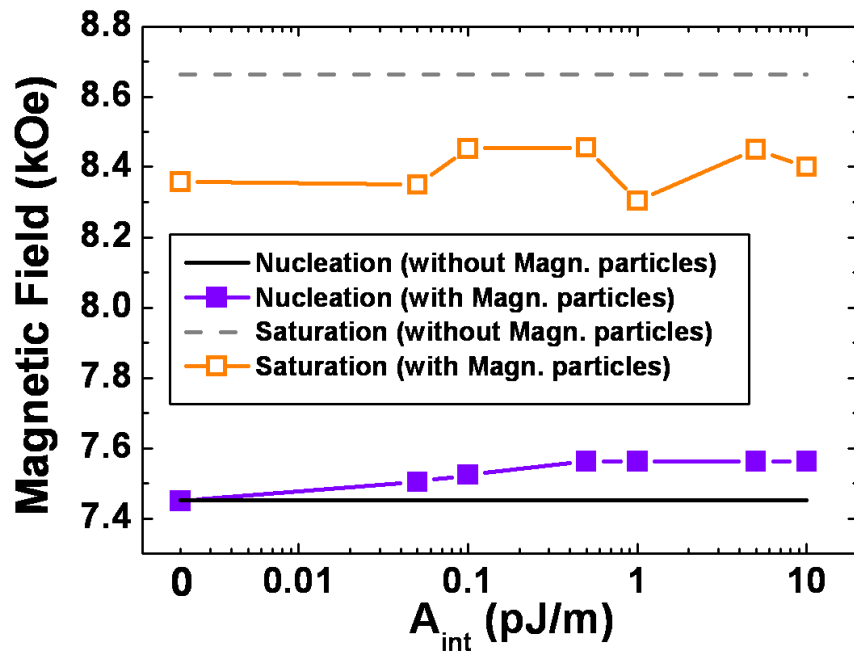


Fig. 128. Nucleation fields and saturation fields of the percolated film, as a function of A_{int} , under the presence of demagnetization field.

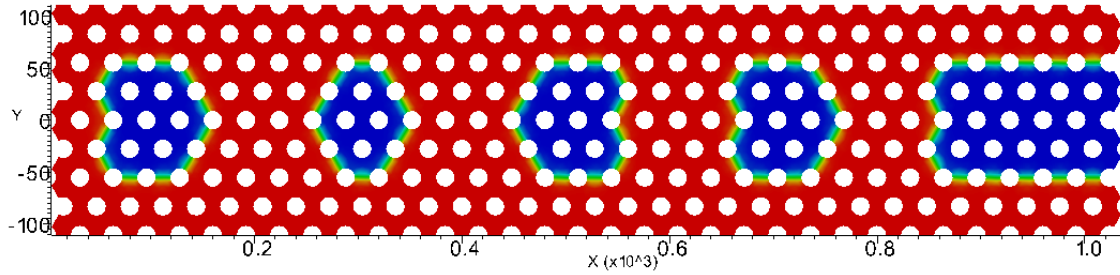


Fig. 129. Written bit states on the perpendicular percolated media.

Recording simulation using moving head field was performed on lengthened Model2, of which dimension is about 1000 nm x 200 nm as shown in Fig. 129. The initial state was assumed to be saturated to +z direction. The writing head with dimensions of 45 nm x 20 nm is flying 5 nm above the percolated media model with a velocity of 20 m/s. From the clearly written bits, it seems to be successful. However, honestly speaking it failed. If it was successful, bits should be written on very narrow region comparable to the head width. In Fig. 129, the bit width of 100 nm corresponds to the width of field box used in recording simulations. The problem of writing simulation on PPM is that nucleation field (7 ~ 8 kOe) is always larger than pinning field (0 ~ 4 kOe) in our modes. In the scheme the recording simulation always fails.

The contribution of the inclined rims shown in Fig. 120 was studied using additional model, shown in Fig. 130. The entire dimension was comparable with the previous model (Fig. 126). The only difference is that the rim of the nanoporations and the side wall of the magnetic dot inside of the hole are inclined towards the center of the nanoporations. The inclination θ was varied from 0 to 30°.

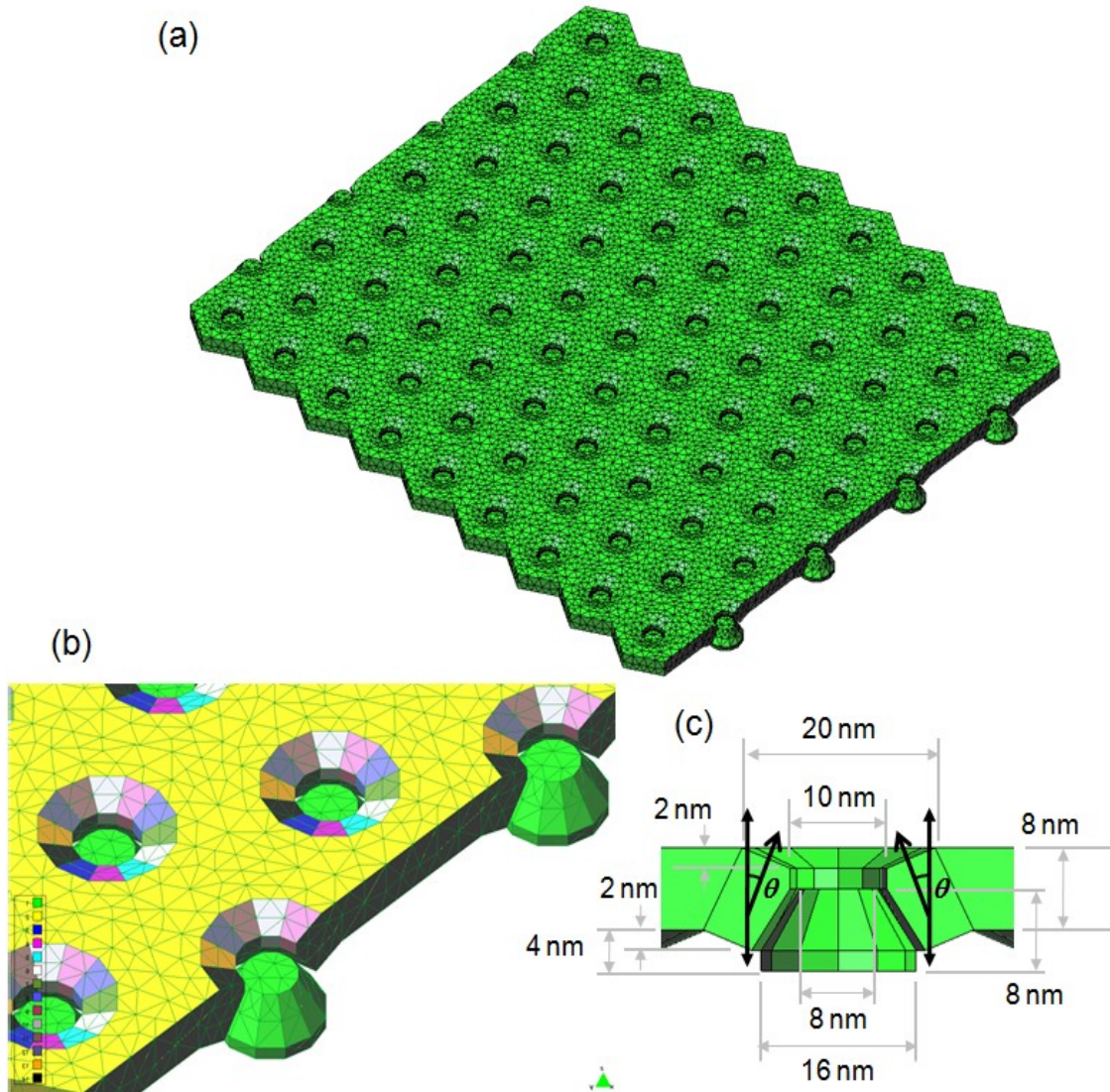


Fig. 130. A modified PPM model for considering realistic geometry, with an inclination angle θ .

In order to investigate the contributions of the magnetic dots, a PPM model with inclined rims without magnetic dots are prepared as well (Fig. 131). From the cross sectional STEM images shown in Fig. 120, the magnetic dots do not have a stripe contrast of Co/Pt multilayer film. The feature means that the magnetic dots' magnetic properties could be far from those of the Co/Pt multilayers in continuous area.

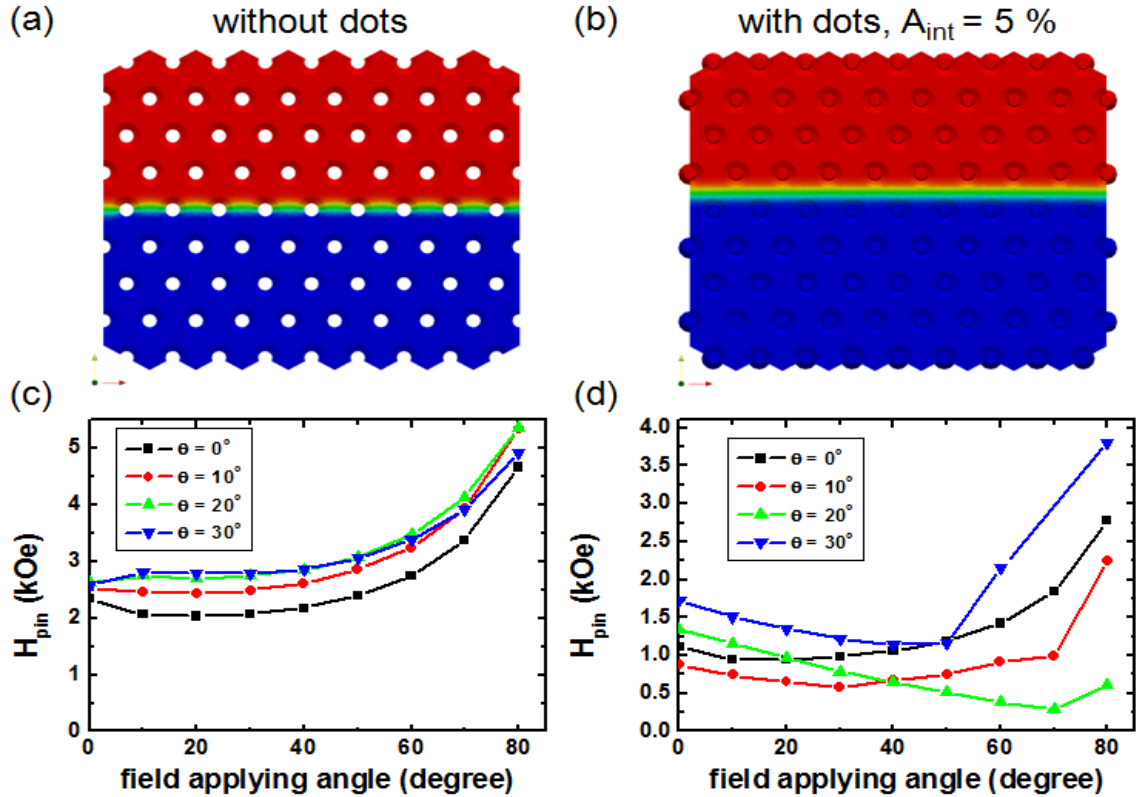


Fig. 131. PPM models with inclined rims (a) without and (b) with magnetic dots inside nanoporations. In (b) the intergranular exchange coupling coefficient $A_{int} = 0.5$ pJ/m. (c-d) Angular dependency of the switching field with various inclination angle θ . (c) is for the model (a) without magnetic dots, where (d) is for (b)

For the case of the model without magnetic dots, the domain wall is stabilized across the nanoporations whereas the domain wall of the model with dots was on the planar film. In the angular dependency of the model without magnetic dots Kondorsky type behaviors are observed. The easy axis inclination θ affected only on the offset among the curves when θ was larger than 10° . On the other hand, under the bits' presence, the Kondorsky type behavior became much weaker: the switching field became more uniform as a function of the field applying angle.

- Conclusion

By analyzing magnetic domain patterns, we have shown that deposition of Co/Pt multilayers onto a nanoporated template with a period of 34 nm results in strong pinning of the magnetic domain walls. Owing to the structural properties at the edges of the nanoporations, exchange coupling between the magnetic material within the perforations (nanodots) and the surrounding film is expected. The influence of the magnetic coupling on the pinning field for the magnetic domain walls was investigated using micromagnetic simulations. It was found that the pinning strength is determined by the intergranular exchange coupling between the film and the nanodots in the system. We showed that magnetic exchange coupling between the material deposited into the perforations and the surrounding magnetic film is an important issue that might limit the performance of this type of PPM.

Furthermore, a reduction of the perforation size and template period is required to allow the media to support 1 Tbit/inch², which is a subject of current research. However, pinning of magnetic domain walls at this ultimate length scales is still an open question.

4. Conclusion

This work has been devoted to the study of advanced recording media including particulate media and sputtered granular for tape recording, FePt $L1_0$ based exchange spring media, bit patterned media, percolated perpendicular media for hard disk. In order to expect the magnetization of a media, at first, the microstructure of the given media is deeply investigated using transmission electron microscopy. The chemical composition and phase distributions were studied by various techniques using electron diffraction and electron energy emission. In many times the microstructure taken by myself was verified by comparing with the results of another measurements performed by other groups: x-ray diffraction, hysteresis loops measurement and atomic/magnetic force microscopy. Micromagnetic simulations were performed based on the information about the microstructure and magnetic properties.

By performing micromagnetic simulations on the realistic advanced recording media, the followings are found.

- (1) In order to recording performance of the coherently switching media such as particulate and granular tape recording media, the writing head field should be homogeneous to magnetize every single particles or grains in a bit. Otherwise the stray field induces larger bit transitions, which reduces the read back performance. SPT head with SUL head field applied on perpendicularly aligned media always show the best recording quality.
- (2) Inhomogeneous magnetization reversal process can be a good approach to reduce switching field of a hard magnetic material, i.e. FePt $L1_0$ phase. One of the best

way is to use exchange spring scheme: adding inhomogeneity on the magnetic properties. Reversal process is triggered at the softer region, then it helps reversal of the hard layer using interlayer exchange coupling.

- (3) Writing head field profile is very crucial for the reversal process of the exchange spring media. Since the writing head field is applied in a very short time (~ 0.1 ns) with a certain large amount of incident angle, the actual reversal process of a magnetic bit is closer to the precessional switching. Sometimes the writing fails in spite of very strong field if the field excitation position is not properly chosen.
- (4) Inducing inhomogeneous magnetization reversal becomes more efficient if the softer layer is exposed to the stronger field by placed on top layer. In this case not only the switching field is reduced, but also the jitter transitions are reduced assuming the same amount of K_1 deviation.
- (5) In exchange spring media, the thickness of the soft layer and the interlayer coupling between the soft and hard layer are very important for the successful operation. If the oxide layer is inserted between the soft and hard layers, the switching field reduction is limited.
- (6) It is said that many interlayers are required between the hard and soft layers to reduce the switching field effectively. However, if the hard and soft layers have a rough interface between them, exchange spring media consisted of only two phases works as good as the graded media with many interlayers. Reversal domain wall nucleation and propagation process of the media is same to the one with many interlayers.

REFERENCE

- [1] V. Poulsen, Method of recording and reproducing sounds or signals, in: U.S.P. Office (Ed.), United States, 1900.
- [2] F. Engel, P. Hammar, R.L. Hess, A Selected History of Magnetic Recording, in, 2006.
- [3] H.J. Richter, The transition from longitudinal to perpendicular recording, *Journal of Physics D: Applied Physics*, 40 (2007) R149.
- [4] A. Shilov, Samsung Shows Off Prototype of 4TB Hard Disk Drive., in, 2011.
- [5] B.C. Stipe, T.C. Strand, C.C. Poon, H. Balamane, T.D. Boone, J.A. Katine, J.-L. Li, V. Rawat, H. Nemoto, A. Hirotsune, O. Hellwig, R. Ruiz, E. Dobisz, D.S. Kercher, N. Robertson, T.R. Albrecht, B.D. Terris, Magnetic recording at 1.5 Pb m⁻² using an integrated plasmonic antenna, *Nat Photon*, 4 (2010) 484-488.
- [6] G. Cherubini, R.D. Cideciyan, L. Dellmann, E. Eleftheriou, W. Haeberle, J. Jelitto, V. Kartik, M.A. Lantz, S. Olcer, A. Pantazi, H.E. Rothuizen, D. Berman, W. Imaino, P.O. Jubert, G. McClelland, P.V. Koeppel, K. Tsuruta, T. Harasawa, Y. Murata, A. Musha, H. Noguchi, H. Ohtsu, O. Shimizu, R. Suzuki, 29.5-Gb/in² Recording Areal Density on Barium Ferrite Tape, *Magnetics, IEEE Transactions on*, 47 (2011) 137-147.
- [7] Wikipedia, Hard disk drive, in, 2011.
- [8] A. Aharoni, Introduction to the theory of ferromagnetism, 2nd ed., Oxford University Press, Oxford ; New York, 2000.
- [9] H. Kronmüller, M. Fähnle, *Micromagnetism and the Microstructure of Ferromagnetic Solids*, Cambridge University Press, Cambridge, 2003.
- [10] R.C. O'Handley, *Modern Magnetic Materials: Principles and Applications*, John Wiley and Sons, Inc., 1999.
- [11] R. Engel-Herbert, T. Hesjedal, Calculation of the magnetic stray field of a uniaxial magnetic domain, *J Appl Phys*, 97 (2005) 074504-074504.
- [12] L.D. Landau, E.M. Lifshitz, On the theory of the dispersion of magnetic permeability in ferromagnetic bodies., *Physikalische Zeitschrift der Sowjetunion*, 8 (1935) 153-169.

- [13] C. Kittel, J.K. Galt, Ferromagnetic Domain Theory, Solid State Physics, 3 (1956) 437.
- [14] M. Sato, Y. Ishii, Simple and approximate expressions of demagnetizing factors of uniformly magnetized rectangular rod and cylinder, J Appl Phys, 66 (1989) 983-985.
- [15] T. Schrefl, J. Fidler, K.J. Kirk, J.N. Chapman, A higher order FEM-BEM method for the calculation of domain processes in magnetic nano-elements, Ieee T Magn, 33 (1997) 4182-4184.
- [16] T.R. Koehler, Hybrid FEM - BEM method for fast micromagnetic calculations, Physica B: Cond. Mat., 233 (1997) 302-307.
- [17] H. Forster, T. Schrefl, R. Dittrich, W. Scholz, J. Fidler, Fast boundary methods for magnetostatic interactions in micromagnetics, Ieee T Magn, 39 (2003) 2513-2515.
- [18] J. Brown, William Fuller, Micromagnetics, Interscience, 1962.
- [19] E.C. Stoner, E.P. Wohlfarth, A mechanism of magnetic hysteresis in heterogeneous alloys, Philos. Trans. Roy. Soc. London, A240 (1948) 599-642.
- [20] R.P. Cowburn, D.K. Koltsov, A.O. Adeyeye, M.E. Welland, D.M. Tricker, Single-Domain Circular Nanomagnets, Phys Rev Lett, 83 (1999) 1042.
- [21] W.v. Engen, micromagnetism, nanomagnetism: magnetic behavior on a small scale, in: Syllabus, Eindhoven University of Technology, Eindhoven, 2011.
- [22] A. Holz, A. Hubert, Wandstrukturen in dünnen magnetischen Schichten, Zeitschrift für Angewandte Physik, 20 (1969) 145-152.
- [23] A. Aharoni, Reduction in Coercive Force Caused by a Certain Type of Imperfection, Physical Review, 119 (1960) 127.
- [24] E. Kondorsky, On the hysteresis in ferromagnetics, J. Phys. (Moscow), II (1940).
- [25] H.J. Richter, Media requirements and recording physics for high density magnetic recording, Magnetics, IEEE Transactions on, 29 (1993) 2185-2201.
- [26] T. Devolder, C. Chappert, Precessional switching of thin nanomagnets: analytical study, The European Physical Journal B - Condensed Matter and Complex Systems, 36 (2003) 57-64.

- [27] W.F. Brown, Theory of the Approach to Magnetic Saturation, *Physical Review*, 58 (1940) 736.
- [28] N. Buiron, S. He, L. Hirsinger, S. Depeyre, M. Bernadou, R. Billardon, From micromagnetic to multiscale modeling of the coupled magnetoelastic behavior of ferromagnetic materials, *Physica B: Condensed Matter*, 306 (2001) 33-37.
- [29] D.Z. Bai, J.-G. Zhu, W. Yu, J.A. Bain, Micromagnetic simulation of effect of stress-induced anisotropy in soft magnetic thin films, *J Appl Phys*, 95 (2004) 6864-6866.
- [30] C. Ragusa, M. d'Aquino, C. Serpico, B. Xie, M. Repetto, G. Bertotti, D. Ansalone, Full Micromagnetic Numerical Simulations of Thermal Fluctuations, *Magnetics, IEEE Transactions on*, 45 (2009) 3919-3922.
- [31] O.A. Chubykalo, B. Lengsfeld, B. Jones, J. Kaufman, J.M. Gonzalez, R.W. Chantrell, R. Smirnov-Rueda, Micromagnetic modelling of thermal decay in interacting systems, *J Magn Magn Mater*, 221 (2000) 132-136.
- [32] G. Hrkac, M. Kirschner, F. Dorfbauer, D. Suess, O. Ertl, J. Fidler, T. Schrefl, Three-dimensional micromagnetic finite element simulations including eddy currents, *J Appl Phys*, 97 (2005) -.
- [33] G. Hrkac, M. Kirschner, F. Dorfbauer, D. Suess, O. Ertl, J. Fidler, T. Schrefl, Influence of eddy currents on the effective damping parameter, *J Appl Phys*, 99 (2006) -.
- [34] O. Ertl, G. Hrkac, D. Suess, M. Kirschner, F. Dorfbauer, J. Fidler, T. Schrefl, Multiscale micromagnetic simulation of giant magnetoresistance read heads, *J. Appl. Phys.*, 99 (2006) 08S303.
- [35] P. Wadhwa, M.B.A. Jalil, S.G. Tan, Micromagnetic modeling with eddy current and current-induced spin torque effect, *J Appl Phys*, 98 (2005) 123902-123904.
- [36] G. Hrkac, T. Schrefl, J. Dean, A. Goncharov, S. Bance, D. Allwood, D. Suess, J. Fidler, Micromagnetics of single and double point contact spin torque oscillators, *J Appl Phys*, 105 (2009) -.
- [37] G. Hrkac, T. Schrefl, J. Dean, A. Goncharov, S. Bance, D. Suess, J. Fidler, Internal effective field sources for spin torque nanopillar oscillators, *J Appl Phys*, 105 (2009) -.

- [38] L. Torres, L. Lopez-Diaz, E. Martinez, G. Finocchio, M. Carpentieri, B. Azzerboni, Coupling of spin-transfer torque to microwave magnetic field: A micromagnetic modal analysis, *J Appl Phys*, 101 (2007) 053914-053918.
- [39] J.-G. Zhu, X. Zhu, Y. Tang, Microwave Assisted Magnetic Recording, *Magnetics, IEEE Transactions on*, 44 (2008) 125-131.
- [40] A.E. LaBonte, Two-Dimensional Bloch-Type Domain Walls in Ferromagnetic Films, *J Appl Phys*, 40 (1969) 2450-2458.
- [41] M.E. Schabes, H.N. Bertram, Magnetization processes in ferromagnetic cubes, *J Appl Phys*, 64 (1988) 1347-1357.
- [42] Y. Nakatani, Y. Uesaka, N. Hayashi, Direct Solution of the Landau-Lifshitz-Gilbert Equation for Micromagnetics, *Japanese Journal of Applied Physics*, 28 (1989) 2485.
- [43] M.R. Scheinfein, J.L. Blue, Micromagnetic calculations of 180° surface domain walls, *J Appl Phys*, 69 (1991) 7740-7751.
- [44] D.V. Berkov, K. Ramstöck, A. Hubert, Solving Micromagnetic Problems. Towards an Optimal Numerical Method, *physica status solidi (a)*, 137 (1993) 207-225.
- [45] J.O. Oti, Numerical micromagnetic techniques and their applications to magnetic force microscopy calculations, *Magnetics, IEEE Transactions on*, 29 (1993) 2359-2364.
- [46] R.D. McMichael, M.J. Donahue, Head to head domain wall structures in thin magnetic strips, *Magnetics, IEEE Transactions on*, 33 (1997) 4167-4169.
- [47] A. Thiaville, D. Tomáš, J. Miltat, On Corner Singularities in Micromagnetics, *physica status solidi (a)*, 170 (1998) 125-135.
- [48] I. Firastrau, D. Gusakova, D. Houssameddine, U. Ebels, M.C. Cyrille, B. Delaet, B. Dieny, O. Redon, J.C. Toussaint, L.D. Buda-Prejbeanu, Modeling of the perpendicular polarizer-planar free layer spin torque oscillator: Micromagnetic simulations, *Phys Rev B*, 78 (2008) 024437.
- [49] C. Seshan, Z. Cendes, Computing magnetic domain patterns for thin film soft magnetic materials, *Magnetics, IEEE Transactions on*, 21 (1985) 2378-2381.
- [50] D. Fredkin, T. Koehler, Numerical micromagnetics by the finite element method, *Magnetics, IEEE Transactions on*, 23 (1987) 3385-3387.

- [51] A. Bagnères-Viallax, P. Baras, J.B. Albertini, 2D and 3D calculations of micromagnetic wall structures using finite elements, *Magnetics, IEEE Transactions on*, 27 (1991) 3819-3822.
- [52] T. Schrefl, J. Fidler, Numerical-Simulation of Magnetization Reversal in Hard Magnetic-Materials Using a Finite-Element Method, *J Magn Magn Mater*, 111 (1992) 105-114.
- [53] K. Ramstöck, T. Leibl, A. Hubert, Optimizing stray field computations in finite-element micromagnetics, *J Magn Magn Mater*, 135 (1994) 97-110.
- [54] R. Hertel, H. Kronmüller, Micromagnetic simulation of the domain structure of a flat rectangular permalloy prism, *J Appl Phys*, 85 (1999) 6190-6192.
- [55] T. Fischbacher, M. Franchin, G. Bordignon, H. Fangohr, A Systematic Approach to Multiphysics Extensions of Finite-Element-Based Micromagnetic Simulations: Nmag, *Magnetics, IEEE Transactions on*, 43 (2007) 2896-2898.
- [56] W. Scholz, J. Fidler, T. Schrefl, D. Suess, R. Dittrich, H. Forster, V. Tsiantos, Scalable parallel micromagnetic solvers for magnetic nanostructures, *Comp Mater Sci*, 28 (2003) 366-383.
- [57] H. Szabolics, J.C. Toussaint, L.D. Buda-Prejbeanu, F. Alouges, E. Krittikis, O. Fruchart, Innovative Weak Formulation for the Landau-Lifshitz-Gilbert Equations, *Magnetics, IEEE Transactions on*, 44 (2008) 3153-3156.
- [58] J. Toussaint, E. Krittikis, F. Alouges, Modélisation Micromagnétique par Eléments Finis avec FEELLGOOD, in.
- [59] H. Fangohr, T. Fischbacher, M. Franchin, G. Bordignon, J. Generowicz, A. Knittel, M. Walter NMAG User Manual, in, 2009.
- [60] A. Vaysset, L. Buda-Prejbeanu, J. Toussaint, U. Ebels, I. Firastrau, B. Die'ny, Numerical evidence of wide frequency tunability of Spin-Transfer Oscillators in absence of applied field., in: *Intermag 2011, Taipei, Taiwan, 2011*, pp. AN-08.
- [61] J. Fidler, T. Schrefl, Micromagnetic modelling - the current state of the art, *J Phys D Appl Phys*, 33 (2000) R135-R156.

- [62] M. Schabes, A. Aharoni, Magnetostatic interaction fields for a three-dimensional array of ferromagnetic cubes, *Magnetics, IEEE Transactions on*, 23 (1987) 3882-3888.
- [63] D. Suess, J. Fidler, T. Schrefl, chapter 2 Micromagnetic Simulation of Magnetic Materials, in: K.H.J. Buschow (Ed.) *Handbook of Magnetic Materials*, Elsevier, 2006, pp. 41-125.
- [64] P. Spekmayer, in, Vienna University of Technology, Vienna, 2003.
- [65] T. Schrefl, J. Fidler, J.N. Chapman, Micromagnetic modelling of multilayer media, *J Phys D Appl Phys*, 29 (1996) 2352-2361.
- [66] D.V. Berkov, Numerical calculation of the energy barrier distribution in disordered many-particle systems: the path integral method, *Journal of Magnetism & Magnetic Materials*, 186 (1998) 199-213.
- [67] G. Henkelman, H. Jonsson, Improved tangent estimate in the nudged elastic band method for finding minimum energy paths and saddle points, *The Journal of Chemical Physics*, 113 (2000) 9978-9985.
- [68] D. Makarov, J. Lee, C. Brombacher, C. Schubert, M. Fuger, D. Suess, J. Fidler, M. Albrecht, Perpendicular FePt-based exchange-coupled composite media, *Appl Phys Lett*, 96 (2010) 062501-062503.
- [69] O. Karlqvist, Calculation of the magnetic field in the ferromagnetic layer of a magnetic drum, *Elanders boktr.; H. Lindståhls bokhandel i distribution, Göteborg, Stockholm*, 1954.
- [70] B.K. Middleton, J.J. Miles, M.M. Aziz, An analytical model of the vector digital magnetic recording process in isotropic thin media, *Journal of Physics D: Applied Physics*, 34 (2001) 879-883.
- [71] R. McCary, Saturation magnetic recording process, *Magnetics, IEEE Transactions on*, 7 (1971) 4-16.
- [72] D. Lindholm, Magnetic fields of finite track width heads, *Magnetics, IEEE Transactions on*, 13 (1977) 1460-1462.
- [73] T. Szczech, P. Iverson, Improvement of the coefficients in field equations for thin-film recording heads, *Magnetics, IEEE Transactions on*, 23 (1987) 3866-3867.

- [74] T. Szczech, P. Iverson, An approach for deriving field equations for magnetic heads of different geometrical configurations, *Magnetics, IEEE Transactions on*, 22 (1986) 355-360.
- [75] J. Norpoth, et al., Straightforward field calculations for uniaxial hardmagnetic prisms: stray field distributions and dipolar coupling in regular arrays, *Journal of Physics D: Applied Physics*, 41 (2008) 025001.
- [76] S. Khizroev, D. Litvinov, Perpendicular magnetic recording: Writing process, *J Appl Phys*, 95 (2004) 4521-4537.
- [77] D. Weller, A. Moser, L. Folks, M.E. Best, L. Wen, M.F. Toney, M. Schwickert, J.U. Thiele, M.F. Doerner, High K_u materials approach to 100 Gbits/in², *Magnetics, IEEE Transactions on*, 36 (2000) 10-15.
- [78] V. Alexandrakis, D. Niarchos, K. Mergia, J. Lee, J. Fidler, I. Panagiotopoulos, Magnetic properties of graded Al/L1[₀] films obtained by heat treatment of FePt/CoPt multilayers, *J Appl Phys*, 107 (2010) 013903-013904.
- [79] S.N. Piramanayagam, K. Srinivasan, Recording media research for future hard disk drives, *J Magn Magn Mater*, 321 (2009) 485-494.
- [80] S. Batra, J.D. Hannay, Z. Hong, J.S. Goldberg, Investigations of perpendicular write head design for 1 Tb/in², *Magnetics, IEEE Transactions on*, 40 (2004) 319-325.
- [81] D. Weller, A. Moser, Thermal effect limits in ultrahigh-density magnetic recording, *Magnetics, IEEE Transactions on*, 35 (1999) 4423-4439.
- [82] T. Fujiwara, Barium Ferrite Media for Perpendicular Recording, *Ieee T Magn*, 21 (1985) 1480-1485.
- [83] J. Lee, M. Fuger, J. Fidler, D. Suess, T. Schrefl, O. Shimizu, Modeling of the write and read back performances of hexagonal Ba-ferrite particulate media for high density tape recording, *J Magn Magn Mater*, 322 (2010) 3869-3875.
- [84] L. Zhang, J.A. Bain, Z. Jian-gang, Dependence of thermomagnetic mark size on applied STM voltage in Co-Pt multilayers, *Magnetics, IEEE Transactions on*, 38 (2002) 1895-1897.

- [85] Z. Jian-Gang, Z. Xiaochun, T. Yuhui, Microwave Assisted Magnetic Recording, Magnetics, IEEE Transactions on, 44 (2008) 125-131.
- [86] D. Suess, J. Fidler, K. Porath, T. Schrefl, D. Weller, Micromagnetic study of pinning behavior in percolated media, J Appl Phys, 99 (2006) 08G905.
- [87] J.G. Zhu, Y. Tang, Micromagnetics of Percolated Perpendicular Media, Magnetics, IEEE Transactions on, 43 (2007) 687-692.
- [88] J. Fidler, T. Schrefl, D. Suess, O. Ertl, M. Kirschner, G. Hrkac, Full micromagnetics of recording on patterned media, Physica B, 372 (2006) 312-315.
- [89] O. Ertl, G. Hrkac, D. Suess, M. Kirschner, F. Dorfbauer, J. Fidler, T. Schrefl, Multiscale micromagnetic simulation of giant magnetoresistance read heads, J Appl Phys, 99 (2006) -.
- [90] H.J. Richter, A.Y. Dobin, R.T. Lynch, D. Weller, R.M. Brockie, O. Heinonen, K.Z. Gao, J. Xue, R.J.M. v. d. Veerdonk, P. Asselin, M.F. Erden, Recording potential of bit-patterned media, Appl Phys Lett, 88 (2006) 222512-222513.
- [91] H.J. Richter, Density limits imposed by the microstructure of magnetic recording media, J Magn Magn Mater, 321 (2009) 467-476.
- [92] J. Lohau, A. Moser, C.T. Rettner, M.E. Best, B.D. Terris, Writing and reading perpendicular magnetic recording media patterned by a focused ion beam, Appl Phys Lett, 78 (2001) 990-992.
- [93] J.P. Adam, et al., Magnetization reversal in Pt/Co(0.5 nm)/Pt nano-platelets patterned by focused ion beam lithography, Nanotechnology, 21 (2010) 445302.
- [94] X. Yang, S. Xiao, W. Wu, Y. Xu, K. Mountfield, R. Rottmayer, K. Lee, D. Kuo, D. Weller, Challenges in 1 Teradot/in². dot patterning using electron beam lithography for bit-patterned media, 25 (2007) 2202-2209.
- [95] A. Kikitsu, Y. Kamata, M. Sakurai, K. Naito, Recent Progress of Patterned Media, Magnetics, IEEE Transactions on, 43 (2007) 3685-3688.
- [96] Hitachi_GST, in, 2004.
- [97] Hitachi_GST, Magnetic Data Storage with Patterned Media, in, 2008.

- [98] X. Yang, S. Xiao, W. Wu, Y. Xu, K. Mountfield, R. Rottmayer, K. Lee, D. Kuo, D. Weller, Challenges in 1 Teradot/in.² dot patterning using electron beam lithography for bit-patterned media, in, AVS, 2007, pp. 2202-2209.
- [99] J.K.W. Yang, K.K. Berggren, Using high-contrast salty development of hydrogen silsesquioxane for sub-10-nm half-pitch lithography, in, AVS, 2007, pp. 2025-2029.
- [100] X. Yang, Y. Xu, C. Seiler, L. Wan, S. Xiao, Toward 1 Tdot/in.[sup 2] nanoimprint lithography for magnetic bit-patterned media: Opportunities and challenges, in, AVS, 2008, pp. 2604-2610.
- [101] T. Thomson, G. Hu, B.D. Terris, Intrinsic Distribution of Magnetic Anisotropy in Thin Films Probed by Patterned Nanostructures, *Phys Rev Lett*, 96 (2006) 257204.
- [102] Y. Ohsawa, K. Yamakawa, H. Muraoka, Irradiation Damage in Fe-Co Thin Films With Low-Energy Ion Beam, *Magnetics, IEEE Transactions on*, 46 (2010) 2044-2047.
- [103] O. Hellwig, A. Berger, T. Thomson, E. Dobisz, Z.Z. Bandic, H. Yang, D.S. Kercher, E.E. Fullerton, Separating dipolar broadening from the intrinsic switching field distribution in perpendicular patterned media, *Appl Phys Lett*, 90 (2007) 162516.
- [104] D.T. Smith, C. Long, J.O. Rantschler, V. Kalatsky, P. Ruchhoeft, S. Khizroev, D. Litvinov, Size Distribution and Anisotropy Effects on the Switching Field Distribution of Co/Pd Multilayered Nanostructure Arrays, *Magnetics, IEEE Transactions on*, 45 (2009) 3554-3557.
- [105] M.K. Grobis, O. Hellwig, T. Hauet, E. Dobisz, T.R. Albrecht, High-Density Bit Patterned Media: Magnetic Design and Recording Performance, *Magnetics, IEEE Transactions on*, 47 (2011) 6-10.
- [106] M.L. Yan, Y.F. Xu, D.J. Sellmyer, Nanostructure and magnetic properties of highly (001) oriented $L1_0$ $(Fe_{49}Pt_{51})_{1-x}Cu_x$ films, *J Appl Phys*, 99 (2006) 08G903.
- [107] D. Makarov, J. Lee, C. Brombacher, C. Schubert, M. Fuger, D. Suess, J. Fidler, M. Albrecht, Perpendicular FePt-based exchange-coupled composite media, *Appl Phys Lett*, 96 (2010) 062501.
- [108] J. Kalezhi, J.J. Miles, B.D. Belle, Dependence of Switching Fields on Island Shape in Bit Patterned Media, *Magnetics, IEEE Transactions on*, 45 (2009) 3531-3534.

- [109] Y.J. Chen, T.L. Huang, J.Z. Shi, J. Deng, J. Ding, W.M. Li, S.H. Leong, B.Y. Zong, H.Y.Y. Ko, S.B. Hu, J.M. Zhao, Individual bit island reversal and switching field distribution in perpendicular magnetic bit patterned media, *J Magn Magn Mater*, In Press, Corrected Proof.
- [110] P. Krone, D. Makarov, M. Albrecht, T. Schrefl, Magnetization reversal of bit patterned media: Role of the angular orientation of the magnetic anisotropy axes, *J Appl Phys*, 108 (2010) 013906.
- [111] D. Suess, T. Schrefl, S. Fahler, M. Kirschner, G. Hrkac, F. Dorfbauer, J. Fidler, Exchange spring media for perpendicular recording, *Appl Phys Lett*, 87 (2005) 012504.
- [112] B.D. Terris, Fabrication challenges for patterned recording media, *J Magn Magn Mater*, 321 (2009) 512-517.
- [113] R.H. Victora, S. Xiao, Composite media for perpendicular magnetic recording, *Magnetics*, *IEEE Transactions on*, 41 (2005) 537-542.
- [114] D. Suess, T. Schrefl, M. Kirschner, G. Hrkac, F. Dorfbauer, O. Ertl, J. Fidler, Optimization of exchange spring perpendicular recording media, *Ieee T Magn*, 41 (2005) 3166-3168.
- [115] D. Suess, J. Lee, J. Fidler, T. Schrefl, Exchange-coupled perpendicular media, *J Magn Magn Mater*, 321 (2009) 545-554.
- [116] D. Goll, A. Breitling, L. Gu, P.A. van Aken, W. Sigle, Experimental realization of graded $L1_0$ -FePt/Fe composite media with perpendicular magnetization, *J Appl Phys*, 104 (2008) 083903-083904.
- [117] R. Ciprian, M. Carbucicchio, G. Turilli, Exchange-spring magnets based on $L1_0$ -FePt ordered phase, in: E. Kuzmann, K. Lázár (Eds.) *ISIAME 2008*, Springer Berlin Heidelberg, 2009, pp. 363-370.
- [118] T. Klemmer, D. Hoydick, H. Okumura, B. Zhang, W.A. Soffa, Magnetic hardening and coercivity mechanisms in $L1_0$ ordered FePd ferromagnets, *Scripta Metall Mater*, 33 (1995) 1793-1805.
- [119] D. Suess, Multilayer exchange spring media for magnetic recording, *Appl Phys Lett*, 89 (2006) 113105.

- [120] T. Shimatsu, H. Sato, T. Oikawa, Y. Inaba, O. Kitakami, S. Okamoto, H. Aoi, H. Muraoka, Y. Nakamura, High-potential magnetic anisotropy of CoPtCr-SiO₂ perpendicular recording media, *Magnetics, IEEE Transactions on*, 41 (2005) 566-571.
- [121] M. Kapoor, R.H. Victora, Comparison of Recording Head Designs for Perpendicular and Exchange-Coupled Composite Media, *Magnetics, IEEE Transactions on*, 43 (2007) 2289-2291.
- [122] K. Miura, H. Muraoka, Y. Nakamura, Effect of head field gradient on transition jitter in perpendicular magnetic recording, *Magnetics, IEEE Transactions on*, 37 (2001) 1926-1928.
- [123] J.S. Goldberg, P. Asselin, S. Batra, Z. Hong, Micromagnetic study of the correlation between head field gradient and jitter in perpendicular recording, *Magnetics, IEEE Transactions on*, 41 (2005) 3091-3093.
- [124] M. Mallery, A. Torabi, M. Benakli, One terabit per square inch perpendicular recording conceptual design, *Magnetics, IEEE Transactions on*, 38 (2002) 1719-1724.
- [125] Y.J. Chen, S.H. Leong, T.L. Huang, K.W. Ng, S.B. Hu, Z.M. Yuan, V. Ng, A comparative study of write field distribution of trailing-edge shielded and unshielded perpendicular write heads by quantitative magnetic force microscopy, *Appl Phys Lett*, 92 (2008) 162505-162503.
- [126] T. Schrefl, M.E. Schabes, D. Suess, O. Ertl, M. Kirschner, F. Dorfbauer, G. Hrkac, J. Fidler, Partitioning of the perpendicular write field into head and SUL contributions, *Ieee T Magn*, 41 (2005) 3064-3066.
- [127] D. Suess, Micromagnetics of exchange spring media: Optimization and limits, *J Magn Magn Mater*, 308 (2007) 183-197.
- [128] A.Y. Dobin, H.J. Richter, Domain wall assisted magnetic recording (invited), *J Appl Phys*, 101 (2007) 09K108-106.
- [129] T.-J. Zhou, B.C. Lim, B. Liu, Anisotropy graded FePt--TiO₂ nanocomposite thin films with small grain size, *Appl Phys Lett*, 94 (2009) 152505.

- [130] F. Wang, X. Xu, Y. Liang, J. Zhang, H. Wu, FeAu/FePt exchange-spring media fabricated by magnetron sputtering and postannealing, *Appl Phys Lett*, 95 (2009) 022516-022513.
- [131] T. Suzuki, Coercivity mechanism in (Co/Pt) and (Co/Pd) multilayers, *Scripta Metall Mater*, 33 (1995) 1609-1623.
- [132] D. Weller, L. Folks, M. Best, E.E. Fullerton, B.D. Terris, G.J. Kusinski, K.M. Krishnan, G. Thomas, Growth, structural, and magnetic properties of high coercivity Co/Pt multilayers, *J Appl Phys*, 89 (2001) 7525-7527.
- [133] C.J. Lin, G.L. Gorman, C.H. Lee, R.F.C. Farrow, E.E. Marinero, H.V. Do, H. Notarys, C.J. Chien, Magnetic and structural properties of Co/Pt multilayers, *J Magn Magn Mater*, 93 (1991) 194-206.
- [134] R. Sbiaa, C.Z. Hua, S.N. Piramanayagam, R. Law, K.O. Aung, N. Thiyagarajah, Effect of film texture on magnetization reversal and switching field in continuous and patterned (Co/Pd) multilayers, *J Appl Phys*, 106 (2009) 023906.
- [135] J.E. Davies, O. Hellwig, E.E. Fullerton, G. Denbeaux, J.B. Kortright, K. Liu, Magnetization reversal of Co/Pt multilayers: Microscopic origin of high-field magnetic irreversibility, *Phys Rev B*, 70 (2004) 224434.
- [136] O. Hellwig, A. Berger, J.B. Kortright, E.E. Fullerton, Domain structure and magnetization reversal of antiferromagnetically coupled perpendicular anisotropy films, *J Magn Magn Mater*, 319 (2007) 13-55.
- [137] A. Perumal, Y.K. Takahashi, T.O. Seki, K. Hono, Particulate structure of $L1_0$ ordered ultrathin FePt films for perpendicular recording, *Appl Phys Lett*, 92 (2008) 132508.
- [138] E. Yang, D.E. Laughlin, $L1_0$ FePt-oxide columnar perpendicular media with high coercivity and small grain size, *J Appl Phys*, 104 (2008) 023904.
- [139] JCPDS-International Center of Diffraction Data, in, 1999.
- [140] R.A. Ristau, K. Barmak, L.H. Lewis, K.R. Coffey, J.K. Howard, On the relationship of high coercivity and $L1_0$ ordered phase in CoPt and FePt thin films, *J Appl Phys*, 86 (1999) 4527-4533.

- [141] S.N. Hsiao, F.T. Yuan, H.W. Chang, H.W. Huang, S.K. Chen, H.Y. Lee, Effect of initial stress/strain state on order-disorder transformation of FePt thin films, *Appl Phys Lett*, 94 (2009) 232505.
- [142] H.J. Richter, A.Y. Dobin, Analysis of magnetization processes in composite media grains, *J Appl Phys*, 99 (2006) 08Q905-903.
- [143] F. Wang, X.-H. Xu, Y. Liang, J. Zhang, J. Zhang, Perpendicular L10-FePt/Fe and L10-FePt/Ru/Fe graded media obtained by post-annealing, *Materials Chemistry and Physics*, 126 (2011) 843-846.
- [144] K.K.M. Pandey, J.S. Chen, G.M. Chow, L1₀ Phase CoPt-TiO₂ / FePt-TiO₂ Exchange Coupled Media With Small Switching Field, *Magnetics, IEEE Transactions on*, 46 (2010) 1955-1958.
- [145] B. Stahl, J. Ellrich, R. Theissmann, M. Ghafari, S. Bhattacharya, H. Hahn, N.S. Gajbhiye, D. Kramer, R.N. Viswanath, Weissm, uuml, J. Iler, H. Gleiter, Electronic properties of 4-nm FePt particles, *Phys Rev B*, 67 (2003) 014422.
- [146] D.H. Wei, T.S. Chin, K.L. You, C.C. Yu, Y. Liou, Y.D. Yao, Enhancement of L10 ordered FePt by Pt buffer layer, *J Magn Magn Mater*, 303 (2006) e265-e269.
- [147] S.N. Hsiao, S.K. Chen, T.S. Chin, Y.W. Hsu, H.W. Huang, F.T. Yuan, H.Y. Lee, W.M. Liao, Early-stage ordering in in-situ annealed Fe₅₁Pt₄₉ films, *J Magn Magn Mater*, 321 (2009) 2459-2466.
- [148] J. Fidler, P. Speckmayer, T. Schrefl, D. Suess, Numerical micromagnetics of an assembly of(Fe,Co)Pt nanoparticles, *J Appl Phys*, 97 (2005) 10E508.
- [149] T. Schrefl, G. Hrkac, D. Suess, W. Scholz, J. Fidler, Coercivity and remanence in self-assembled FePt nanoparticle arrays, *J Appl Phys*, 93 (2003) 7041-7043.
- [150] P. Fredriksson, Calculated Fe-Pt diagram, in, NIMS, 2001.
- [151] T. Shima, K. Takanashi, Y.K. Takahashi, K. Hono, Preparation and magnetic properties of highly coercive FePt films, *Appl Phys Lett*, 81 (2002) 1050-1052.
- [152] J. Allouche, D. Lantiat, M. Kuemmel, M. Faustini, C. Laberty, C. Chanéac, E. Tronc, C. Boissière, L. Nicole, C. Sanchez, D. Grosso, Direct electrogeneration of FePt

nanoparticles into highly ordered Inorganic NanoPattern stabilising membranes, *Journal of Sol-Gel Science and Technology*, 53 (2010) 551-554.

[153] D.C. Berry, K. Barmak, The A1 to L1₀ transformation in FePt and FeCuPt thin films: Determination of isothermal transformation kinetics from nonisothermal measurements, *J Appl Phys*, 99 (2006) 08G901.

[154] Z.R. Dai, S. Sun, Z.L. Wang, Phase Transformation, Coalescence, and Twinning of Monodisperse FePt Nanocrystals, *Nano Letters*, 1 (2001) 443-447.

[155] JCPDS-International_Center_of_Diffraction_Data, JCPDS-International Center of Diffraction Data, in, 1999.

[156] D.B. Williams, C.B. Carter, *Transmission Electron Microscopy*, 2nd ed., Plenum publishing corporation, New York, 2009.

[157] Y. Misumi, S. Masatsuji, R. Sahara, S. Ishii, K. Ohno, A lattice Monte Carlo simulation of the FePt alloy using a first-principles renormalized four-body interaction, *The Journal of Chemical Physics*, 128 (2008) 234702-234705.

[158] J. Lee, V. Alexandrakis, M. Fuger, B. Dymerska, D. Suess, D. Niarchos, J. Fidler, FePt L1₀ / A1 graded media with a rough interphase boundary, *Appl Phys Lett*, 98 (2011) accepted.

[159] N. Murayama, S. Soeya, Y. Takahashi, M. Futamoto, Ordering and grain growth of FePt thin films by annealing, *J Magn Magn Mater*, 320 (2008) 3057-3059.

[160] V. Alexandrakis, T. Speliotis, E. Manios, D. Niarchos, J. Fidler, J. Lee, G. Varvaro, Hard/graded exchange spring composite media based on FePt, *J Appl Phys*, 109 (2011) 07B729.

[161] J.M. Rickman, W.S. Tong, K. Barmak, Impact of heterogeneous boundary nucleation on transformation kinetics and microstructure, *Acta Materialia*, 45 (1997) 1153-1166.

[162] W.S. Tong, J.M. Rickman, K. Barmak, Impact of short-range repulsive interactions between nuclei on the evolution of a phase transformation, *The Journal of Chemical Physics*, 114 (2001) 915-922.

- [163] D. Berman, R. Biskeborn, N. Bui, E. Childers, R.D. Cideciyan, W. Dyer, E. Eleftheriou, D. Hellman, R. Hutchins, W. Imano, G. Jaquette, J. Jelitto, P.O. Jubert, C. Lo, G. McClelland, S. Narayan, S. Oelcer, T. Topuria, T. Harasawa, A. Hashimoto, T. Nagata, H. Ohtsu, S. Saito, 6.7 Gb/in² recording areal density on barium ferrite tape, *IEEE Trans. Magn.*, 43 (2007) 3502-3508.
- [164] H. Sugihara, Y. Imaoka, Technical trends in tape recording fine particles. A short review, *Industrial and Engineering Chemistry Product Research and Development*, 23 (1984) 330-333.
- [165] B. Gustard, M.R. Wright, New Gamma-Fe₂O₃ Particle Exhibiting Improved Orientation, *Ieee T Magn*, 8 (1972) 426-427.
- [166] A. Mali, A. Ataie, Influence of Fe/Ba molar ratio on the characteristics of Ba-hexaferrite particles prepared by sol-gel combustion method, *J. Alloys. Compd.*, 399 (2005) 245-250.
- [167] T. Harasawa, R. Suzuki, O. Shimizu, S. Ölçer, E. Eleftheriou, Barium-Ferrite particulate media for high-recording-density tape storage systems, *IEEE Trans. Magn.*, 46 (2010) 1894-1897.
- [168] S.J.F. Chadwick, A.E. Virden, V. Haehnel, J.D. Dutson, K. Matsumoto, T. Yoshida, T. Sawano, T. Goto, K. Ikari, K. O'Grady, Development of metal particle (MP) technology for flexible recording media, *J. Phys. D: Appl. Phys.*, 41 (2008) 134018.
- [169] O. Shimizu, T. Harasawa, M. Oyanagi, Particle orientation effects of barium ferrite particulate media, *IEEE Trans. Magn.*, 46 (2010) 1607-1609.
- [170] T. Fujiwara, Barium Ferrite Media for Perpendicular Recording, *IEEE Trans. Magn.*, 21 (1985) 1480-1485.
- [171] F. Sarigoz, G. Li, V.K.V. Kumar, J.A. Bain, Z. Jian-Gang, Analysis of dropout peakshift in magnetic tape recording, *Magnetics, IEEE Transactions on*, 36 (2000) 2170-2172.
- [172] P.O. Jubert, B. Biskeborn, D. Qiu, A. Matsumoto, H. Noguchi, O. Shimizu, Noise and recording properties of barium-ferrite particulate media studied by micromagnetic modeling, *IEEE Trans. Magn.*, 47 (2011) 386-394.

- [173] A. Donev, F.H. Stillinger, P.M. Chaikin, S. Torquato, Unusually dense crystal packings of ellipsoids, *Phys Rev Lett*, 92 (2004) 255506.
- [174] P.O. Jubert, B. Biskeborn, D. Qiu, H. Nuguchi, O. Shimizu, Noise properties of barium ferrite particulate media studied by micromagnetic modeling, in: 11th Joint MMM-Intermag Conference, Washington, DC, USA, 2010, pp. CF-12.
- [175] M.P. Sharrock, personal communication, in, 2010.
- [176] M. Fuger, J. Lee, J. Fidler, D. Suess, T. Schrefl, C. Vogler, O. Shimizu, in, 2010, to be published.
- [177] D. Suess, T. Schrefl, J. Fidler, J.N. Chapman, Micromagnetic simulation of the long-range interaction between NiFe nano-elements using the BE-method, *J Magn Magn Mater*, 197 (1999) 617-619.
- [178] T. Schrefl, W. Scholz, D. Suess, J. Fidler, Computational micromagnetics: prediction of time dependent and thermal properties, *J Magn Magn Mater*, 226 (2001) 1213-1219.
- [179] W.H. Press, S.A. Teukolsky, W.T. Vetterling, B.P. Flannery, *Numerical Recipes in Fortran 77: The Art of Scientific Computing*, Cambridge University Press, Cambridge, 1992.
- [180] G. Mian, T.D. Howell, Determining a signal to noise ratio for an arbitrary data sequence by a time domain analysis, *Magnetics, IEEE Transactions on*, 29 (1993) 3999-4001.
- [181] INSIC, *International Magnetic Tape Storage Roadmap*, in, 2008.
- [182] Speedtech, in.
- [183] *Coating_Technology_Corea*, in.
- [184] S. Matsunuma, T. Inoue, T. Doi, T. Matsuu, A. Hashimoto, K.I. Hirata, S. Nakagawa, Comparison of Playback Performance of Facing Targets Sputtered Perpendicular and Longitudinal Tape Media, *Magnetics, IEEE Transactions on*, 45 (2009) 3598-3600.
- [185] T. Matsuu, K. Hirata, S. Gomi, A. Hashimoto, S. Matsunuma, T. Inoue, T. Doi, S. Nakagawa, Si/NiFe/FeCoB Crystalline SUL to Reduce Ru Intermediate Layer Thickness

- for CoPtCr-SiO₂ Granular Perpendicular Magnetic Recording Media, *Magnetics*, IEEE Transactions on, 45 (2009) 3572-3575.
- [186] S. Matsunuma, T. Inoue, T. Watanabe, T. Doi, Y. Mashiko, S. Gomi, K. Hirata, S. Nakagawa, Playback performance of perpendicular magnetic recording tape media for over-50-TB cartridge by facing targets sputtering method, *J Magn Magn Mater*, In Press, Corrected Proof.
- [187] H.J. Hilhorst, Asymptotic statistics of the n -sided planar Poisson–Voronoi cell: II. Heuristics, *Journal of Statistical Mechanics: Theory and Experiment*, 2009 (2009) P05007.
- [188] G. Voronoi, Nouvelles applications des paramètres continus à la théorie des formes quadratiques, *Journal für die reine und angewandte Mathematik (Crelles Journal)*, 133 (1907) 97-178.
- [189] S.H. Park, S.O. Kim, T.D. Lee, H.S. Oh, Y.S. Kim, N.Y. Park, D.H. Hong, Effect of top Ru deposition pressure on magnetic and microstructural properties of CoCrPt--SiO₂ media in two-step Ru layer, *J Appl Phys*, 99 (2006) 08E701-703.
- [190] Wikipedia, Distance Transformation, in.
- [191] N. Itagaki, et al., 4.8 nm diameter Ru grains grown on a large-grain seed layer for perpendicular magnetic recording media, *Journal of Physics D: Applied Physics*, 41 (2008) 152006.
- [192] N. Itagaki, S. Saito, M. Takahashi, Small, highly oriented Ru grains in intermediate layer realized through suppressing relaxation of low-angle grain boundaries for perpendicular recording media, *J Appl Phys*, 105 (2009) 07B734-733.
- [193] D. Navas, F. Ilievski, C.A. Ross, CoCrPt antidot arrays with perpendicular magnetic anisotropy made on anodic alumina templates, *J Appl Phys*, 105 (2009) 113921-113926.
- [194] S. Matsunuma, Schematic diagram of CoCrPt-SiO₂ prepared by FTS., in, 2010.
- [195] S.Y. Chou, M.S. Wei, P.R. Krauss, P.B. Fischer, Single-domain magnetic pillar array of 35 nm diameter and 65 Gbits/in.[sup 2] density for ultrahigh density quantum magnetic storage, *J Appl Phys*, 76 (1994) 6673-6675.

- [196] F. Luo, L.J. Heyderman, H.H. Solak, T. Thomson, M.E. Best, Nanoscale perpendicular magnetic island arrays fabricated by extreme ultraviolet interference lithography, *Appl Phys Lett*, 92 (2008) 102505-102503.
- [197] O. Hellwig, J.K. Bosworth, E. Dobisz, D. Kercher, T. Hauet, G. Zeltzer, J.D. Risner-Jamtgaard, D. Yaney, R. Ruiz, Bit patterned media based on block copolymer directed assembly with narrow magnetic switching field distribution, *Appl Phys Lett*, 96 (2010) 052511.
- [198] P. Kappenberger, F. Luo, L.J. Heyderman, H.H. Solak, C. Padeste, C. Brombacher, D. Makarov, T.V. Ashworth, L. Philippe, H.J. Hug, M. Albrecht, Template-directed self-assembled magnetic nanostructures for probe recording, *Appl Phys Lett*, 95 (2009) 023116-023113.
- [199] J.-G. Zhu, Y. Tang, A medium microstructure for high area density perpendicular recording, *J Appl Phys*, 99 (2006) 08Q903-903.
- [200] D.E. Laughlin, Y. Peng, Y.L. Qin, M. Lin, J.G. Zhu, Fabrication, Microstructure, Magnetic, and Recording Properties of Percolated Perpendicular Media, *Magnetics, IEEE Transactions on*, 43 (2007) 693-697.
- [201] A.-C. Sun, J.-H. Hsu, P.C. Kuo, H.L. Huang, Magnetic Properties of Percolated Perpendicular FePt-MgO Films, *Magnetics, IEEE Transactions on*, 43 (2007) 2130-2132.
- [202] M.T. Rahman, L. Chih-Huang, D. Vokoun, N.N. Shams, A Simple Route to Fabricate Percolated Perpendicular Magnetic Recording Media, *Magnetics, IEEE Transactions on*, 43 (2007) 2133-2135.
- [203] M.T. Rahman, N.N. Shams, Y.-C. Wu, C.-H. Lai, D. Suess, Magnetic multilayers on porous anodized alumina for percolated perpendicular media, *Appl Phys Lett*, 91 (2007) 132505-132503.
- [204] M.T. Rahman, N.N. Shams, C.H. Lai, J. Fidler, D. Suess, Co/Pt perpendicular antidot arrays with engineered feature size and magnetic properties fabricated on anodic aluminum oxide templates, *Phys Rev B*, 81 (2010) 014418.

- [205] D. Makarov, E. Bermudez-Urena, O.G. Schmidt, F. Liscio, M. Maret, C. Brombacher, S. Schulze, M. Hietschold, M. Albrecht, Nanopatterned CoPt alloys with perpendicular magnetic anisotropy, *Appl Phys Lett*, 93 (2008) 153112-153113.
- [206] D. Makarov, F. Klimenta, S. Fischer, F. Liscio, S. Schulze, M. Hietschold, M. Maret, M. Albrecht, Nonepitaxially grown nanopatterned Co--Pt alloys with out-of-plane magnetic anisotropy, *J Appl Phys*, 106 (2009) 114322-114327.
- [207] C. Brombacher, M. Saitner, C. Pfahler, A. Plettl, P. Ziemann, D. Makarov, D. Assmann, M.H. Siekman, L.A. Abelman, Manfred Tailoring particle arrays by isotropic plasma etching: an approach towards percolated perpendicular media, *Nanotechnology*, 20 (2009) 105304.
- [208] A. Fisher, M. Kuemmel, M. Järn, M. Linden, C. Boissière, L. Nicole, C. Sanchez, D. Grosso, Surface Nanopatterning by Organic/Inorganic Self-Assembly and Selective Local Functionalization, *Small*, 2 (2006) 569-574.
- [209] M. Kuemmel, J. Allouche, L. Nicole, C. Boissière, C. Laberty, H. Amenitsch, C. Sanchez, D. Grosso, A Chemical Solution Deposition Route To Nanopatterned Inorganic Material Surfaces, *Chemistry of Materials*, 19 (2007) 3717-3725.
- [210] D. Makarov, P. Krone, D. Lantiat, C. Schulze, A. Liebig, C. Brombacher, M. Hietschold, S. Hermann, C. Laberty, D. Grosso, M. Albrecht, Magnetization Reversal in Arrays of Magnetic Nanoperforations, *Magnetics, IEEE Transactions on*, 45 (2009) 3515-3518.
- [211] M. Kuemmel, C. Boissière, L. Nicole, C. Laberty-Robert, C. Sanchez, D. Grosso, Highly ordered metal oxide nanopatterns prepared by template-assisted chemical solution deposition, *Journal of Sol-Gel Science and Technology*, 48 (2008) 102-112.
- [212] M. Ghidini, G. Zangari, I.L. Prejbeanu, G. Pattanaik, L.D. Buda-Prejbeanu, G. Asti, C. Pernechele, M. Solzi, Magnetization processes in hard Co-rich Co--Pt films with perpendicular anisotropy, *J Appl Phys*, 100 (2006) 103911-103910.
- [213] C. Bran, A.B. Butenko, N.S. Kiselev, U. Wolff, L. Schultz, O. Hellwig, ouml, szlig, U.K. ler, A.N. Bogdanov, V. Neu, Evolution of stripe and bubble domains in

antiferromagnetically coupled [(Co/Pt)₈/Co/Ru]₁₈ multilayers, Phys Rev B, 79 (2009) 024430.

[214] T. Suzuki, N. Honda, K. Ouchi, Magnetization reversal process in polycrystalline ordered Fe--Pt(001) thin films, J Appl Phys, 85 (1999) 4301-4303.

[215] J. Becker, Reversal mechanism in copper-modified cobalt-rare-earths, Magnetics, IEEE Transactions on, 12 (1976) 965-967.

[216] T. Schrefl, J. Fidler, Numerical micromagnetics for granular magnetic materials, J Magn Magn Mater, 157 (1996) 331-335.

[217] J. Burkardt, UCD File Format, in.

[218] L. CYBERNET SYSTEMS Co., MicroAVS: personal visualization system, in.

[219] Kitware, Paraview, in.

APPENDIX

During the time of Ph.D. course, some short computer programs are developed by myself to support micromagnetic simulations and the analysis of the results for advanced media recording. This chapter is written to help others to use the programs, and also for audiences to help understanding of my thesis in precise details.

- Preprocessing

Finite Element MicroMagnEtic (FEMME), simulation software developed by T. Schrefl and D. Suess et al. has a set of input files.

file extension (<i>modelname.???</i>)	contents
.inf	Number of nodes, volume and surface elements
.knt	Cartesian node coordinate
.ijb	List of surface triangles
.ijk	List of volume tetrahedrons
.ijl	List of line elements (<i>should be empty</i>)
.ini	Initial magnetizations in each material. Or, magnetization output from Macro spin mode
.krn	Material parameters
.gbe	Intergraular exchange
.inp	Magnetization data in each node. Optionally used as a initial state.

The programs listed below helps to modify one of the input file.

: **krmaker**

The *krmaker* is a C programmed executive program that generates *.krn* file which contains material parameters with desired easy axes distributions on given number of grains or particles.

Usage:

```
> krnmaker cfgfile(.cfg)
```

Structure of the configuration (.cfg) file:

```
#####  
# Name of KRN file to be generated (.krn will be added at the end)  
#-----  
KRNfilename = "outfilename"; ← outputfile : outfilename.krn  
#  
#####  
# TextureType : type of texture (should be one of "p", "r", "f")  
# "p" : in-plane random texture  
# "r" : 3-dimensional random texture  
# "f" : uni-directional fiber texture  
#-----  
TextureType = "f";  
#  
#####  
# TextureOrientation : orientation of texture ([float, float, float])  
# if TextureType is "p" or "r" : these values do not work.  
#-----  
TextureOrientation = [0.0, 0.0, 1.0];  
#  
#####  
# Full Width Half Maximum of the Gaussian easy axis distribution (float, unit: degree)  
# this value corresponds to (1.178 x st.dev.)  
#-----  
TexOriFWHM = 1.0;  
#  
#####  
# Magnetic Properties of grains  
# 95% of grains will be placed in +-2*st.dev.  
# K1 : mean of K1 (float, unit: J/m^3)  
# dK1 : standard deviation of K1 (float, relative value of K1: 0.1 means 10%)  
# K2 : mean of K2 (float, unit: J/m^3)  
# dK2 : standard deviation of K2 (float, relative value of K2: 0.1 means 10%)  
# Js : saturated polarization (float, unit: T)  
# dJs : standard deviation of Js (float, relative value of Js: 0.1 means 10%)  
# A : Intra-granular Exchange constant ((float, unit: J/m)  
# alpha : Gilbert damping constant (float, unit: dimensionless)  
#-----  
K1 = 3e5;  
dK1 = 0.01;  
K2 = 0e0;  
dK2 = 0;  
Js = 0.346;  
dJs = 0.0;  
A = 1e-11;  
alpha = 0.02;  
#  
#####  
# GrainNr : number of grains (integer)  
#-----  
GrainNr = 100000;
```

: cubearraymaker

The *cubearraymaker* is a python program to generate a batch file for GiD, a pre- and postprocessing software. The finite element model for FEMME is able to be prepared using GiD, and it becomes easier with a batch file (*.bch*). A tetragonal structure is prepared by given edge lengths, and it is copied to x, y and z directions as many as defined in the input parameter. The cubes have a certain interphase boundary thickness between them. Each individual tetrahedron has its own material number.

Usage:

```
> cubearraymaker.py  
or,  
>python cubearraymaker.py
```

Structure of the configuration file:

```
# noutfile      : output filename (.bch for GiD batch file)  
# origin(x,y,z) : a corner of model (float, unit: nm)  
# box(x,y,z)   : cube edge lengths (float, unit: nm)  
# thick(x,y,z) : grain boundary thicknesses (float, unit: nm)  
# number(x,y,z): number of boxes in x,y,z direction (integer)  
# ver         : GiD version to import the batch file  
#             1 = 7.2  
#             2 = 9.x  
noutfile = 'cubearray.bch'  
origin = (0.0, 0.0, 0.0)  
box = (1.0, 1.0, 1.0)  
thick = (0.1, 0.1, 0.1)  
number = (30, 1, 15)  
ver = 1
```

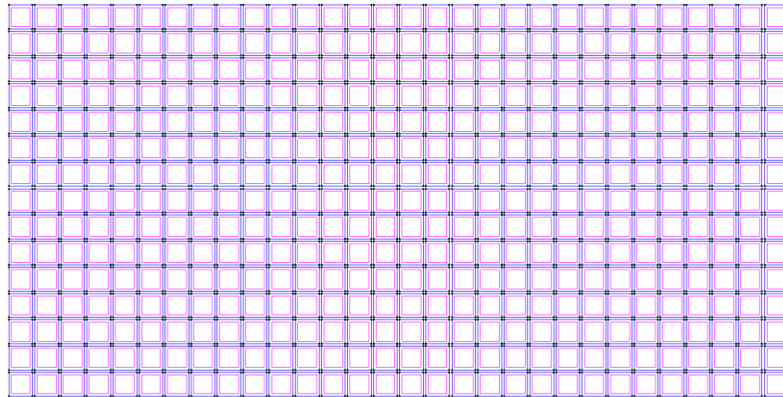


Fig. 132. A rectangular model with 450 (30 x1x15) cubes, of which x, y, z edge lengths are 1 nm. The intergranular phase thickness is fixed as 0.1 nm.

: phasemaker

The *phasemaker* is a C programmed executive program that generates *.krn* file. This program is useful to make phase graded media models as shown in Fig. 98 in page 139. The material parameters of two phases are given in the *.cfg* file, and the targets of phase 2 grains are listed in the array *phase2grains*. Grain with its number equal or larger than *grain2after* belongs to *phase2grains*, as well.

Usage:

```
> phasemaker cfgfile(.cfg)
```

Structure of the configuration (*.cfg*) file:

```
#####  
# KRNfilename : Name of KRN file to be generated  
#-----  
# Magnetic Properties of grains (float values)  
# phase1 : material parameters of the 1st phase  
# phase2 : material parameters of the 2nd phase  
#-----  
# numgrain : number of grains (integer)  
#-----  
KRNfilename = "random"; ← outputfile : random.krn  
phase1 = "0.000 0.000 5.0E+6 0.0 1.58 1.0E-11 0.02 ";  
phase2 = "0.000 0.000 0.1E+6 0.0 1.00 1.0E-11 0.02 ";  
numgrain = 450;  
phase2grains = [  
1, 2, 6, 8, 9, 11, 16, 17, 19, 22, 23, 25, 29, 32, 33, 34, 36, 38, 40, 41, 42, 47, 49, 53, 58, 59, 60,  
  
.....(omitted)....  
  
439, 440, 441, 443  
];  
phase2after = 445;
```

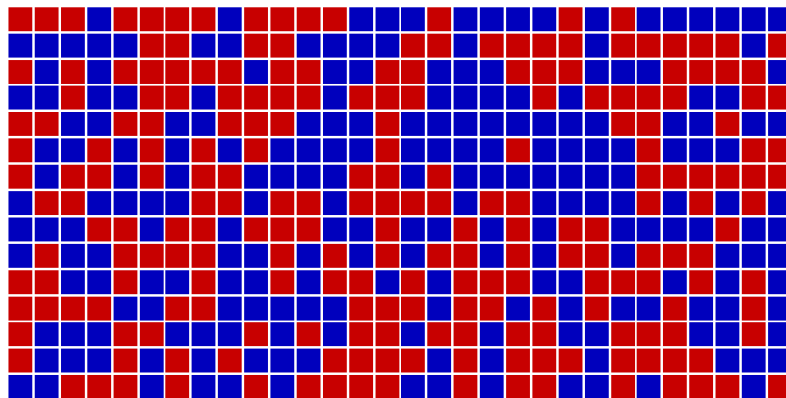


Fig. 133. Phase 1 and 2 assigned on the volumes of the model shown in Fig. 132, with the same portions of them. Red and blue grains stand for the phase 1 and 2, respectively.

: replace-data

The *replace-data* is a *python* program. Input parameters and main code are in a same file, therefore it should be treated carefully not to change the source code unintended. This program is useful with a batch file, when we run a lot of micromagnetic simulations with changing only one value in a certain file.

Usage:

```
> replace-data.py
or,
>python replace-data.py
```

Header of the file with input parameters:

```
# target : the name of file to be modified
target = 'modelname.krn'
# data position : location of the data in a line
#         the first data is 1, the second is 2, the third is 3, ....
datapos = 1
# new data : a data to be replaced
ndata = '0.100'
#####
```

: replace-line

The *replace-line* is a *python* program. It works similar to *replace-data*, but not a data but a line. It reads the *target* file, and replaces the string written as *oline* with the *nline*.

Usage:

```
> replace-line.py
or,
>python replace-line.py
```

Header of the file with input parameters:

```
# target : the name of file to be modified
target = 'master.par'
# oline : line to be changed in the file
oline = 'alphanot = 0.01\n' ← please do not forget to put "\n" at the end
# new line : a new line to be written
nline = 'alphanot = 1.0\n' ← please do not forget to put "\n" at the end
#####
```

: **anafield**

The *anafield* is a program that fills a given field box with an analytic field profile. Ring type writing head field (Middleton, Karlqvist, Lindholm, Szczech), single pole tip (SPT) head field with saturated magnet assumption, homogenous field, and Oersted field for spin torque transfer simulation is possible to be prepared. The dimensions and cell size of the resultant field box is defined by the one used for input.

Usage:

```
> anafield inputfieldboxfile(box.?????.inp) cfgfile(.cfg)
```

Structure of the configuration (.cfg) file:

```
#####  
# FieldBoxFile : Name of Field box file to be generated  
#-----  
FieldBoxFile = "fieldboxfilename"; ← outputfile : fieldboxfilename.box.0001.inp  
#  
#####  
# FieldType : type of field box (integer)  
#-----  
# 1 : Middleton  
# 2 : Karlqvist  
# 3 : Lindholm  
# 4 : Szczech - Szech head field requires a few more parameters  
#   p : finite head length of pole 1 (float, unit: nm)  
#   q : finite head length of pole 2 (float, unit: nm)  
#   usp : undershoot parameter of pole 1 (float, 0 = no undershoot, 1 = full undershoot)  
#   usq : undershoot parameter of pole 2 (float, 0 = no undershoot, 1 = full undershoot)  
# 5 : Single Pole Type Perpendicular Head (saturated assumption)  
#   Js : saturation polarization of magnetic pole (float, unit: T)  
#   c : height of SPT head (float, unit : nm)  
# 6 : Homogeneous field in the given volume  
# 7 : Oersted Field inside a current carrying conductor  
#   j0 : current density (float, unit : A/m^2)  
#   center : the {x,y,z} coordinates where the conductor passes through (float, unit: nm)  
#   direction : direction where the current flows.  
#           Should be chosen among {+x, -x, +y, -y, +z, -z}  
#-----  
FieldType = 3;  
#  
# For the case of Szczech Head Field  
p = 100.;  
q = 100.;  
usp = 0.;  
usq = 0.;  
# For Single Pole Type Head,  
Js = 2.4;  
c = 1000.;  
# For Oersted field,  
j0 = 2e10;  
center = [0.,0.,0.];  
direction = "+z";
```

```

#####
# Ring head data
#-----
# x0 : minimum x-coordinate of the Gap of ring head (or SPT head, float, unit : nm)
# x1 : maximum x-coordinate of the Gap of ring head (or SPT head, float, unit : nm)
# y0 : minimum y-coordinate of the head ( float, unit : nm)
# y1 : maximum y-coordinate of the head ( float, unit : nm)
# z0 : z-coordinate of the basal plane of ring head ( float, unit : nm)
# I : head efficiency * number of coil * coil current ( float)
# Hx1 : Valid only in Type 6, x-component of the field inside the box (float, unit: T)
# Hy1 : Valid only in Type 6, y-component of the field inside the box (float, unit: T)
# Hz1 : Valid only in Type 6, z-component of the field inside the box (float, unit: T)
# Hx2 : Valid only in Type 6, x-component of the field outside the box (float, unit: T)
# Hy2 : Valid only in Type 6, y-component of the field outside the box (float, unit: T)
# Hz2 : Valid only in Type 6, z-component of the field outside the box (float, unit: T)
#-----
x0 = 100.;
x1 = 300.;
y0 = -150.;
y1 = 150.;
z0 = 0;
#
I = 0.2912;
Hx1 = 0.0;
Hy1 = 0.0;
Hz1 = -1.0;
Hx2 = 0.0;
Hy2 = 0.0;
Hz2 = 0.0;

```

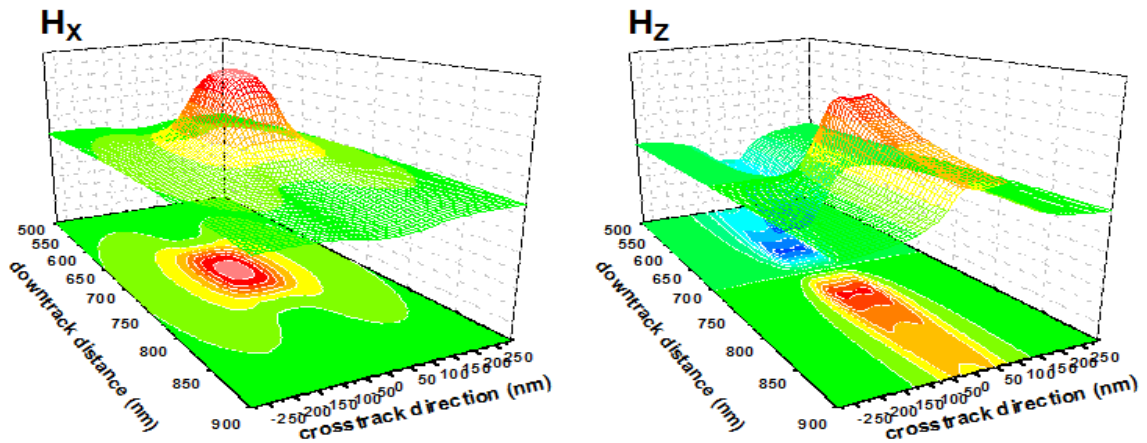


Fig. 134. Longitudinal and perpendicular head field profile of the Lindholm head, with gap length = 100nm and head width = 100 nm. The field profiles are calculated in a field box of which down track and cross track dimensions are 400 nm and 600 nm, respectively.

: hexGen

This simple *python* program produces a file which contains the scale factor multiplied on a scale factor as a function of time. There are two ways in determination of the period of the scale factor. One is by bit length (*method* = 1, *bleng* unit : nm), and the other is by linear density (*method* = 2, *bleng* unit : kfc).

Usage:

```
> hexGen.py  
or,  
>python hexGen.py
```

Header of the file with input parameters:

```
# Input Parameters -----  
#  
# fname : profile file name  
# scftr : scale factor  
# rtime : field rise time (ns)  
# headv : head velocity (m/s)  
# mleng : media length to be written (nm)  
# mthod : method of bit length definition.  
#       mthod = 1 : by bit length  
#       mthod = 2 : by linear density  
# bleng : bit length defined by mthod (nm or kfc)  
#  
#####  
#  
fname = 'hex.dat' ← outfile : hex.dat  
scftr = 1.186  
rtime = 0.1  
headv = 20.0  
mleng = 1200  
mthod = 1  
bleng = 60.0  
#
```

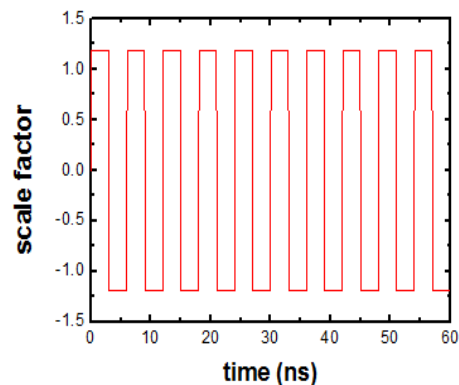


Fig. 135. Scale factor generated by the parameters described above, *scftr* = 1.186, *rtime* = 0.1, *headv* = 20.0, *mleng* = 1200, *mthod* = 1 and *bleng* = 60.0.

- Postprocessing

After micromagnetic simulations using FEMME, the log files (*.log* file and *.txt* file) and magnetization configuration files (*.inp* files) are obtained. In order to analyze the simulation results more efficiency, I have provided the following programs.

: SFTPautodownmaker

In many cases a plenty number of simulations is required to find a precise tendency or to draw a phase diagram. In this time downloading the log files is a big deal as itself. *SFTPautodownmaker* is a python program to generate another python program (*noutfile*) to connect the server with given *server*'s IP address, *ID* and *PW* and download the files. The list of the files should be supplied in another file (*ninfile*).

Usage:

```
> SFTPautodownmaker.py  
or,  
>python SFTPautodownmaker.py
```

Header of the file with input parameters:

```
# Input Parameters -----  
#  
# ninfile : name of the list file  
# noutfile : name of the automatic download python file  
# server : IP address of the server  
# ID : ID on the server  
# PW : PW for the ID  
#####  
ninfile = 'listfilename.dat'  
noutfile = 'SFTPdown.py' ← outputfile : SFTPdown.py  
server = '123.456.78.9'  
ID = 'my_ID'  
PW = 'my_password'  
#
```

Structure of the list file:

```
1_Remote_path 2_Remote_file_name 3_Local_file_name  
/scratch/lee/subdir0/subdir1 hysteresis.txt 0.01.txt  
/scratch/lee/subdir0/subdir2 hysteresis.txt 0.2.txt  
/scratch/lee/subdir0/subdir2 hysteresis.txt 0.4.txt  
/scratch/lee/subdir0/subdir2 hysteresis.txt 0.6.txt
```

.....(continued).....

After running *SFTPautodownmaker*, the main program *SFTPdown.py* is generated.

Usage:

```
> SFTPdown.py  
or,  
>python SFTPdown.py
```

By running *SFTPdown.py*, the files listed in the list file will be downloaded on the local directory where the *SFTPdown* is running.

: inp2dat

The *.inp* file has the UCD format [217]. It can be directly read in MicroAVS [218] and paraview [219]. Sometimes another format of the visualizations is required, such as *Tecplot*. MicroAVS and paraview have nicely rendered 3-dimensional vectors, and Tecplot has a better 2-dimensional view accompanying a background area with scales. The *inp2dat* converts *.inp* file without any configuration file.

Usage:

```
> inp2dat infile(.inp) ← outfile : infile.dat
```

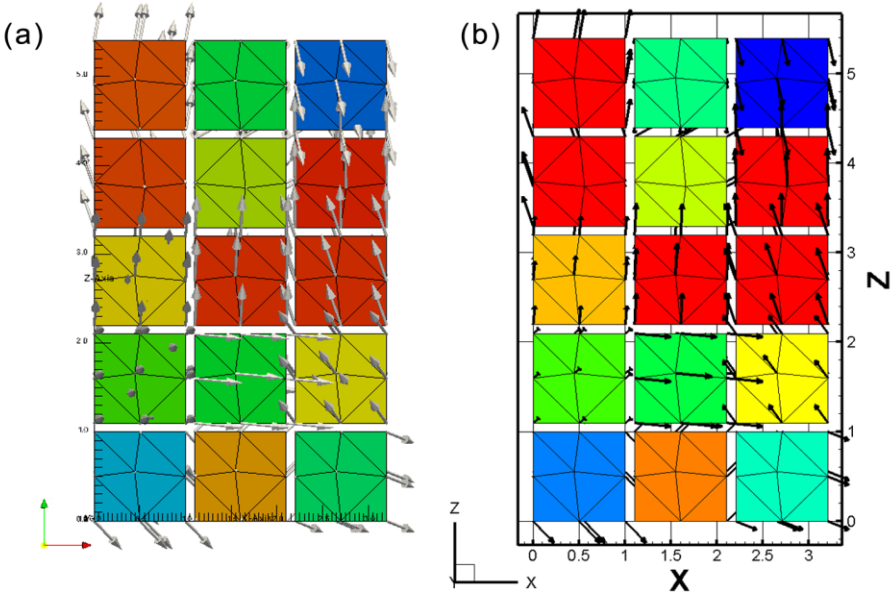


Fig. 136. Visualization of the same model and data using (a) paraview and (b) Tecplot.

The file structure of *.inp* file is converted onto *.dat* file by *inp2dat* as following.

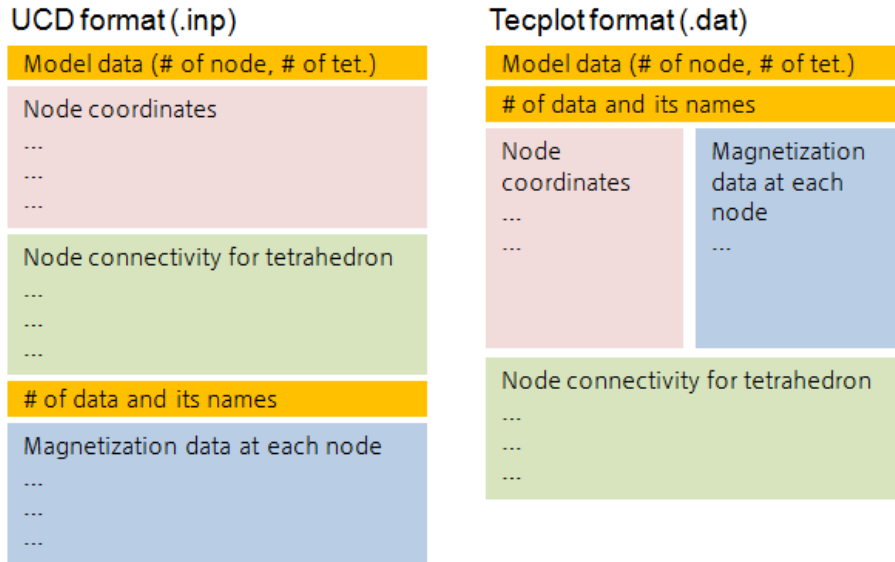


Fig. 137. Data structure comparison between UCD format and Tecplot format.

Another advantage of the Tecplot format is that the magnetization data of the nodes are placed on the same line. The feature enables us to sort the magnetizations as a function of the *x*, *y*, or *z* coordinate: this is very useful in bit transition parameter estimation as shown in Fig. 138.

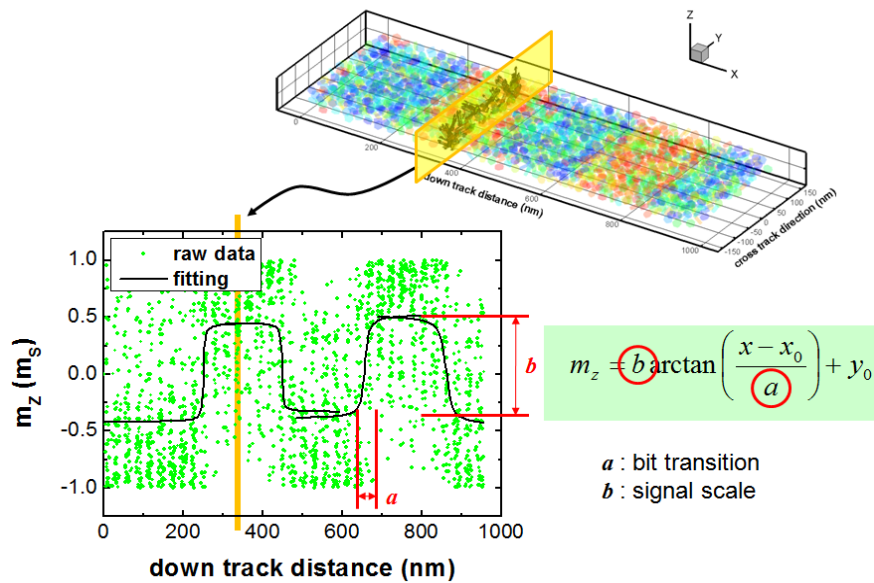


Fig. 138. Bit transition estimations on h-BaFe particulate media.

: inp2mag

In spite of the compatibility of *Tecplot* format file, it is still too large to be easily dealt with. For the purpose of make it simpler, *inp2mag* is developed to minimize the file structure. The *.inp* files are once more simplified by *inp2mag*, only the node data and their magnetizations are remaining.

Usage:

```
> inp2mag infile(.inp) ← outfile : infile.dat
```

only node and magnetization (.dat)

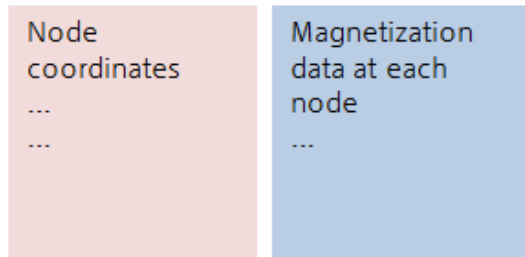


Fig. 139. Data structure of *.dat* file generated by *inp2mag*.

: inisort

For the micromagnetic simulations with thousands of magnetic particle or grains, the *.dat* file generated by *inp2mag* is still too heavy to handle. Utilizing that the particles are regarded as a macro spin therefore the magnetization vectors in a particle or grains are uniform, *inisort* generates only one data point for a particle. The *inisort* detect the center coordinate of grain, and attach the magnetization of the particle beside it. After a result file (*.txt*) is obtained, it automatically sorts the *.txt* file on x-coordinate, then produce *Xsort.txt* file. *inisort* requires *.inf*, *.knt* and *.ijk* file to read the coordinates and connectivity of the nodes and elements to find the grain centers.

Usage:

```
> inisort infile(.ini) ← outfile : inifile.txt, inifileXsort.txt
```

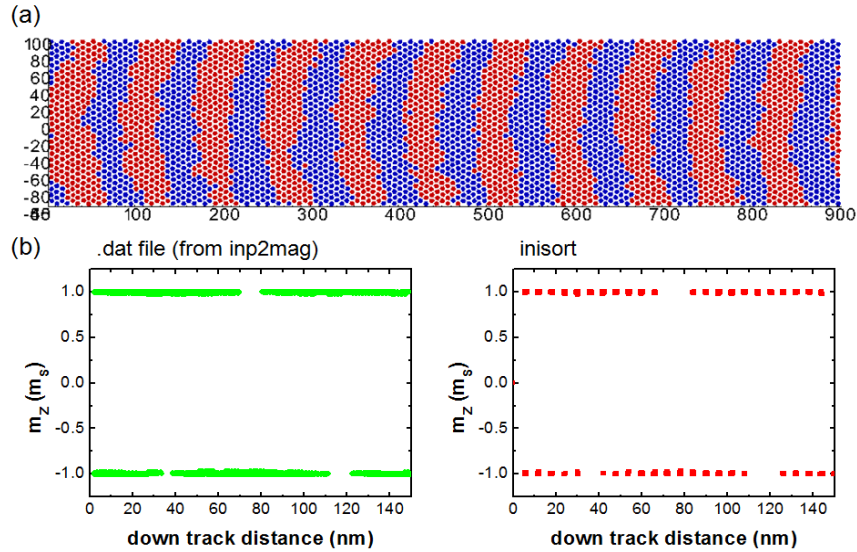


Fig. 140. (a) Written bits of the CoCrPt-SiO₂ sputtered media using SPT head with SUL. (b) Comparison of magnetization analysis from .dat file produced by *inp2mag*, and .txt file by *inisor*.

Fig. 140 shows the written bits on the CoCrPt-SiO₂ sputtered media, and the magnetizations obtained by *ini2mag* and *inisor*. The .txt file has much less data points by factor of 21, but the quality of data is comparable to the results from the full nodes.

: SNR calculation using SignalAdd

The signal-to-noise ratio (SNR) is one of the most important statistic characters of recording performance. In experiments, SNR is obtained by analysis of a huge number of bits' recording performance, several tens of micrometers. However, that is not easy to be done in micromagnetic simulation owing to the limited computational resources to handle such a large model. Therefore we have introduced a numerical trick. The shift distance is less than a bit length, but larger than a particle diameter. An example of h-BaFe is shown in Fig. 141. Three recording simulations were performed on one model, with a shift of initial head position. In the example 20 nm of head position shift was chosen, from the bit length = 60 nm and particle diameter = 16 nm. The writing simulations and read back processes should be performed individually for the three cases.

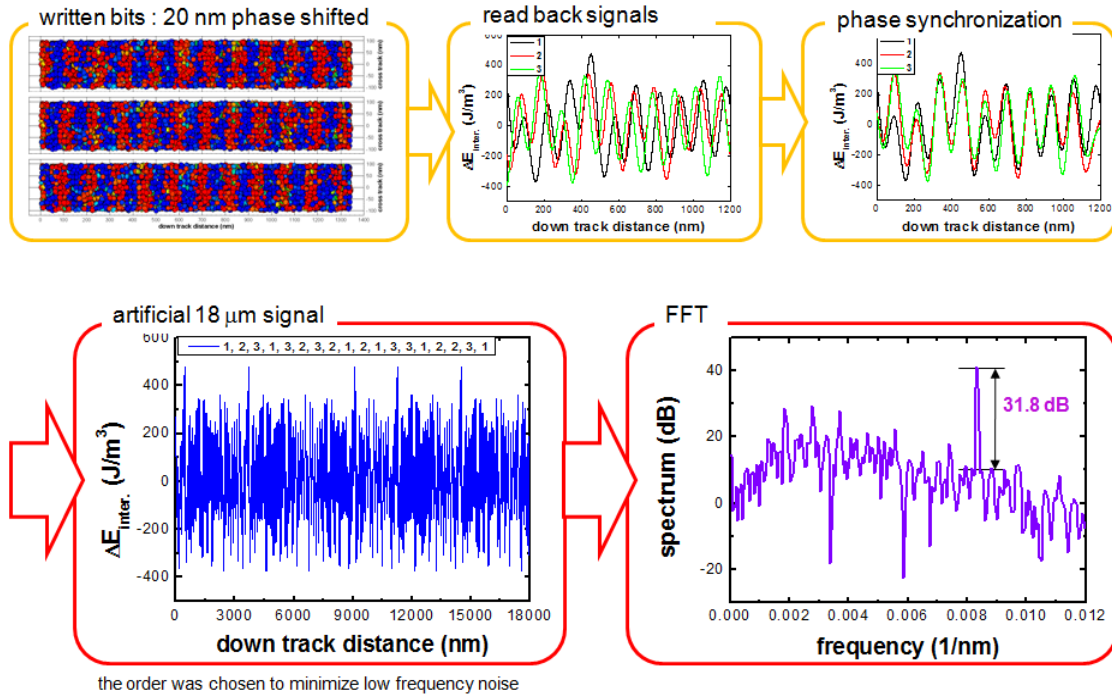


Fig. 141. An example of SNR calculation procedure used in this thesis, for h-BaFe particulate media.

The method of read back simulation does not matter. Any of the three cases described in Fig. 48 may be used. In this example the reciprocity theorem using double Szczech head field was used. The read back signals would have a phase shift, as much as given in the writing simulations. The difference between the signals is not compensated simply by phase synchronization, due to the media noise. Please remind that all other parameters are same except for the write head position used in writing processes. An artificial long signal was obtained by attaching the synchronized signals in a certain order. From trials and errors the sequence of (1,2,3,1,3,2,3,2,1,2,1,3,3,1,2,2,3,1) is found to be the best one which minimizes the low frequency noise. Since a signal is 1 μm long, The artificial signal becomes 18 μm . Another artificial long signal is obtained by another

sequence, (2,3,1,3,2,3,2,1,2,1,3,3,1,2,2,3,1,1), one signal shifted from the previous one. Let me name the sequences as A and B . Physically A and B are just another possibility of combination. Therefore the average of A and B would suppress the uncertainty of recording process, in other words, noise. On the other hand, the difference between A and B would reduce the data but enhance the difference. Consequently, $(A+B)/2$ and $(A-B)/2$ are regarded as a *signal* and *noise*, respectively. The SNR is obtained by performing FFT on the *signal*. As shown at the last box in Fig. 141, the FFT result shows a sharp peak at the desired point, 0.00833 nm^{-1} which corresponds to 60 nm bit length. Finally, SNR is calculated by the difference between the peak and base of the FFT results.

SignalAdd performs most of the part of this process automatically.

Usage:

```
> signaladd cfgfile(.cfg)
```

Structure of the configuration (.cfg) file:

```
OutFile = "problemname"; ← outfile : problemname.txt
#-----
# Filename : common name of the files to be read.
# Filenumber : number of the files to be read. (integer, at least 2)
# If the Filename is 'test' and the Filenumber is 'n',
# The input file names will be considered as
# 'test1.log', 'test2.log', 'test3.log',..., 'testn.log'
# velocity : velocity of the Field box used for the reciprocity theorem (m/s)
# timestep : timestep between each step (ns)
# wavel : wavelength of the signal (nm) = 2 * bit length
# waven : number of the wavelengths to be read in a file (integer)
# offset : offset between each writing simulations (nm)
# order : order to add up the signals
# The first file will be generated as the given order, i.e. '1234'
# the second fill will have a shifting order, i.e. '2341'.
# cutoff : cutting out a certain length (nm) to remove the edge effect
#####
Filename = "perp-"; ← name of the log file series
velocity = 6.0; ← velocity of the read head
timestep = 0.02; ← time step in read back log file
wavel = 120.0;
waven = 9; ← recommend: 1 or 2 less than wavel / bitlength
offset = -20.;
order = [1, 2, 3, 1, 3, 2, 3, 2, 1, 2, 1, 3, 3, 1, 2, 2, 3, 1];
cutoff = 100.; ← if the noise is strangely large, try to increase this and reduce waven
```


PERSONAL

Name Jehyun Lee (이재현, 李濟鉉)
Born 24. Feb. 1979, Seoul, Republic of Korea

EDUCATION

Incheon Science High School, Incheon, Republic of Korea **3/1994 – 2/1997**

Bachelor course at Seoul National University, Seoul, Republic of Korea **3/1997 – 8/2001**
School of Materials Science & Engineering, Department of engineering
Thesis title: "Mechanical Behaviors of DLC/W multilayer"

Integrated Master and Ph.D. course at Seoul National University, Seoul, Republic of Korea **9/2001 – 9/2008**

School of Materials Science & Engineering, Department of engineering
Studying at Lab. Of Materials Deformation and Processing. (Prof. Kyu Hwan Oh)
Dissertation Title: "A study on the effect of the convex grain surface on the magnetic behavior from the viewpoint of magnetic recording"

Ph.D. course at Vienna University of Technology, Vienna, Austria **9/2008 – 6/2011 (planned)**

Institute of solid state physics
Studying at Advanced Magnetism Group.
Dissertation Title: "Inhomogeneous magnetization processes in advanced recording media"

RESEARCH VISITS

Korea Institute of Science and Technology, Seoul, Republic of Korea **7/1999 – 8/1999**
Research Assistant as a Bachelor candidate
Working in the laboratory of Dr. Kwang Ryeol Lee, Thin Film Research Center

Korea Institute of Science and Technology, Seoul, Republic of Korea **8/2001 – 8/2004**
Research Assistant as a Graduate school student
Working in the laboratory of Dr. Kwang Youn Kim, Nano Device Research Center

Vienna University of Technology, Vienna, Austria **3/2005 – 2/2006**
Guest researcher
Working in the research group of Prof. Josef Fidler, Institute of Solid State Physics.

Visit was funded by the BK21 project of the Ministry of Education and Human Resource Foundation, Republic of Korea.

Vienna University of Technology, Vienna, Austria **2/2007**
Guest researcher
Working in the research group of Prof. Josef Fidler, Institute of Solid State Physics.
Financially supported by the BK21 project of the Ministry of Education and Human Resource Foundation, Republic of Korea.

Vienna University of Technology, Vienna, Austria **12/2007 – 8/2008**
Guest researcher
Working in the research group of Prof. Josef Fidler, Institute of Solid State Physics.
Financially supported by the project of the FWF (Austrian Science Fund), Austria and the KOSEF (Korean Science Foundation), Republic of Korea.

APPOINTMENTS (2)

School of Materials Science and Engineering, Seoul National University **9/2004 – 12/2004**
Work as a teaching assistant in the research group of Prof. Kyu Hwan Oh.
Subject : "Electric Circuits"

School of Materials Science and Engineering, Seoul National University **9/2007 – 12/2007**
Work as a teaching assistant in the research group of Prof. Kyu Hwan Oh.
Subject : "Numerical Image Analysis"

PRESENTATIONS IN INTERNATIONAL CONFERENCES (32)

2011

1. **J. Lee**, M. Fuger, D. Suess and J. Fidler, "Performance of Single Pole Tip head on h-BaFe particulate tape recording media", Apr. 25–29, 2011, Intermag Conference 2011, Taipei International Convention Center, Taipei, Taiwan.
2. **J. Lee**, V. Alexandrakis, M. Fuger, D. Suess, D. Niarchos and J. Fidler, "Micromagnetic simulations on FePt L1₀/A1 phase graded media", Apr. 25–29, 2011, Intermag Conference 2011, Taipei International Convention Center, Taipei, Taiwan.
3. M. Albrecht, C. Schulze, C. Brombacher, **J. Lee**, J. Fidler, M. Faustini, D. Grosso, D. Makarov and M. Grobis, "Magnetic films on templates: A route towards percolated media", Apr. 25–29, 2011, Intermag Conference 2011, Taipei International Convention Center, Taipei, Taiwan.

2010

4. **J. Lee**, D. Makarov, C. Brombacher, B. Dymerska, M. Fuger, D. Suess, M. Albrecht and J. Fidler, "TEM Studies on RTA treated FePt-based Exchange Coupled Composite Media", Nov. 14–18, 2010, MMM Conference 2010, Hyatt Regency Atlanta, Atlanta, USA.

5. C. Vogler, F. Bruckner, M. Fuger, **J. Lee**, J. Fidler and D. Suess, "3D-MRAM Device based on Resonant AC-Spin Polarized Currents", Nov. 14–18, 2010, MMM Conference 2010, Hyatt Regency Atlanta, Atlanta, USA.
6. M. Fuger, **J. Lee**, J. Fidler, D. Suess and T. Schrefl, "Modeling of the influence of the passivation shell on the magnetization process of advanced MP tape recording films", Nov. 14–18, 2010, MMM Conference 2010, Hyatt Regency Atlanta, Atlanta, USA.
7. F. Bruckner, C. Vogler, M. Fuger, **J. Lee**, J. Fidler and D. Suess, "Simultaneously solving magnetostatic Maxwell equations and LLG for extended micromagnetic simulations", Nov. 14–18, 2010, MMM Conference 2010, Hyatt Regency Atlanta, Atlanta, USA.
8. M. Fuger, **J. Lee**, J. Fidler, D. Suess, "Micromagnetic study of the recording performance of advanced h-BaFe based tape recording materials", Aug. 23–28, 2010, Joint European Magnetic Symposia (JEMS) 2010, Jagiellonian University, Krakaw, Poland.
9. **J. Lee**, D. Makarov, B. Dymerska, C. Brombacher, J. Fidler, M. Fuger, D. Suess and M. Albrecht, "TEM study of interface properties of FePtCu-based exchange coupled composite media", Aug. 23–28, 2010, Joint European Magnetic Symposia (JEMS) 2010, Jagiellonian University, Krakaw, Poland.
10. Josef Fidler, **Jehyun Lee**, Markus Fuger, Dieter Suess, and Thomas Schrefl, "Material and Nanosensor design by finite element Micromagnetic Modeling", Jun. 7–8, 2010, ROMSC 2010, "Alexandru Ioan Cuza", University of Iasi, Iasi, Romania.
11. D. Makarov, C. Brombacher, **J. Lee**, J. Fidler and M. Albrecht, "Scaling dependence of the switching field of the hard layer in perpendicular FePt-based exchange coupled composite media", Sep. 13–17, 2010, Nano 2010, University La Sapienza, Rome, Italy.
12. Josef Fidler, **Jehyun Lee**, Markus Fuger, Dieter Suess, and Thomas Schrefl, "Particular and granular magnetic nanostructures for advanced magnetic recording schemes", Sep. 13–17, 2010, Nano 2010, University La Sapienza, Rome, Italy.
13. **Jehyun Lee**, Josef Fidler, Thomas Uhrmann, Theodore Dimopoulos, and Hubert Brückl, "TEM study on the diffusion process of Si/NiFe Schottky barrier and Si/MgO/NiFe tunneling diode", Jan. 18-22, 2010, Joint MMM/Intermag Conference 2010, Marriott Wardman Park, Washington D.C., USA.
14. M. Fuger, **J. Lee**, J. Fidler, D. Suess and T. Schrefl, "Micromagnetic study of particulate media reversal for tape recording", Jan. 18-22, 2010, Joint MMM/Intermag Conference 2010, Marriott Wardman Park, Washington D.C., USA.
15. G. Fiedler, M. Janisch, **J. Lee**, M. Fuger, J. Fidler and T. Schrefl, "Direct calculation of the attempt frequency of magnetic nanostructures using FEM", Jan. 18-22, 2010, Joint MMM/Intermag Conference 2010, Marriott Wardman Park, Washington D.C., USA.

2009

16. Thomas Schrefl, David Hahn, M.A. Bashir, Alexander Goncharov, Gino Hrkac, Julian Dean, **Jehyun Lee**, and Dieter Suess, "Numerical methods help to optimize hard disks", The 20th Magnetic Recording Conference (TMRC), Oct. 5–7, 2009, University of Alabama, Tuscaloosa, AL, USA.

17. **J. Lee**, J. Fidler, V. Alexandrakis, and D. Niarchos, "High Resolution TEM study of exchange coupled FePt/CoPt thin films", Microscopy Conference 2009, Aug. 30 – Sep. 4, 2009, Congress Graz, Graz, Austria.
18. **Jehyun Lee**, Dieter Suess, Thomas Schrefl, Josef Fidler, "Head Field Gradient Effect on Magnetic Recording", Intermag Conference 2009, May 4-8, 2009, Convention Center, Sacramento, USA.

2008

19. **Jehyun Lee**, Dieter Suess, Josef Fidler, Thomas Schrefl, Eu Sun Yu, You Sub Lee, Kyu Hwan Oh, "Contribution of the Convex Surfaces on Magnetostatic Interaction in Granular Medium", Asian Magnetism Conference 2008, December 9-13, 2008, Paradise Hotel, Busan, Korea.
20. **Jehyun Lee**, Josef Fidler, Dieter Suess, Thomas Schrefl, Sanghwan Park, Kyu Hwan Oh, "Micromagnetic analysis of the switching field of CoCrPt-SiO₂ and CoPt-TiO₂ bilayers", 53rd MMM Conference 2008, November 10-14, 2008, Hilton Austin Convention Center, Austin, Texas, USA.
21. **Jehyun Lee**, Dieter Suess, Thomas Schrefl, Kyu Hwan Oh, Josef Fidler, "Nucleation field reduction due to convex surface in magnetic recording media", Joint European Magnetic Symposia 2008, September 14-19, 2008, Trinity College, Dublin, Ireland.
22. Josef Fidler, **Jehyun Lee**, Dieter Suess and Thomas Schrefl, "Tuning of coercive field of nanostructured hard magnetic films", Workshop on Rare Earth Permanent Magnets, September 8-10, 2008, Movenpick Hotel, Kronoss, Greece.
23. Josef Fidler, Dieter Suess, **Jehyun Lee** and Thomas Schrefl, "Exchange-coupled magnets: Challenges", Workshop on Research Trends in Novel Magnets for Electromagnetic Applications, September 3-5, Hotel Santorini Palace, Santorini, Greece.

2007

24. **Jehyun Lee**, Dieter Suess, Rok Dittrich, Thomas Schrefl, Kyu Hwan Oh and Josef Fidler, "Contribution of the convex grain surface on magnetic behavior", 52nd MMM Conference 2007, November 5-9, 2007, Marriott Waterside Hotel, Tampa, USA
25. **Jehyun Lee**, M. Kim, D. Suess, T. Schrefl, K. Oh, J. Fidler, "Magnetic Characteristics of Co nano particle", Joint MMM/Intermag Conference 2007, January 7-11, 2007, Marriott Waterside Hotel & Marina, Baltimore, USA.

2006

26. Thomas Schrefl, Dieter Suess, **Jehyun Lee**, Rok Dittrich, Florian Dorfbauer, Josef Fidler, Manfred Schabes, "Nanomagnetic simulations of recording media", APS March meeting, March 13-17, 2006, The Baltimore Convention Center, Baltimore, USA.
27. **J.Lee**, D.Suess, T.Schrefl, K.Oh and J. Fidler, "Contribution of non-uniform magnetic states on Gilbert-damping in perpendicular media", Joint MMM/Intermag Conference, May 8-12, 2006, Town & Country Hotel, San Diego, USA.
28. **J.Lee**, D.Suess, T.Schrefl, K.Oh and J. Fidler, "Magnetic recording on patterned media prepared by ion beam irradiations", Joint MMM/Intermag Conference, May 8-12,

2006, Town & Country Hotel, San Diego, USA.

29. **Jehyun Lee**, Dieter Suess, Thomas Schrefl, Kyu Hwan Oh, Josef Fidler, "Magnetic Characteristics of Ferromagnetic Nanotube", ICM2006, August 20-25, 2006, Kokusaikaikan, Kyoto, Japan.

2005

30. Josef Fidler, Dieter Suess, Karina Porath, **Jehyun Lee**, Thomas Schrefl, "Optimization of advanced perpendicular media by micromagnetic modeling", The 16th Annual Magnetic Recording Conference, August 15-17, 2005, Stanford University, CA, USA.

2004

31. **J. Lee**, S. Jang, Y. Kim, K. Oh, D. Kim and K. Kim, "Effect of the thickness of base layer on properties of Si-based magnetic tunnel transistor", 9th Joint MMM-Intermag Conference, January 5-9, 2004, Anaheim, CA, USA.

2003

32. **J. Lee**, K. Oh, H. Kim and K. Kim, "Magnetization reversal process of the nanosized elliptical permalloy magnetic dots with various aspect ratios". International Conference on Magnetism 2003, July 27-August1, 2003, Roma, Italy.

PUBLICATIONS ON SCI JOURNALS (25)

2011

1. **Jehyun Lee**, Vasilis Alexandrakis, Markus Fuger, Barbara Dymerska, Dieter Suess, Dimitris Niarchos and Josef Fidler, "FePt L10 / A1 graded media with a rough interphase boundary", Appl. Phys. Lett. 98 (2011) 222501.
2. V. Alexandrakis, Th. Speliotis, E. Manios, D. Niarchos, J. Fidler, and **Jehyun Lee**, G. Varvaro "Hard/graded exchange spring composite media based on FePt", J. Appl. Phys. 109 (2011) 07B729.

2010

3. C. Schulze, M. Faustini, **J. Lee**, H. Schletter, P. Krone, M. Gass, K. Sader, A. L. Bleloch, M. Fuger, D. Suess, J. Fidler, M. U. Lutz, U. Wolff, V. Neu, M. Hietschold, D. Makarov and M. Albrecht "Magnetic Films On Nanoperfoated Templates: A Route Towards Percolated Perpendicular Media", Nanotechnology 21 (2010) 495701.
4. J. Schratzberger, **J. Lee**, M. Fuger, J. Fidler, G. Fiedler, T. Schrefl, and D. Suess "Validation of the transition state theory with Langevin-dynamics simulations", J. Appl. Phys. 108 (2010) 033915.
5. **Jehyun Lee**, Markus Fuger, Josef Fidler, Dieter Suess, Thomas Schrefl and Osamu Shimizu, "Modeling of the write and read back performances of hexagonal Ba-ferrite particulate

media for high density tape recording", J. Magn. Magn. Mater. 322 (2010) 3869.

6. D. Suess, D. Punz, **J. Lee**, M. Fuger, J. Fidler and T. Schrefl, "Theory and Micromagnetics of Pinning Mechanism at Cylindrical Defects in Perpendicular Magnetic Films", J. Appl. Phys. 107 (2010) 113926.
7. **Jehyun Lee**, Thomas Uhrmann, Theodoros Dimopoulos, Hubert Brückl, and Josef Fidler, "TEM Study on Diffusion Process of NiFe Schottky and MgO/NiFe Tunneling Diodes for Spin Injection in Silicon", IEEE Trans. Magn. 46 (2010) 2067.
8. Denys Makarov, **Jehyun Lee, (D. Makarov and J. Lee are equally contributed)** Christoph Brombacher, Christian Schbert, Markus Fuger, Josef Fidler and Manfred Albrecht, "Perpendicular FePt-based exchange-coupled composite media", Appl. Phys. Lett., 96 (2010) 062501
9. V. Alexandrakis, D. Niarchos, K. Mergia, **Jehyun Lee**, J. Fidler, I. Panagiotopoulos, "Magnetic Properties of Graded Al/L10 films obtained by heat-treatment of FePt/CoPt multilayers", J. Appl. Phys., 107 (2010) 013903.

2009

10. **Jehyun Lee**, Dieter Suess, Thomas Schrefl, Julian Dean, Josef Fidler, "Increases in effective head field gradients in exchange spring media", Appl. Phys. Lett., 95 (2009) 172509.
11. G. Winkler, D. Suess, **J. Lee**, J. Fidler, M. A. Bashir, J. Dean, A. Goncharov, G. Hrkac, S. Bance, and T. Schrefl, "Microwave-assisted three-dimensional multilayer magnetic recording", Appl. Phys. Lett., 94 (2009) 232501.
12. D. Suess, **J. Lee**, J. Fidler, H. S. Jung, E. M. T. Velu, W. Jiang, S. S. Malhotra, G. Bertero, and T. Schrefl, "Effect of Intergranular Exchange on Thermal Stability and Coercive Field of Perpendicular, Single Phase, Exchange Spring, and Coupled Granular Continuous", IEEE Trans. Magn., 45 (2009) 88.
13. Ji Woo Kim, Oliver Friedrichs, Jae-Pyoung Ahn, Do-Hyun Kim, Seul-Cham Kim, Arndt Remhof, Hee-Suk Chung, **Jehyun Lee**, Jae-Hyeok Shim, Young Whan, "Transmission electron microscopy study on the microstructural change of 2LiBH₄/Al with hydrogen sorption cycling", Scripta Materialia, 60 (2009) 1089.
14. **Jehyun Lee**, Dieter Suess, Thomas Schrefl, Eu Sun Yu, You Sub Lee, Kyu Hwan Oh and Josef Fidler, "Contribution of Convex Surfaces to Magnetostatic Interaction in Granular Medium", IEEE Trans. Magn., 45 (2009) 2655.
15. **Jehyun Lee**, Dieter Suess, Thomas Schrefl, Kyu Hwan Oh and Josef Fidler, "Grain geometry induced reversal behavior alteration", J. Phys. D: Appl. Phys., 42 (2009) 045005.
16. D. Suess, **J. Lee**, J. Fidler, T. Schrefl, "Exchange-coupled perpendicular media", J. Magn. Magn. Mater., 321 (2009) 545.

2008

17. **Jehyun Lee**, Dieter Suess, Thomas Schrefl, Kyu Hwan Oh and Josef Fidler,

"Contribution of the shrunk interface and the convex surface of grains on magnetic behavior in granular film", J. Appl. Phys., (2008).

2007

18. **J. Lee**, D. Suess, T. Schrefl, K. Oh, J. Fidler, "Magnetic Characteristics of Ferromagnetic Nanotube", J. Magn. Magn. Mater., 310 (2007) 2445.
19. **J. Lee**, D. Suess, T. Schrefl, K. Oh, J. Fidler, "Micromagnetic study of recording on ion-irradiated granular-patterned media", J. Magn. Magn. Mater., 319 (2007) 5.
20. D. Suess, S. Eder, **J. Lee**, R. Dittrich, J. Fidler, J. W. Harrell, T. Schrefl, G. Hrkac, M. Schabes, N. Supper, A. Berger, "Reliability of Sharrocks equation for exchange spring bilayers", Phys. Rev. B., 75 (2007) 174430.

2006

21. **J. Lee**, D. Suess, T. Schrefl, K. Oh, J. Fidler, "Contribution of Local Incoherency on Gilbert-Damping", IEEE Trans. Magn., 42 (2006) 3210.

2005

22. Jang, S.H., Kim, Y.W., **Lee, J.H.**, Kim, K.Y., "Si -based magnetic tunnel transistor with single CoFe base layer ", J. Appl. Phys., 98 (2005) 094502.

2004

23. **J. Lee**, K. Oh, H. Kim, K. Kim, "Magnetization reversal process of the nanosized elliptical permalloy magnetic dots with various aspect ratios", J. Magn. Magn. Mater., 272-276 (2004) 736.
24. S. Jang, T. Kang, **J. Lee**, K. Kim, "Si-based magnetic tunnel transistor with high transfer ratio", J. Magn. Magn. Mater., 272-276 (2004) 1930.
25. D. Kim, J. Kim, B. Park, J. Lee, J. Kim, **J. Lee**, J. Chang, H. Kim, I. Kim, Y. Park, "SrFeO3 nanoparticles-dispersed SrMoO4 insulating thin films deposited from Sr2FeMoO6 target in oxygen atmosphere", Appl. Phys. Lett., 84 (2004) 5037.

OTHERS (3)

2010

1. **Program Committee, Editor of the Book of Proceedings**
EU-Korea Conference on Science and Technology 2010,
July 29-31, 2010, The Vienna Imperial Riding School, Vienna, Austria.

2007

2. **Official home page design, official poster design and web programming**,
The 4th Conference of the Asian Consortium on Computational Materials Science,

September 13-16, 2007, Korea Institute of Science and Technology, Seoul, Korea.

2006

3. Official poster design

The International Conference on Advanced Structural Steels, August 22-24, 2006, Gyeongju Hilton Hotel, Gyeongju, Korea.

AWARDS AND REMARKS

1. Best poster award (2011)

J. Lee, V. Alexandrakis, M. Fuger, D. Suess, D. Niarchos and J. Fidler, "Micromagnetic simulations on FePt L1₀/A1 phase graded media", Apr. 25-29, 2011, Intermag Conference 2011, Taipei International Convention Center, Taipei, Taiwan.

2. Chosen as "Research Highlights" in Journal of Applied Physics (2010)

V. Alexandrakis, D. Niarchos, K. Mergia, **Jehyun Lee**, J. Fidler, I. Panagiotopoulos, "Magnetic Properties of Graded Al/L10 films obtained by heat-treatment of FePt/CoPt multilayers", J. Appl. Phys., 107 (2010) 013903.

COMPUTER SKILLS

Operating Systems :	MS DOS, MS Windows, Linux
Word Processing :	MS Office
Programming Languages :	C/C++, Visual Basic, Python, HTML
Graphics Programs :	Digital Micrograph, Adobe Photoshop, Adobe Illustrator, Gimp
CAD and Visualizations :	Cadence, AutoCAD, GiD, MicroAVS, Tecplot, Paraview
Mathematical Software :	Origin, Matlab, Mathematica

EXPERIMENTAL SKILLS

Specimen Preparation :	PECVD, DC/RF magnetron sputtering, Ion Milling, PIPS
Micro / Nano Fabrication :	Mask aligner(MA-6), Wire bonder
Microscopy :	TEM specimen preparation (Vienna University of Technology)
	AFM (licence A : Korea Institute of Science and Technology)
	MFM (licence A : Korea Institute of Science and Technology)
	TEM (licence C : Seoul National University)
	TEM (full time user, Vienna University of Technology)

LANGUAGES

Native Language :	Korean	
Other Languages :	English	German
Reading skills	good	basic
Writing skills	good	basic
Verbal skills	good	basic